RUHR-UNIVERSITÄT BOCHUM

RUB

Computational study of metal-support interactions for carbon-supported palladium nanoparticles

Dissertation

zur Erlangung des Doktorgrades der Naturwissenschaften

vorgelegt von **Lisa Warczinski**

Ruhr-Universität Bochum

Lehrstuhl für Theoretische Chemie

RUHR-UNIVERSITÄT BOCHUM

RUB

Computational study of metal-support interactions for carbon-supported palladium nanoparticles

Dissertation

zur Erlangung des Doktorgrades der Naturwissenschaften

vorgelegt von **Lisa Warczinski**

Datum der Abgabe: 07.10.2020
Datum der Verteidigung: 11.12.2020
Gutachter: Prof. Dr. Christof Hättig
Prof. Dr. Robert Franke
Prof. Dr. Reinhold Fink

Ruhr-Universität Bochum
Fakultät für Chemie und Biochemie
Lehrstuhl für Theoretische Chemie

Die vorliegende Dissertation wurde in der Zeit von Oktober 2017 bis Oktober 2020 am Lehrstuhl für Theoretische Chemie an der Fakultät für Chemie und Biochemie der Ruhr-Universität Bochum angefertigt. Die Arbeit wurde am 07.10.2020 bei der Fakultät eingereicht und am 11.12.2020 verteidigt.

Gutachter: Prof. Dr. Christof Hättig
Prof. Dr. Robert Franke
Prof. Dr. Reinhold Fink

Acknowledgment

Throughout my doctorate studies and the writing process of this thesis I have received a great deal of support and assistance.

I would first like to thank Professor Dr. Christof Hättig for supervising me and giving me the opportunity to work on such an interesting project. I greatly acknowledge all his efforts, guidance and help, that brought my work to a higher level.
Furthermore, I am thankful to Professor Dr. Robert Franke who steadily supported me all the way since my Master's studies and also was supervising my doctorate.
Professor Dr. Reinhold Fink I would like to thank for being the external reviewer of this thesis.
I am grateful to the members of the Laboratory of Industrial Chemistry of Professor Dr. Martin Muhler, especially to Dr. Baoxiang Peng, for the pleasant and fruitful collaboration and for initiating this collaborative project.

Furthermore, I thank all colleagues of the theoretical chemistry department, especially Dr. Alireza Marefat Khah and Dr. Sebastian Wingbermühle, for numerous productive discussions and valuable scientific input.
My special thanks belong to Prof. Dr. Volker Staemmler for all his guidance and support in the last years.
For help with administration and technical issues I would like to thank Sylke Kohlpoth, Doris Fischer–Niess, Dr. Holger Langer, Dr. Harald Forbert and Niklas Caesar.

My family has been unconditionally supportive of me throughout this entire process, has made numerous sacrifices and encouraged me several times to follow my way. For this, I am extremely grateful.

Finally, I acknowledge funding from the Deutsche Forschungsgemeinschaft within the framework of the Sino-German initiative "Novel Functional Materials for Sustainable Chemistry" as well as from the Studienstiftung des Deutschen Volkes through a doctoral fellowship.

Lisa Warczinski
Bochum, October 2020

Contents

Part I

Introductory Remarks

1 Introduction

1.1 Motivation and Aim of the Project

The modern definition of catalysis was originally proposed by Wilhelm Ostwald around the year 1900. It states that a catalyst is a substance which affects the rate of a chemical reaction without being part of its end products.[1]

During a chemical reaction bonds between atoms are cleaved and new bonds are formed. The energy barrier, which has to be surmounted by the reactants, is called activation energy. The probability of a reaction taking place increases with higher temperatures or with lower activation energies. Catalysts decrease the activation energy of a reaction without being part of any of its end products. Accordingly, in the last step of each reaction cycle the catalyst is rebuilt and separated from the reaction reactants and products. The catalyst is then ready to take part in the next reaction cycle.[2]

Catalysts allow for the highly selective formation of desired products at rates that are commercially feasible. Therefore, for almost 90 % of all commercially produced chemicals a catalyst is utilized at some stage of the production process. The global industrial catalyst market was valued at over USD 17 billion in 2014 and was expected to reach USD 22 billion by 2020, corresponding to more than 6,400 kilotons in volume[3]. The production of thousands of products required by modern societies, including pesticides, polymers, antibiotics, cosmetics and cleaning products, would not be possible without catalysts. Furthermore, catalysts are essential in advancing the reduction of air and water pollution.[4,5]

Industrial catalysis is divided into two types: homogeneous and heterogeneous catalysis. In heterogeneous catalysis the catalyst and the reactants are located in different physical phases, whereas in homogeneous catalysis both are located in the same phase. As the separation of the catalyst from the reactants and the products

is less demanding in heterogeneous catalysis compared to homogeneous catalysis, most industries prefer to utilize heterogeneous catalysis (global industrial catalyst market share of around 65 % in 2019[6]).[4]

The most common catalysts in industrial heterogeneous catalysis are metals dispersed on high-surface-area solids. These metal nanoparticles have a size of 1 to 20 nm.[5] The high-surface-area solids serve as their support and make the catalyst more easily separable from fluid products and reactants. Furthermore, the support material enables the catalyst to be packed into reactor vessels and avoids its agglomeration. A large surface area formed by the support's pores is essential for highly active catalysts.[4]
Catalysis with supported metal nanoparticles has first been used in photography and in the decomposition of hydrogen peroxide in the 19th century.[7] In 1940, Nord reported on the use of supported metal nanoparticles in nitrobenzene reduction.[8] Another pioneering catalytic application of supported metal nanoparticles was the hydrogen atom transfer between benzene and cyclohexane performed by Parravano in 1970.[9] Starting with Haruta's study on the CO oxidation catalyzed by oxide-supported gold nanoparticles[10], several studies on the use of supported nanoparticles in the fields of redox catalysis, photocatalysis, hydrogenation of unsaturated substrates and oxidation have been performed.[11] Since the beginning of the 21st century, the number of publications in the field of catalysis with supported metal nanoparticles has increased exponentially. The main goals of this research are to achieve improvements in catalyst activities and selectivities as well as to deepen the understanding of the underlying catalytic mechanisms.[12]

Today, the metal nanoparticles are often supported by novel 2D carbon support materials[13], e.g. by single-walled or multi-walled carbon nanotubes, which possess, due to their unique nanostructure, exceptional properties, such as a

very high thermal stability[14]. A quite recently developed carbon material is mesoporous carbon (CMC), which is composed of amorphously linked graphitic domains. As CMC shows a very large surface area and can be easily synthesized at a low cost, it is a promising alternative support material for metal nanoparticle catalysts.[15]

Both, carbon nanotubes and CMC, can be doped with nitrogen- and oxygen-containing functional groups. In recent years, this modification of carbon materials has attracted tremendous attention. Several studies have revealed that introducing surface defects and heteroatoms in the carbon support material significantly affects the metal-support interactions of the catalyst systems and, thus, tunes the catalytic properties of the supported nanoparticles.[16]

One of the most important industrial applications of metal nanoparticles on carbon support materials in heterogeneous catalysis is the hydrogenation of aromatic compounds. For instance, the catalytic hydrogenation of chloronitrobenzenes produces chloroanilines, which are important precursors for many industrially produced organic materials.[17]

Even though the process of heterogeneous catalysis has widely been utilized in the chemical industry for more than a century and the first industrial heterogeneous catalysis dates back to the Haber-Bosch process starting in the year 1913[18], the details of heterogeneous catalysis are still not completely understood. As a consequence, numerous challenges in industrial applications, e.g. in industrial hydrogenations, remain.[19] For example, the process of dechlorination significantly reduces the selectivity of the catalytic hydrogenation of chloronitrobenzenes to chloroanilines.[17] This side reaction can only be avoided by adding basic molecules, such as the quinoline molecule, to the system. A promising alternative to admix such additional dehalogenation inhibitors to the reaction could be the application of nitrogen-containing mesoporous carbon (NMC) as a strong basic support, which

has seldom been explored so far. Another example for the lack of a detailed understanding of heterogeneous catalysis is the hydrogen spillover process. When hydrogen is attached to a supported metal nanoparticle catalyst, the hydrogen atoms could migrate from the metal to the support material. It has been shown that this so-called 'hydrogen spillover' process might play an important role in hydrogenation reactions.[20] However, the elementary steps of hydrogen spillover and its detailed effects on hydrogenation reactions have not been understood satisfyingly.[21]

In general, heterogeneous catalysis on supported metals is very difficult to study as the process is very complex and goes across several scales of space and time. The catalytic performance is affected by multiple aspects, e.g. by the type and structure of the support and of the nanoparticles, by diffusion processes or by transfers of heat and mass.[22] Accordingly, for a full description of heterogeneous catalysis on supported metal nanoparticles, metal-support interactions, metal-substrate interactions, surface processes and potentially interactions with the solvent have to be taken into account. As an example, the relatively simple gas phase hydrogenation of ethylene on carbon-supported Pd nanoparticles can already depend on several different interactions, e.g. on hydrogen-Pd, ethylene-Pd, carbon-Pd, hydrogen-carbon, ethylene-carbon or ethylene-hydrogen interactions.
The catalyzed reaction processes occur typically on femto- to picosecond timescales. Most established spectroscopy techniques applicable to such heterogeneous systems possess a resolution in the order of microseconds. Accordingly, these techniques can only reflect macroscopic and average information.[22] Consequently, heterogeneous catalysis on supported metals should not be investigated by purely experimental means. Quantum chemistry holds a great potential for supporting and advancing the experimental research in this field as it provides detailed insights into reaction pathways and mechanisms, which can complement experimental

results.[23] Density functional theory (DFT), the preferred method for studies on heterogeneous catalysis, can obtain accurate total energies with comparable low computational costs. Bond lengths and lattice constants of solids can be predicted within one or two hundredths of an angstrom. Furthermore, vibrational frequencies can be obtained with an accuracy of around 5 % and adsorption energies within around 0.15 eV.[23]

However, the full potential of quantum chemistry and of combined experimental and theoretical approaches in the field of heterogeneous catalysis on supported metals has not yet been used. For example, there are numerous computational studies on the interaction between reaction substrates and metal catalysts. Though, already the interaction between the metal nanoparticles and the support materials has not been studied satisfyingly[24]. Most of the few existing studies on metal-support interactions in catalysis use either metal atoms or very small metal clusters, which are not able to model real reactions on metal nanoparticles.[25,26] Another example is the investigation concerning dopants in the support material. Whereas several computational studies on the electronic structure of carbon materials and their functionalization with nitrogen- and oxygen-containing groups exist, the influence of nitrogen- and oxygen dopants on the supported metal nanoparticles has seldom been explored so far.[27] Computational studies on the influence of nitrogen- and oxygen dopants being present simultaneously are not available at all.

The aim of this project is to improve the understanding of heterogeneous catalysis and to allow for the design of novel more active, more selective and more sustainable catalysts. In detail, we intend to reveal the influence of support materials on the electronic properties of metal catalysts and their influence on the mechanisms and barriers of the catalyzed reactions.
For this purpose, we perform a density functional theory (DFT) study and focus

on promising catalyst systems and their most important industrial application, i.e. on mesoporous carbon supported palladium nanoparticles (Pd/CMC) and on catalytic hydrogenations. One of our main interests is to reveal the influence of nitrogen dopants in nitrogen-containing mesoporous carbon (NMC) on the metal-support interactions and on the catalyzed hydrogenation reactions.
The findings of our computational studies should establish a correlation with experimental results. The computational study is performed as a part of the project 'Mesoporous Carbon Supported Metal Catalysts for Sustainable Hydrogenation Reactions', which is funded by the Deutsche Forschungsgemeinschaft and the National Natural Science Foundation of China. In the scope of this project we collaborate with the Laboratory of Industrial Chemistry of Professor Martin Muhler at the Ruhr-University Bochum, especially with Dr. Baoxiang Peng and Dr. Bin Hu, who perform state-of-the-art experiments and spectroscopy on transition metal nanoparticle decorated mesoporous carbon.

The following introductory sections will provide all the basic information of this project. On the one hand, the actual state of research at the beginning of the project is described and all leading research questions are defined (Section 1.2). On the other hand, the relevant computational methodology is shown and evaluated (Chapter 2). In detail, Section 2.1 gives an overview of the different available surface models. Periodic boundary approaches (Section 2.1.1) as well as finite cluster approaches (Section 2.1.2) are presented and their strengths, weaknesses and applicability are compared. Section 2.2 gives a detailed description of the chosen computational approach for this project. In Section 2.2.1 the setup of the model systems is shown. Subsequently, the utilized computational methods are described and discussed (Section 2.2.2). Moreover, the special requirements of the catalyst systems for the setup of the computational studies are compiled (Section 2.2.3).

1.2 State of Research and Research Questions

This section will give an overview of the experimental studies that motivated our computational study on carbon-supported Pd nanoparticles. The experimental results lead to several open questions, which could only be answered with the help of quantum chemistry and, therefore, became the leading research questions of this project. Furthermore, this section provides a review of computational studies on Pd/CMC, Pd/NMC or similar systems, which were available at the starting point of the project and were directly related to our research questions.

This project was mainly motivated by the idea that nitrogen-doped mesoporous carbon (NMC) could be a promising support material for Pd nanoparticles applied in hydrogenation reactions.
First of all, this idea was based on the relatively high catalytic activity of mesoporous carbon supported metal nanoparticles in hydrogenations compared to their active carbon (AC) supported or oxide-supported counterparts. In 2010, Shi et al.[28] prepared Co-Mo/CMC and Ni-Mo/CMC catalysts and utilized these in the hydrodesulfurization of organic sulfides. They found that Co-Mo/CMC was much more active than Co-Mo/AC and the commercial catalyst Co-Mo/γ-Al_2O_3 for the hydrodesulfurization of thiophene. The same effect could be observed for Ni-Mo/CMC applied in the hydrodesulfurization of dibenzothiophene, which showed a significantly higher catalytic activity compared to the commercially available FH-98 catalyst (composed of WO_3, MoO_3 and NiO). In 2011, Chen et al.[29] reported on the hydrogenation of the large molecule β-sitosterol to β-sitostanol using Pd/CMC. Also in this study, the mesoporous carbon supported catalyst was shown to provide a much higher activity compared to the active carbon supported catalyst (Pd/AC), which was explained with the larger pore size of CMC in favor of the diffusion of larger molecules.

Secondly, several experimental studies on the nitrogen doping of carbon nanotubes indicated that the nitrogen doping of mesoporous carbon might lead to extraordinary catalytic activities and selectivities. As an example, Xia et al.[30] synthesized Pd nanoparticles supported on nitrogen-doped carbon nanotubes (Pd/NCNT) and utilized them in the hydrogenation of cyclooctadiene. Compared to the nitrogen-free oxygen-functionalized carbon nanotube system (Pd/OCNT), Pd/NCNT showed a much better catalytic performance in terms of activity, selectivity and stability.

To allow for the design and utilization of novel Pd/NMC catalysts possessing the desired high catalytic performance in hydrogenation reactions, it is essential to understand the relevant metal-support interactions as well as the fundamental processes on the catalyst surface. As a first step, the nitrogen-free Pd/CMC system has to be investigated as this unmodified carbon support material serves as a reference for studying the effects of nitrogen doping later.
At the starting point of this project, there were only a few computational studies on the metal-support interactions between transition metal clusters and carbon materials available. In 2013, Auer et al.[31] studied the interactions of Pt clusters containing 1, 10, 18, and 37 atoms with small graphene sheets using density functional theory (DFT). They found that the metal-support interactions for small Pt clusters are composed of covalent and dispersive contributions and that the dispersion contribution increases with the size of the cluster. In 2017, Lenz Baldez et al.[24] performed a periodic DFT study on transition metal clusters of Ti, Pd, Pt and Au containing 6 and 13 atoms and their interaction with graphene. Their results indicate that the binding strength of the transition metal clusters to graphene can be tuned by varying the size and the composition of the clusters.
A further step towards the study of hydrogenation reactions on Pd/CMC is to investigate the interaction of hydrogen with the carbon-supported Pd nanoparticles.

The hydrogen adsorption on Pd crystal surfaces and free Pd clusters has been the subject of several computational studies. As an example, Lischka et al.[32] investigated the adsorption of atomic and molecular hydrogen on the Pd (210) surface using periodic DFT calculations. In this study, the authors were able to reveal the details of the interaction of a H_2 molecule with Pd, which is composed of a Pd 5s - H_2 σ_g and of a Pd $4d_{xz}$ - H_2 σ_u^* charge transfer as well as of a repulsive interaction between the Pd $4d_{z^2}$ and the H_2 σ_g orbital (based on a coordinate system with the x-axis parallel to the H_2 bond and the z-axis along the line from the Pd atom to the H_2 bond center). In 2017, Shamsiev et al.[33] performed a DFT study on the hydrogen dissociation on the Pd_{21} cluster. It was found that, in the most energetically stable configuration of hydrogen on Pd_{21}, two H atoms occupy adjacent face-centered cubic (fcc) sites. Furthermore, they reported that H atoms can diffuse on the cluster with low barriers.

For the interaction of hydrogen with carbon-supported Pd clusters only very few computational studies were available at the starting point of this project. In 2015, Ramos-Castillo et al.[26] studied the hydrogen adsorption on carbon-supported Pd_1, Pd_2, Pd_3 and Pd_4 using periodic DFT and found that the H_2 adsorption energy depends on the cluster size and on the adsorption site. In 2017, Granja-DelRío et al.[34] compared the hydrogen adsorption on free and on carbon-supported Pd_6 clusters in a periodic DFT study. It was found that both free and carbon-supported Pd_6 can adsorb and dissociate several hydrogen molecules. However, the free Pd_6 shows a significantly higher hydrogen saturation limit compared to the carbon-supported cluster as the carbon support sterically hinders the adsorption and dissociation of hydrogen at the bottom of the cluster.

Based on these results, our research on the Pd/CMC systems was determined by the following questions:

i What are the metal-support interactions in Pd/CMC made up of? Are these interactions covalent or do they also include dispersion interactions?

ii How does hydrogen adsorption proceed on carbon-supported Pd nanoparticles? Are there any differences compared to free Pd nanoparticles?

iii What are preferential adsorption sites of hydrogen on carbon-supported Pd nanoparticles? Are hydrogen atoms mobile on the Pd surface?

When the basic properties of Pd/CMC are sufficiently understood, the effect of nitrogen doping can be studied in detail.

The few existing computational studies on the effect of nitrogen doping on carbon-supported transition metals suggested that doping with nitrogen-containing functional groups strengthens the metal-support interactions between the transition metal and the carbon support material. In their DFT study on carbon-supported Pt clusters Auer et al.[31] also introduced graphitic nitrogen atoms in the graphene surface (an sp^2 hybridized N atom replaces a carbon atom bound to three other carbon atoms) and found that these increase the adsorption energy of the Pt clusters due to stronger covalent contributions. Rangel et al.[35] performed periodic DFT calculations and reported binding energies of small Pd clusters (1 to 4 atoms) on pyridinic nitrogen doped graphene (sp^2 hybridized N atom bound to only two sp^2 hybridized C atoms) that were four times higher compared to nitrogen-free graphene surfaces. Results of Bulushev et al.[36] furthermore indicated that pyridinic nitrogen dopants can significantly affect the heterogeneous catalyzed reactions. In a joint computational (DFT) and experimental study, they found that the catalytic activity of Pd supported on nitrogen-doped graphene in the decomposition of formic acid was three times higher than the catalytic activity of Pd supported on nitrogen-free carbon materials. Based on their quantum chemical calculations, Bulushev et al. proposed that the observed higher catalytic activity can be explained with the existence of Pd^{2+} species, stabilized by pyridinic nitrogen atoms.

For our study on Pd/NMC the following questions remained:

iv How does nitrogen doping affect the metal-support interactions of carbon-supported Pd nanoparticles? What is the effect of different nitrogen species like graphitic and pyridinic nitrogen?

v How does the nitrogen doping affect the properties of the supported Pd nanoparticles?

vi Where do the higher catalytic activity and higher selectivity in the nitrogen-doped systems compared to the nitrogen-free systems come from?

Besides the effect of nitrogen doping, the possible effect of hydrogen spillover on carbon-supported Pd catalysts also motivated parts of this project. During the first months of the project, Yang et al.[37] performed a study on the hydrogenation of nitrobenzene to aniline on a Pt/NMC catalyst. Based on temperature-programmed nitrobenzene desorption studies they found that the capacity of Pt/NMC for storing hydrogen is much higher compared to free Pt, which indicates the formation of spillover hydrogen species on the NMC support material. Furthermore, it was concluded that these spillover species are mobile on the support material and can migrate back to the Pt nanoparticles, where they could take part in the nitrobenzene hydrogenation. As a second step, Yang et al. repeated the nitrobenzene desorption experiments in the presence of CO, which occupies the active sites on the Pt nanoparticles and, as a result, inhibits nitrobenzene hydrogenation on the Pt. As no formation of aniline was observed for this experiment, they concluded that spillover hydrogen atoms, as long as they are located on the support material, cannot take part in hydrogenation reactions and that on Pt/NMC hydrogenation occurs exclusively on the Pt nanoparticles. Furthermore, they proposed that spillover hydrogen is stored on the carbon support material in a chemically inactive state, most probably as protons, which could further be stabilized by residual moisture in the sample.

In general, the results of Yang et al. for Pt/NMC indicate that hydrogen could be

reversibly stored on the carbon-support material of Pd/NMC, where it can serve as hydrogen source (buffer) for catalyzed hydrogenation reactions. The existence of reversibly stored hydrogen on Pd/NMC would also open up the possibility of applying it as a storage system for hydrogen as an energy source. Even though Pd is rather expensive, it is considered for hydrogen storage systems, especially as an 'assistant' for the hydrogen storage on other materials like lightweight and inexpensive carbon materials.[38]

Two available computational studies on pure carbon supported Pt_4 clusters indicated that the hydrogen spillover process should not be possible on such systems. In a DFT study, Psofogiannakis et al.[39] found an energy barrier of more than 250 kJ mol^{-1} for the spillover of hydrogen atoms from the Pt_4 cluster to coronene. Juarez-Mosqueda et al.[40] studied the same process for Pt_4 supported on single-walled carbon nanotubes using DFT and obtained an energy barrier of more than 190 kJ mol^{-1}, even for a system in which the Pt nanoparticle is fully saturated with adsorbed and dissociated hydrogen. That hydrogen spillover to pure carbon support materials should not be possible was also found by Blanco-Rey et al.[41], who performed ab initio molecular dynamics (AIMD) simulations of Pd_6 and Pd_{13} clusters supported on graphene and have not observed a single case of hydrogen spillover to the support material.

To the best of my knowledge, the only available study on the hydrogen spillover process on nitrogen-doped carbon-supported transition metal nanoparticles was performed by Rangel et al.[25], who investigated the hydrogen spillover on Pd_4 clusters supported on pyridinic and pyrrolic nitrogen doped graphene using periodic DFT. They found, in comparison to the previously mentioned studies on N-free carbon-supported Pt_4, significantly lower energy barriers of around 77 kJ mol^{-1} (pyridinic defect) and 48 kJ mol^{-1} (pyrrolic defect) for the spillover from the Pd cluster at full hydrogen saturation.

Based on these findings, several research questions for our computational study arose:

vii Is hydrogen spillover possible on Pd/CMC?

viii How does nitrogen doping affect this process?

ix Could Pd/CMC and Pd/NMC be suitable systems for reversible hydrogen storage, applicable in hydrogenation reactions or to store hydrogen as an energy source?

x How do the properties of spillover hydrogen atoms and of hydrogen atoms adsorbed on the supported Pd nanoparticles differ? Are spillover hydrogens stored as protons on the carbon surface, which can be stabilized by water molecules as H_3O^+?

xi Can spillover hydrogens take part in the catalyzed hydrogenation reactions?

All the research questions i to x will be addressed in the computational studies presented in the main part of this thesis. Some preliminary results for research question xi are shown in the concluding section.

2 Methodology

2.1 Available Surface Models

In the literature, several computational approaches for describing heterogeneous catalysis can be found. This section should give an overview of the available surface models, which could be used to model the structure and properties of the Pd/CMC and Pd/NMC catalysts. In general, the existing surface models can be divided in two categories: periodic boundary and finite cluster approaches.[42]

2.1.1 Periodic Boundary Approaches

In periodic boundary approaches, periodic boundary conditions are chosen to approximate a large or infinite system on the basis of a small part of the system, called unit cell.[43] These approaches have their roots in Bloch's theorem for the description of the electronic structure of crystals, which states that the electronic wave function in a crystal can be expressed as the product of a plane wave and a function obeying the spatial periodicity of the crystal. Using the translational symmetry of the crystal, this allows for the treatment of the electronic structure problem for infinite solids by a 3D simulation cell.[42]

The most common periodic boundary approach for modeling a catalyst surface is the slab-supercell model.[44–48] In this approach, the catalyst model is built in the following way: First, a slab, i.e. a finite number of parallel atomic layers, is cut from the bulk structure of the surface. The slab can be chosen such that it possesses the desired surface termination. In a second step, periodic boundary conditions are applied to the slab in two dimensions. In the third dimension, the slab is separated from its periodic images by a region of vacuum. This accounts

for the lateral periodicity of the catalyst surface. It is important to guarantee a sufficiently broad vacuum region (to decouple the slabs) as well as a sufficient slab thickness (to mimic a semi-infinite crystal structure, which is particularly important for systems with strong interactions between the crystal's layers , i.e. for metals and ionic crystals).[49] Usually, the unit cell of the model, i.e. the chosen slab, is composed of multiple crystallographic unit cells and is, therefore, called supercell. As an example, for a Pd/CMC catalyst system the carbon support would be modeled by a slab of graphene layers. The Pd nanoparticle could be added as small finite cluster at the top of the graphene slab. Alternatively, the Pd nanoparticle could be modeled as a slab of Pd bulk structure, which is aligned to the graphene slab and is equal in size in the two lateral dimensions. For Pd/NMC, a certain number of carbon atoms in the graphene slab would be replaced by nitrogen functional groups.

The slab-supercell model shows a good convergence with the slab thickness, reproduces a proper surface electronic structure and allows for the utilization of plane wave basis sets.[50,51] Accordingly, it is well suitable for describing bulk properties of surfaces, e.g. of metals or of metal supports. However, the slab-supercell model is inherently expensive. For studying chemical reactions, which always locally disturb the periodicity of the system, a very large unit cell is needed to avoid significant interactions between neighboring periodic images of the reacting agents. This makes calculations often unfeasible.[44,52]

A cost-efficient approximation of the slab-supercell model can be achieved by the cyclic cluster approach[53], mainly implemented by Bredow et al.[54–56]. In the cyclic cluster model, cyclic boundary conditions, originally proposed by Born and van Kármán, are applied directly to the cluster. As a consequence, the unit cell of the model system is equal to the whole surface of interest. Figuratively, this means that one edge of the cluster is directly tied to its other edge. In the implementation of the cyclic cluster model, the interatomic distance and direction

cosine matrices of each atom have to be modified and the integration is carried out in real space. Furthermore, the number of orbitals is determined by the size of the cluster.[42] The basic idea of the cyclic cluster approach dates back to the nineteen-seventies[57,58] and was first proposed at a semiempirical level. Today, the cyclic cluster approach has still not been implemented for all quantum chemical methods and its applications have become very rare in the literature.
In general, it is difficult to accurately model amorphous materials as the CMC support material using periodic boundary approaches as amorphous materials actually do not possess an ordered crystalline structure.

2.1.2 Finite Cluster Approaches

In finite cluster approaches the surface is modeled as a small and finite cluster of atoms. This leads to a loss of periodicity and the cluster should be embedded somehow to account for the missing chemical bonds and to restore the original bonding and Madelung potential of the crystal.[42]
The simplest way of embedding is to saturate the dangling bonds of the surface with hydrogen atoms. This approach is called molecular cluster model and is based on the assumption that the electronic states of solids can be well modeled by localized bonds and that there is no strong Madelung field.[42] As an example, the carbon support material of the Pd/CMC catalyst system would be modeled by a hydrogen terminated graphene layer. The missing local C-C bonds at the edges of the surface are replaced by local C-H bonds, which show relatively similar properties and, thus, are a simple and good approximation. In this approach, the Pd nanoparticle would be modeled by a small Pd cluster attached to the graphene surface without further embedding.
The molecular cluster model can be comparatively cheap for small clusters using local basis sets and is perfect for describing local effects like defects (e.g. the nitrogen doping of CMC) and chemical reactions. In contrast, it is often not

suitable for studying bulk properties as these show only a slow convergence with the cluster size. For example, the band gap of metals cannot be described properly.[59]

As an alternative to the saturation with hydrogen atoms, various embedding techniques have been proposed and implemented.[60,61] In all approaches, a finite cluster of atoms is treated quantum-mechanically while its interaction with the missing surrounding is approximated to some extent. A relatively cheap example of such an embedding approach is the periodic electrostatic embedded cluster method (PEECM), which was developed by Burow et al.[62], especially for the treatment of ionic systems. In this approach the rest of the surface is approximated by point charges in order to account for the missing long-range electrostatic interactions. Accordingly, the PEECM splits the catalyst system into three regions: 1) inner region: finite cluster; treated quantum-mechanically; 2) outer region: embedding potential consisting of a periodic array of point charges reproducing the Madelung potential due to long-range electrostatic interactions; 3) intermediate region: negative point charges and pseudopotentials; avoids that positive point charges over-polarize the electron density of the inner region. For modeling the carbon support material of Pd/CMC even such a cheap embedding approach would not be worthwhile as the missing C-C bonds can be better approximated simply by local C-H bonds. Furthermore, CMC is actually not an ordered crystalline system but an amorphous mesoporous network of polycyclic aromatic hydrocarbons of varying size and shape.

2.2 Computational Approach

This section will give a detailed description of the chosen catalyst model systems and the utilized computational methods for this project and will give reasons for the choices made. Furthermore, some special requirements are discussed, which have to be fulfilled by the calculations to obtain converged and reliable results.

2.2.1 Catalyst Model Systems

In this project, we are especially interested in studying the effect of nitrogen doping on the Pd/CMC catalyst system and aim to study hydrogenation reactions on such catalysts. Therefore, we decided to model the palladium nanoparticles supported on mesoporous carbon using the most appropriate method for studying local defects and chemical reactions; i.e. we used a finite cluster approach.

For the mesoporous carbon support material, consisting of amorphously linked graphitic domains, we set up two molecular cluster models of a graphene surface in which all dangling bonds are saturated with hydrogen (cmp. Figure 2.1). The surfaces comprise 96 and 150 carbon atoms so that they are large enough to support the palladium clusters.

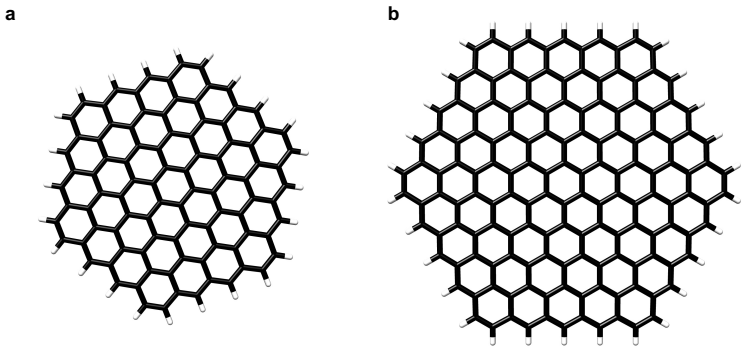

Figure 2.1: Model systems for the CMC support material: (a) graphene surface of 96 C atoms; (b) graphene surface of 150 C atoms.

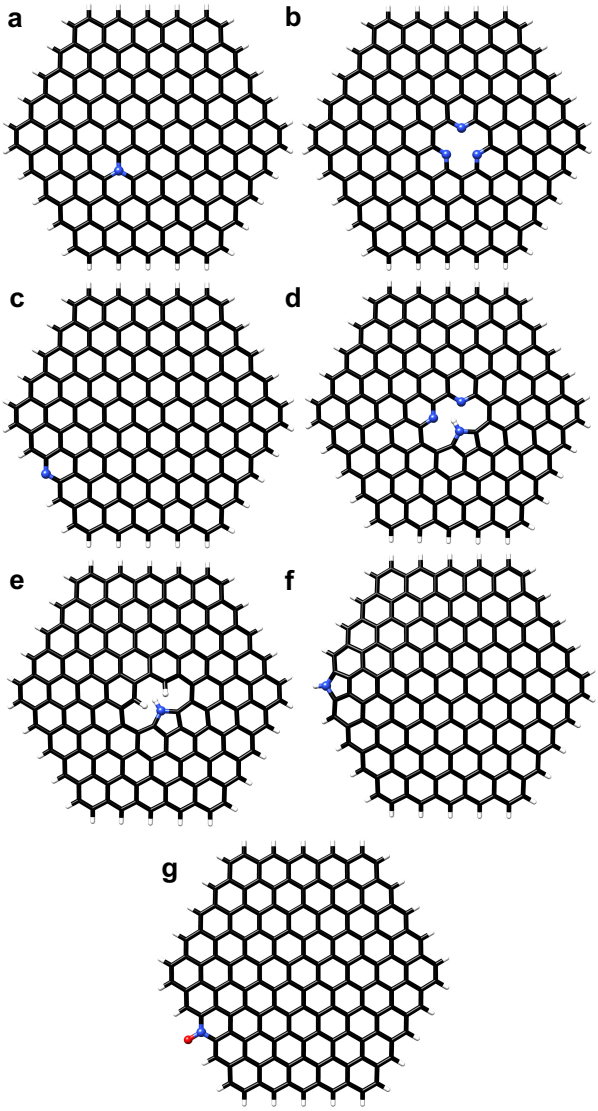

Figure 2.2: Model systems for the NMC support material: (a) graphitic N; (b) 1 C atom vacancy surrounded by 3 pyridinic N atoms; (c) pyridinic N at the edge replacing a C-H group; (d) 2 C atom vacancy surrounded by 1 pyrrolic and 2 pyridinic N atoms; (e) 2 C atom vacancy surrounded by 1 pyrrolic N atom and 2 C-H groups; (f) pyrrolic N containing five-membered ring at the edge; (g) N-O-like species at the edge.[1]

[1] Warczinski, L.; Hu, B.; Eckhard, T.; Peng, B.; Muhler, M.; Hättig, *C. Phys. Chem. Chem. Phys.* **2020**, *22*, 21317 - 21325. - Reproduced by permission of the PCCP Owner Societies

To model the nitrogen-doped mesoporous carbon support material (NMC), we introduced nitrogen atoms in form of four different functional groups into the graphene layer: 1) graphitic N: one sp^2 hybridized C atom bound to three neighboring sp^2 hybridized C atoms is one-by-one replaced by an sp^2 hybridized N atom; 2) pyridinic N: sp^2 hybridized N atom with two neighboring sp^2 hybridized C atoms; 3) pyrrolic N: N atom incorporated in a five-membered heterocyclic ring; 4) N-O-like species. In total, we set up seven different NMC models based on the graphene surface of 150 carbon atoms, which are shown in Figure 2.2.

At this stage, surface deformations, including bending of the graphene sheet, defects from five- and seven-membered rings and holes as well as unpaired electrons are not considered. Even though all these are present in the real CMC support material, including them would introduce too many degrees of freedom, which cannot be studied all at the same time. This already implies that a computational study including such an amorphous support material as CMC can only describe trends and achieve qualitative, at best semi-quantitative results.

The palladium nanoparticles are modeled by small, finite Pd clusters. Their size was chosen such that the clusters are not too large for electronic structure calculations but large enough to act as models for palladium nanoparticles as they are used in experimental studies. The experimentally determined Pd particle size distribution for Pd/CMC (cmp. Figure 1 in Chapter 6) reveals supported Pd nanoparticles of 1 to 8 nm. The mean Pd particle size is around 3.6 nm. Roughly estimated, Pd nanoparticles of experimental Pd/CMC catalyst systems should possess between 30 and 1000 Pd atoms. The experimentally determined Pd particle size distribution for Pd/NMC (cmp. Figure 1 in Chapter 6) is relatively similar to the one of Pd/CMC. However, Pd/NMC also shows some sub-1 nm Pd nanoparticles, which should possess less than 30 Pd atoms.

We started with the octahedral Pd_6 cluster, whose initial structure was taken from Ahlrichs et al.[63], and optimized its geometry on the small graphene surface starting from different initial orientations. The most stable structure of Pd_6 on the graphene surface is shown in Figure 2.3. This model system for Pd/CMC is relatively small (around 0.3 nm) and contains six palladium atoms with exactly the same number of neighboring Pd atoms. Consequently, the Pd_6 cluster is a good starting point for studying the metal-support interactions between the palladium clusters and the graphene surface.

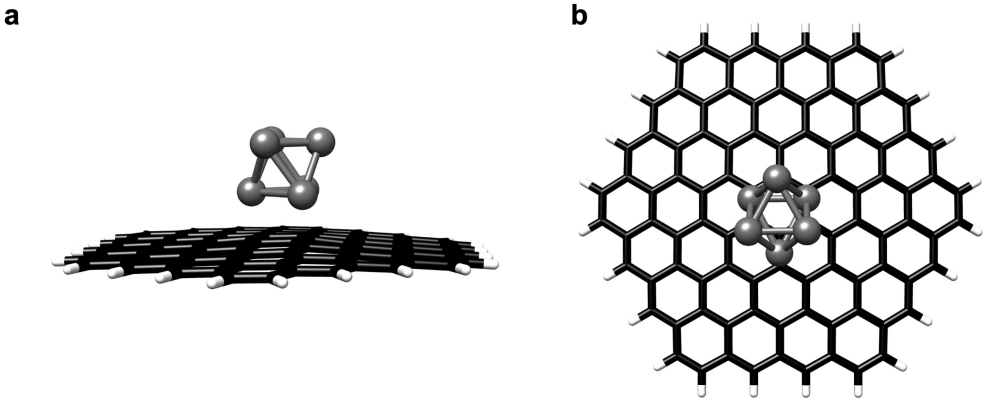

Figure 2.3: Most stable structure of Pd_6 on the graphene surface of 96 C atoms: (a) side view; (b) top view.

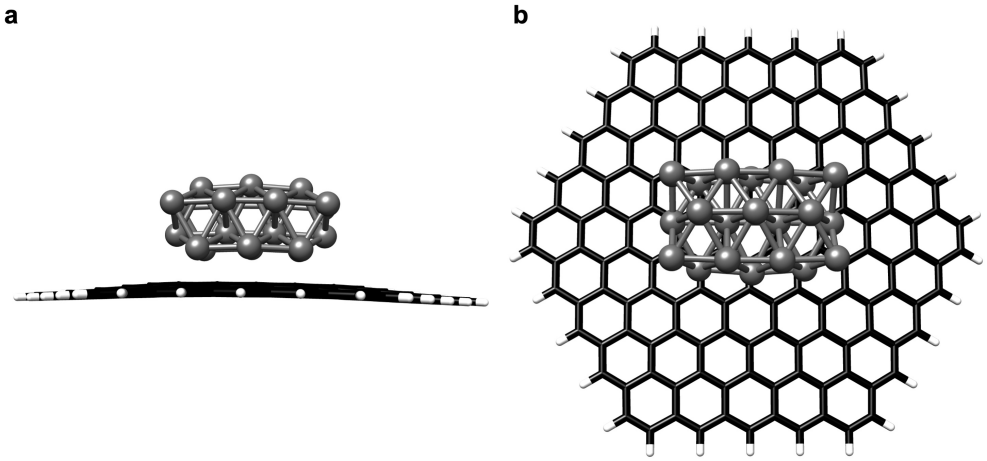

Figure 2.4: Most stable structure of Pd_{21} on the graphene surface of 150 C atoms: (a) side view; (b) top view.[1]

[1] Warczinski, L.; Hu, B.; Eckhard, T.; Peng, B.; Muhler, M.; Hättig, *C. Phys. Chem. Chem. Phys.* **2020**, *22*, 21317 - 21325. - Adapted by permission of the PCCP Owner Societies

Palladium nanoparticles, as they are used in experimental studies, usually form a face-centered cubic (fcc) structure. To model this fcc structure, it needs at least a Pd_{21} cluster[33]. As a consequence, for the more ambitious studies of this project, we used a Pd_{21} cluster, initially taken from Shamsiev et al.[33], optimized on the larger graphene sheet as Pd/CMC model system (cmp. Figure 2.4). The diameter of the Pd_{21} cluster is around 0.85 nm and, therefore, at the lower boundary of experimental Pd particle size distributions for Pd/CMC and Pd/NMC.

As several of the NMC support model systems either include functional groups at the edge of the support material (cmp. Figure 2.2c, f and g) or large surface deformations (cmp. Figure 2.2e), which would both include undesired side effects in the computational study of reactions, the structure of the Pd_{21} cluster was optimized on only three of the NMC support model systems (cmp. Figures 2.5, 2.6 and 2.7).

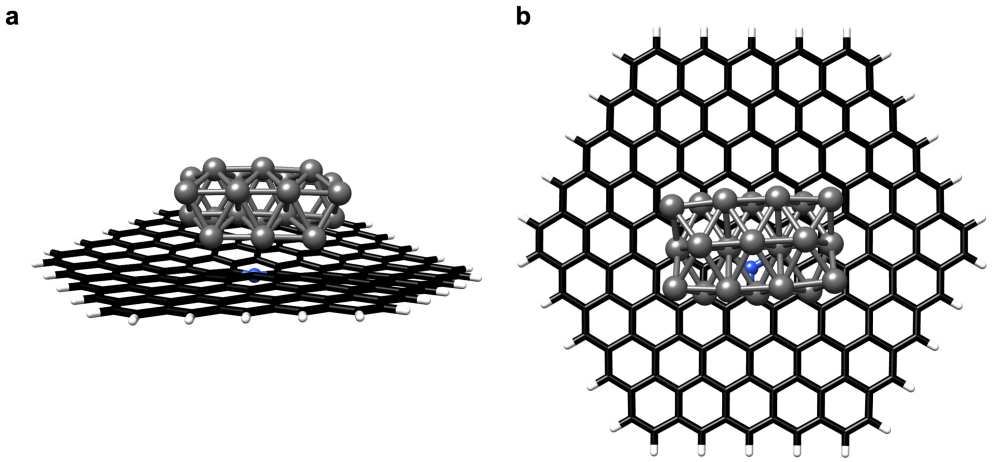

Figure 2.5: Most stable structure of Pd_{21} on the graphitic N carbon support material: (a) side view; (b) top view.[1]

[1] Warczinski, L.; Hu, B.; Eckhard, T.; Peng, B.; Muhler, M.; Hättig, *C. Phys. Chem. Chem. Phys.* **2020**, *22*, 21317 - 21325.- Adapted by permission of the PCCP Owner Societies

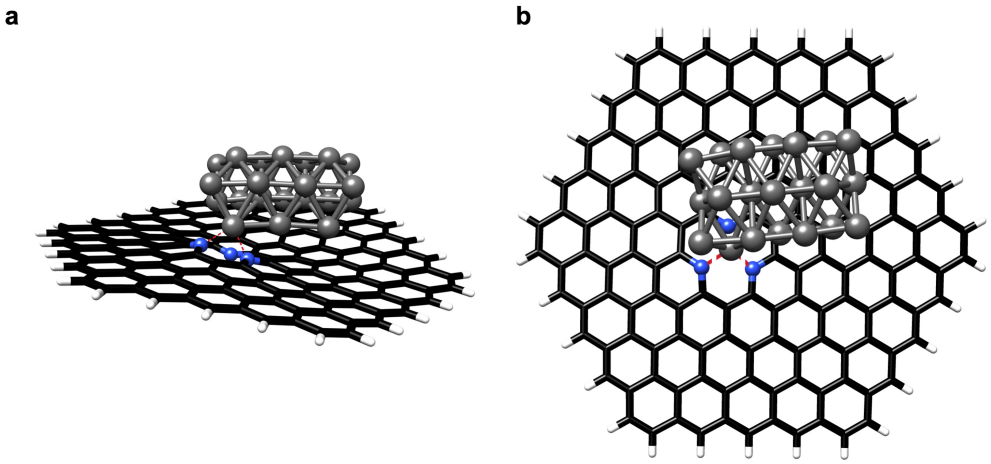

Figure 2.6: Most stable structure of Pd_{21} on the pyridinic N carbon support material: (a) side view; (b) top view.[1]

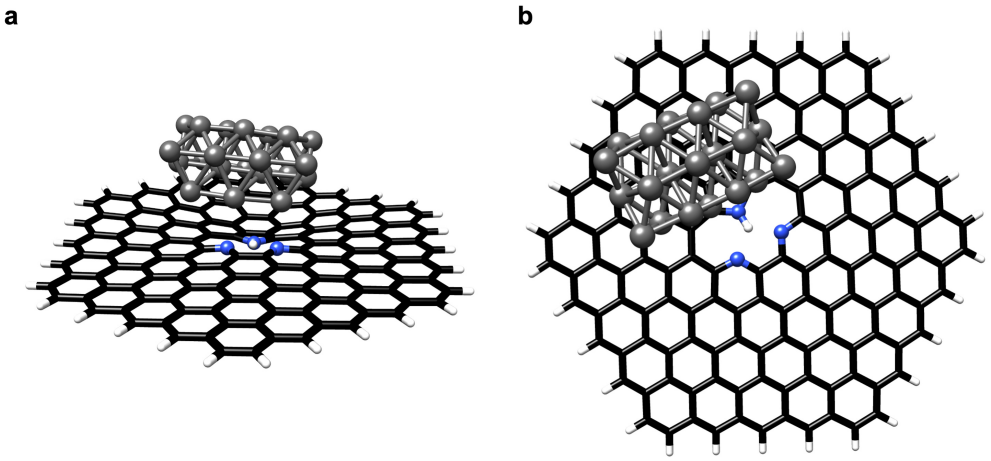

Figure 2.7: Most stable structure of Pd_{21} on the pyrrolic N carbon support material: (a) side view; (b) top view.[1]

2.2.2 Computational Methods

The quantum chemical treatment of the previously shown Pd/CMC and Pd/NMC model systems is particularly difficult as they include a very large number of electrons. Furthermore, the Pd clusters show plenty of low-lying nearly degenerate electronic states, which introduce static correlation effects that somehow have to be accounted for in the calculations.[64]

[1] Warczinski, L.; Hu, B.; Eckhard, T.; Peng, B.; Muhler, M.; Hättig, *C. Phys. Chem. Chem. Phys.* **2020**, *22*, 21317 - 21325. - Adapted by permission of the PCCP Owner Societies

In general, the available methods in the field of quantum chemistry can be divided into three groups: wave function methods, semi-empirical methods and density functional theory (DFT). All calculations of this project utilized density functional theory (DFT) with the def2-SVP[65] basis set and the TPSS[66] functional and were performed with the TURBOMOLE[67] program package.

The most accurate quantum chemical methods can be found in the group of wave function methods (e.g. the 'gold standard' CCSD(T)[68]). Wave function theory employs a 3N-dimensional antisymmetric wave function for a system of N electrons.[69] Static correlation can be included by adding several additional electronic configurations together with the orbital optimization, i.e. by employing multi-reference Hartree-Fock[70] or variances of it like DMRG[71]. The Pd_{21}/CMC and Pd_{21}/NMC model systems possess around 1900 electrons. For a multi-reference treatment at least all electrons of the Pd 4d5s and of the graphene π orbitals would have to be included in the active space, which is just impossible with today's program codes and computer resources.

The computationally cheapest available methods in quantum chemistry are semi-empirical ones[72], like MSINDO[73], DFT-B[74] or the novel GFN-xTB-variants[75,76]. However, the accuracy of all these methods is significantly limited by the availability of well-optimized and suitable parameters for the involved atoms, which also have to fit for the relevant systems and binding situations.

Over the last years, density functional theory (DFT) has become the preferred method for electronic structure calculations in the field of heterogeneous catalysis as it is the most accurate method for geometry optimizations, reactions pathways and vibrational frequencies, which still can treat such a large amount of electrons present in the systems under consideration.[77] Furthermore, DFT remains simple

for multi-reference systems. For such systems it also uses a single-determinant ansatz and static correlation effects are somehow mimicked by the local or semi-local exchange.[78] Even though the manner of including static correlation effects in DFT is unspecified and uncontrolled[79], DFT often gives sufficiently accurate results for multi-reference systems[77], especially when static correlation effects are relatively small and a proper description of different spin states is not important (e.g. for large transition metal clusters).
Its performance in relation to computational costs and accuracy for metal clusters and organic molecules also made DFT our method of choice for studying the carbon-supported Pd nanoparticles.

Density functional theory, as it is used today (Kohn-Sham formulation), requires the selection of a functional of the spin density. The easiest and oldest choice for such a functional is the local density approximation (LDA), which is only based on the spin density derived from the uniform electron gas. More complex are generalized gradient approximation (GGA) functionals, which include on top of the spin density also the gradient of the spin density, or meta-GGAs, which furthermore add the Laplacian or the kinetic energy density. Today, the most popular functionals are hybrid functionals such as the famous B3LYP[80]. These functionals incorporate a portion of exact exchange from Hartree-Fock theory.[81]

We decided to use the meta-GGA TPSS[66] functional as it uses only a few fit parameters and generally shows a very good cost/performance ratio throughout the periodic table.[82] It also performs notably well in studying transition metals, including systems with relatively high multi-reference character[83]. In contrast to that, hybrid functionals, such as B3LYP or TPSSh[84], are not the functionals of choice for studying carbon-supported Pd nanoparticles. The included Hartree-Fock exchange cannot deal with the near degeneracy of states, i.e. with static correlation

effects, in metal clusters and calculations fail badly for several systems, although the cost is significantly higher than that for meta-GGAs.[82]

Even though DFT calculations are relatively insensitive to the choice of basis set compared to correlated wave function methods[85,86], this choice has still some effect on the quality of the calculations. We applied the def2-SVP basis set[65], which employs Stuttgart-Cologne effective core potentials[87] for the Pd atoms. The Karlsruhe 'def2' basis set family is designed to give similar errors all across the periodic table. It is a revision of the older Karlsruhe basis set family (SVP/def-SVP, TZVP/def-TZVP, etc.), which had some imbalances between (transition) metal and the main group III-X elements and used older, less accurate effective core potentials (ECPs) for the heavier atoms.[65] For systems including heavier atoms (typically beyond Kr), like Pd, ECPs are a reasonable choice as they significantly reduce the computational cost and, by construction, account for relativistic effects in the deep core electrons.[88] The polarization functions allow for a reasonable description of chemical bonds without significantly increasing the computational costs.[89]

Several studies suggest that triple-zeta basis sets should be applied for well converged energetics and structural properties[90–92], where 'converged' means that with such basis sets the remaining basis set incompleteness errors are usually smaller than the errors from the DFT functional. However, single point calculations on the Pd_{21}/CMC model with the triple-zeta type basis including polarization functions of the Karlsruhe family (def2-TZVP[65]) already need nearly five times more computer time compared to the same calculations with the def2-SVP basis set. Due to the amorphous and relatively undefined structure of the experimental catalyst systems, this project should (only) provide qualitative but preferably representative insights. As a consequence, it is more important to qualitatively study several different systems and configurations than studying a few systems

with a high accuracy. An extensive computational study on several systems and configurations, which also includes costly transition state searches, on our model systems using the def2-TZVP basis set would be unfeasible. In our case, the def2-SVP basis set offers a very good cost/performance ratio.

In general, DFT energetics are, in any case, obtained with a limited accuracy as results can differ in the range of several kJ/mol per bond depending on the chosen functional and basis set. Because of this and, even more important, because of the limited comparability of the experimental catalysts and our model systems, we have decided to limit ourselves to the investigation of energetic trends and do not compare our results to specific experimental values.

2.2.3 Special Requirements for the Studied Catalyst Systems

A main preparatory task of the project was to establish a feasible setup of the calculations. It turned out that, besides a reasonable choice of the density functional and the basis set, DFT calculations of the heterogeneous catalyst systems have to fulfill special requirements to provide converged and reliable results:

1. For an appropriate description of the catalyst structure, which also includes non-covalent metal-support interactions, it is essential to properly include London dispersion interactions[31]. As these are, by construction, not included in local or semi-local density functionals, several techniques of dispersion correction have been developed[93,94]. Among these, the semi-empirical DFT-D3 approach by Grimme et al.[95] was proven to predict van der Waals interactions with a high accuracy[96]. Therefore, we included the D3 dispersion correction in all our calculations.

2. Metal clusters, such as carbon-supported Pd nanoparticles, possess a very small HOMO-LUMO gap, making it significantly complicated to determine the occupations of orbitals near the Fermi energy[97]. To determine the correct ground state multiplicity of each system, we included a Fermi smearing[97] of the occupation numbers in preliminary single point calculations and later analyzed the eigenvalues of the singlet and triplet stability matrices.

3. The calculations on the catalyst model systems are relatively slow and the convergence of the self-consistent field iterations to the convergence criterion is very difficult to achieve. To guarantee sufficiently fast and converging calculations, RI[98] and MARI-J[99] approximations (for accelerating the calculations) as well as higher DIIS[100] start damping factors of 15 or 30 (to avoid non-convergent oscillatory behavior) have to be included.

4. The potential energy surface of reactions on the Pd nanoparticles is very flat, which makes it often extremely difficult to find well converged minima or transition state structures that do not show additional very small imaginary frequencies in the vibrational analysis. A possible way to achieve well converged minima or transition states is to increase the quality of the geometry optimization, e.g. by choosing a finer DFT grid[101] or including derivatives of the quadrature weights of the DFT energy expression. Also, distorting the molecule along a mode with a negative eigenvalue using the screwer module of TURBOMOLE can be helpful to converge to the searched-for stationary point.

This is in agreement with a study of Banerjee et al.[102], in which similar requirements (for applying the cluster approach to structures of an organic molecule adsorbed on metallic surfaces) have been reported.

3 Thesis Outline

This thesis is structured in the following way: Chapter 4 shows the first study of the project, which deals with the metal-support interactions in Pd/CMC as well as with the hydrogen adsorption and dissociation on such catalyst systems. This study forms the basis for all subsequent studies. The effect of nitrogen doping on the metal-support interactions is evaluated in the study on Pd/NMC in Chapter 5, in which our computational approach is combined with experimental X-ray photoelectron spectroscopy (XPS) results. Also Chapter 6 presents a combined experimental and computational project. This study gives an example of how the nitrogen doping of the CMC support material can affect the catalyzed hydrogenation reactions. Using our DFT approach, the adsorption of H_2 and formic acid on Pd_{21} bound to two pyridinic nitrogen atoms is analyzed. The obtained results support experimental findings, which report on novel reaction conditions, allowing for a highly selective hydrogenolysis of 5-hydroxymethylfurfural to 2,5-dimethylfuran. The research questions concerning hydrogen spillover are addressed in the manuscript in Chapter 7 and in the preliminary study presented in Chapter 8. Chapter 7 shows a computational study on the hydrogen spillover mechanism on Pd/CMC and the effect of nitrogen doping on such processes. Furthermore, the properties of spillover hydrogen on nitrogen-free and on nitrogen-doped graphene are investigated. Chapter 8 summarizes some preliminary investigations dealing with the question if spillover hydrogen atoms located on the carbon support material can take part in hydrogenation reactions. As a case study, the hydrogenation reaction of ethylene with hydrogen atoms on Pd/CMC is compared to the equivalent reaction with spillover hydrogen atoms.

Finally, Chapter 9 highlights the achievements of this project and gives evidence for future research questions based on our findings.

Part II

Results of the Project

4 A Quantum Chemical Study of Hydrogen Adsorption on Carbon-Supported Palladium Clusters

This chapter shows the first study of the project published in the Journal *Physical Chemistry Chemical Physics*. In this study, we used the two model systems for Pd/CMC introduced in Chapter 2 (cmp. Figures 2.3 and 2.4) to obtain an insight into the relevant metal-support interactions in carbon-supported Pd nanoparticles. The Pd_6 cluster was used as a starting point to become versed in treating these kinds of systems. The larger Pd_{21} cluster was then included to allow our results to be qualitatively compared to experimental observations.

Additionally, this study comprises, as a first step of studying hydrogenation reactions, the investigation of several aspects of the interaction of hydrogen with our model systems: H_2 adsorption energies, H_2 dissociation pathways, the adsorption and dissociation of several H_2 molecules, hydrogen atom diffusion on Pd nanoparticles.

As this study provides an in-depth insight into the relevant metal-support interactions in Pd/CMC and into the hydrogen dissociation on such catalyst systems, it forms the basis for all subsequent studies dealing with the effect of nitrogen doping of the carbon support material as well as with the processes of hydrogenation and hydrogen spillover.

Reproduced from Ref. 103[1] and Ref. 104[2] with permission from the PCCP Owner Societies.[3]

[1] Article: https://doi.org/10.1039/C9CP04606B
SI: reproduced in the appendix on pages 147 - 149

[2] Correction for Ref. 103: https://doi.org/10.1039/D0CP90079F

[3] These publications have been compiled by me, including performing and analyzing the calculations, writing text and corresponding with the editor, supervised by Professor Hättig.

PCCP

PAPER

Cite this: *Phys. Chem. Chem. Phys.*, 2019, **21**, 21577

A quantum chemical study of hydrogen adsorption on carbon-supported palladium clusters†

Lisa Warczinski * and Christof Hättig

Received 20th August 2019,
Accepted 3rd September 2019

DOI: 10.1039/c9cp04606b

rsc.li/pccp

A key step for achieving better insight into catalytic hydrogenation reactions is to understand in detail the process of hydrogen adsorption on the catalyst. The present article focuses on hydrogen adsorption on carbon-supported palladium clusters, which are nowadays one of the most common catalysts in industrial applications. Density functional theory is applied to study Pd_6 and Pd_{21} clusters to reveal the influence of the carbon support material on the properties of the catalyst as well as on the mechanisms and energetics of the hydrogen adsorption. In general, a stepwise hydrogen adsorption process is observed consisting of molecular adsorption followed by dissociative chemisorption. The carbon support material does not noticeably affect the reaction mechanisms, but has a large influence on energy barriers and preferential adsorption sites. Our comparison of Pd_6 and Pd_{21} systems reveals that small clusters, such as Pd_6, are able to model some but not all important properties of palladium nanoparticles and, therefore, it is essential to also study larger cluster sizes.

1 Introduction

Hydrogenation is one of the industrial catalytic processes with the longest history and is among the most important processes in petrochemical and fine chemical industries.[1–4] For instance, hydrogenation reactions are used to convert chloronitrobenzenes to chloroanilines, which are essential organic feedstocks,[5] and are part of the biomass conversion process of lignin to phenol and phenol derivatives.[6] The most common catalysts in hydrogenation reactions are metal-nanoparticles, often palladium, carried by a high-surface-area support material.[7] In early industrial applications oxide materials were the support material of choice. Over the years porous oxide supports have been replaced by novel 2D carbon support materials with high surface areas, as these are resistant to both acidic and basic media and facilitate the recovery of the metal. Another advantage of these carbon materials is that their surface properties can be fine-tuned with great precision, *e.g.*, by nitrogen or oxygen doping.[8] Even though the first industrially applied catalytic hydrogenation processes date back to more than a century ago, there are still numerous challenges in industrial catalytic hydrogenation and a detailed understanding of hydrogenation reactions, especially on carbon-supported metal-nanoparticles, has not yet been achieved.[1]

A key step in hydrogenation reactions is the hydrogen adsorption on the catalyst. Hydrogen adsorption on palladium crystal surfaces and free palladium clusters has been studied intensively in experiments[9–13] as well as in theory.[14–23] However, when it comes to hydrogen adsorption on carbon-supported palladium clusters only few publications are available in the literature. Most of the existing studies focus on hydrogen storage and are restricted to single palladium atoms or small palladium clusters with up to six palladium atoms.[24–26] To gain further insight into hydrogen adsorption in the context of hydrogenation reactions, it is important to take also larger cluster sizes into account, which are more realistic models of the palladium-nanoparticles that are used in experiments. Furthermore, it is important to study the whole process of hydrogen adsorption including reaction pathways on carbon-supported clusters and to compare them with the results for free palladium clusters.

The purpose of the current study is to shed light on the influence of carbon support materials on the electronic properties of palladium metal catalysts and their influence on hydrogen adsorption in the context of hydrogenation reactions. To study the complex interplay between hydrogen, the palladium-nanoparticles and the carbon support material, we performed state-of-the-art electronic structure calculations using density functional theory (DFT) with a meta-GGA functional.

As a part of a project on mesoporous carbon supported metal catalysts for sustainable hydrogenation reactions we are interested in palladium nanoparticles on mesoporous carbon. We chose as model systems octahedral Pd_6, which lends itself

Lehrstuhl für Theoretische Chemie, Ruhr-Universität Bochum, 44780 Bochum, Germany. E-mail: lisa.warczinski@rub.de

† Electronic supplementary information (ESI) available. See DOI: 10.1039/c9cp04606b

to provide a quick first insight, and a Pd_{21} cluster, which is the smallest cluster capable of representing the palladium nanoparticles used in experiments, because it reflects the palladium {111} facet and possesses two adjacent face centered cubic sites at its top. Mesoporous carbon is one of the several novel 2D carbon support materials, has an amorphous, partly graphitic structure and can be doped with nitrogen or oxygen containing groups.[27–29] As we plan to investigate in forthcoming studies the effect of nitrogen and oxygen doping of mesoporous carbon on hydrogenation reactions, which we believe is in the first place an effect taking place in the π-system of the graphitic parts, we decided to model the carbon support material by a hydrogen-terminated graphene layer.

2 Computational details

The present quantum chemical study was performed on the basis of density functional theory (DFT) with the TPSS[30] functional and the def2-SVP[31] basis set, which employs Stuttgart–Cologne effective core potentials (def2-ecp)[32] for the palladium atoms. We have chosen the meta-GGA TPSS functional, as TPSS offers a very good cost/performance ratio throughout the periodic table, also in transition metal chemistry,[33] and meta-GGA functionals have turned out to be an efficient and reliable tool to investigate surface interactions in previous studies.[34,35]

All calculations were carried out using the TURBOMOLE[36] program package and include the multipole accelerated resolution of identity (MARI-*J*) approximation[37] with optimized auxiliary basis sets[38] and Grimme's D3 correction[39] for London dispersion interactions.

The most stable structures of the palladium clusters on the support material as well as the minima of the reaction pathways were determined by ground-state geometry optimizations. We determined the ground state multiplicity of each system by including in preliminary single point calculations a Fermi smearing of the occupation numbers and by analyzing later on the eigenvalues of the singlet and triplet stability matrices. For relative energies single point energies were combined with a vibrational analysis yielding zero-point vibrational energy (ZPVE) corrections. For the largest carbon-supported palladium clusters included in this study (Pd_{21} clusters on 150 carbon atoms) full vibrational analysis for all structures would have been too time consuming. The results for Pd_6 and an exemplary calculation for Pd_{21} show, however, that the carbon support material makes only a minor contribution to the ZPVE correction to the adsorption and reaction energies. Therefore, the relative energies for carbon-supported Pd_{21} were corrected using the ZPVEs of the corresponding free clusters. The results of the vibrational analysis were also used to calculate Gibbs free reaction enthalpies and free activation enthalpies within the harmonic oscillator and the rigid rotor approximation under reaction conditions of 298.15 K and 0.1 MPa. As mentioned above, vibrational analysis for the Pd_{21} clusters on 150 carbon atoms has not been performed and, thus, Gibbs free reaction enthalpies and free activation enthalpies are not available for these systems.

The chain-of-state method implemented in the woelfling module of TURBOMOLE[40] was used for determining reaction pathways and locating initial transition state structures. The transition state structures from the reaction pathways were used as a start guess for a further optimization with the eigenvalue-following trust-region image minimization (TRIM)[41] algorithm and validated by intrinsic reaction coordinate (IRC)[42] calculations. For reasons of computational costs, the transition states for the largest systems included in this study (Pd_{21} clusters on 150 carbon atoms) were directly taken from the reaction pathway optimization without further optimization. We expect the errors introduced by this approximation to be negligible for this system.

To simplify the comparison of reaction energies and Gibbs free reaction enthalpies, adsorption energies and dissociation energies are provided with a negative sign. Energy barriers like activation barriers are characterized by a positive sign. Of course, DFT energetics provide at this level only a qualitative accuracy and the results obtained with different functionals and basis sets can differ in the range of some kJ mol^{-1} per bond (some exemplary comparisons of the TPSS/def2-SVP results with the BP86[43,44] and PBE[45] functionals and with the def2-TZVP[31] basis set can be found in the ESI†). Therefore, we have limited ourselves to the discussion of energetic trends, which turned out to be the same for different functionals and basis sets (see the incremental adsorption energies in the ESI†), and we refrained from a comparison with experimental energies.

To investigate the details of the electronic structure we calculated electron densities and generated electron density difference plots and visualized intrinsic bond[46] orbitals (IBOs). For these we used at Pd a 1s1p1d subset of the atomic orbitals in the cc-pVTZ-PP basis set.[47]

3 Results and discussion

3.1 Carbon-supported palladium clusters

As a first step, model systems for the carbon-supported palladium clusters have to be set up. The palladium clusters have to be chosen such that they are not too large for electronic structure calculations, but can act as models for palladium nanoparticles, as they are used in experimental studies as well as in industrial hydrogenation reactions. The carbon surface has to be large enough to support the clusters.

In the present work the octahedral Pd_6 cluster on a carbon support with 96 carbon atoms and a Pd_{21} cluster on a carbon support with 150 carbon atoms are used as model systems. The Pd_6 cluster, whose structure is shown in Fig. 1, is relatively

Fig. 1 Structure of the octahedral Pd_6 cluster.

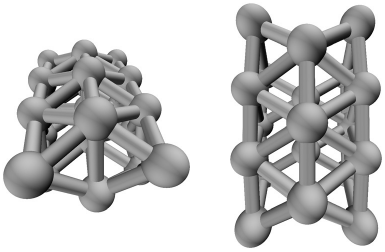

Fig. 2 Structure of the selected Pd_{21} cluster: side view (left) and view from the top (right).

small and contains six palladium atoms that have all exactly the same coordination. The Pd_6 cluster lends itself to obtain a quick insight into the metal–support interactions between palladium clusters and the carbon support.

To model palladium nanoparticles, as they are used in experiments, and their adsorption interaction with H_2 molecules, we chose a Pd_{21} cluster, whose structure is shown in Fig. 2. Even though the top of the cluster is nonplanar, the arrangement of the upper face atoms reflects the palladium {111} facet. Furthermore, the cluster possesses two adjacent face centered cubic (fcc) sites at the top, which are known to be the preferred positions for dissociative hydrogen adsorption.[23]

The carbon support materials are modelled by a hydrogen terminated graphene layer. The initial geometries of the palladium clusters were taken from Ahlrichs *et al.*[48] and Shamsiev *et al.*[23] To find the most stable structures of the clusters on the graphene support material, ground-state geometry optimizations starting from different initial orientations have been carried out. The most stable structures of the carbon-supported clusters are shown in Fig. 3 and 4.

The octahedral Pd_6 cluster is oriented such that a palladium triangle is aligned in a parallel fashion to the graphene surface at a distance of about 2.17 Å. The three lower palladium atoms interact each with two carbon atoms (so in total with six carbon atoms) of the support material. In its ground state the carbon-supported Pd_6 cluster has singlet multiplicity.

For the Pd_{21} system, the {111} facet as well as the two fcc sites should be located at the top of the carbon-supported cluster, where the hydrogen adsorption process is expected to proceed. In the most stable structure meeting this requirement, the lowest layer of the Pd_{21} cluster is located at around 2.21 Å from the graphene surface. The six palladium atoms of the lowest layer interact in total with 12 carbon atoms (again each palladium atom interacts with two carbon atoms) of the support material. As the Pd_6 cluster, also the carbon-supported Pd_{21} cluster has singlet multiplicity in its ground state.

To characterize the metal–support interactions and to obtain a measure for the importance of the dispersion contribution, we calculated the binding energy of the systems, once with and once without the D3 correction. Even though the D3 correction cannot be identified one-to-one with the total London dispersion energy, as it only accounts for the long-range part of the latter, it should reproduce for the Pd–support interaction the qualitative trends. Both the Pd_6 and Pd_{21} systems show binding energies of 195.7 kJ mol^{-1} and 549.7 kJ mol^{-1} respectively with quite strong attractive palladium–carbon–support interactions. The total binding energy increases from the Pd_6 to the Pd_{21} system. The interaction per palladium atom, however, decreases from 32.6 kJ mol^{-1} to 26.2 kJ mol^{-1}. This agrees with the slightly larger cluster-surface-distance in the Pd_{21} system compared to the Pd_6 system. For Pd_6 the dispersion contribution of 95.0 kJ mol^{-1} makes up around 50% of the total interaction. For the Pd_{21} system a dispersion contribution of 301.5 kJ mol^{-1} was obtained, which corresponds to about 55% of the total interaction energy. This is in agreement with previous computational studies indicating that the dispersion contribution to metal–support interactions increases with the size of the transition metal cluster.[49] The PBE[45] functional provides slightly lower dispersion contributions for both systems but also shows the trend of higher dispersion contributions for larger clusters (detailed energies can be found in the ESI†).

The electronic effect of the support material on the Pd clusters is rather small. Therefore, no effect on the Pd–Pd bonding orbitals is noticeable. However, the support material influences the electron density of the clusters. Fig. 5 shows the electron

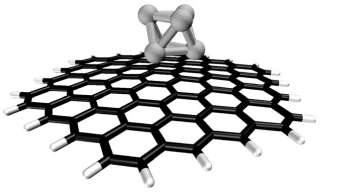

Fig. 3 Most stable structure of the carbon-supported Pd_6 cluster.

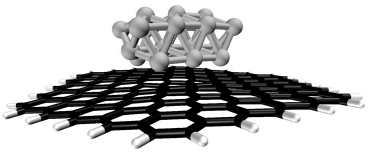

Fig. 4 Most stable structure of the carbon-supported Pd_{21} cluster with the {111} facet and fcc sites located at the top of the cluster.

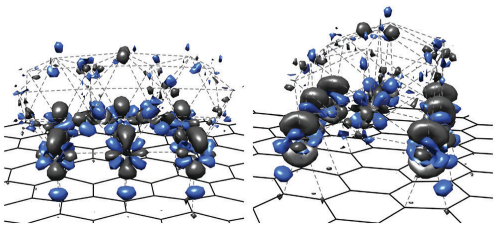

Fig. 5 Change in the electron density induced by the interaction between the Pd_{21} cluster and the support material from two different perspectives. Density gain is colored in blue; density loss is in grey.

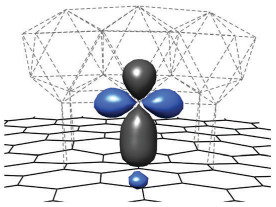

Fig. 6 Visualization of the Pd–C bonding orbital (IBO) for the carbon-supported Pd_{21} cluster.

density difference plot for the interaction between the Pd_{21} cluster and the support material. Electron density is shifted from the lowest layer of the Pd cluster into Pd–C connecting lines. This agrees with the above conclusion that the interaction of the support material and the Pd cluster is covalent with a strong dispersion contribution. The support has a mostly local effect in the Pd cluster. No charge-transfer into or major changes within the support material are observed. Fig. 6 depicts a Pd–C bonding orbital which has a large Pd d and a smaller C p contribution.

3.2 Hydrogen adsorption on Pd

As already described in previous studies, *e.g.*, by Lischka *et al.*,[16] the adsorption of a hydrogen molecule on a palladium atom leads to an interaction of the empty Pd 5s with the occupied H_2 σ_g orbital and of the occupied Pd $4d_{xz}$ with the empty H_2 σ_u* orbital (assuming a coordinate system with the *x*-axis parallel to the H_2 bond and the *z*-axis parallel to the line from the Pd atom to the H_2 bond center). Fig. 7 shows a visualization of the corresponding IBOs. Furthermore, there is a repulsive interaction between the Pd $4d_{z^2}$ and the H_2 σ_g orbital. As the anti-bonding σ_u* is populated, the H–H bond is weakened and elongated to 0.93 Å compared to the H–H bond length of 0.76 Å in the isolated H_2 molecule. On the other hand, the Pd–H bond is strengthened.

Fig. 8 shows the corresponding electron density difference plot. In accordance with the appearance of the bonding orbitals it shows an electron density gain for the 5s Pd and the σ_u* H_2 orbital and a decreased electron density for the $4d_{xz}$ Pd orbital and the σ_g H_2 orbital.

3.3 Hydrogen adsorption on Pd_6

The adsorption of H_2 molecules from the gas phase on carbon-supported Pd_6 has been studied and compared to H_2 adsorption

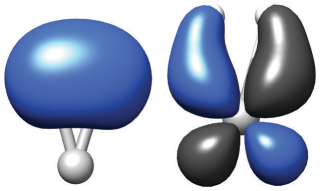

Fig. 7 Visualization of the bonding orbitals (IBOs) of the Pd–H_2 system: 5s–σ_g (left) and $4d_{z^2}$–σ_u* (right).

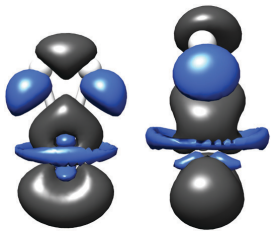

Fig. 8 Electron density difference plot for the Pd–H_2 system from two different perspectives. Density gain is colored in blue; density loss is colored in grey.

on free Pd_6. For both free Pd_6 and carbon-supported Pd_6 molecular hydrogen adsorption can be observed. On free Pd_6 the H_2 molecule adsorbs without a barrier on top of one of the palladium atoms. The adsorption is connected with an energy gain of $\Delta E_{ads} = -49.2$ kJ mol^{-1}. In the product (shown in Fig. 9) the H–Pd distance is 1.76 Å. The H–H distance of the H_2 molecule is stretched by around 10% to 0.85 Å compared to the H–H bond length of 0.76 Å in the gas phase molecule. However, the H–H bond is not broken.

As mentioned before, the results obtained with different functionals and basis sets can differ in the range of some kJ mol^{-1} per bond. For a comparison Table 1 shows the hydrogen adsorption energy on the free Pd_6 cluster for the different functionals TPSS,[31] BP86[43,44] and PBE.[45] Further exemplary comparisons can be found in the ESI.†

On carbon-supported Pd_6 molecular H_2 adsorption takes preferentially place at one of the palladium atoms located at the top of the cluster. In general, the adsorption process is very similar to the adsorption on the Pd_6 system without carbon support. As for the free Pd_6, the adsorption is barrierless and is connected with an energy gain. However, the adsorption energy is -56.2 kJ mol^{-1} on the supported cluster and, therefore, a little bit higher than that for the free cluster. The geometry of

Fig. 9 Product geometry of molecular adsorbed H_2 on free Pd_6.

Table 1 Comparison of the hydrogen adsorption energies ΔE_{ads} in kJ mol^{-1} on free Pd_6 using three different functionals

Functional	ΔE_{ads}
TPSS	−49.2
PBE	−63.4
BP86	−61.0

Fig. 10 Product geometry of molecular adsorbed H_2 on carbon-supported Pd_6. The carbon support material located below the cluster is not shown.

the product, which is shown in Fig. 10, is very similar to the product geometry without carbon support. A H–Pd distance of 1.78 Å and a H–H distance of 0.84 Å are observed. Only the position of the H_2 molecule with respect to the palladium atom is slightly shifted from a perfect atop position.

It is well known that palladium clusters are favourable systems for hydrogen storage. Therefore, it is expected that not only one but several H_2 molecules can adsorb on the Pd_6 clusters. To study this behaviour, we have increased the number of molecular hydrogens adsorbed on the clusters. The incremental adsorption energies ΔE_{ads} and free enthalpies ΔG_{ads} for an increasing number of H_2 molecules are shown for the free and for the carbon-supported Pd_6 clusters in Tables 2 and 3.

In the case of the free cluster the seventh H_2 molecule is attached to the same palladium atom as the H_2 molecule number 1. For the carbon-supported Pd_6 the first three H_2 molecules are attached to the palladium atoms at the top of the cluster. The fourth H_2 molecule is either added to a palladium atom at the lower layer of the cluster (4) or alternatively to the same palladium atom as the H_2 molecule number 1 at the top of the cluster (4s). In general, the negative incremental adsorption energies and incremental adsorption free enthalpies in Tables 2 and 3 show that both free and carbon-supported Pd_6 clusters can achieve a very high H_2 coverage.

When a second H_2 molecule is added to a palladium atom (*e.g.* H_2 molecule number 4s for the carbon-supported cluster)

Table 2 Incremental adsorption energies ΔE_{ads} and Gibbs free enthalpies ΔG_{ads} in kJ mol^{-1} for an increasing number of H_2 molecules on free Pd_6

Number of H_2	ΔE_{ads}	ΔG_{ads}
1	−49.2	−31.3
2	−43.8	−39.3
3	−43.7	−36.8
4	−37.8	−36.5
5	−33.7	−36.5
6	−24.2	−37.2
7	−64.8	−54.0

Table 3 Incremental adsorption energies ΔE_{ads} and Gibbs free enthalpies ΔG_{ads} in kJ mol^{-1} for an increasing number of H_2 molecules on carbon-supported Pd_6

Number of H_2	ΔE_{ads}	ΔG_{ads}
1	−56.2	−36.2
2	−33.3	−42.0
3	−33.6	−27.1
4	−66.8	−53.0
4s	−30.5	−47.2

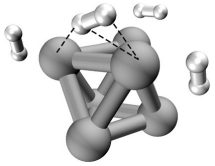

Fig. 11 The fourth H_2 molecule of the 4s geometry of carbon-supported Pd_6 is shared between two palladium atoms. The carbon support material located below the cluster is not shown.

the additional H_2 molecule is shared between two palladium atoms (see Fig. 11). If one adds a seventh H_2 molecule to the free Pd_6 cluster, in which all palladium atoms have already been covered with one H_2 molecule, not only one but three H_2 molecules are shared. Thus, each palladium atom can just carry one full H_2 molecule and if the coverage exceeds one H_2 molecule per palladium atom, the H_2 molecules have to be shared. For the carbon-supported Pd_6 cluster the H_2 sharing can also be observed for H_2 molecules, which are added to free palladium atoms of the lower layer of the cluster (*e.g.*, H_2 molecule number 4). Accordingly, the palladium atoms at the lower layer cannot carry one full H_2 molecule. As it would have been expected, the hindrance of the support material reduces the number of H_2 molecules, which can be added to the Pd_6 cluster.

Starting from physisorbed molecular H_2, the molecules can undergo dissociative chemisorption. A possible reaction pathway for the H_2 dissociation on a carbon-supported Pd_6 cluster is shown in Fig. 12.

As a first step, the H_2 molecule adsorbs at one of the palladium atoms located at the top of the cluster. This is, as described before, related to an energy gain of $\Delta E_{ads} = -56.2$ kJ mol^{-1}. Starting from the corresponding minimum of molecular adsorbed hydrogen, the system has to surpass an activation barrier. We have found two different possible transition states, in which one hydrogen atom is bound to one palladium atom and the other hydrogen atom bridges a Pd–Pd bond: (a) a transition state from a spin-restricted closed-shell calculation with an energy barrier of 42.0 kJ mol^{-1} and a free activation enthalpy of 3.3 kJ mol^{-1} showing a *cis*-configuration of the hydrogen atoms and (b) an energetically lower lying transition state from a spin-unrestricted calculation with an energy barrier of 21.6 kJ mol^{-1} and a free activation enthalpy of 4.1 kJ mol^{-1} showing a perpendicular configuration. Starting from the reactants (carbon-supported Pd_6 and a H_2 molecule in the gas phase), the hydrogen dissociation releases an energy of $\Delta E_{diss} = -100.0$ kJ mol^{-1}. In the product, the H_2 molecule is fully dissociated; the two hydrogen atoms are located on triangular positions each bridging three palladium atoms. The shown reaction pathway and the free activation enthalpies of 3.3 kJ mol^{-1} and 4.1 kJ mol^{-1} indicate that hydrogen dissociation on a carbon-supported Pd_6 cluster could occur spontaneously at room temperature. The minimal activation energy needed is relatively low (21.6 kJ mol^{-1}) and is already provided more than twice by the molecular adsorption process.

As a comparison, Fig. 13 shows the corresponding pathway on free Pd_6. Here, just the energetically lower lying open-shell transition state is included.

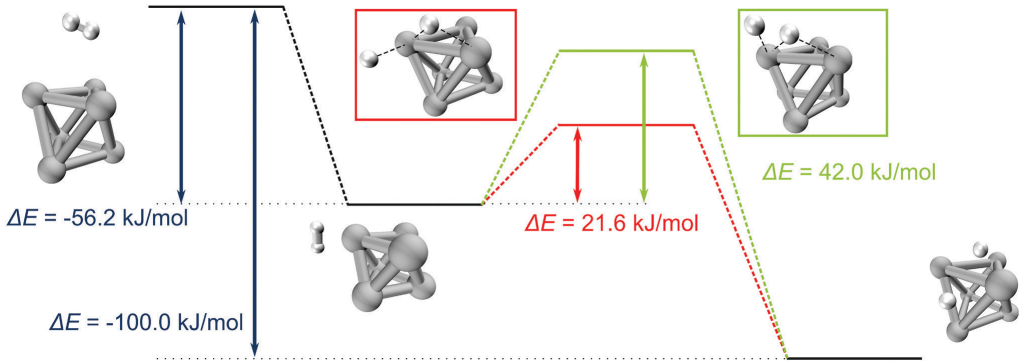

Fig. 12 Possible hydrogen dissociation pathways on carbon-supported Pd_6; red – the result of a spin-unrestricted calculation with a lower energy barrier and green – the result of a spin-restricted closed-shell calculation with a higher energy barrier. The carbon support material located below the clusters is not shown.

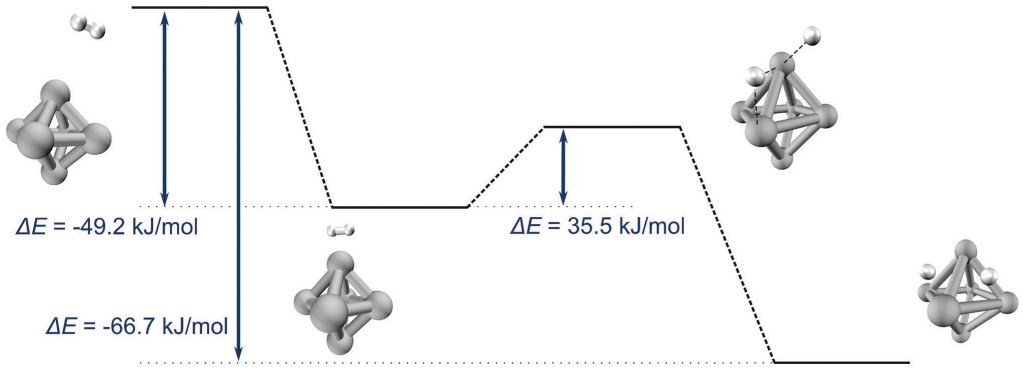

Fig. 13 A possible hydrogen dissociation pathway on free Pd_6.

In general, the dissociation mechanism on free Pd_6 is very similar to the mechanism on carbon-supported Pd_6. However, the observed energy differences deviate. The adsorption energy ΔE_{ads} and the dissociation energy ΔE_{diss} are -49.2 kJ mol^{-1} and -66.7 kJ mol^{-1} and, therefore, smaller than the corresponding energies of -56.2 kJ mol^{-1} and -100.0 kJ mol^{-1} respectively for the carbon-supported system. The activation energy barrier is 35.5 kJ mol^{-1} which is 13.9 kJ mol^{-1} higher than that for the carbon-supported system. Hence, the carbon support material increases the energy gain of the hydrogen adsorption and dissociation as well as it decreases the activation energy barrier, which has to be surmounted. Therefore, hydrogen adsorption and dissociation are energetically facilitated on carbon-supported Pd_6 clusters compared to free Pd_6. The free activation enthalpy of the free system is also very low (1.4 kJ mol^{-1}) which shows that hydrogen dissociation on free Pd_6 also occurs spontaneously at room temperature.

Palladium clusters can support the dissociation of more than one H_2 molecule. We have studied the dissociation of several H_2 molecules one after the other. For the carbon-supported Pd_6 cluster the hydrogen atoms have been added starting from the top of the cluster. The resulting incremental dissociation energies ΔE_{diss} and free enthalpies ΔG_{diss} for an increasing number of H_2 molecules for the free and for the carbon-supported Pd_6 cluster are shown in Tables 4 and 5.

In general, the dissociation energies ΔE_{diss} and the dissociation enthalpies ΔG_{diss} in Tables 4 and 5 indicate that a lot of H_2 molecules can be dissociated on the clusters.

Table 4 Incremental dissociation energies ΔE_{diss} and Gibbs free enthalpies ΔG_{diss} in kJ mol^{-1} for an increasing number of H_2 molecules on free Pd_6

Number of H_2	ΔE_{diss}	ΔG_{diss}
1	−66.7	−42.4
2	−45.7	−26.7
3	−71.5	−32.5
4	−68.8	−37.6

Table 5 Incremental dissociation energies ΔE_{diss} and Gibbs free enthalpies ΔG_{diss} in kJ mol^{-1} for an increasing number of H_2 molecules on carbon-supported Pd_6

Number of H_2	ΔE_{diss}	ΔG_{diss}
1	−100.0	−51.0
2	−62.8	−28.9
3	−106.1	−51.3

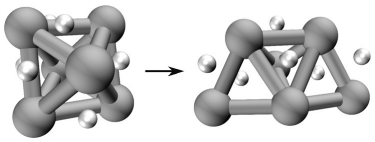

Fig. 14 The geometry of three dissociated hydrogen molecules on carbon-supported Pd_6 before and after geometry optimization. The carbon support material located below the clusters is not shown.

It is important to note that the third H_2 molecule has a dissociation energy of 34.6 kJ mol^{-1} and a free enthalpy of 18.8 kJ mol^{-1} more favourable for the carbon-supported system compared to the free system, even though the hydrogen atoms have to be added to the unfavourable lower layer of the cluster. The highly favourable ΔE_{diss} and ΔG_{diss} for the third dissociated H_2 molecule on the carbon-supported system can be explained by the fact that adding the two hydrogen atoms of the third H_2 molecules to the lower layer of the cluster leads to a deformation of the cluster (see Fig. 14), which forms a more favourable geometry connected to a favourable dissociation energy and enthalpy. This behaviour can also be observed, if one adds one hydrogen atom of the second H_2 molecule not to the top, but to the unfavourable lower layer of the cluster. During the geometry optimization the cluster deforms and the system still shows a favourable dissociation energy of −64.3 kJ mol^{-1} and a favourable dissociation enthalpy of −18.8 kJ mol^{-1}.

As such deformations cannot be observed for the free systems, the support material seems to stabilize them. Thus, a high hydrogen coverage on a carbon-supported Pd_6 cluster leads to a deformation of the cluster to a favourable geometry, which is stabilized by the support material. Therefore, the support material allows the cluster for a high hydrogen coverage, in spite of hindrance due to the support material, and facilitates the dissociation of several H_2 molecules compared to free Pd_6.

3.4 Hydrogen adsorption on Pd_{21}

As a model system, which should be closer to real systems under experimental conditions, we studied the adsorption of H_2 molecules from the gas phase on carbon-supported Pd_{21} and compared the results to the H_2 adsorption on free Pd_{21}. On the Pd_{21} systems molecular H_2 adsorption is possible at many different positions with different coordinations. We have studied six different positions for molecular H_2 adsorption, which are shown in Fig. 15. The corresponding adsorption energies ΔE_{ads} for the free and for the carbon-supported Pd_{21} clusters are shown in Tables 6 and 7.

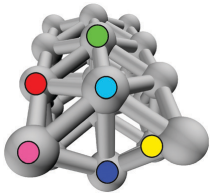

Fig. 15 Studied positions for molecular hydrogen adsorption on Pd_{21}.

Table 6 Adsorption energies ΔE_{ads} in kJ mol^{-1} for the different positions studied on free Pd_{21}

Position colored in	ΔE_{ads}
Green	−55.9
Light blue	−45.6
Pink	−40.6
Yellow	−34.8
Dark blue	−29.9
Red	−21.1

Table 7 Adsorption energies ΔE_{ads} in kJ mol^{-1} for the different studied positions on carbon-supported Pd_{21}

Position colored in	ΔE_{ads}
Green	−45.6
Light blue	−42.9
Pink	−34.4
Yellow	Not stable
Dark blue	−32.6
Red	−30.1

For the free Pd_{21} cluster the different H_2 positions are quite similar to each other. The adsorption energies range from −21.1 kJ mol^{-1} to −55.9 kJ mol^{-1}. In general, the positions at the top of the cluster (green and light blue) are preferred.

The carbon support material reduces the adsorption energies of the positions colored in green, light blue and pink as well as it increases the corresponding adsorption energies for the dark blue and red positions. The position at the bottom of the cluster (yellow) is not stable, due to steric hindrance by the support material. The adsorption energies for the carbon-supported Pd_{21} cluster range from −30.1 kJ mol^{-1} to −45.6 kJ mol^{-1}. Accordingly, the most attractive positions for molecular H_2 adsorption on carbon-supported Pd_{21} clusters are around 10 kJ mol^{-1} less favourable than that on free Pd_{21}. However, the support material decreases the range of adsorption energies to only 15.5 kJ mol^{-1} and therefore levels out the differences between the different positions.

Fig. 16 shows the electron density difference plot for the H_2 molecular adsorption on carbon-supported Pd_{21}. As one would expect, it looks very similar to the electron density difference plot for the H_2 adsorption on a Pd atom. Also here, there is an electron density gain for the 5s Pd and the σ_u^* H_2 orbital and a decreased electron density for the $4d_{xz}$ Pd orbital and the σ_g H_2 orbital. However, it can be observed that, compared to the Pd atom, the Pd cluster allows a partial depopulation of the $4d_{z^2}$

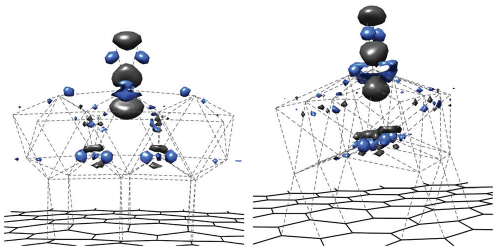

Fig. 16 Electron density difference plot for the H_2 molecular adsorption on carbon-supported Pd_{21} from two different perspectives. Density gain is colored in blue; density loss is colored in grey.

orbital in favour of some other orbitals in the Pd cluster, decreasing the repulsive effect of the $4d_{z^2}$–σ_g interaction.

The details of the electronic effect of the carbon support material on the molecular hydrogen adsorption are provided in Fig. 17 showing the electron density difference plot for the interaction between the carbon support and the most stable Pd_{21}–H_2 system. We observe that the supported system has a higher population of the $4d_{z^2}$ orbital of the Pd atom that adsorbed the H_2. This increases the repulsion between the $4d_{z^2}$ Pd orbital and the σ_g H_2 orbital and, therefore, destabilizes

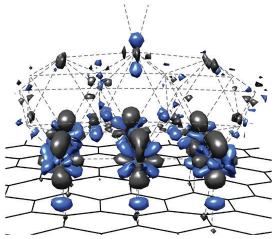

Fig. 17 Electron density difference plot for the interaction between the carbon support and the most stable Pd_{21}–H_2 system. Density gain is colored in blue; density loss is colored in grey.

the Pd–H_2 bond and reduces the adsorption energy relative to the unsupported system. The increased adsorption energies for the dark blue and red H_2 positions are probably due to some favorable changes in the geometries. Together these effects reduce the differences between the adsorption energies at the different sites and increase the mobility of the hydrogen on the Pd cluster.

Also on Pd_{21} molecular adsorbed H_2 can undergo dissociative chemisorption. A possible reaction pathway for the H_2 dissociation on a carbon-supported Pd_{21} cluster is shown in Fig. 18. In the first step the H_2 molecule is adsorbed at the most favourable site (green position in Fig. 15) releasing an energy of $\Delta E_{ads} = -45.6$ kJ mol^{-1}. Starting from this minimum, the system goes through a transition state with an energy barrier of 22.5 kJ mol^{-1} and then forms the fully dissociated hydrogen product, in which the two hydrogen atoms are located at the adjacent fcc sites. The overall dissociation energy ΔE_{diss} is -108.8 kJ mol^{-1}. The corresponding pathway on free Pd_{21} looks very much the same. However, the reaction energies are slightly different. As mentioned above, the adsorption energy of H_2 at the most favourable position for the free cluster is -55.9 kJ mol^{-1} and, therefore, higher than that for the carbon-supported cluster. Also the dissociation energy is higher for the free cluster (-127.9 kJ mol^{-1}). In contrast to this, the activation energy barrier is slightly reduced to 11.3 kJ mol^{-1} which corresponds to a free activation enthalpy of 2.7 kJ mol^{-1}. Close to the transition state the potential energy surface of the system is very flat. Thus, a full transition state optimization was not possible and the vibrational analysis of the transition state described here still shows three negative eigenvalues. However, we expect the errors introduced by this to be negligible. For the calculation of the free activation enthalpy, the additional negative eigenvalues have not been included in the zero-point vibrational energy.

It is important to note that the hydrogen dissociation pathways on carbon-supported Pd_6 and carbon-supported Pd_{21} are very similar to each other. Even the observed adsorption and dissociation energies and the activation barriers agree very well. Also hydrogen dissociation on a carbon-supported Pd_{21} cluster can occur spontaneously at room temperature.

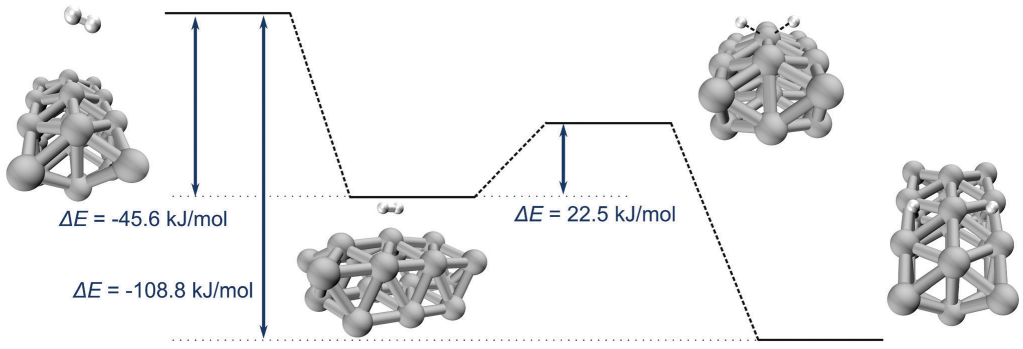

Fig. 18 A possible hydrogen dissociation pathway on carbon-supported Pd_{21}. The carbon support material located below the clusters is not shown.

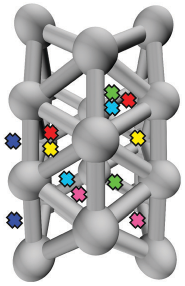

Fig. 19 Studied configurations for dissociated hydrogen on Pd_{21}.

Table 8 Dissociation energies ΔE_{diss} in kJ mol^{-1} for the different studied positions on free Pd_{21}

Positions colored in	ΔE_{diss}
Yellow	−127.9
Red	−124.6
Light blue	−109.1
Green	−107.6
Pink	−102.4
Dark blue	−88.7

Table 9 Dissociation energies ΔE_{diss} in kJ mol^{-1} for the different studied positions on carbon-supported Pd_{21}

Positions colored in	ΔE_{diss}
Yellow	−108.8
Red	−98.5
Light blue	−93.5
Green	−93.6
Pink	−101.5
Dark blue	−95.0

On the Pd_{21} clusters the H_2 molecule has different possibilities to dissociate. We have studied six different configurations for the two hydrogen atoms, which are shown in Fig. 19. The corresponding dissociation energies ΔE_{diss} for the free and for the carbon-supported Pd_{21} clusters are listed in Tables 8 and 9.

For the free Pd_{21} cluster the different configurations of the two hydrogen atoms are quite similar to each other. The dissociation energies ΔE_{diss} range from −88.7 kJ mol^{-1} to −127.9 kJ mol^{-1}. In general, the positions at the top of the cluster (yellow, red, light blue and green) are preferred over configurations in which one (pink) or both (dark blue) hydrogen atoms are located at the side of the cluster. In the most favourable configuration (yellow) the two hydrogen atoms are located at the adjacent fcc sites. The effect of the carbon support material on the dissociation energies is quite similar to its effect on the H_2 adsorption energies. The dissociation energy for the most favourable configurations is decreased by around 20 kJ mol^{-1} compared to the free Pd_{21} system. The range of dissociation energies is reduced to only 15.3 kJ mol^{-1}. As a conclusion, the carbon support material also levels out the differences between different configurations of the hydrogen atoms after H_2 dissociation.

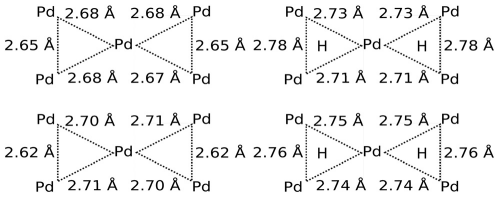

Fig. 20 Sketch of the six relevant Pd–Pd distances for the free (top) and carbon-supported (bottom) systems each with (right) and without (left) dissociated H_2 at the fcc positions.

The electron density difference plot for the influence of the carbon support material on the hydrogen dissociation on Pd_{21} does not show any relevant shifts in the electron density. However, the H_2 dissociation on both free and carbon-supported Pd_{21} is connected to quite a strong change of geometry around the hydrogen atoms. Fig. 20 shows a sketch of the six relevant Pd–Pd distances for the free and carbon-supported systems each with and without dissociated H_2 at the fcc positions.

If the hydrogen atoms are added to the free cluster, the Pd–Pd bonds are elongated. The largest change can be observed at the edge of the cluster, where the bond is elongated by 0.13 Å from 2.65 to 2.78 Å. The Pd–Pd distances at the top of the cluster show changes between 0.03 Å and 0.05 Å. For the carbon-supported cluster a very similar behavior can be observed. There, the Pd–Pd bonds are elongated by 0.14 Å at the edge of the cluster and from 0.03 Å to 0.05 Å at the top of the cluster. In general, the distances on the free and on carbon-supported clusters are nearly the same, both with and without dissociated H_2. However, the support material hinders the relaxation of the rest of the system after the Pd–Pd bond elongation and, as can be seen in the geometry, leads to a deformation of the support material. This explains the decreased H_2 dissociation energy for the carbon-supported cluster. The increased H_2 dissociation energy for the pink and the dark blue systems is probably due to some geometrical changes in the H_2 positions.

The hydrogen atoms can migrate between the different positions on the cluster. A possible migration pathway between the yellow and the red configuration on carbon-supported Pd_{21} is shown in Fig. 21. The transition state, in which one hydrogen atom bridges a Pd–Pd bond, has an activation energy barrier of 9.3 kJ mol^{-1} starting from the less favourable red configuration and an activation energy barrier of 19.6 kJ mol^{-1} starting from the most favourable yellow configuration. Accordingly, hydrogen atom migration on carbon-supported Pd_{21} could occur spontaneously at room temperature, especially when the hydrogen atoms are not located in the most stable configuration.

The migration pathway on free Pd_{21} looks exactly the same as the pathway on carbon-supported Pd_{21} in Fig. 21. The activation energy barrier for the migration from the less favourable red configuration is 8.3 kJ mol^{-1} and, therefore, very similar to the corresponding activation barrier of the carbon-supported system. However, the activation energy barrier for the migration starting from the yellow configuration is only 11.6 kJ mol^{-1}.

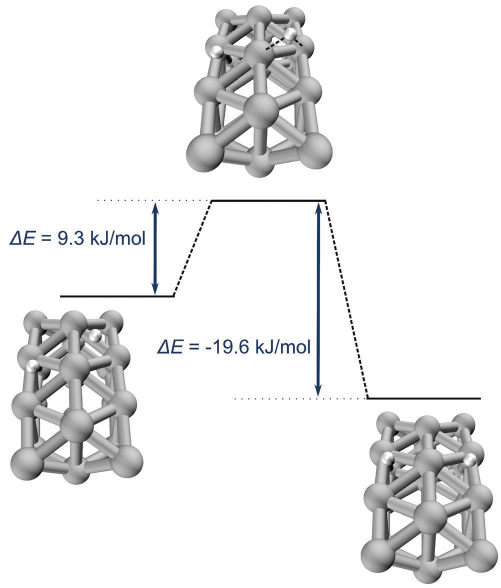

Fig. 21 Hydrogen migration pathway from the red to the yellow configuration on carbon-supported Pd_{21}. The carbon support material located below the clusters is not shown.

The free activation enthalpies are 10.5 kJ mol^{-1} for the migration from the red configuration and 6.3 kJ mol^{-1} for the migration from the yellow configuration. This confirms the conclusion drawn from the activation energies that hydrogen migration on Pd_{21} clusters should occur spontaneously at room temperature.

4 Conclusions

The present study provided an in-depth insight into metal–support interactions for carbon-supported palladium clusters and their influence on hydrogen adsorption. Palladium clusters show quite strong attractive palladium–carbon interactions. The dispersion contribution to the interaction increases with the system size. The support material has a rather small and local effect on the electronic structure. No changes in bonding orbitals can be observed. The metal–support interaction is based on a shift of electron density from the lowest layer of the cluster to the support-metal connecting line, indicating directed partially covalent Pd–C interactions.

In general, hydrogen adsorption on palladium clusters could at low temperatures proceed stepwise. First, the H_2 molecule is physisorbed. In the second step, the H_2 molecule undergoes dissociative chemisorption. The corresponding reaction pathways for the systems with and without carbon support are very similar to each other. However, the carbon support material has an effect on the observed energies. In the case of Pd_6 the carbon support increases the adsorption and dissociation energy and lowers the activation energy barrier. For the Pd_{21} systems the effect of the carbon support material depends on the position. All in all, the support decreases the adsorption energies at the top site by hindering the depopulation of the $4d_{z^2}$ orbital and also decreases the dissociation energies at these sites by geometrical constrains. However, destabilization of the quite attractive palladium–hydrogen interaction might be in favour of catalytic activity as it increases the mobility of the hydrogen on the cluster. Furthermore, the support material reduces the differences between different positions and facilitates the H_2 adsorption and dissociation at different positions on the cluster. The free activation enthalpies show that at room temperature H_2 dissociation should occur spontaneously both on free and on carbon-supported palladium clusters.

With and without the carbon support material palladium clusters can adsorb several hydrogen molecules. If one adds more than one H_2 molecule per palladium atom the palladium atoms start to share hydrogen molecules. For the carbon-supported systems the hindrance of the support material reduces the number of H_2 molecules, which can be added to the cluster. Dissociation of several hydrogen molecules on free and on carbon-supported palladium clusters is energetically favourable and shows negative reaction enthalpies at room temperature. The carbon support material facilitates the dissociation of several hydrogen molecules on the clusters, especially by stabilizing geometrical deformations. Hydrogen atom migration can occur spontaneously at room temperature on free and on carbon-supported palladium clusters.

In general, Pd_6 and Pd_{21} systems show very similar pathways and energies. Accordingly, already the quite small carbon-supported Pd_6 clusters are good model systems for reaction pathways. However, Pd_6 cannot model special properties of palladium nanoparticles. So it does not show the decrease in adsorption and dissociation energies caused by the carbon support material, which might increase the catalytic activity of the palladium cluster. Furthermore, the hydrogen atom migration or the differences between different adsorption sites, which will definitely affect the hydrogenation process in experiments, cannot be studied on Pd_6. Therefore it is essential to also take larger cluster sizes as Pd_{21} into account.

The present study on hydrogen adsorption helps to obtain a deeper understanding of hydrogenation reactions employing mesoporous carbon as the support material and will be a good starting point for subsequent studies focusing on the effect of nitrogen or oxygen doping on the hydrogenation reactions. For instance, in experiments it can be observed that hydrogen atoms, which are attached to a carbon-supported metal-nanoparticle, can migrate from the metal to the support material. This so called hydrogen spillover especially occurs on nitrogen-doped carbon support materials and might play an important role in hydrogenation reactions.[50] The low energy barriers and low free activation enthalpies for hydrogen atom migration on Pd_{21} clusters obtained in the present study provide some evidence that hydrogen spillover might actually be possible. We plan to investigate the hydrogen spillover in more detail in a subsequent study.

Conflicts of interest

There are no conflicts to declare.

Acknowledgements

This work was supported by the Deutsche Forschungsgemeinschaft and the National Natural Science Foundation of China within the framework of the Sino-German initiative ''Novel Functional Materials for Sustainable Chemistry'' through grant Ha 2588/9-1.

References

1 W. Ludwig, A. Savara, K.-H. Dostert and S. Schauermann, *J. Catal.*, 2011, **284**, 148–156.
2 F. Zaera, *ACS Catal.*, 2017, **7**, 4947–4967.
3 A. Stanislaus and B. H. Cooper, *Catal. Rev.: Sci. Eng.*, 1994, **36**, 75–123.
4 *Catalytic Hydrogenation*, ed. L. Cervený, Elsevier Science, 1986, vol. 27.
5 V. Kratky, M. Kralik, M. Mecarova, M. Stolcova, L. Zalibera and M. Hronec, *Appl. Catal., A*, 2002, **235**, 225–231.
6 D. M. Alonso, J. Q. Bond and J. A. Dumesic, *Green Chem.*, 2010, **12**, 1493–1513.
7 A. T. Bell, *Science*, 2003, **299**, 1688–1691.
8 N. M. Julkapli and S. Bagheri, *Int. J. Hydrogen Energy*, 2015, **40**, 948–979.
9 T. E. Felter, E. C. Sowa and M. A. Van Hove, *Phys. Rev. B: Condens. Matter Mater. Phys.*, 1989, **40**, 891–899.
10 K. Christmann, *Surf. Sci. Rep.*, 1988, **9**, 1–163.
11 M. Johansson, E. Skúlason, G. Nielsen, S. Murphy, R. Nielsen and I. Chorkendorff, *Surf. Sci.*, 2010, **604**, 718–729.
12 A. Tomaszewska, A. Ciszewski and Z. M. Stepień, *Appl. Surf. Sci.*, 2008, **254**, 4386–4390.
13 T. Mitsui, M. Rose, E. Fomin, D. Ogletree and M. Salmeron, *Surf. Sci.*, 2003, **540**, 5–11.
14 J.-F. Paul and P. Sautet, *Phys. Rev. B: Condens. Matter Mater. Phys.*, 1996, **53**, 8015–8027.
15 V. Ledentu, W. Dong and P. Sautet, *Surf. Sci.*, 1998, **412–413**, 518–526.
16 M. Lischka and A. Groß, *Phys. Rev. B: Condens. Matter Mater. Phys.*, 2002, **65**, 075420.
17 Y. Zhao and D. Tian, *Comput. Theor. Chem.*, 2012, **991**, 40–43.
18 J. Moc, D. G. Musaev and K. Morokuma, *J. Phys. Chem. A*, 2000, **104**, 11606–11614.
19 J. Moc, D. G. Musaev and K. Morokuma, *J. Phys. Chem. A*, 2003, **107**, 4929–4939.
20 Y. Wang, Z. Cao and Q. Zhang, *Chem. Phys. Lett.*, 2003, **376**, 96–102.
21 C. Zhou, S. Yao, J. Wu, R. C. Forrey, L. Chen, A. Tachibana and H. Cheng, *Phys. Chem. Chem. Phys.*, 2008, **10**, 5445–5451.
22 A. W. Pelzer, J. Jellinek and K. A. Jackson, *J. Phys. Chem. A*, 2015, **119**, 3594–3603.
23 R. S. Shamsiev and F. O. Danilov, *Russ. Chem. Bull.*, 2017, **66**, 395–400.
24 A. Granja-DelRío, J. A. Alonso and M. J. López, *Comput. Theor. Chem.*, 2017, **1107**, 23–29.
25 I. López-Corral, E. Germán, A. Juan, M. A. Volpe and G. P. Brizuela, *J. Phys. Chem. C*, 2011, **115**, 4315–4323.
26 C. Ramos-Castillo, J. Reveles, R. Zope and R. de Coss, *J. Phys. Chem. C*, 2015, **119**, 8402–8409.
27 A. Lu, A. Kiefer, W. Schmidt and F. Schüth, *Chem. Mater.*, 2004, **16**, 100–103.
28 Y. Huang, F. Yang, Z. Xu and J. Shen, *J. Colloid Interface Sci.*, 2011, **363**, 193–198.
29 J. Cai, S. Bennici, J. Shen and A. Auroux, *Microporous Mesoporous Mater.*, 2015, **212**, 156–168.
30 J. Tao, J. P. Perdew, V. N. Staroverov and G. E. Scuseria, *Phys. Rev. Lett.*, 2003, **91**, 146401.
31 F. Weigend and R. Ahlrichs, *Phys. Chem. Chem. Phys.*, 2005, **7**, 3297–3305.
32 D. Andrae, U. Häußermann, M. Dolg, H. Stoll and H. Preuß, *Theor. Chim. Acta*, 1990, **77**, 123–141.
33 F. Furche and J. P. Perdew, *J. Chem. Phys.*, 2006, **124**, 044103.
34 D. Stodt, H. Noei, C. Hättig and Y. Wang, *Phys. Chem. Chem. Phys.*, 2013, **15**, 466–472.
35 J. Koßmann and C. Hättig, *Phys. Chem. Chem. Phys.*, 2012, **14**, 16392–16399.
36 TURBOMOLE V7.1 2016, V7.2.1 2017 and V7.3 2018, a development of University of Karlsruhe and Forschungszentrum Karlsruhe GmbH, 1989-2007, TURBOMOLE GmbH, since 2007, available from http://www.turbomole.com.
37 M. Sierka, A. Hogekamp and R. Ahlrichs, *J. Chem. Phys.*, 2003, **118**, 9136–9148.
38 F. Weigend, *Phys. Chem. Chem. Phys.*, 2006, **8**, 1057–1065.
39 S. Grimme, J. Antony, S. Ehrlich and H. Krieg, *J. Chem. Phys.*, 2010, **132**, 154104.
40 P. Plessow, *J. Chem. Theory Comput.*, 2013, **9**, 1305–1310.
41 T. Helgaker, *Chem. Phys. Lett.*, 1991, **182**, 503–510.
42 K. Fukui, *Acc. Chem. Res.*, 1981, **14**, 363–368.
43 A. D. Becke, *Phys. Rev. A: At., Mol., Opt. Phys.*, 1988, **38**, 3098–3100.
44 J. P. Perdew, *Phys. Rev. B: Condens. Matter Mater. Phys.*, 1986, **33**, 8822–8824.
45 J. P. Perdew, K. Burke and M. Ernzerhof, *Phys. Rev. Lett.*, 1996, **77**, 3865–3868.
46 G. Knizia, *J. Chem. Theory Comput.*, 2013, **9**, 4834–4843.
47 K. A. Peterson, D. Figgen, M. Dolg and H. Stoll, *J. Chem. Phys.*, 2007, **126**, 124101.
48 P. Nava, M. Sierka and R. Ahlrichs, *Phys. Chem. Chem. Phys.*, 2003, **5**, 3372–3381.
49 W. B. Schneider, U. Benedikt and A. A. Auer, *ChemPhysChem*, 2013, **14**, 2984–2989.
50 W. C. Conner and J. L. Falconer, *Chem. Rev.*, 1995, **95**, 759–788.

PCCP

ROYAL SOCIETY OF CHEMISTRY

CORRECTION

Cite this: *Phys. Chem. Chem. Phys.*, 2020, **22**, 8233

Correction: A quantum chemical study of hydrogen adsorption on carbon-supported palladium clusters

Lisa Warczinski* and Christof Hättig

DOI: 10.1039/d0cp90079f

rsc.li/pccp

Correction for 'A quantum chemical study of hydrogen adsorption on carbon-supported palladium clusters' by Lisa Warczinski *et al.*, *Phys. Chem. Chem. Phys.*, 2019, **21**, 21577–21587, DOI: 10.1039/c9cp04606b.

We correct an error to our previous paper,[1] which does not affect the key statements of the paper but changes some values and one minor conclusion. In our previous paper, the calculation of the Gibbs free enthalpies was missing electronic contributions and an incorrect scaling parameter for the vibrational frequencies was used. Here, we report the corrected values for the Gibbs free enthalpies including all necessary contributions and employing the correct vibrational frequency scaling parameter of 1.0190 for the def2-SVP basis set and the TPSS functional.[2]

The first values we need to correct are the Gibbs free enthalpies of adsorption of several hydrogen molecules on Pd_6. The corrected values are shown in the reproduced Tables 2 and 3. All the corresponding conclusions are still valid.

Table 2 Incremental adsorption energies ΔE_{ads} and Gibbs free enthalpies ΔG_{ads} in kJ mol^{-1} for an increasing number of H_2 molecules on free Pd_6

Number of H_2	ΔE_{ads}	ΔG_{ads}
1	−49.2	−24.8
2	−43.8	−9.7
3	−43.7	−20.1
4	−37.8	−10.0
5	−33.7	−9.4
6	−24.2	+6.8
7	−64.8	−22.5

Table 3 Incremental adsorption energies ΔE_{ads} and Gibbs free enthalpies ΔG_{ads} in kJ mol^{-1} for an increasing number of H_2 molecules on carbon-supported Pd_6

Number of H_2	ΔE_{ads}	ΔG_{ads}
1	−56.2	−28.5
2	−33.3	−3.2
3	−33.6	−12.0
4	−66.8	−27.7
4s	−30.5	+9.7

In contrast to that, the free activation enthalpies for the hydrogen dissociation on Pd_6 changed noticeably:

- free Pd_6: 40.4 kJ mol^{-1} (old: 1.4 kJ mol^{-1})
- carbon-supported *cis*-configuration: 45.2 kJ mol^{-1} (old: 3.3 kJ mol^{-1})
- carbon-supported perpendicular configuration: 22.2 kJ mol^{-1} (old: 4.1 kJ mol^{-1})

Therefore, we have to correct our conclusion that hydrogen dissociation on free Pd_6 should occur spontaneously at room temperature. $\Delta G^{\ddagger}$ is, at 40.4 kJ mol^{-1}, rather high for this. However, this further confirms our result that it is essential to also study larger cluster sizes (*vide infra*). Additionally, the conclusion that hydrogen dissociation on carbon-supported Pd_6 should occur

Lehrstuhl für Theoretische Chemie, Ruhr-Universität Bochum, 44780 Bochum, Germany. E-mail: lisa.warczinski@rub.de

Table 4 Incremental dissociation energies ΔE_{diss} and Gibbs free enthalpies ΔG_{diss} in kJ mol^{-1} for an increasing number of H_2 molecules on free Pd_6

Number of H_2	ΔE_{diss}	ΔG_{diss}
1	−66.7	−36.3
2	−45.7	−15.7
3	−71.5	−42.7
4	−68.8	−32.4

Table 5 Incremental dissociation energies ΔE_{diss} and Gibbs free enthalpies ΔG_{diss} in kJ mol^{-1} for an increasing number of H_2 molecules on carbon-supported Pd_6

Number of H_2	ΔE_{diss}	ΔG_{diss}
1	−100.0	−72.1
2	−62.8	−33.1
3	−106.1	−71.9

spontaneously at room temperature is still valid. The free activation barrier for the dissociation is smaller than the Gibbs free enthalpy change for the initial molecular adsorption step.

Also, the values for the Gibbs free enthalpies of dissociation of several hydrogen molecules on Pd_6 are affected. However, all the corresponding conclusions are still valid. Tables 4 and 5 are reproduced here and list the corrected values. Further changes are:

• The third hydrogen molecule has a free dissociation enthalpy 36.7 kJ mol^{-1} more favourable for the carbon-supported system compared to the free system (old: 18.8 kJ mol^{-1}).

• If one adds one hydrogen atom of the second hydrogen molecule not to the top, but to the unfavourable lower layer of the cluster, the cluster deforms and shows a favourable free dissociation enthalpy of −48.3 kJ mol^{-1} (old: −18.8 kJ mol^{-1}).

Also, the changes for the Pd_{21} systems are negligible and all conclusions drawn previously are still valid. The following list reports the changes which occurred due to the correction of the mistake for the Pd_{21} systems:

• Free activation enthalpy for the hydrogen dissociation on free Pd_{21}: 13.8 kJ mol^{-1} (old: 2.7 kJ mol^{-1})

• Free activation enthalpy for the H atom migration from the red configuration: 6.6 kJ mol^{-1} (old: 10.5 kJ mol^{-1})

• Free activation enthalpy for the H atom migration from the yellow configuration: 5.0 kJ mol^{-1} (old: 6.3 kJ mol^{-1})

The Royal Society of Chemistry apologises for these errors and any consequent inconvenience to authors and readers.

References

1 L. Warczinski and C. Hättig, *Phys. Chem. Chem. Phys.*, 2019, **21**, 21577–21587.

2 M. K. Kesharwani, B. Brauer and J. M. L. Martin, *J. Phys. Chem. A*, 2015, **119**, 1701–1714.

5 Anchoring of Palladium Nanoparticles on N-Doped Mesoporous Carbon

In the previous chapter, we have investigated the metal-support interactions in Pd/CMC. The study in this chapter, which was published in the Journal *Physical Chemistry Chemical Physics*, focuses on the properties of Pd/NMC and was performed in collaboration with the research group of Professor Muhler.

As a first step, we used the model systems for the NMC support material shown in Chapter 2 (cmp. Figure 2.2) to interpret experimental N 1s X-ray photoelectron spectra and, therefore, to determine the composition of nitrogen functional groups in the NMC support. On the basis of these results, we studied the interaction of Pd with the detected N functional groups. For this purpose, we performed calculations on the metal-support interactions in the Pd/NMC model systems (cmp. Figures 2.5, 2.6 and 2.7) and analyzed experimental Pd 3d X-ray photoelectron spectra.

Reproduced from Ref. 105[1] with permission from the PCCP Owner Societies.[2]

[1] Article: http://dx.doi.org/10.1039/D0CP03234D
SI: reproduced in the appendix on pages 150 - 215

[2] The underlying quantum chemical calculations as well as the writing and submission process for this publication were under my responsibility, supervised by Professor Hättig and Professor Muhler. Experimental details, spectra, evaluation and text components were provided by Dr. Bin Hu, Till Eckhard and Dr. Baoxiang Peng (Muhler Group).

PCCP

ROYAL SOCIETY OF CHEMISTRY

PAPER

Cite this: *Phys. Chem. Chem. Phys.*, 2020, **22**, 21317

Anchoring of palladium nanoparticles on N-doped mesoporous carbon†

Lisa Warczinski, *[a] Bin Hu, [bc] Till Eckhard, [b] Baoxiang Peng, [bc] Martin Muhler [bc] and Christof Hättig [a]

Received 16th June 2020,
Accepted 19th August 2020

DOI: 10.1039/d0cp03234d

rsc.li/pccp

Pd nanoparticles deposited on nitrogen-doped mesoporous carbon are promising catalysts for highly selective and effective catalytic hydrogenation reactions. To design and utilize these novel catalysts, it is essential to understand the effect of N doping on the metal–support interactions. A combined experimental (X-ray photoelectron spectroscopy) and computational (density functional theory) approach is used to identify preferential adsorption sites and to give detailed explanations of the corresponding metal–support interactions. Pyridinic N atoms turned out to be the preferential adsorption sites for Pd nanoparticles on nitrogen-doped mesoporous carbon, interacting through their lone pairs (LPs) with the Pd atoms *via* N-LP – Pd d_σ and N-LP – Pd s and Pd d_π – π^* charge transfer, which leads to a change in the Pd oxidation state. Our results evidence the existence of bifunctional palladium nanoparticles containing Pd^0 and Pd^{2+} centers.

Introduction

Carbon materials are among the most commonly used support materials for metal nanoparticle catalysts. They are highly resistant to both acidic and basic media and as a support material for metal nanoparticles (NPs) they also facilitate an easy recovery of the metal. Another advantage of carbon materials is that their surface properties can be fine-tuned with great precision.[1] For industrial heterogeneous catalysis two carbon support materials have attracted tremendous attention: carbon nanotubes and mesoporous carbon. Carbon nanotubes are among the most intensively studied materials in surface chemistry in recent years. Due to their unique crystalline structure, carbon nanotubes show high thermal stability.[2] Mesoporous carbon is a novel promising support material in heterogeneous catalysis. With its irregular porosity, mesoporous carbon is characterized by a very large surface area and can be easily synthesized at a low cost.[3]

One main focus of carbon research is the modification of carbon materials. The influence of surface defects, functional groups and heteroatoms on the structure and functionality of carbon materials, in the first place on carbon nanotubes, has been addressed in several studies. It has been shown that these surface defects, functional groups and heteroatoms also affect the interaction between a carbon surface and deposited metal nanoparticles. Nitrogen and oxygen on the surface of carbon support materials change the properties of the supported metal nanoparticles. As a consequence, nitrogen- and oxygen-containing functional groups can be used to tune the dispersion, morphology, crystal structure, electronic structure, mobility/stability and the catalytic performance of the supported nanoparticles.[4]

One of the most important industrial applications of metal nanoparticles on carbon support materials in heterogeneous catalysis is the hydrogenation of aromatic compounds. For instance, the catalytic hydrogenation of chloronitrobenzenes produces chloroanilines, which are precursors for many important organic materials. The major side reaction, which reduces the selectivity of these hydrogenation reactions towards chloroanilines, is the process of dechlorination.[5] To improve the selectivity, dehalogenation inhibitors like quinoline have to be added to the reaction system. We aim at designing novel catalyst support materials with moderate to strong surface basicity, which seems to be a promising alternative to adding basic molecules to the hydrogenation reaction. A key step for accomplishing this goal is to fully understand the fundamental processes occurring on the catalyst surface.

The purpose of this study is to shed light on the properties of Pd nanoparticles deposited on nitrogen-doped mesoporous carbon (Pd/NMC) compared to Pd on nitrogen-free mesoporous carbon (Pd/CMC). We aim to identify the preferential adsorption sites of Pd and to give an in-depth insight into the effect of nitrogen doping on the corresponding metal–support interactions.

[a] *Chair of Theoretical Chemistry, Ruhr-University Bochum, 44780 Bochum, Germany. E-mail: lisa.warczinski@rub.de*
[b] *Laboratory of Industrial Chemistry, Ruhr-University Bochum, 44780 Bochum, Germany*
[c] *Max Planck Institute for Chemical Energy Conversion, 45470 Mülheim a.d. Ruhr, Germany*

† Electronic supplementary information (ESI) available. See DOI: 10.1039/d0cp03234d

For this purpose we combine experimental X-ray photoelectron spectroscopy (XPS) with a computational density functional theory (DFT) study. As theoretical model systems, we use a Pd_{21} cluster on a hydrogen terminated graphene layer, which has successfully been used as a model system for Pd/CMC in a previous study.[6]

Methodology

Synthesis of mesoporous carbon

Mesoporous carbon (CMC) was prepared from fructose (99% ADM) using $ZnCl_2$ as the template and catalyst.[7] N-Containing mesoporous carbon (NMC) was synthesized *via* carbonization of melamine (99%, Sigma-Aldrich) and formaldehyde (37 wt% in water, Sigma-Aldrich) using $CaCl_2$ (>95%, Fluka) as the template according to a previous report.[3] The as-prepared NMC and CMC were purified using a 1.5 M HNO_3 aqueous solution at room temperature for 72 h, followed by washing and filtration in deionized water several times until the pH of the filtrate became neutral. The purified NMC and CMC were dried at 80 °C overnight and ground for further use.

Catalyst preparation

Pd/NMC and Pd/CMC were prepared using a sol-immobilization method. Briefly, an aqueous solution of $PdCl_2$ (99%, Sigma-Aldrich) of the desired concentration was prepared. Subsequently, a polyvinyl alcohol (PVA) solution (1 wt%, M_W = 9000–10 000 g mol^{-1}) was added (PVA/Pd (wt/wt) = 1.2). Afterwards, a freshly prepared $NaBH_4$ aqueous solution (0.1 M, 10 times excess) was added, which immediately formed a dark-brown colloidal solution containing the Pd nanoparticles. As $NaBH_4$ is a very strong reducing agent, the complete reduction of the Pd^{2+} precursor to Pd^0 has been clearly demonstrated *via* UV-vis spectroscopy after the addition of $NaBH_4$ as reported in the literature.[8,9] After 30 min of sol generation, the powder support was added into the dark-brown colloidal solution at a proper pH under vigorous stirring. The required amount of the support was calculated to achieve a Pd loading of 1 wt%. After 2 h, the catalyst was obtained after filtration, washing with distilled water several times to remove boron and chloride, and drying at 80 °C overnight.

The supported catalysts and mesoporous supports were characterized *via* N_2 physisorption, XRD, and TEM and their properties have been reported in a previous study.[10] In brief, CMC and NMC exhibited comparable mesoporous structures, for example, similar average pore sizes of 5.0 and 4.9 nm, pore volumes of 1.2 and 0.7 cm^3 g^{-1}, and specific surface areas of 997 and 657 m^2 g^{-1}, respectively (Table S1, ESI†). After the deposition of Pd, the pore sizes, pore volumes, and BET surface areas of both catalysts were slightly decreased compared with those of the parent materials. The actual Pd loadings of the catalysts were found to be *ca.* 1.0 wt%. Compared with Pd/CMC, no significant Pd reflections were identified for Pd/NMC *via* XRD (Fig. S1, ESI†), suggesting higher Pd dispersion on NMC and the crucial role of N atoms as strong anchoring sites for Pd nanoparticles. The mean Pd particle sizes for Pd/NMC and Pd/CMC were rather similar amounting to 3.4 and 4.2 nm, respectively (Fig. S2, ESI†), allowing a direct comparison of metal–support interactions, excluding the effect of particle size.

X-ray photoelectron spectroscopy

X-ray photoelectron spectroscopy (XPS) measurements were performed in an ultrahigh vacuum setup equipped with a high-resolution Gammadata Scienta SES 2002 analyzer. A monochromatic Al Kα X-ray source (1486.6 eV, the anode operating at 14.5 kV and 30.5 mA) was used as the incident radiation source. The pressure inside the measuring chamber was kept in the range of 3.5 to 7 × 10^{-10} mbar during each measurement. The slit width of the analyzer was set at 0.3 mm and the pass energy was fixed at 200 eV for all measurements. The overall energy was better than 0.5 eV. Charging effects due to the insufficient conductivity of the carbon materials were mediated by using a flood gun (SPECS). All spectra were calibrated based on the C 1s binding energy of 284.5 eV. The CASA XPS program was used to analyze the XPS spectra, and a mixed Gaussian–Lorentzian function and Shirley background subtraction were applied in the fitting of the XPS data. The XPS survey spectra of the catalysts verified the presence of C, N, O, and Pd as well as the absence of B and Cl residues (Fig. S3, ESI†). Elemental analysis and XPS results demonstrated similar bulk and surface N abundances in NMC and Pd/NMC (Table S2, ESI†), indicating a homogenous distribution of N in NMC. Furthermore, CMC and Pd/CMC exhibit comparable but slightly higher surface oxygen contents compared to NMC and Pd/NMC (Table S2, ESI†).

Computational methods and model systems

The quantum chemical calculations were performed at the level of density functional theory (DFT) with the TPSS[11]/def2-SVP[12] functional and basis set and carried out using the TURBOMOLE[13] program package. For the palladium atoms Stuttgart–Cologne effective core potentials (def2-ecp)[14] were employed. All calculations include the multipole accelerated resolution of identity (MARI-J)[15] approximation with optimized auxiliary basis sets[16] and Grimme's D3[17] correction for London dispersion interactions.

To obtain an insight into the role of dispersion on the binding energies, single point energies were calculated with and without the D3 correction. Zero-point vibrational energy (ZPVE) corrections from the vibrational analysis were added to the energy differences.

To study the details of the electronic structure natural population analyses (NPAs)[18] were performed. As the π-system of the different support materials can be well described using Hückel theory, we also looked at Hückel-based population analyses. Furthermore, we calculated electron densities, generated electron density difference plots and visualized intrinsic bond orbitals (IBOs),[19] for which we used a 1s1p1d subset of the atomic orbitals in the cc-pVTZ-PP basis set for Pd.[20] To validate the experimental N 1s and Pd 3d XPS spectra, we calculated the density of states (DOS) based on a Mulliken

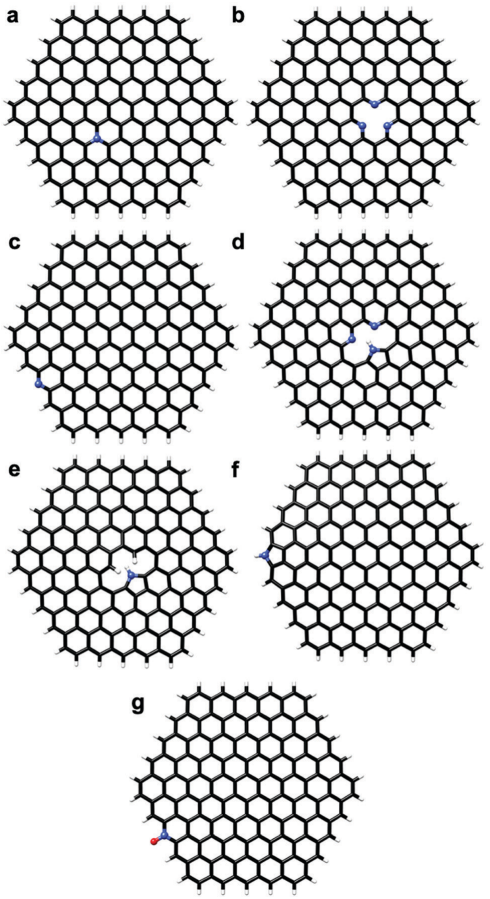

Fig. 1 Model systems for the NMC support material: (a) graphitic N; (b) pyridinic N b; (c) pyridinic N c; (d) pyrrolic N d; (e) pyrrolic N e; (f) pyrrolic N f; and (g) N–O-like N.

population analysis,[21] for Pd with a full electron ansatz (SVPall[22]). The absolute orbital energies are usually far away from experimental ionization energies. However, the Kohn–Sham eigenvalues provide a good estimate of the core level binding energy shifts.[23] Therefore, qualitative trends and energy differences for significantly different functional groups should be in good agreement with the experiment. Previously, it was shown that also the ΔSCF method can be used to accurately estimate N 1s core level binding energies.[24,25]

To model the Pd/CMC system we chose a Pd_{21} cluster on a hydrogen terminated graphene layer of 150 carbon atoms, which proved to be a reasonable choice in a previous study.[6] For the NMC systems we set up seven support material models for four different N atom types: graphitic N, pyridinic N, pyrrolic N and N–O like species (compare Fig. 1).

In the model for graphitic N, one C atom in the graphene layer was substituted by a N atom (compare Fig. 1a). For pyridinic N several different atomic arrangements would be possible. Based on a 2D TOF-SIMS study, which shows that pyridinic N atoms are usually distributed in domains,[26] we chose a support model system with a high density of pyridinic N, *i.e.* a model including a one C atom vacancy surrounded by three pyridinic N atoms (pyridinic b; compare Fig. 1b). As the three pyridinic nitrogen atoms show slightly different N 1s orbital energies, we set up a second support model for pyridinic N (one N atom replacing a C–H group at the edge of the graphene sheet; pyridinic c; compare Fig. 1c), which was used for calibrating the DOS calculations. Based on the results of a previous study, which show that the N 1s binding energies of pyridinic N atoms at different positions in the support material do not significantly differ from each other,[27] this should not introduce any significant uncertainty.

Furthermore it was shown that pyrrolic N atoms at different positions in the support material do show significantly different N 1s binding energies.[27] Accordingly, we set up three different support material models for pyrrolic N: (1) a one C atom vacancy surrounded by one pyrrolic N–H group and two pyridinic N atoms (pyrrolic d; compare Fig. 1d), (2) a one C atom vacancy surrounded by one pyrrolic N–H group and two C–H groups (pyrrolic e; compare Fig. 1e), and (3) a five-membered ring at the edge of the graphene sheet including a N–H group (pyrrolic f; compare Fig. 1f).

For the N–O-like species a model system of a N–O group replacing a C–H group at the edge of the graphene sheet was set up (compare Fig. 1g).

As the pyridine-like support model c, the pyrrole-like support models e and f and the model for the N–O-like nitrogen atom contain functional groups that are located on the edges of the support material, which would introduce undesired side effects in the geometry of the supported nanoparticles, these systems have only been considered for the DOS calculations and not as support materials for the Pd_{21} clusters.

The most stable structures of the support models as well as of Pd_{21} on the different support materials were determined *via* ground-state geometry optimizations. The model system for Pd/CMC is shown in Fig. 1. For Pd/NMC two different graphitic structures, two different pyridinic structures (both on the pyridinic support model b), and one pyrrolic structure (for the pyrrolic support model d) were investigated (compare Fig. 2–5).

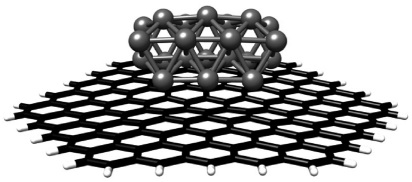

Fig. 2 Most stable structure of Pd_{21} on N-free carbon support (the model for Pd/CMC).

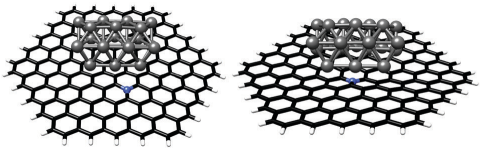

Fig. 3 Most stable structures of Pd_{21} on graphitic N carbon support: 1 (left; graphitic N on the side of Pd_{21}) and 2 (right; graphitic N below Pd_{21}) (models for Pd/NMC).

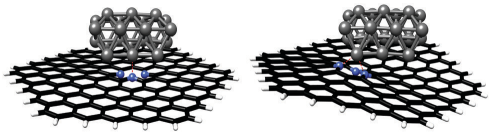

Fig. 4 Most stable structures of Pd_{21} on pyridinic N carbon support b: 1 (left; one pyridinic N connected to Pd_{21}) and 2 (right; two pyridinic N connected to Pd_{21}) (models for Pd/NMC).

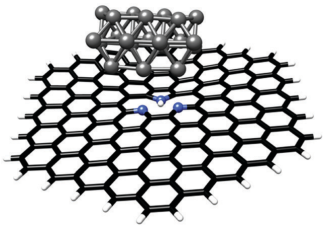

Fig. 5 Most stable structure of Pd_{21} on pyrrolic N carbon support d (model for Pd/NMC).

It has been well established by combined experimental and DFT studies that the oxygen functionalization of carbon nanotubes enhances the binding energy of Pd;[28–30] however, the interaction between Pd and surface oxygen is relatively weak.[28] Furthermore, considering the similar surface oxygen contents in Pd/CMC and Pd/NMC (Table S2, ESI†) and the same type of oxygen functional groups originated from the HNO_3 treatment, the influence of surface oxygen is neglected in the present study.

Results and discussion

Preferential adsorption sites

The N 1s core level XPS spectra of NMC and Pd/NMC are presented in Fig. 6. The deconvoluted N 1s spectrum of NMC reveals that nitrogen is embedded into the carbon structure in four different forms.[3,31] The first peak at 398.0 eV refers to the pyridine-like N atoms (N1). The second peak at 399.8 eV (N2) is tentatively assigned to N atoms in the pyrrole-like configuration, but considering previous studies[32] this may need to be further confirmed. The third peak at 401.0 eV (N3) can be assigned to quaternary-like N atoms, and the fourth peak at

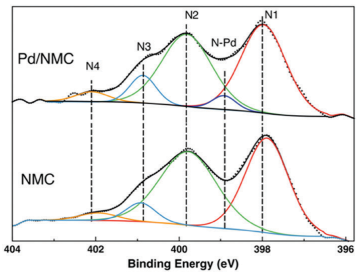

Fig. 6 N 1s regions of the deconvoluted XPS results for NMC and Pd/NMC.

Table 1 N 1s binding energies (eV) for the different N species

Model system	Calibrated DOS calculation	Experimental value
Pyridinic b	397.6–397.9	N1, 398.0
Pyridinic c	398.0	N1, 398.0
Pyrrolic d	399.0	N2, 399.8
Pyrrolic e	400.1	N2, 399.8
Pyrrolic f	400.1	N2, 399.8
Graphitic	401.5	N3, 401.0
N–O-like	402.0	N4, 402.0

402.0 eV (N4) to oxidized or NO-like N atoms.[33] This can further be validated by the N 1s binding energies obtained from our DOS calculations. The total DOS energies differ from the experimental results by an approximately constant shift of about 14 eV. Therefore, we used the pyridinic support model c to calibrate the calculations and shifted all the calculated binding energies by 14.3 eV (compare Table 1.). The energy trend and the energy differences between the different nitrogen species match very well. There are debates on whether pyrrolic and graphitic N can be distinguished in literature reports.[32] Because of the much better deconvoluted results as well as the better agreement of binding energies between the experimental and calculated values (Table 1), we decided to use 4 peaks for the N 1s XPS deconvolution in the present study.

The relative chemical abundance of each N functional group on the NMC surface was determined from the XPS data using tabulated theoretical photoelectron cross sections[34] and is summarized in Table 2. It shows that the embedded N is mainly in the state of pyridinic (N1, 45%) and pyrrolic (N2, 46.1%) groups, which are basic. The overall N abundance, especially the abundance of the N1 species, slightly decreases due to Pd loading, suggesting that pyridinic nitrogen species are probably the preferential anchoring sites for Pd NPs.

Table 2 Relative abundance (%) of the components in the N 1s spectra

Sample	Component/binding energy (eV)			
	N1	N2	N3	N4
	398.0	399.8	401.0	402.0
NMC	45.0	46.1	6.0	3.0
Pd/NMC	41.1	44.5	7.6	3.3

Table 3 Calculated adsorption energies for the different Pd_{21} systems shown in Fig. 2–5

Model system	Adsorption energy with D3 (kJ mol^{-1})	Adsorption energy without D3 (kJ mol^{-1})	Dispersion energy (kJ mol^{-1})	Dispersion contribution (%)
Pd_{21}/carbon support	549.7	248.2	301.5	54.9
Pd_{21}/graphitic N support 1	574.3	278.1	296.2	51.6
Pd_{21}/graphitic N support 2	607.9	296.9	311.0	51.2
Pd_{21}/pyridinic N support 1	657.4	367.5	289.9	44.1
Pd_{21}/pyridinic N support 2	704.8	401.1	303.7	43.1
Pd_{21}/pyrrolic N support	579.1	272.2	306.9	53.0

To validate this experimental observation, we calculated the adsorption energies for the different Pd_{21} systems shown in Fig. 2–5. The results are listed in Table 3.

In general, N doping increases the adsorption energy of the Pd_{21} cluster on the carbon support material. This effect is, in the first place, of covalent character, as it was previously reported for the interaction of platinum nanoparticles with nitrogen-doped carbon support materials.[35] For the graphitic system, the configuration in which Pd_{21} is located directly over the N atom (graphitic N support 2, compare Fig. 3) is more stable than the configuration with the N atom on the side of the cluster (graphitic N support 1, compare Fig. 3). The pyrrolic N system (compare Fig. 5) behaves very similar to the graphitic N support 1 system.

The adsorption energies for the pyridinic systems are significantly higher. The highest adsorption energy can be observed for the configuration in which two pyridinic N atoms interact with one Pd atom (pyridinic N support 2, compare Fig. 4).

This confirms that pyridinic nitrogen species should be the preferential anchoring sites for Pd NPs on NMC, which is in agreement with previous reports suggesting that N-functionalized carbon materials can effectively anchor and stabilize the supported metal NPs.[36,37]

Details of the metal–support interactions

To understand the details of the previously described metal–support interactions, we calculated the electron densities for Pd_{21} on the graphitic N support 2, on the pyridinic N support 2 and on the pyrrolic N support. The corresponding electron density difference plots are shown in Fig. 8–10. For comparison, we reproduce the electron density difference plot for the N-free system from our previous study[6] (compare Fig. 7), showing that the electron density is shifted from the lower layer of the cluster to the Pd–C connecting lines. This indicates directed partially covalent metal–support interactions.

In the plot for the graphitic N support 2 shown in Fig. 8 no direct Pd–N bond can be observed. However, close to the graphitic N atom even more electron density is shifted to the Pd–C connecting lines compared to the N-free carbon support. This is in agreement with our result that the binding of Pd_{21} on N-doped support materials is more covalent. To explain this phenomenon, we performed a natural population analysis for the Pd_{21}/graphitic N support 2 model system as well as a Hückel-based population analysis for the support material. Based on these results, the stronger covalent Pd–C binding can be explained by two facts: (1) The graphitic N atom brings

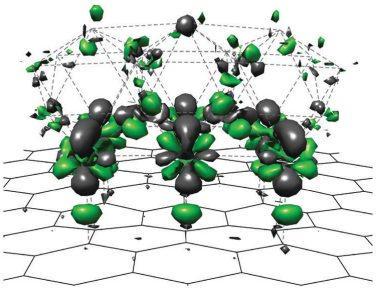

Fig. 7 Change in the electron density induced by the interaction between the Pd_{21} cluster and the N-free support material. Density gain is colored in green; density loss is in grey.

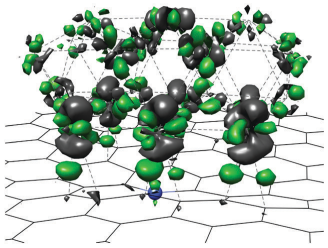

Fig. 8 Change in the electron density induced by the interaction between the Pd_{21} cluster and the graphitic N support material 2. Density gain is colored in green; density loss is in grey.

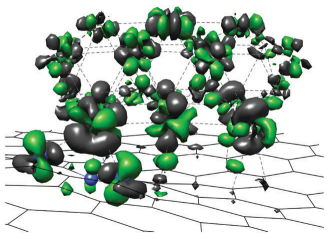

Fig. 9 Change in the electron density induced by the interaction between the Pd_{21} cluster and the pyridinic N support material 2. Density gain is colored in green; density loss is in grey.

in an additional electron, which in the interacting system is (partially) located on the Pd_{21} cluster. The, in general, positive

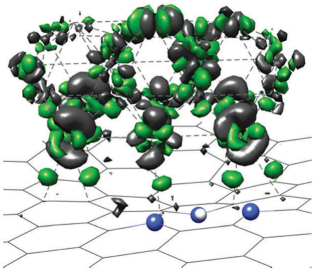

Fig. 10 Change in the electron density induced by the interaction between the Pd_{21} cluster and the pyrrolic N support material. Density gain is colored in green; density loss is in grey.

charge of the carbon supported Pd_{21} cluster is decreased. (2) The graphitic N atom and the neighboring C atoms are positively charged, which leads to an additional electrostatic contribution to the binding energy.

The plot for the pyrrolic N support system in Fig. 10 is very similar to that for graphitic N support 2. Also for this system no direct Pd–N bond and a stronger electron density shift to the Pd–C connecting lines compared to the N-free carbon support can be observed. However, this effect is slightly smaller compared to the effect of the graphitic N support 2 and can mainly be explained by the induced positive charge at the neighboring carbon atoms.

The plot for the pyridinic N support 2 (compare Fig. 9) shows a much more complicated electron density difference at the two pyridinic N atoms bound to the Pd_{21} cluster. This special structure can be explained with the help of an intrinsic bond orbital analysis. Each pyridinic N atom possesses a lone pair (LP), located in an sp^2-orbital lying in the support plane. For the two pyridinic N atoms directly bound to the Pd_{21} cluster this LP sp^2-orbital is tilted up by around 5° towards the cluster (compare Fig. 11), which is associated with an N-LP – Pd d_σ and an N-LP – Pd s interaction. Furthermore, a Pd d_π – π^* interaction can be observed.

Moreover, the XP Pd 3d spectra of Pd/NMC and Pd/CMC were investigated, which help to further understand the metal–support interactions between Pd and the pyridine-like nitrogen species. The deconvoluted Pd 3d spectra are shown in Fig. 12. For Pd/NMC, three different palladium species at 335.2–335.5 eV (Pd1), 336.8 eV (Pd2), and 337.9 eV (Pd3) can be distinguished from the $3d_{5/2}$ portion of the XP Pd 3d spectra. In comparison,

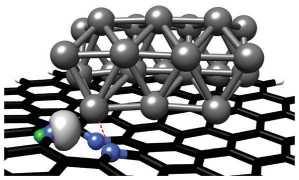

Fig. 11 Visualization of one N lone pair (IBO) in the pyridinic N support 2 system.

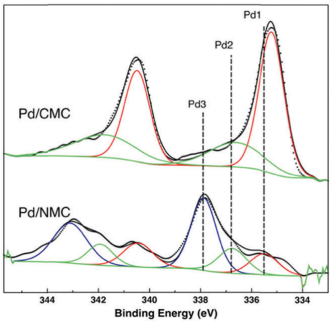

Fig. 12 Pd 3d regions of the deconvoluted XPS results for Pd/CMC and Pd/NMC.

Table 4 Relative abundance (%) of the components in the Pd $3d_{5/2}$ spectra

	Component/binding energy (eV)		
	Pd1	Pd2	Pd3
	335.2	336.8	337.9
Sample	Pd^0	$Pd^{\delta+}$	Pd^{2+}
Pd/NMC	21	25	54
Pd/CMC	68	32	—

only Pd1 and Pd2 are observed for Pd/CMC. The relative abundance of these three species is summarized in Table 4.

The Pd1 peak (335.2 eV) for Pd/CMC is slightly shifted to a higher binding energy with respect to the reported bulk-like metallic palladium (335.0 eV). Thus, it can be assigned to the Pd^0 nanoparticles with varying extents of interaction with the carbon surface. Compared to that of Pd/CMC, the Pd1 peak for Pd/NMC (335.5 eV) is also slightly shifted to a higher binding energy by around 0.3 eV, which can be attributed to more pronounced final-state effects in small Pd NPs (2–5 nm).[37,38] This observation suggests the predominant existence of smaller Pd nanoparticles in Pd/NMC compared with Pd/CMC. According to our previous study, the Pd2 species is suggested to be located on the surface region of Pd nanoparticles/clusters and is electronically modified by oxygen atoms bound to the surface, resulting in a partial positive charge ($Pd^{\delta+}$).[39]

Compared to the $3d_{5/2}$ part of the XP Pd 3d spectra for Pd/CMC, which is dominated by the Pd1 species, a new Pd3 peak at 337.9 eV is predominant for Pd/NMC. A significant electronic modification by the N dopants is presumably responsible for the change of the Pd oxidation state.[40] Based on our DOS calculations, the new peak can be assigned to a divalent Pd center stabilized by the strong interaction with two pyridine-like N atoms: for the Pd_{21}/pyridinic N support 2 model, in which one Pd atom interacts with two pyridinic N atoms, one 3d orbital (delocalized, but with a main contribution of the Pd atom interacting with two pyridinic N atoms) has a binding energy of 262.6 eV. This is noticeably higher than the binding

energies of the remaining 3d orbitals and, furthermore, lies in the region of the Pd 3d orbital energy of an isolated Pd^{2+} atom (a DOS energy of around 262.2 eV). Such high binding energies cannot be observed for the Pd_{21}/carbon, Pd_{21}/graphitic N and Pd_{21}/pyrrolic N support systems (compare Fig. S4, ESI†). These results show that pyridinic nitrogen in the support material stabilizes bifunctional palladium nanoparticles containing both Pd^0 and Pd^{2+} centers.

Our results are in agreement with a previous study, in which Pd^{2+} ions coordinated by nitrogen species of the carbon support were reported based on a study of XPS and NEXAFS[35]. Earlier, Stonkus *et al.*[41] confirmed that the deposition of palladium on N-functionalized carbon nanofibers contributes to a change in the redox properties of Pd as compared to that of Pd on N-free carbon nanofibers.

For Pd/NMC, a better fitting of the N 1s spectrum (Fig. 6) was obtained, assuming the presence of one more type of nitrogen species with a binding energy of 398.9 eV (shifted by 0.9 eV). Based on the DOS for the Pd_{21}/pyridinic N support 2 model showing two different binding energies (one for the two interacting N atoms and one for the non-interacting N atom) separated by around 0.7 eV, this new peak could be assigned to the pyridinic nitrogen species interacting with Pd NPs (the N–Pd component).

This is also in agreement with a study by Bulusheva and coworkers,[36] who also detected a new peak in the same region after depositing single Pd atoms on N-functionalized mesoporous carbon materials. Meanwhile, similar changes in the NEXAFS spectra of nitrogen after Pd deposition were observed and the new species could be assigned to the formation of a bond of palladium atoms with pyridinic nitrogen atoms.

Conclusions

With the combined experimental and computational approach, we were able to identify the preferential adsorption sites of Pd nanoparticles on NMC and, furthermore, to provide an in-depth insight into the corresponding metal–support interactions.

Nitrogen is embedded into the carbon structure in four forms: pyridinic, pyrrolic, graphitic and oxidized or NO-like N species. The majority of the N atoms are in the state of pyridinic and pyrrolic groups. In general, N doping increases the adsorption energy of the Pd clusters, which is, in the first place, an effect of the covalent and electrostatic character. For graphitic nitrogen this effect can be explained by stronger covalent Pd–support bonds due to the additional electron and the charge redistribution introduced by the graphitic N atom. Stronger covalent Pd–support bonds can also be observed for pyrrolic nitrogen, which is mainly caused by a charge redistribution.

According to our XPS and DFT results, pyridinic nitrogen atoms are the preferential adsorption sites for Pd nanoparticles on NMC. When a Pd cluster is adsorbed on pyridinic nitrogen, two N atoms interact with one Pd atom *via* an N-LP – Pd d_σ and an N-LP – Pd s as well as a Pd d_π – π^* charge transfer. This interaction results in a change in the Pd oxidation state and leads to a bifunctional palladium nanoparticle containing Pd^0 and Pd^{2+} centers.

In summary nitrogen-doped mesoporous carbon can effectively anchor Pd nanoparticles, especially due to strong interactions with pyridinic nitrogen atoms. These results raise the question of how N doping affects the catalytic hydrogenation reactions on carbon-supported Pd nanoparticles. As the majority of the N atoms are in the state of pyridinic and pyrrolic groups, which are basic, Pd/NMC should provide moderate to strong surface basicity, desired for highly selective and effective hydrogenation reactions. Furthermore, the coexistence of Pd^0 and Pd^{2+} centers is expected to influence the mechanisms of these reactions.

Conflicts of interest

The authors declare no competing financial interest.

Acknowledgements

The authors gratefully acknowledge the financial support by Deutsche Forschungsgemeinschaft within the framework of the Sino-German initiative ''Novel Functional Materials for Sustainable Chemistry'' through grant Ha 2588/9-1, by Deutsche Forschungsgemeinschaft (grant MU 1327/10-1) and by the Max Planck society (Max Planck fellowship).

References

1 K. P. De Jong and J. W. Geus, Carbon Nanofibers: Catalytic Synthesis and Applications, *Catal. Rev.*, 2000, **42**(4), 481–510.
2 C. Li, A. Zhao, W. Xia, C. Liang and M. Muhler, Quantitative Studies on the Oxygen and Nitrogen Functionalization of Carbon Nanotubes Performed in the Gas Phase, *J. Phys. Chem. C*, 2012, **116**(39), 20930–20936.
3 Y. a. Huang, F. Yang, Z. Xu and J. Shen, Nitrogen-containing mesoporous carbons prepared from melamine formaldehyde resins with $CaCl_2$ as a template, *J. Colloid Interface Sci.*, 2011, **363**(1), 193–198.
4 W. Xia, Interactions between metal species and nitrogen-functionalized carbon nanotubes, *Catal. Sci. Technol.*, 2016, **6**(3), 630–644.
5 V. Kratky, M. Kralik, M. Mecarova, M. Stolcova, L. Zalibera and M. Hronec, Effect of catalyst and substituents on the hydrogenation of chloronitrobenzenes, *Appl. Catal., A*, 2002, **235**(1), 225–231.
6 L. Warczinski and C. Hättig, A quantum chemical study of hydrogen adsorption on carbon-supported palladium clusters, *Phys. Chem. Chem. Phys.*, 2019, **21**(38), 21577–21587.
7 Y. a. Huang, S. Hu, S. Zuo, Z. Xu, C. Han and J. Shen, Mesoporous carbon materials prepared from carbohydrates with a metal chloride template, *J. Mater. Chem.*, 2009, **19**(41), 7759–7764.

8 S. Alijani, S. Capelli, S. Cattaneo, M. Schiavoni, C. Evangelisti, K. M. H. Mohammed, P. P. Wells, F. Tessore and A. Villa, Capping Agent Effect on Pd-Supported Nanoparticles in the Hydrogenation of Furfural, *Catalysts*, 2020, **10**(1), 11.

9 R. Redón, S. K. Rendón-Lara, A. L. Fernández-Osorio and V. Ugalde-Saldívar, Aerobic Synthesis of Palladium Nanoparticles, *Rev. Adv. Mater. Sci.*, 2011, **27**, 31–42.

10 B. Hu, L. Warczinski, Q. Fu, M. Lu, M. Li, C. Hättig, M. Muhler and B. Peng, Selective Hydrogenolysis of 5-Hydroxymethylfurfural to 2,5-Dimethylfuran by Formic Acid over Pd Supported on N-doped Mesoporous Carbon, 2020, under review.

11 J. Tao, J. P. Perdew, V. N. Staroverov and G. E. Scuseria, Climbing the Density Functional Ladder: Nonempirical Meta-Generalized Gradient Approximation Designed for Molecules and Solids, *Phys. Rev. Lett.*, 2003, **91**(14), 146401.

12 F. Weigend and R. Ahlrichs, Balanced basis sets of split valence, triple zeta valence and quadruple zeta valence quality for H to Rn: Design and assessment of accuracy, *Phys. Chem. Chem. Phys.*, 2005, **7**(18), 3297–3305.

13 Turbomole V7.3 2018, a development of University of Karlsruhe and Forschungszentrum Karlsruhe GmbH, 1989–2007, TURBOMOLE GmbH, since 2007, available from http://www.turbomole.com.

14 D. Andrae, U. Häußermann, M. Dolg, H. Stoll and H. Preuß, Energy-adjusted *ab initio* pseudopotentials for the second and third row transition elements, *Theor. Chim. Acta*, 1990, **77**(2), 123–141.

15 M. Sierka, A. Hogekamp and R. Ahlrichs, Fast evaluation of the Coulomb potential for electron densities using multipole accelerated resolution of identity approximation, *J. Chem. Phys.*, 2003, **118**(20), 9136–9148.

16 F. Weigend, Accurate Coulomb-fitting basis sets for H to Rn, *Phys. Chem. Chem. Phys.*, 2006, **8**(9), 1057–1065.

17 S. Grimme, J. Antony, S. Ehrlich and H. Krieg, A consistent and accurate *ab initio* parametrization of density functional dispersion correction (DFT-D) for the 94 elements H-Pu, *J. Chem. Phys.*, 2010, **132**(15), 154104.

18 A. E. Reed, R. B. Weinstock and F. Weinhold, Natural population analysis, *J. Chem. Phys.*, 1985, **83**(2), 735–746.

19 G. Knizia, Intrinsic Atomic Orbitals: An Unbiased Bridge between Quantum Theory and Chemical Concepts, *J. Chem. Theory Comput.*, 2013, **9**(11), 4834–4843.

20 K. A. Peterson, D. Figgen, M. Dolg and H. Stoll, Energy-consistent relativistic pseudopotentials and correlation consistent basis sets for the 4d elements Y–Pd, *J. Chem. Phys.*, 2007, **126**(12), 124101.

21 R. S. Mulliken, Electronic Population Analysis on LCAO–MO Molecular Wave Functions. I, *J. Chem. Phys.*, 1955, **23**(10), 1833–1840.

22 A. Schäfer, C. Huber and R. Ahlrichs, *J. Chem. Phys.*, 1994, **100**, 5829.

23 N. Pueyo Bellafont, F. Illas and P. S. Bagus, Validation of Koopmans' theorem for density functional theory binding energies, *Phys. Chem. Chem. Phys.*, 2015, **17**(6), 4015–4019.

24 P. S. Bagus, Self-Consistent-Field Wave Functions for Hole States of Some Ne-Like and Ar-Like Ions, *Phys. Rev.*, 1965, **139**(3A), A619–A634.

25 J. M. Kahk and J. Lischner, Core electron binding energies of adsorbates on Cu(111) from first-principles calculations, *Phys. Chem. Chem. Phys.*, 2018, **20**(48), 30403–30411.

26 Z. Luo, S. Lim, Z. Tian, J. Shang, L. Lai, B. MacDonald, C. Fu, Z. Shen, T. Yu and J. Lin, Pyridinic N doped graphene: synthesis, electronic structure, and electrocatalytic property, *J. Mater. Chem.*, 2011, **21**(22), 8038–8044.

27 I. Matanovic, K. Artyushkova, M. B. Strand, M. J. Dzara, S. Pylypenko and P. Atanassov, Core Level Shifts of Hydrogenated Pyridinic and Pyrrolic Nitrogen in the Nitrogen-Containing Graphene-Based Electrocatalysts: In-Plane *vs.* Edge Defects, *J. Phys. Chem. C*, 2016, **120**(51), 29225–29232.

28 J. J. Adjizian, P. De Marco, I. Suarez-Martinez, A. A. El Mel, R. Snyders, R. Y. N. Gengler, P. Rudolf, X. Ke, G. Van Tendeloo, C. Bittencourt and C. P. Ewels, Platinum and palladium on carbon nanotubes: Experimental and theoretical studies, *Chem. Phys. Lett.*, 2013, **571**, 44–48.

29 T. Prasomsri, D. Shi and D. E. Resasco, Anchoring Pd nanoclusters onto pristine and functionalized single-wall carbon nanotubes: A combined DFT and experimental study, *Chem. Phys. Lett.*, 2010, **497**(1), 103–107.

30 W. Sun, Z. Liu, C. Jiang, Y. Xue, W. Chu and X. Zhao, Experimental and theoretical investigation on the interaction between palladium nanoparticles and functionalized carbon nanotubes for Heck synthesis, *Catal. Today*, 2013, **212**, 206–214.

31 J. Cai, S. Bennici, J. Shen and A. Auroux, Influence of N addition in mesoporous carbons used as supports of Pt, Pd and Ru for toluene hydrogenation and iron oxide for benzene oxidation, *React. Kinet., Mech. Catal.*, 2015, **115**(1), 263–282.

32 M. Figueras, I. J. Villar-Garcia, F. Viñes, C. Sousa, V. A. de la Peña O'Shea and F. Illas, Correcting Flaws in the Assignment of Nitrogen Chemical Environments in N-Doped Graphene, *J. Phys. Chem. C*, 2019, **123**(17), 11319–11327.

33 E. Raymundo-Piñero, D. Cazorla-Amorós and A. Linares-Solano, The role of different nitrogen functional groups on the removal of SO_2 from flue gases by N-doped activated carbon powders and fibres, *Carbon*, 2003, **41**(10), 1925–1932.

34 J. J. Yeh and I. Lindau, Atomic subshell photoionization cross sections and asymmetry parameters: $1 \leq Z \leq 103$, *At. Data Nucl. Data Tables*, 1985, **32**(1), 1–155.

35 W. B. Schneider, U. Benedikt and A. A. Auer, Interaction of Platinum Nanoparticles with Graphitic Carbon Structures: A Computational Study, *ChemPhysChem*, 2013, **14**(13), 2984–2989.

36 D. A. Bulushev, M. Zacharska, E. V. Shlyakhova, A. L. Chuvilin, Y. Guo, S. Beloshapkin, A. V. Okotrub and L. G. Bulusheva, Single Isolated Pd^{2+} Cations Supported on N-Doped Carbon as Active Sites for Hydrogen Production from Formic Acid Decomposition, *ACS Catal.*, 2016, **6**(2), 681–691.

37 R. Arrigo, M. E. Schuster, Z. Xie, Y. Yi, G. Wowsnick, L. L. Sun, K. E. Hermann, M. Friedrich, P. Kast, M. Hävecker, A. Knop-Gericke and R. Schlögl, Nature of the N–Pd Interaction in Nitrogen-Doped Carbon Nanotube Catalysts, *ACS Catal.*, 2015, **5**(5), 2740–2753.

38 R. Arrigo, M. E. Schuster, S. Abate, S. Wrabetz, K. Amakawa, D. Teschner, M. Freni, G. Centi, S. Perathoner, M. Hävecker and R. Schlögl, Dynamics of Palladium on Nanocarbon in the Direct Synthesis of H_2O_2, *ChemSusChem*, 2014, **7**(1), 179–194.
39 P. Chen, A. Khetan, F. Yang, V. Migunov, P. Weide, S. P. Stürmer, P. Guo, K. Kähler, W. Xia, J. Mayer, H. Pitsch, U. Simon and M. Muhler, Experimental and Theoretical Understanding of Nitrogen-Doping-Induced Strong Metal–Support Interactions in Pd/TiO_2 Catalysts for Nitrobenzene Hydrogenation, *ACS Catal.*, 2017, **7**(2), 1197–1206.
40 J. Graciani, A. Nambu, J. Evans, J. A. Rodriguez and J. F. Sanz, Au ↔ N Synergy and N-Doping of Metal Oxide-Based Photocatalysts, *J. Am. Chem. Soc.*, 2008, **130**(36), 12056–12063.
41 O. A. Stonkus, L. S. Kibis, O. Yu. Podyacheva, E. M. Slavinskaya, V. I. Zaikovskii, A. H. Hassan, S. Hampel, A. Leonhardt, Z. R. Ismagilov, A. S. Noskov and A. I. Boronin, Palladium Nanoparticles Supported on Nitrogen-Doped Carbon Nanofibers: Synthesis, Microstructure, Catalytic Properties, and Self-Sustained Oscillation Phenomena in Carbon Monoxide Oxidation, *ChemCatChem*, 2014, **6**(7), 2115–2128.

6 Formic Acid-Assisted Selective Hydrogenolysis of HMF to DMF over Bifunctional Pd Nanoparticles Supported on N-doped Mesoporous Carbon

Like the previous chapter, this chapter also shows a combined experimental and computational study. The reproduced manuscript[1,2], which has been submitted to the journal *Angewandte Chemie*, demonstrates how the bifunctionality of Pd nanoparticles in Pd/NMC proven in the previous chapter can affect hydrogenation reactions catalyzed on such catalyst systems.

The hydrogenolysis of 5-hydroxymethylfurfural (HMF) to 2,5-dimethylfuran (DMF) was studied experimentally. During their investigations, the experimentalists found a HMF conversion of more than 99.9 % and a DMF yield of more than 97 % when conducting the experiments on Pd/NMC under an atmosphere of both H_2 and formic acid. To provide some explanation for such a high reactivity and selectivity, we performed a computational study on the adsorption behavior of H_2 and formic acid on Pd/NMC compared to Pd/CMC. We particularly focused on the bifunctional Pd nanoparticles on NMC, i.e. on the Pd/NMC model system in which one Pd atom of the Pd_{21} cluster interacts with two pyridinic N atoms.

[1] SI: reproduced in the appendix on pages 216 - 238

[2] This manuscript was compiled on the basis of a purely experimental draft of our experimental collaborators, in which I added, under the supervision of Professor Hättig, sections dealing with the details, results, analysis and conclusions of the calculations I performed.

RESEARCH ARTICLE

Formic Acid-Assisted Selective Hydrogenolysis of 5-Hydroxymethylfurfural to 2,5-Dimethylfuran over Bifunctional Pd Nanoparticles Supported on N-doped Mesoporous Carbon

Bin Hu[a],[b], Lisa Warczinski[c], Xiaoyu Li[a], Mohong Lu[d], Johannes Bitzer[a], Markus Heidelmann[e], Till Eckhard[a], Qi Fu[a], Jonas Schulwitz[a], Mariia Merko[a], Mingshi Li[d], Wolfgang Kleist[a], Christof Hättig[c], Martin Muhler[a],[b], and Baoxiang Peng*[a],[b]

[a] Dr. B. Hu, X. Li, J. Bitzer, T. Eckhard, Q. Fu, J. Schulwitz, M. Merko, Prof. Dr. W. Kleist, Prof. Dr. M. Muhler, Dr. B. Peng
Laboratory of Industrial Chemistry
Ruhr-University Bochum
Universitätsstraße 150, 44780 Bochum, Germany
E-mail: baoxiang.peng@techem.rub.de
[b] Dr. B. Hu, Prof. Dr. M. Muhler, Dr. B. Peng
Max Planck Institute for Chemical Energy Conversion,
Stiftstraße 34-36, 45470 Mülheim a.d. Ruhr, Germany
[c] L. Warczinski, Prof. Dr. C. Hättig
Chair of Theoretical Chemistry
Ruhr-University Bochum
Universitätsstraße 150, 44780 Bochum, Germany
[d] Prof. Dr. M. Lu, Prof. Dr. M. Li
Jiangsu Key Laboratory of Advanced Catalytic Materials and Technology
School of Petrochemical Engineering, Changzhou University, China
[e] Dr. M. Heidelmann
Interdisciplinary Center for Analytics on the Nanoscale
University of Duisburg-Essen, 47057 Duisburg, Germany

Supporting information for this article is given via a link at the end of the document.

Abstract: Biomass-derived 5-hydroxymethylfurfural (HMF) is regarded as one of the most promising platform chemicals to produce 2,5-dimethylfuran (DMF) as a potential liquid transportation fuel. Pd nanoparticles supported on N-containing and N-free mesoporous carbon materials were prepared, characterized, and applied in the catalytic hydrogenolysis of HMF to DMF under mild reaction conditions. Quantitative conversion of HMF to DMF was achieved in the presence of formic acid (FA) and H_2 over Pd/NMC within 2 h. The reaction mechanism, especially the multiple roles of FA, was explored through a detailed comparative study by varying hydrogen source, additive, and substrate as well as by applying *in situ* ATR-IR spectroscopy. The major role of FA is to shift the dominant reaction pathway from the hydrogenation of the aldehyde group to the hydrogenolysis of the hydroxymethyl group via the protonation by FA at the C−OH group, lowering the activation barrier of the C−O bond cleavage and thus significantly enhancing the reaction rate. XPS results and DFT calculations revealed that Pd^{2+} species interacting with pyridine-like nitrogen atoms significantly enhance the selective hydrogenolysis of the C−OH bond in the presence of FA due to their high ability for the activation of FA and the stabilization of H^-.

Introduction

The utilization of renewable feedstocks, especially of lignocellulosic biomass for the production of biofuels and commodity chemicals, has attracted significant attention.[1-4] 5-Hydroxymethylfurfural (HMF) obtained from biomass-derived hexoses via catalytic hydrolysis is regarded as one of the most important platform chemicals during biomass transformation.[5-10] Various chemicals and biofuels, such as levulinic acid (LA)[11], 2,5-dimethylfuran (DMF)[12], 2,5-furandicarboxylic acid (FDCA)[13], ethyl levulinate (EL)[14] and 2,5-diformylfuran (DFF)[15], can be produced from HMF. The selective hydrogenolysis of HMF to DMF is a promising utilization route for obtaining biofuel from renewable feedstock.[16] DMF is considered as a potential liquid transportation biofuel, which has a higher octane number (RON =119) than ethanol, superior energy intensity (35 MJ kg^{-1}), nearly ideal boiling point (92-94 °C), excellent miscibility with gasoline and immiscibility with water (2.3 g L^{-1}).[17-19] Moreover, DMF is also a renewable source for the production of *p*-xylene via the Diels-Alder reaction.[20, 21]

The common route to produce DMF is the hydrogenolysis of carbohydrates or HMF with hydrogen, for which a large variety of catalysts has been investigated. In 2007, Dumesic et al. first reported a two-step catalytic process, resulting in 71% yield of DMF from fructose via HMF as intermediate over Cu/C at 220 °C and 6.8 bar H_2.[12,22] In 2010, Bell et al. reported a two-step approach for the conversion of glucose to DMF, achieving 15% DMF yield based on Pd/C in ionic liquid under high pressure of H_2 (62 bar).[23] Recently, Abu-Omar and co-workers synthesized a bimetallic catalyst containing Lewis-acidic Zn and Pd/C species and applied it in the hydrogenolysis of HMF to DMF, leading to 99% conversion and 85% DMF selectivity, but the bimetallic catalyst suffered from deactivation after the 4th recycle.[24] Yang et al. reported that Ru-MoO_x/C led to a DMF yield of 79% at 180 °C and 15 bar H_2.[25] Generally, relative harsh reaction conditions, especially high pressures of H_2, were employed to obtain appropriate conversion due to the low solubility of H_2.[26] Another key challenge for upgrading HMF is to obtain high product

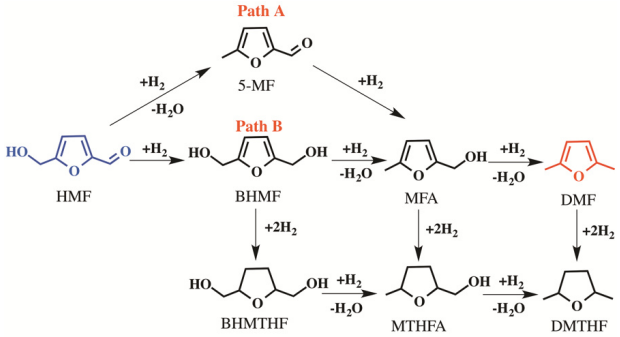

Scheme 1. Reaction network for the hydrogenolysis of HMF to DMF.

selectivity. The chemical transformation of HMF to DMF is a multistep process, including the hydrogenolysis of the hydroxymethyl group and the hydrogenation of the aldehyde group (Scheme 1). Importantly, the main side reaction of furan-ring hydrogenation should be avoided. Overall, the highly selective full conversion of HMF to DMF under mild reaction conditions is still a challenge.

Molecular hydrogen is widely employed in hydrogenation /hydrogenolysis processes, owing to its high availability and facile activation on metal surfaces. Formic acid (FA), which can be produced from lignocellulosic biomass or from electrochemical reduction of CO_2, is being considered for reversible hydrogen storage as well as a hydrogen donor for catalytic hydrogenation/hydrogenolysis.[27,28] Compared with H_2, FA not only has a higher energy density of 6.4 MJ L^{-1},[29] but also has excellent stability with a narrow flammability range (18-57% by volume) and low toxicity, which is desirable for safe storage and transportation.[30,31] Rauchfuss et al. reported the conversion of HMF with FA under mild conditions over Pd/C, yielding 95% DMF in 15 h.[32,33] The key strategy is the utilization of FA, which serves multiple roles as acidic catalyst, hydrogen donor, catalyst moderator inhibiting decarbonylation and ring hydrogenation, and as precursor to formate esters, which are key intermediates that are activated toward the selective hydrogenolysis of the C−OH bond. Nevertheless, the different roles of FA have not yet been elucidated in detail up to now.

Pd exhibits high catalytic activity in the hydrogenolysis of HMF to DMF using FA as the hydrogen source, and it is usually supposed to be the optimum metal for the decomposition of formic acid.[34,35] Nitrogen-doped carbon materials have been proven to be promising catalytic supports.[36] Doping with electron-rich nitrogen atoms modifies the surface structure of carbon materials and endows improved π-binding ability and enhanced basicity,[37] which enhances the catalytic activity of supported metal catalysts (Pd, Pt, Ni, et al.).[38-40] For example, isolated Pd^{2+} cations supported on N-doped carbon were identified as active sites for the hydrogen production from FA, which showed an enhanced reaction rate of 2-3 times compared with Pd supported on N-free carbon or unsupported Pd powder.[41] It was also demonstrated that the Pd^{2+} species are coordinated by pyridinic nitrogen of the support according to XPS, NEXAFS, and STEM studies.[41] Arrigo et al. reported a detailed study of metal-support interactions of N-doped carbon nanotubes with Pd^{2+} species.[42] In our previous study, we have been able to prove the presence of bifunctional Pd nanoparticles (NPs) supported on N-doped mesoporous carbon (NMC), containing both Pd^0 and Pd^{2+} active sites.[43]

Our present work aims at developing the quantitative conversion of HMF to DMF under mild reaction conditions, obtaining a comprehensive understanding of the versatile roles of FA, and revealing the influence of the bifunctionality of the Pd NPs supported on NMC on the reaction. Therefore, a systematic comparative study was performed by variation of the catalyst support (N-rich vs. N-free mesoporous carbon (CMC)) and the hydrogen donor (H_2, FA, both H_2 and FA). *In situ* ATR-IR spectroscopy was employed to monitor the reaction progress and to explore the reaction pathways. Density functional theory (DFT) was applied to models of Pd NPs supported on NMC and CMC to gain further insight into the bifunctional electronic properties of Pd/NMC and its interaction with FA.

Results and Discussion

Characterization of the carbon supports and supported Pd catalysts. The textural properties and Pd loadings of all the supported catalysts and supports are summarized in Table 1. The actual Pd loadings of the catalysts determined by AAS were found to be ca. 1.0 wt% without significant variation close to their theoretical expected values. The isotherms can be classified as type IV with H3 hysteresis loops for CMC and NMC representing typical mesopores (Figure S1). CMC displays a large specific surface area of 997 $m^2 g^{-1}$, while the surface area of N-containing NMC is smaller but still exhibits a surface area of 657 $m^2 g^{-1}$. The pore volumes of CMC and NMC are 1.2 and 0.7 $cm^3 g^{-1}$, respectively. The similar average pore sizes of these two carbon materials clearly indicate comparable mesoporous structures. After the deposition of Pd, the BET surface areas, pore sizes, and pore volumes of both supported Pd catalysts slightly decreased compared with those of the parent materials. For comparison, the properties of active carbon (AC) and Pd/AC are also listed.

Table 1. Physicochemical properties of the carbon materials and supported catalysts.

Sample	Pd[a] [wt%]	S_{BET}[b] [m^2g^{-1}]	V_{pore} [cm^3g^{-1}]	D_{pore}[c] [nm]	$D_{particle}$[d] [nm]
NMC	–	657	0.7	4.9	–
CMC	–	997	1.2	5.0	–
AC	–	617	0.5	3.3	–
Pd/NMC	0.95	625	0.7	4.7	3.4
Pd/CMC	0.98	971	1.2	4.9	4.2
Pd/AC	0.98	473	0.4	3.4	7.8

[a] Pd loading determined by AAS; [b] Specific surface area (BET method); [c] Average pore diameter (BJH method); [d] Mean particle size from TEM.

Table 2. Chemical compositions of NMC, CMC, Pd/NMC, and Pd/CMC.

Sample	Pd (wt/at %)		N (wt/at %)		O (at %)
	bulk[a]	surf.[b]	bulk[c]	surf.[b]	surf.[b]
NMC	–	–	13.4	10.6	6.3
CMC	–	–	–	–	11.0
Pd/NMC	0.95	0.61	13.3	10.9	7.4
Pd/CMC	0.98	1.83	–	–	11.5

[a] Bulk composition determined by AAS; [b] Surface composition determined by XPS; [c] Bulk composition determined by elemental analysis.

XRD patterns of the mesoporous carbon materials and the supported Pd samples are shown in Figure S2. All samples exhibit the characteristic reflections of graphitic carbon at ca. 26°. Despite similar Pd loadings, Pd/CMC shows clearly visible Pd(111) reflections at 40.2°, while no significant Pd reflections are identified in Pd/NMC, suggesting a higher Pd dispersion on the NMC support and/or a smaller number of larger Pd NPs (> 5 nm), which can be detected by XRD.[44,45] This result points to the crucial role of N atoms in NMC as strong anchoring sites for Pd NPs. The observation is in good agreement with previous reports, showing that N-functionalized carbon materials and TiO_2 can effectively anchor metal NPs and enhance their dispersion.[46,47]

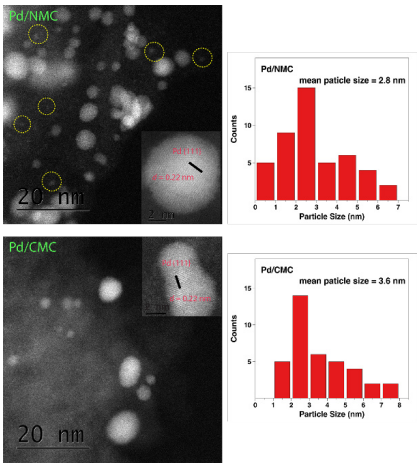

Figure 1. HAADF-STEM images and Pd particle size distributions for Pd/NMC and Pd/CMC. The yellow circles refer to sub-1 nm Pd NPs or clusters.

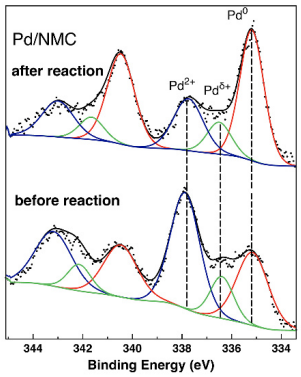

Figure 2. Pd 3d regions of the deconvoluted (Pd^0, $Pd^{\delta+}$, and Pd^{2+}) XPS results for Pd/NMC before and after reaction in the presence of FA and H_2.

The particle size distribution and the morphology of the catalysts were investigated using TEM and HAADF-STEM. Pd NPs in the range of 2 to 5 nm can be clearly seen in the TEM images of both Pd/NMC and Pd/CMC (Figure S3). The mean Pd particle sizes for Pd/NMC and Pd/CMC are relatively similar amounting to 2.8 and 3.6 nm, respectively, allowing a direct comparison of their activities for HMF hydrogenolysis. Nevertheless, the HAADF-STEM images show that there are some sub-1 nm Pd NPs or clusters in Pd/NMC, while these sub-1 nm NPs are rarely detected in Pd/CMC (Figure 1). The lattice fringe spacings of both catalysts are determined to be 0.22 nm representing Pd(111) lattice planes. The mesoporous morphology of the catalysts is comparable regardless of the N doping. By comparison, Pd/AC has a larger mean Pd particle size of 4.4 nm as well as a significantly larger number of NPs above 5 nm (Figure S4).

XPS was employed to investigate the surface chemistry of Pd/NMC and Pd/CMC (Figure S6). The bulk and surface compositions of the catalysts are summarized in Table 2. The surface Pd concentration of Pd/NMC (0.61 at%) is much lower than that of Pd/CMC (1.83 at%). As both catalysts have similar bulk Pd loadings and Pd/NMC has smaller particle size and better dispersion than Pd/CMC according to the STEM measurements, the significant difference in the surface Pd concentration implies that Pd is presumably homogeneously dispersed both on the outer and inner surface of NMC due to the incorporation of N atoms, while Pd prefers to interact with the oxygen-functionalized groups and deposits on the outer CMC surface. Both bulk and surface N abundances in Pd/NMC are similar to those in the NMC support, indicating a homogenous distribution of N in NMC. In addition, CMC exhibits a higher surface oxygen content than NMC, suggesting CMC to be the more oxidized support. Furthermore, the N 1s core level XP spectra of NMC demonstrate the presence of pyridinic (N1, 45%), pyrrolic (N2, 46%), quaternary-like (N3, 6%), and oxidized or NO-like N atoms (N4, 3%) in NMC (Figure S7).[43] For Pd/NMC, a better fitting of the N 1s spectrum was obtained when assuming the presence of another nitrogen species interacting with Pd NPs (N-Pd component).

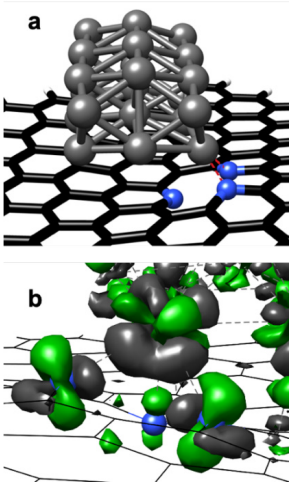

Figure 3. DFT calculations for Pd/NMC model: (a) most stable structure of Pd_{21} on pyridinic carbon support (two pyridinic N connected to Pd_{21}); (b) change in the electron density induced by the interaction between the Pd_{21} cluster and the pyridinic nitrogen atoms (green: density gain; grey: density loss).

In our previous studies, we were able to achieve an in-depth insight into the metal-support interactions of Pd/CMC and Pd/NMC.[43,48] In general, the Pd NPs interact via directed and partially covalent Pd–C interactions with the carbon support.[48] Figure 3a shows the most stable structure of a Pd_{21} cluster with a calculated diameter of 0.85 nm on the NMC support determined by ground-state geometry optimization. Two pyridinic N atoms are interacting with one Pd atom, suggesting pyridinic N atoms as the preferential adsorption sites for Pd clusters. The relevant part of the corresponding electron density difference is reproduced in Figure 3b. The complicated structure can be explained with the help of an intrinsic bond orbital analysis, which shows that the pyridinic N atoms possess a lone pair (LP), located in a sp^2-orbital lying in the support plane. When a Pd cluster is adsorbed on pyridinic nitrogen, two N atoms are interacting with one Pd atom via an N-LP - Pd d_σ and an N-LP – Pd s as well as a Pd d_π - π^* charge transfer. The interaction of the N-LP orbitals with the Pd atom leads to a density loss in the N-LP orbital, while the Pd d_π - π^* interaction increases the density in the N π-orbital and leads to a change in the Pd oxidation state to Pd^{2+}. Indeed, only Pd^0 at 335.2 eV and $Pd^{\delta+}$ at 336.8 eV are observed by XPS for Pd/CMC (Figure S8), whereas an additional peak at 337.9 eV, which can be attributed to a divalent Pd species stabilized by the strong interaction with pyridine-like nitrogen atoms[42], is observed for Pd/NMC (Figure 2). The relative abundance of these three Pd species is summarized in Table S1. Pd^0 (68%) is the dominant species for Pd/CMC, while Pd^{2+} (50%) is the main species for Pd/NMC. These results prove the presence of bifunctional Pd NPs containing both Pd^0 and Pd^{2+} active sites, supported by pyridinic nitrogen atoms in the NMC.[43] The higher oxidation state of Pd in Pd/NMC compared with Pd/CMC is also verified by the TPR experiments (see the detailed description in supporting information and Figure S10).

XAS spectra were recorded to confirm the oxidation state and to investigate the local chemical environment around the Pd centers. The analysis of the XANES spectra revealed that Pd/NMC and Pd/CMC contain a mixture of $Pd^{2+}/Pd^{\delta+}$ and Pd^0 (see Figure S11 and detailed analysis in supporting information). In accordance with the XPS results, the slightly higher intensity of the whiteline and the slightly larger shift of the edge indicate that a larger fraction of Pd is oxidized in Pd/NMC compared with Pd/CMC. The best EXAFS structure fitting was obtained assuming two different shells of backscatterers (Table 3). The first shell consisted of light backscatterers (N, O or C) and was found at 2.02 and 2.06 Å for Pd/CMC and Pd/NMC, respectively. Although we assumed O and N neighbors for the respective materials during the fitting, this technique cannot distinguish these elements due to their similar backscattering properties. The numbers of backscatterers close to 4 is in accordance with a square-planar coordination geometry, which is typical for many Pd complexes. The second shell was found at 2.76 Å for both materials, which is consistent with Pd backscatterers in a Pd^0 crystal lattice. The number of Pd backscatterers (1.96 for Pd/CMC, 0.80 for Pd/NMC) is small compared with a bulk Pd crystal (expected: 12.0), suggesting that very small Pd particles or clusters are present as shown by the (S)TEM images. In summary, these results support the assumed structure model of small Pd clusters containing oxidized $Pd^{\delta+}$ or Pd^{2+} centers at their edges, which are attached to the support via oxygen or nitrogen atoms.

Table 3. EXAFS fitting results. Detailed results and fitting curves are presented in the supporting information (Figure S11, Figure S12 and Table S2).

Sample	Abs-Bs[a]	N(Bs)[b]	R(Abs-Bs)[c] [Å]	σ^2 [d] [Å²]
Pd/CMC	Pd – O	3.45 ± 0.85	2.02 ± 0.02	0.0062 ± 0.0034
	Pd – Pd	1.96 ± 0.31	2.76 ± 0.03	0.0048*
Pd/NMC	Pd – N	4.38 ± 0.52	2.06 ± 0.02	0.0031 ± 0.0012
	Pd – Pd	0.80 ± 0.20	2.76 ± 0.03	0.0048*

[a] Abs = X-ray absorbing atom, Bs = backscattering atom. [b] Number of backscattering atoms. [c] Distance between absorbing and backscattering atom. [d] Debye-Waller factor. * Fixed parameter.

Catalytic conversion of HMF to DMF. The conversion of HMF can proceed via two pathways, depending on the sequence of hydrogenolysis of the hydroxymethyl group and hydrogenation of the aldehyde group (Scheme 1). These two pathways produce distinct intermediates: 5-methylfurfural (5-MF) for path A and 2,5-bis(hydroxymethyl)furan (BHMF) for path B. Both paths A and B proceed further to the common intermediate 2-(hydroxymethyl)-5-methylfuran (MFA) followed by subsequent hydrogenolysis to DMF. The hydrogenation of the furan ring leads to undesired byproducts. The hydrogenolysis of HMF to DMF with different hydrogen sources over carbon-supported Pd catalysts was investigated at 160 °C. HMF conversion, DMF selectivities, and product yields after 3 h are summarized in Table 4.

When H_2 was used for HMF hydrogenolysis, the blank experiment led to only 4.6% HMF conversion, and DMF was not observed (Table 4, entry 1). The control experiments with NMC and CMC resulted in similar conversion as the blank experiment. The degrees of HMF conversion over the Pd-based catalysts were 99.9%, 78.8%, and 19.4% for Pd/NMC, Pd/CMC, and Pd/AC (Table 4, entries 2, 3, 4), respectively. The yields of DMF were found to be rather similar for the mesoporous carbon-supported

Table 4. Product distributions of HMF hydrogenolysis over the supported Pd catalysts[a].

Entry	Catalysts	Hydrogen Source	Conversion (mol %)	DMF Selectivity (mol %)	Product yields (mol %)				
					DMF	BHMF	5-MF	MFA	Others[e]
1	-	H_2[b]	4.6	-	-	2.2	2.4	-	-
2	Pd/NMC	H_2[b]	> 99.9	35.3	35.3	-	-	42.0	22.7
3	Pd/CMC	H_2[b]	78.8	49.2	38.8	-	6.6	18.3	15.1
4	Pd/AC	H_2[b]	19.4	38.3	7.4	1.9	8.4	0.6	1.0
5	Pd/NMC	FA[c]	60.8	64.3	39.1	-	11.5	10.2	-
6	Pd/CMC	FA[c]	21.4	62.9	13.5	-	7.9	-	-
7	Pd/NMC	FA+H_2[d]	> 99.9	> 97.0	97.1	-	2.9	-	-
8	Pd/CMC	FA+H_2[d]	90.1	80.0	72.1	-	18.0	-	-

[a] Reaction conditions: 1.5 mmol HMF, 50 mg catalysts, 160 °C, 3 h; [b] 5 bar H_2; [c] 45 mmol FA (30 equiv.) at 5 bar N_2 and [d] H_2; [e] mainly ring-hydrogenated products including 2,5-bis(hydroxymethyl)tetrahydrofuran (BHMTHF), 5-methyltetrahydrofurfuryl alcohol (MTHFA), and 2,5-dimethyltetrahydrofuran (DMTHF).

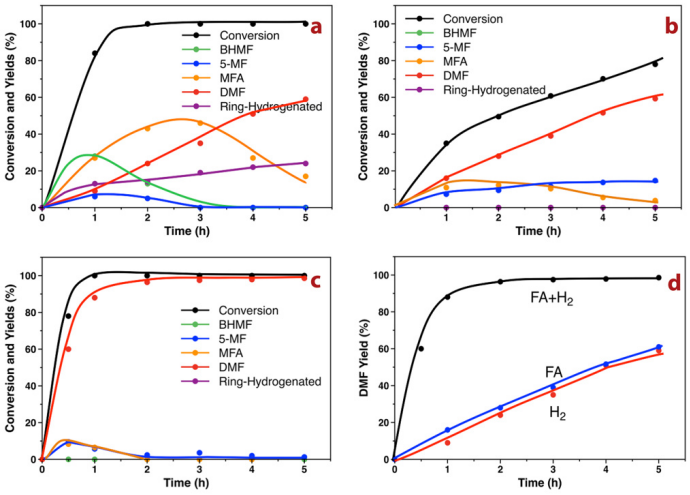

Figure 4. Time course of the hydrogenolysis of HMF to DMF over Pd/NMC with (a) 5 bar H_2; (b) FA and 5 bar N_2; (c) FA and 5 bar H_2. (d) Comparison of DMF yields using different hydrogen donors over time.

Pd catalysts, amounting to 35.3% for Pd/NMC and 38.8% for Pd/CMC, while the yield was significantly lower for Pd/AC. The poor catalytic activity of Pd/AC is due to the larger Pd particle size and the lower Pd dispersion. Besides, mainly furan-ring-hydrogenation products were obtained as byproducts. The hydrogenolysis of HMF over Pd/NMC as a function of time was further studied (Figure 4a). The conversion of HMF proceeded very fast, obtaining full conversion within 2 h. BHMF and 5-MF were the primary intermediates, which reached a maximum yield within 1 h and then gradually decreased to zero after 4 h. By comparison, the maximum yield of BHMF was much higher than that of 5-MF, suggesting that the BHMF reaction pathway (path B) excels the 5-MF pathway (path A) for HMF hydrogenolysis in the presence of H_2. MFA was found to be the secondary intermediate, which reached a maximum yield of 42% at 3 h and then gradually decreased to 17.8% accompanied by an increase in DMF yield to 59.6% after 5 h. Additionally, the ring-hydrogenation products continuously increased to 20%, which is commonly observed using H_2 as the hydrogen source in accordance with literature reports.[49-51] By comparison, the product evolution profiles over Pd/CMC are rather similar to that over Pd/NMC, but with slightly lower activity (Figure S13).

When formic acid was used as a hydrogen donor for HMF hydrogenolysis, the degrees of conversion and product distributions changed significantly for both Pd/NMC and Pd/CMC (Table 4, entries 5 and 6). The degrees of HMF conversion decreased strongly, and the selectivities to DMF increased by 13-29%. Ultimately, it resulted in a similar DMF yield (39% vs. 35%) over Pd/NMC after 3 h compared to that in H_2 atmosphere. Notably, the hydrogenation of the furan ring, which commonly occurs and is difficult to avoid in the presence of molecular hydrogen, is completely suppressed in the presence of FA. This

can be explained by the sterically hindered adsorption of the furan ring, because the active Pd sites are preferably covered by the more strongly bound formate anions. To better understand the reaction pathway, the hydrogenolysis of HMF by FA as a function of time over Pd/NMC is shown in Figure 4b. In contrast to the reaction in H_2, BHMF was not detected, while only 5-MF with similar concentration (ca. 10%) was observed during the whole reaction time. This result suggests that the hydrogenolysis of the hydroxymethyl group (path A) precedes the hydrogenation of the aldehyde group (path B) in FA. After 5 h, a conversion of 78.1% and a DMF yield of up to 60% were obtained. By extending the reaction time further to 12 h, the DMF yield increased to almost 90%. It is worth noting that the yield of the primary intermediate 5-MF slowly but continuously increased, while the secondary intermediate MFA first reached a plateau and then gradually decreased after 3 h. This observation suggests that the hydrogenation of 5-MF to MFA is the rate-determining step (rds) because of the relatively poor hydrogenation ability of Pd/NMC in FA.

In order to enhance the reaction rate of the rds, the conversion of HMF with FA was also conducted in the presence of additional external H_2. The yields of DMF over Pd/NMC and Pd/CMC increased strongly to 97.5% and 73.9% (Table 4, entries 7 and 8), respectively. In contrast to a previous study reporting the formation of ring-hydrogenated products in the presence of FA and H_2 over Pd/C,[33] our results show that the furan ring-hydrogenation is still inhibited by FA even in the presence of additional external H_2 over Pd/NMC, pointing to the unique role of Pd/NMC in the reaction (*vide infra*). Similar to the reaction progress in FA, Figure 4c shows that BHMF was not detected and

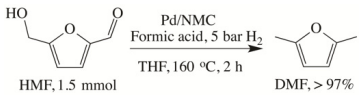

Scheme 2. Quantitative conversion of HMF to DMF with FA and H_2 over Pd/NMC.

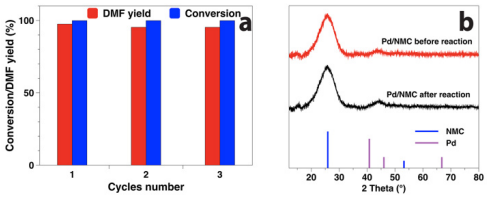

Figure 5. Reusability of Pd/NMC in the hydrogenolysis of HMF to DMF in the presence of FA and H_2 (a), and XRD patterns of Pd/NMC before and after reaction (b).

path A (5-MF) is the main reaction pathway in the presence of external H_2. The difference is that the change of MFA yield occurred concurrently with that of 5-MF, indicating that the reaction rate of the hydrogenation of 5-MF to MFA was significantly enhanced. Finally, the quantitative conversion of HMF to DMF is achieved within only 2 h over Pd/NMC (Scheme 2). Compared with Pd/CMC, Pd/NMC exhibits superior catalytic activity (Figure S13) with doubled TOF values both in FA and in H_2+FA (Table S3), suggesting strong promoting effects of FA and the N species in Pd/NMC. Furthermore, Pd/NMC outperforms other reported catalysts in terms of TOF (Table S3), which can be attributed to smaller Pd NPs, strong metal-support interactions and modified electronic properties by the N species.

By comparison, the combination of FA and H_2 strongly enhances the hydrogenolysis of HMF to DMF, obtaining excellent HMF conversion and DMF yield in short reaction time (Figure 4d). The addition of FA changes the reaction pathway from path B to path A, enhances the hydrogenolysis ability, and inhibits the ring-hydrogenation, whereas the presence of H_2 ensures the fast hydrogenation step.

The stability and the reusability of Pd/NMC were also evaluated. The used catalyst kept its high catalytic activity after three runs, and the yield of DMF slightly decreased from 97.5% to 95.1% (Figure 5a). The low degree of Pd leaching, which is only 0.06 % (0.9 ppm) of the total Pd, indicates an efficient stabilization of the Pd NPs by the NMC support. Furthermore, the recycled catalyst was characterized by XRD, TEM, and XPS (Figures 5b, S5, and 2). The Pd(111) reflection at 40.2° in the used catalyst is still hardly visible without significant changes as compared to the fresh catalyst. The mean Pd particle size only increased slightly from 2.8 to 2.9 nm and the sub-1 nm Pd NPs are still visible. After reaction, the relative abundance of Pd^0 in Pd/NMC increased from 36 to 59%, while Pd^{2+} decreased from 50 to 30% (Figure2, Table S1). For comparison, Pd/CMC was almost completely reduced to Pd^0 (91%) after reaction. The moderate reduction of Pd/NMC even in the presence of FA and H_2 is ascribed to the strong anchoring by pyridinic N species. In conclusion, Pd/NMC is highly stable during the reaction and exhibits excellent reusability.

Reaction mechanism. *In situ* ATR-IR spectroscopy was employed to investigate the reaction pathway and product distributions with different hydrogen donors. Figure 6a and 6b depict the time-resolved ATR-IR spectra collected during the hydrogenolysis of HMF to DMF over Pd/NMC at 160 °C by H_2 and by H_2+FA, respectively. The reference spectra of the main compounds, including HMF, DMF, 5-MF, and BHMF, are shown in Figure S14.

The assignment of the characteristic bands to the reactant and intermediates is summarized in Table S4. Due to the similarity of the intermediates and the reactant, the differentiation of C=O and C=C stretching vibrations is impossible, and therefore, the bands of out-of-plane C−H bending were compared in detail, using the characteristic C−H bending vibrations for HMF (805, 779, 767 and 756 cm^{-1}), DMF (781 cm^{-1}), 5-MF (796 and 765 cm^{-1}), and BHMF (792 cm^{-1}).

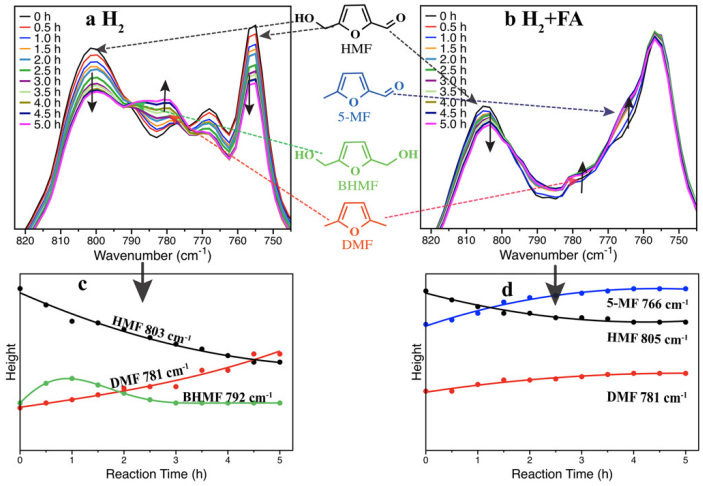

Figure 6. *In situ* ATR-IR spectra and qualitative trends of peak heights during the hydrogenolysis HMF over Pd/NMC in (a) (c) 10 bar H_2 after subtraction of the background of THF at 160 °C; (b) (d) 15 mL FA at 10 bar H_2 after subtraction of the background of THF and FA at 160 °C. Reaction conditions: 45 mmol HMF, 500 mg catalysts, 120 mL THF, 10 bar H_2, 160 °C, 500 rpm.

Using H_2 as the hydrogen donor, the intensity of the IR bands at 805 and 756 cm^{-1} (HMF) continuously declined, whereas the intensity of the IR band at 781 cm^{-1} (DMF) gradually increased. The IR peak of 5-MF was not detected probably due to the low concentration, while the peak at 792 cm^{-1} (BHMF) first formed and then declined. The time-resolved evolution of these peaks is presented in Figure 6c, which once again verifies the conclusion that Pd/NMC tends to catalyze the hydrogenation of the aldehyde group (path B) compared with the hydrogenolysis of the hydroxymethyl group (path A) in the presence of H_2.

In the case of FA and H_2 as hydrogen donors, the consumption of HMF and the formation of DMF were still observed as a function of reaction time (Figure 6b). Nevertheless, the intensities of the IR bands at 765 and 796 cm^{-1} (5-MF) increased significantly without the formation of BHMF in good agreement with the GC results (Table 4, Figure 4). These bands were deconvoluted to determine the changes of individual bands, which are plotted in Figure 6d. The decrease of HMF as well as the increase of DMF and the primary intermediate 5-MF (path A) can be clearly observed in the presence of both FA and H_2.

With respect to the mechanism, FA not only changes the dominant reaction pathway from path B to path A, but also significantly improves the conversion of HMF to DMF over Pd/NMC, which is proposed to proceed via the enhancement of the hydrogenolysis of the C−OH bond (path A). On the contrary, path B was identified as the main reaction pathway over Pd/C in the presence of FA and H_2 in a previous report,[33] implying that Pd/NMC may also play a role in the shift of reaction pathway.

Formic acid is considered to serve multiple roles: it acts as a mild hydrogen source, a catalyst moderator inhibiting ring hydrogenation, and a precursor to formate esters as key intermediates that are activated toward selective hydrogenolysis of C−OH bonds.[32,33] The role of FA as a hydrogen source in the absence of external H_2 is rather clear. The suppression of ring-hydrogenation resulting in improved selectivity has been clearly observed in the present study, but the differentiation or clarification of other roles affecting catalytic activity has not been investigated yet. Therefore, further experiments were conducted to probe the influence of FA on the hydrogenolysis and hydrogenation of furanic substrates catalyzed by Pd/NMC with additional external H_2 (Table 5). When strongly decreasing the molar ratio of FA to HMF from 30 via 3 to 0.3, only a slight decrease of HMF conversion and DMF yield was observed (Table 5, entries 3, 4, 5), implying that FA only has a limited role as a hydrogen source in the presence of external H_2. Furthermore, by addition of only 0.3 equiv. FA, the yield of DMF increased significantly from 35.3% to 76.0%. Although ester formation was restricted using such a low concentration of FA, excellent DMF yield was still obtained. This result suggests that the formate ester pathway might not be the main route for HMF hydrogenolysis under the employed reaction conditions. In order to further verify the role of the formate ester, the conversion of 5-[(formyloxy)methyl]furfural (FMF) to DMF was investigated (Table 5, entries 8, 9, 10). Compared with the conversion of HMF using different hydrogen donors, lower degrees of conversion and DMF yields were obtained for all cases. Thus, it can be concluded that the reaction pathway of formate ester as an intermediate is a minor route for the hydrogenolysis of HMF to DMF. Note that FMF was not detected in all experiments, probably because the conversion of FMF to DMF is much faster than the formation of FMF under the present reaction conditions.

Table 5. Effect of additives on the conversion of HMF and FMF to DMF[a].

Entry	Catalysts	Reactant	Additive[b]	Gas Phase	Conversion (mol %)	DMF Yield (mol %)
1	Pd/NMC	HMF	-	H_2	> 99.9	35.3
2	Pd/NMC	HMF	FA	N_2	60.8	39.1
3	Pd/NMC	HMF	FA	H_2	> 99.9	> 97.0
4	Pd/NMC	HMF	FA (3 equiv.)	H_2	92.0	89.3
5	Pd/NMC	HMF	FA (0.3 equiv.)	H_2	82.1	76.0
6	Pd/NMC	HMF	AcOH[c]	N_2	10.6	Trace
7	Pd/NMC	HMF	AcOH[c]	H_2	95.1	85.5
8	Pd/NMC	FMF	-	H_2	66.1	46.0
9	Pd/NMC	FMF	FA	N_2	34.2	20.5
10	Pd/NMC	FMF	FA	H_2	83.1	67.3

[a] Reaction conditions: 1.5 mmol HMF or FMF, 50 mg catalysts, 160 °C, 5 bar H_2 or N_2, 3 h; [b] 45 mmol FA (30 equiv.); [c] 45 mmol acetic acid (30 equiv.).

Furthermore, the addition of acetic acid (pK_a 4.74 *vs.* 3.77 for FA) instead of FA led to only 10.6% HMF conversion and traces of DMF (Table 5, entry 6), demonstrating that acetic acid cannot be used as the hydrogen donor under the present conditions. Nevertheless, excellent HMF conversion and DMF yield of 85.5% were obtained in the presence of acetic acid and additional external H_2 (Table 5, entry 7). In addition, 5-MF was detected as primary intermediate and BHMF was not detected in good agreement with the result using FA. These results suggest that the acids probably enhance the hydrogenolysis of the RCH_2-OH bond via an acid-catalyzed route. Assary et al.[52] reported an investigation of the reaction mechanism of fructose dehydration to HMF using high-level quantum chemical methods. It was demonstrated that the acidity of the solution is essential to lower the activation energy barrier by involving initial protonation. Moreover, Lercher et al.[53] reported a catalytic pathway for the cleavage of the C−O bond in benzyl phenyl ether using Ni- and zeolite-based catalysts. DFT calculations suggested that the ether is initially protonated rather than the direct cleavage of the ether bond in the proposed C−O bond cleavage mechanisms due to the lower activation energy. Combining our experimental observations and these literature reports, we propose that the hydrogenolysis of RCH_2-OH in the presence of acids also proceeds via a similar protonation process initially, which can lower the activation barrier of the C-O bond cleavage.

Overall, FA serves multiple roles in the hydrogenolysis of HMF to DMF: 1) suppressing ring-hydrogenation to improve the DMF selectivity, 2) acting as a mild hydrogen source, 3) producing the formate esters as intermediates, 4) forming a protonated intermediate and thus lowering the activation barrier of the C-O bond cleavage. Functions 2-4 contribute together to the activity improvement, among which the protonation mechanism results in the reaction pathway shift from path B to path A, being the main reason for the significant catalytic activity enhancement.

The catalytic performance of the hydrogenolysis of HMF over Pd/NMC and Pd/CMC with different hydrogen donors is presented in Figure 7. A significant difference in the reaction rate of the hydrogenolysis of the C−O bond was observed for N-functionalized and N-free carbon-supported Pd catalysts. When H_2 was employed, Pd/NMC and Pd/CMC led to similar DMF yields, implying their comparable catalytic activities for the hydrogenolysis of HMF in H_2. Using FA as the hydrogen source, Pd/NMC resulted in both higher activity and DMF yield compared to Pd/CMC. In FA and H_2, much higher conversion and yield over Pd/NMC were also obtained. As the main reaction pathway is the hydrogenolysis path A in the presence of FA or FA+H_2, the higher catalytic activity of Pd/NMC can be attributed to the improved activity of the hydrogenolysis of the C−OH bond. Since Pd/NMC and Pd/CMC exhibit similar Pd particle sizes and mesoporous structures, the nature of the nitrogen atoms and different oxidation states of Pd species caused by strong metal-support interactions should provide a clue.

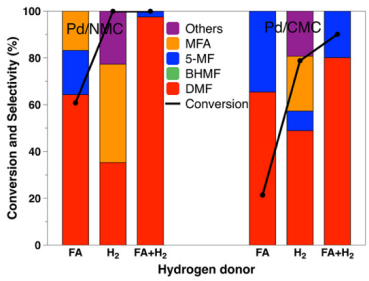

Figure 7. Comparison of Pd/NMC and Pd/CMC with respect to the conversion of HMF to DMF using different hydrogen sources after 3 h.

To further identify the effect of FA and of the N doping of the support material on the hydrogenolysis of the C−O bond, a DFT study of hydrogen and FA on Pd/CMC and Pd/NMC was performed (see Supporting Information for detailed procedures and results). The DFT calculations support the hypothesis that FA does not only act as a mild hydrogen source (function 2), but also can form protonated intermediates (function 4), as it interacts with carbon-supported Pd NPs in two ways: a) FA binds via the C atom (Figure 8a), subsequently decomposing into H_2 and CO_2; b) FA binds via the C=O group (Figure 8b), subsequently decomposing into the formate anion and H^+.

At the Pd_{21} cluster bound to NMC, we find that at the Pd^{2+} centers FA binds exclusively via the C=O bond and decomposes with a small activation energy (ΔE = 5.3 kJ mol^{-1}, neglecting solvation effects) into the formate anion and H^+. The adsorption via the C atom as well as the reaction pathway to the formation of

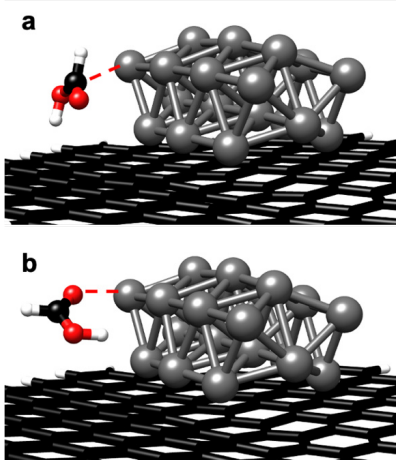

Figure 8. Two different binding configurations of FA on carbon-supported Pd_{21} (model for Pd/CMC): (a) FA binds via the C atom; (b) FA binds via the C=O group.

H_2 and CO_2 are unfavorable (Table S5). Accordingly, the bond to the positively charged center enhances the acidity of FA, which facilitates the hydrogenolysis of the C−OH bond of HMF. This is in agreement with previous studies, in which Pd^{2+} species were identified as the active sites for the selective decomposition of formic acid.[41,54] For example, Pd^{2+} species supported on N-functionalized mesoporous carbon showed 3 times higher catalytic activity in FA decomposition compared with the activity of Pd supported on N-free carbon.[41] The isolated Pd^{2+} species stabilized by the pyridinic nitrogen atoms were identified as the active sites.

Furthermore, H^- formed by heterolytic H_2 dissociation on the Pd nanoparticle binds significantly stronger to Pd/NMC compared with Pd/CMC, preferring positions close to the Pd^{2+} center (Table S6). This can be explained by the higher positive charge of Pd NPs on NMC, especially close to the Pd^{2+} center. The stabilization of H^- on Pd/NMC increases the nucleophilicity, and, therefore, also the selectivity of hydrogen as a reducing agent.

In summary, the remarkable catalytic activity of Pd/NMC for HMF conversion in FA can be attributed to the shift to reaction path A and to the presence of Pd^{2+} species, showing higher catalytic activity in the FA dissociation to the formate anion and H^+ as well as in the H^- stabilization, which jointly improve the hydrogenolysis of the C−OH bond significantly.

Based on the kinetic, spectroscopic and computational results, the following reaction pathway for the bifunctional Pd/NMC in FA is proposed (Scheme 3). First, formic acid is activated via Pd^{2+} species and Pd NPs. The reversible reaction between HMF and FMF exists in the presence of FA, but the HMF pathway is the main route instead of the formate ester pathway. Then, Pd^{2+} species bind the oxygen atom of the C−OH group, which is protonated by formic acid. The hydrogenolysis of the hydroxymethyl group occurs via the cleavage of the C-OH bond forming 5-MF. During the process, Pd^{2+} species and FA cooperate synergistically in the hydrogenolysis of the C−OH bond. Furthermore, Pd^0 NPs bind the C=O double bond leading to the fast hydrogenation of 5-MF to MFA. Subsequently, MFA is directly converted to DMF via a similar process like the hydrogenolysis of HMF to 5-MF. In the case of FA and H_2 as hydrogen donors, H_2 is activated by the Pd^0 NPs supported on NMC, which are more active for hydrogenation steps such as 5-MF to MFA and HMF to BHMF. H_2 may also directly contribute to the hydrogenolysis reactions, but probably plays a minor role in the presence of FA.

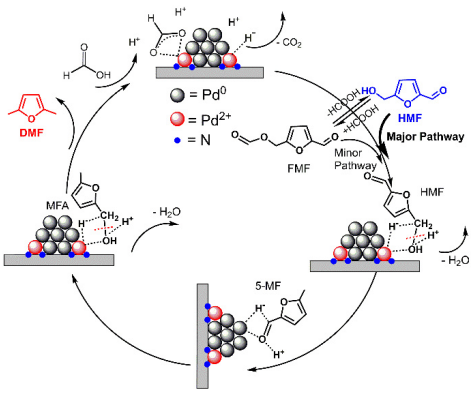

Scheme 3. Proposed reaction pathway for the conversion of HMF to DMF over Pd/NMC using formic acid.

Conclusion

Pd NPs supported on N-doped and N-free mesoporous carbon materials (Pd/NMC and Pd/CMC) were successfully synthesized via the immobilization method and characterized by N_2 physisorption, XRD, TEM, XPS and XAS. These catalysts exhibit similar Pd particle sizes, but sub-1 nm Pd NPs or clusters were only observed in Pd/NMC. DFT calculations and XPS measurements revealed the strong metal-support interactions between Pd^{2+} species and pyridine-like N atoms for Pd/NMC. The hydrogenolysis of HMF to DMF over the Pd-based catalysts was systematically investigated by varying different hydrogen sources. A favorable HMF conversion of > 99.9%, DMF yield of > 97% and a higher TOF of 150 h^{-1} were obtained with Pd/NMC in the presence of FA and H_2 after 2 h.

Detailed comparative studies mainly by varying hydrogen source, additive, and reactant as well as by applying *in situ* ATR-IR spectroscopy and DFT calculations were performed to explore the reaction mechanism. FA tunes not only the reactivity of HMF but also its reaction pathways, serving multiple roles, such as suppressing ring-hydrogenation, acting as a mild reducing agent, producing the formate esters as intermediates, and forming a protonated intermediate, thus lowering the activation barrier of the C-OH bond cleavage. Protonation results in a reaction pathway shift from the hydrogenation of the C=O bond (path B) to the hydrogenolysis of the C–OH bond (path A) and is the main reason for the significant catalytic activity enhancement. Furthermore, a synergistic effect between FA and the Pd^{2+} species of Pd/NMC was observed for the hydrogenolysis of the C−OH bond, with Pd^{2+} exhibiting higher catalytic activity for the activation of FA and stabilization of H^-.

Acknowledgements

The authors gratefully acknowledge financial support by Deutsche Forschungsgemeinschaft (grant MU 1327/10-1 and grant Ha 2588/9-1) and by the Max Planck Society (Max Planck fellowship). We acknowledge DESY (Hamburg, Germany), a member of the Helmholtz Association HGF, for the provision of experimental facilities. Parts of this research were carried out at PETRA III and we would like to thank Dr. Edmund Welter for assistance in using P65 (I-20191191).

Keywords: Pd • HMF• hydrogenolysis • formic acid • DFT • metal-support interactions

[1] G. W. Huber, S. Iborra, A. Corma, *Chem. Rev.* **2006**, *106*, 4044-4098.
[2] A. Corma, S. Iborra and A. Velty, *Chem. Rev.* **2007**, *107*, 2411-2502.
[3] G. W. Huber, J. N. Chheda, C. J. Barrett, J. A. Dumesic, *Science* **2005**, *308*, 1446.
[4] D. M. Alonso, J. Q. Bond, J. A. Dumesic, *Green Chem.* **2010**, *12*, 1493-1513.
[5] R. Carrasquillo-Flores, M. Käldström, F. Schüth, J. A. Dumesic, R. Rinaldi, *ACS Catal.* **2013**, *3*, 993-997.
[6] R.-J. van Putten, J. C. van der Waal, E. de Jong, C. B. Rasrendra, H. J. Heeres, J. G. de Vries, *Chem. Rev.* **2013**, *113*, 1499-1597.
[7] J. M. R. Gallo, D. M. Alonso, M. A. Mellmer, J. A. Dumesic, *Green Chem.* **2013**, *15*, 85-90.
[8] A. A. Rosatella, S. P. Simeonov, R. F. M. Frade, C. A. M. Afonso, *Green Chem.* **2011**,*13*, 754-793.
[9] S. Chen, R. Wojcieszak, F. Dumeignil, E. Marceau, S. Royer, *Chem. Rev.* **2018**, *118, 22,* 11023–11117.
[10] H. Xia, S. Xu, H. Hu, J. An, C. Li, *RSC Adv.* **2018**, 8, 30875-30886.
[11] B. Girisuta, L. P. B. M. Janssen, H. J. Heeres, *Green Chem.* **2006**, *8*, 701-709.
[12] Y. Román-Leshkov, C. J. Barrett, Z. Y. Liu, J. A. Dumesic, *Nature* **2007**, *447*, 982-985.
[13] B. Siyo, M. Schneider, J. Radnik, M.-M. Pohl, P. Langer, N. Steinfeldt, *Appl. Catal., A* **2014**, *478*, 107-116.
[14] G. Wang, Z. Zhang, L. Song, *Green Chem.* **2014**, *16*, 1436-1443.
[15] J. Ma, Z. Du, J. Xu, Q. Chu, Y. Pang, *ChemSusChem* **2011**, *4*, 51-54.
[16] D. Scholz, C. Aellig, I. Hermans, *ChemSusChem* **2014**, *7*, 268-275.
[17] F. K. Kazi, A. D. Patel, J. C. Serrano-Ruiz, J. A. Dumesic, R. P. Anex, *Chem. Eng. J.* **2011**, *169*, 329-338.
[18] S. P. Teong, G. Yi, Y. Zhang, *Green Chem.* **2014**, *16*, 2015-2026.
[19] M. Braun, M. Antonietti, *Green Chem.* **2017**, *19*, 3813-3819.
[20] C. L. Williams, C.-C. Chang, P. Do, N. Nikbin, S. Caratzoulas, D. G. Vlachos, R. F. Lobo, W. Fan, P. J. Dauenhauer, *ACS Catal.* **2012**, *2*, 935-939.
[21] C.-C. Chang, S. K. Green, C. L. Williams, P. J. Dauenhauer, W. Fan, *Green Chem.* **2014**, *16*, 585-588.
[22] Y. Román-Leshkov, J. N. Chheda, J. A. Dumesic, *Science* **2006**, *312*, 1933.
[23] M. Chidambaram, A. T. Bell, *Green Chem.* **2010**, *12*, 1253-1262.
[24] B. Saha, C. M. Bohn, M. M. Abu-Omar, *ChemSusChem* **2014**, *7*, 3095-3101.
[25] Y. Yang, Q. Liu, D. Li, J. Tan, Q. Zhang, C. Wang, L. Ma, *RSC Adv.* **2017**, *7*, 16311-16318.
[26] M. J. Gilkey, B. Xu, *ACS Catal.* **2016**, *6*, 1420-1436.
[27] F. Jin, J. Yun, G. Li, A. Kishita, K. Tohji, H. Enomoto, *Green Chem.* **2008**, *10*, 612-615.
[28] W. Leitner, *Angew. Chem. Int. Ed.* **1995**, *34*, 2207-2221.
[29] F. Valentini, V. Kozell, C. Petrucci, A. Marrocchi, Y. Gu, D. Gelman, L. Vaccaro, *Energy Environ. Sci.* **2019**, *12*, 2646-2664.
[30] N. Onishi, M. Iguchi, X. Yang, R. Kanega, H. Kawanami, Q. Xu, Y. Himeda, *Adv. Energy Mater.* **2019**, *9*, 1801275.
[31] P. Makowski, A. Thomas, P. Kuhn, F. Goettmann, *Energy Environ. Sci.* **2009**, *2*, 480-490.
[32] T. Thananatthanachon, T. B. Rauchfuss, *Angew. Chem. Int. Ed.* **2010**, *49*, 6616-6618.
[33] J. Mitra, X. Zhou, T. Rauchfuss, *Green Chem.* **2015**, *17*, 307-313.
[34] B. J. O'Neill, E. I. Gürbüz, J. A. Dumesic, *J. Catal.* **2012**, *290*, 193-201.
[35] K. Tedsree, T. Li, S. Jones, C. W. A. Chan, K. M. K. Yu, P. A. J. Bagot, E. A. Marquis, G. D. W. Smith, S. C. E. Tsang, *Nat. Nanotechnol.* **2011**, *6*, 302-307.
[36] X. Wang, G. Sun, P. Routh, D.-H. Kim, W. Huang, P. Chen, *Chem. Soc. Rev.* **2014**, *43*, 7067-7098.
[37] Y. Liang, Y. Li, H. Wang, J. Zhou, J. Wang, T. Regier, H. Dai, *Nat. Mater.* **2011**, *10*, 780-786.
[38] F. Yang, B. Hu, W. Xia, B. Peng, J. Shen, M. Muhler, *J. Catal.* **2018**, *365*, 55-62.
[39] Y. Wang, J. Yao, H. Li, D. Su, M. Antonietti, *J. Am. Chem. Soc.* **2011**, *133*, 2362-2365.
[40] X.-L. Du, L. He, S. Zhao, Y.-M. Liu, Y. Cao, H.-Y. He, K.-N. Fan, *Angew. Chem. Int. Ed.* **2011**, *50*, 7815-7819.
[41] D. A. Bulushev, M. Zacharska, E. V. Shlyakhova, A. L. Chuvilin, Y. Guo, S. Beloshapkin, A. V. Okotrub, L. G. Bulusheva, *ACS Catal.* **2016**, *6*, 681-691.
[42] R. Arrigo, M. E. Schuster, Z. Xie, Y. Yi, G. Wowsnick, L. L. Sun, K. E. Hermann, M. Friedrich, P. Kast, M. Hävecker, A. Knop-Gericke, R. Schlögl, *ACS Catal.* **2015**, *5*, 2740-2753.
[43] L. Warczinski, B. Hu, T. Eckhard, B. Peng, M. Muhler, C. Hättig, *Phys. Chem. Chem. Phys.* **2020**, *22,* 21317-21325.
[44]. R. Wojcieszak, M. J. Genet, P. Eloy, P. Ruiz, E. M. Gaigneaux, *J. Phys. Chem. C* **2010**, *114*, 16677-16684.
[45]. E. Bailón-García, F. Carrasco-Marín, A. F. Pérez-Cadenas, F. J. Maldonado-Hódar, *J. Catal.* **2015**, *327*, 86-95.
[46]. P. Chen, A. Khetan, F. Yang, V. Migunov, P. Weide, S. P. Stürmer, P. Guo, K. Kähler, W. Xia, J. Mayer, H. Pitsch, U. Simon, M. Muhler, *ACS Catal.* **2017**, *7*, 1197-1206.
[47]. J. Graciani, A. Nambu, J. Evans, J. A. Rodriguez, J. F. Sanz, *J. Am. Chem. Soc.* **2008**, *130*, 12056-12063.
[48]. L. Warczinski, C. Hättig, *Phys. Chem. Chem. Phys.* **2019**, *21*, 21577-21587.
[49]. W. Yang, A. Sen, *ChemSusChem* **2010**, *3*, 597-603.
[50]. R. Alamillo, M. Tucker, M. Chia, Y. Pagán-Torres, J. Dumesic, *Green Chem.* **2012**, *14*, 1413-1419.
[51]. T. S. Hansen, K. Barta, P. T. Anastas, P. C. Ford, A. Riisager, *Green Chem.* **2012**, *14*, 2457-2461.
[52]. R. S. Assary, P. C. Redfern, J. Greeley, L. A. Curtiss, *J. Phys. Chem. B* **2011**, *115*, 4341-4349.
[53]. J. He, L. Lu, C. Zhao, D. Mei, J. A. Lercher, *J. Catal.* **2014**, *311*, 41-51.
[54]. Y. Zhao, L. Deng, S.-Y. Tang, D.-M. Lai, B. Liao, Y. Fu, Q.-X. Guo, *Energ. Fuel* **2011**, *25*, 3693-3697.

RESEARCH ARTICLE

Entry for the Table of Contents

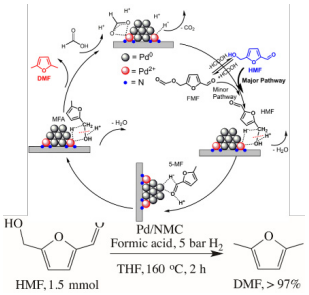

Quantitative conversion of HMF to DMF was achieved in the presence of formic acid and H_2 over the bifunctional Pd/NMC catalyst within 2 h. Experimental investigation and DFT calculation revealed that formic acid significantly enhances the reaction rate and shifts the dominant reaction pathway from the hydrogenation of the aldehyde group to the hydrogenolysis of the hydroxymethyl group via its protonation.

7 How N Doping Affects Hydrogen Spillover on Carbon-Supported Pd Nanoparticles: New Insights from DFT

This chapter presents a manuscript[1,2] which deals in detail with the process of hydrogen spillover on Pd/CMC and Pd/NMC. The aim of this study was to validate if hydrogen spillover on such catalyst systems could actually be possible. In a first step, we investigated the properties of spillover hydrogen on the CMC support material. For this purpose, we studied the binding of hydrogen to a carbon atom of our smaller CMC model system (cmp. Figure 2.1a) and analyzed the corresponding H_2 dissociation energy, its interaction with water molecules as well as the corresponding electronic structure including analysis of partial charges, electron densities and effects on the π-system. Secondly, we investigated how the doping of the CMC support material with nitrogen functional groups affects the properties of spillover hydrogen and focused on spillover hydrogen close to graphitic and pyridinic nitrogen atoms. Additionally, we studied the pathways of the hydrogen spillover process on Pd/CMC and Pd/NMC, using our model system of carbon-supported Pd_{21} (cmp. Figure 2.4) and the two Pd/NMC model systems including graphitic N and pyridinic N carbon support materials (cmp. Figures 2.5 and 2.6). As Pd/CMC and Pd/NMC are also expected to be promising materials for hydrogen storage, spillover hydrogen atom diffusion and spillover hydrogen desorption have also been taken into account.

[1] SI: reproduced in the appendix on pages 239 - 247

[2] The writing of this manuscript and all underlying calculations and analyses have been performed by me under the supervision of Professor Hättig.

How N Doping Affects Hydrogen Spillover on Carbon-Supported Pd Nanoparticles: New Insights from DFT

Lisa Warczinski[a,*], Christof Hättig[a]

[a] *Chair of Theoretical Chemistry, Ruhr-University Bochum, Universitätsstraße 150, 44780 Bochum, Germany*

Abstract

The process of hydrogen spillover on metal nanoparticle decorated carbon surfaces has been discussed for many years due to its importance for heterogeneous catalysis and hydrogen storage. The present density functional theory (DFT) study supports recent experimental observations of the hydrogen spillover process. Using model systems of carbon-supported palladium nanoparticles the details of hydrogen spillover are investigated and the effects of nitrogen doping on such processes are elucidated. It was found that graphitic nitrogen atoms significantly facilitate the hydrogen spillover reaction and serve as anchoring sites for the spillover hydrogen atoms.

Keywords: Density functional theory (DFT), Hydrogen spillover, Hydrogen storage, Carbon support, Nitrogen doping, Palladium, Nanoparticles

1. Introduction

In a hydrogen spillover process activated hydrogen species adsorbed or formed on a first surface are moved to a second surface, on which, under the same conditions, these activated hydrogen species could not adsorb or form[1]. For the first time, the hydrogen spillover effect was reported in 1964 by Khoobiar,

*Corresponding author at: Chair of Theoretical Chemistry, Ruhr-University Bochum, Universitätsstraße 150, 44780 Bochum, Germany

Email address: lisa.warczinski@rub.de (Lisa Warczinski)

October 6, 2020

who observed a transport of hydrogen atoms from Pt to WO_3[2]. In the last decade, hydrogen spillover from metal nanoparticles onto carbon materials has attracted tremendous attention as the spillover effect significantly enhances the carbon material's capability of storing hydrogen[3, 4, 5, 6, 7]. This opens up the possibility of using metal nanoparticle decorated carbon materials as hydrogen storage in future fuel cell systems. Also the usage of reversibly stored spillover hydrogen for heterogeneous catalyzed reactions, e.g. for hydrogenation reactions, is of high interest.[8]

Up to the present, several experimental studies have tried to shed light on the details of the hydrogen spillover mechanism, which turned out to be quite difficult due to the complicated characterization of the carbon support and the hydrogen spillover species[2]. In recent years, Li et al.[9] and Wang et al.[10] observed that surface functional groups and residual moisture significantly enhance the spillover process. In a comprehensive study on hydrogen spillover on platinum/nitrogen-doped mesoporous carbon (NMC) composites from the year 2018, Yang et al.[8] provided novel insights into the hydrogen spillover effect. They were able to generate and to give experimental evidence of spillover hydrogen on the nitrogen-doped carbon support material. Furthermore, they characterized spillover hydrogen as a mobile and reversibly stored hydrogen species, present in a chemically inactive state. Based on these observations they suggested that spillover hydrogen is adsorbed as protons on the carbon support material, which might be further stabilized by water molecules.

In general, it is very difficult to detect spillover hydrogen species in experiments[1, 11, 12]. Several experimental results on the hydrogen spillover effect were later proven to be erroneous[2]. Therefore, the purpose of the present study is to use quantum chemistry to support the recent experimental observations[8, 9, 10] and to improve the understanding of the hydrogen spillover process and of the properties of spillover hydrogen. We particularly aim to shed light on the effect of different nitrogen functional groups on the properties of spillover hydrogen and to elucidate how nitrogen doping could enhance the hydrogen spillover on carbon-supported metal nanoparticles. Furthermore, we study the

interaction of spillover hydrogen atoms with water molecules. For this purpose, we apply density functional theory (DFT) to models of mesoporous carbon supported palladium nanoparticles, in which a Pd_{21} cluster is supported on a hydrogen terminated graphene layer. As we have shown that graphitic nitrogen (6 % relative abundance in the NMC support material) and pyridinic nitrogen species (45 % relative abundance in the NMC support material) significantly tune the properties of the anchored Pd nanoparticles in a previous study[13], the nitrogen doping is modelled by incorporated graphitic and pyridinic nitrogen atoms.

Similar approaches have been used in several studies and have provided valuable insights into the properties of carbon-supported Pd nanoparticles. However, most of these studies used single Pd atoms or very small Pd clusters.[14, 15, 16] As an example, Rangel et al.[17] investigated the hydrogen spillover process on Pd_4 clusters. One of our previous studies[18] has demonstrated that it is essential to also consider larger cluster sizes like Pd_{21}, which are closer to Pd nanoparticle sizes present in experimental systems.

In general, the experimentally observed hydrogen spillover is a complex multi-step process, influenced by several aspects as hydrogen pressure, temperature, impurities and catalyst morphology. The experimental Pd/CMC and Pd/NMC catalyst systems include surface deformations, further defects like five- and seven-membered rings, or surfactants. As studying all these aspects at the same time would introduce too many degrees of freedom, the present study utilizes model systems and deals with the different steps of the hydrogen spillover process separately. As a consequence, we focus on qualitative observations and do not compare our results to specific experimental values. Elucidating the energetics of the individual steps constitutes an important step towards a better understanding of hydrogen spillover and of the effect of nitrogen doping on such processes. Furthermore, the present study can give some computational evidence if hydrogen could actually be reversibly stored on Pd/NMC.

2. Computational details

2.1. Model systems

To model the pure mesoporous carbon support material (CMC) we chose a hydrogen terminated graphene layer comprising 96 carbon atoms (cmp. Figure 1). In nitrogen-doped mesoporous carbon the nitrogen atoms can be present in four forms: graphitic N, pyridinic N, pyrrolic N, and N-O like species.[13] As pyrrole- and N-O-like nitrogen atoms are either located on the edges of the support material or include large surface deformations, which both would introduce undesired side effects in the electronic structure calculations of the reactions, these systems have not been considered. Accordingly, to model the NMC support material, one (graphitic N, cmp. Figure 2a) or three (pyridinic N, cmp. Figure 2b) carbon atoms of the graphene layer were replaced by nitrogen atoms.

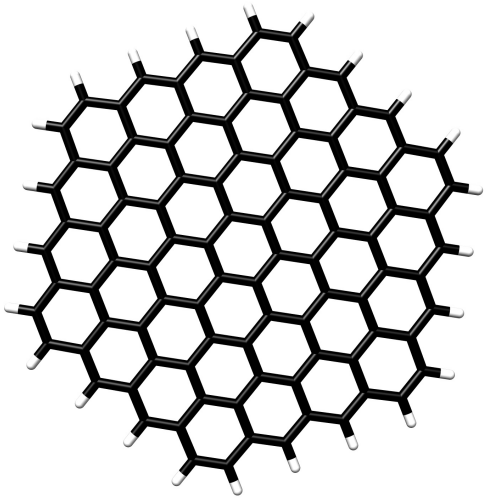

Figure 1: Model system for the pure mesoporous carbon support material (CMC).

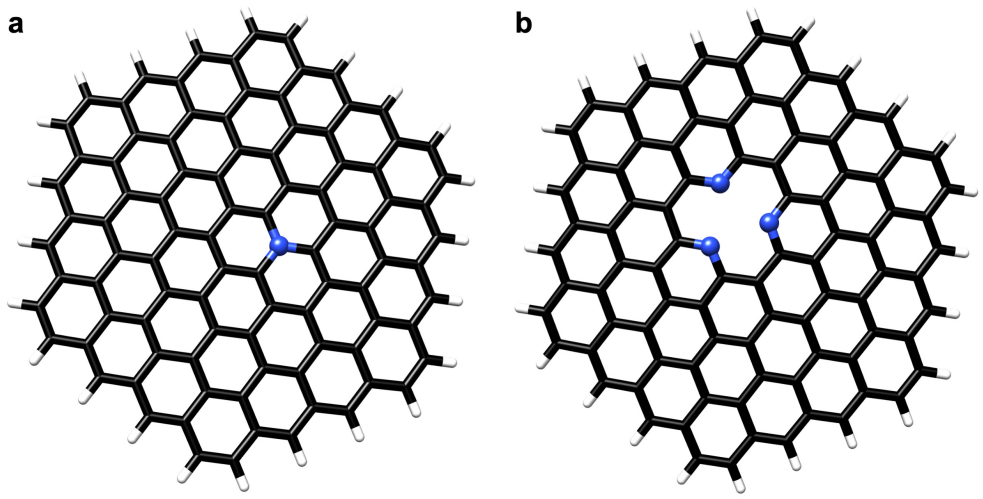

Figure 2: Model systems for the the nitrogen-doped mesoporous carbon support material (NMC): (a) graphitic N support; (b) pyridinic N support.

To model the carbon-supported palladium nanoparticles (Pd/CMC) we chose a Pd_{21} cluster supported by a hydrogen terminated graphene layer of 150 carbon atoms (cmp. Figure 3). The Pd_{21} cluster possesses a diameter of around 0.85 nm, corresponding to sizes at the lower boundary of experimentally determined particle size distributions for Pd/CMC and Pd/NMC, which show nanoparticles of 1 to 8 nm as well as some sub-1 nm Pd particles[19].

Again, for the nitrogen-doped systems (Pd/NMC) one or three carbon atoms were replaced by nitrogen atoms to model, respectively, graphitic or pyridinic N-sites. The configurations of Pd_{21} on the supports with graphitic and pyridinic N for the present study, which have before been validated and used in two previous studies[13, 19], are shown in Figure 4.

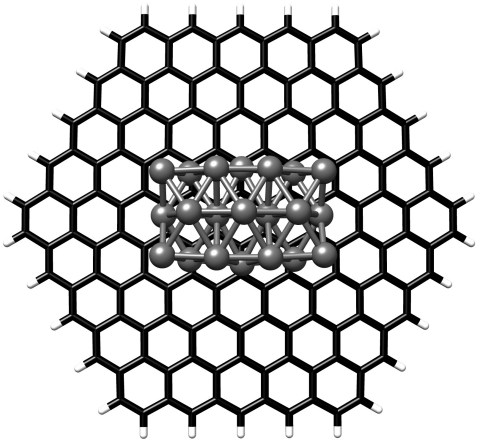

Figure 3: Model system for Pd on the mesoporous carbon support material (Pd/CMC). Adapted from Ref. 13 with permission from the PCCP Owner Societies.

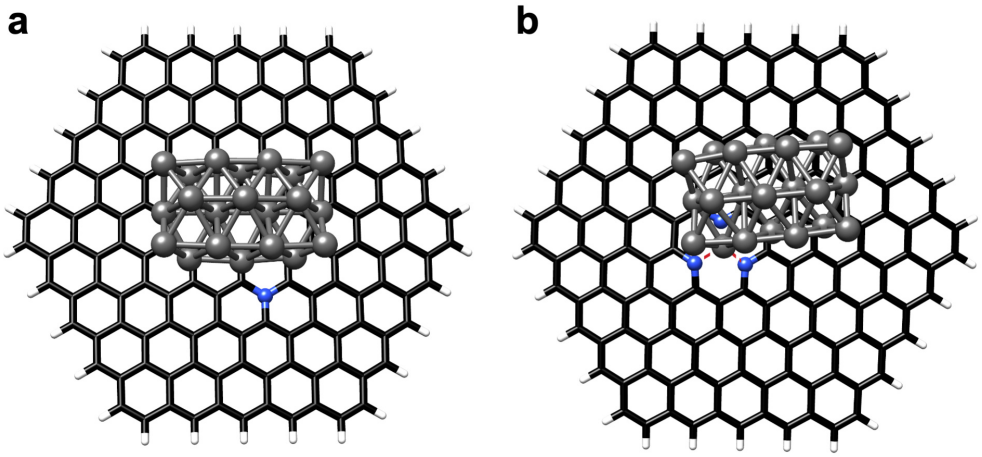

Figure 4: Model systems for Pd on the nitrogen-doped mesoporous carbon support material (Pd/NMC): (a) Pd on graphitic N support; (b) Pd on pyridinic N support. Adapted from Ref. 13 with permission from the PCCP Owner Societies.

90 *2.2. Methodology*

The present density functional theory (DFT) study was performed using the TURBOMOLE[20] program package with the TPSS[21] functional and the def2-SVP[22] basis set. Stuttgart-Cologne 28-electron effective core potentials (def2-

ecp)[23] were used for the Pd atoms. All calculations included the multipole accelerated resolution of identity (MARI-J)[24] approximation with optimized auxiliary basis sets[25] and Grimme's D3[26] correction for London dispersion interactions. The most stable structures of our model systems as well as the minima of hydrogen on these systems were determined by ground-state geometry optimizations. To obtain accurate relative energies, single point energies were combined with zero-point vibrational energies (ZPVEs) from vibrational analysis.

At this level, results from DFT with different functionals and basis sets can differ in the range of some kJ mol^{-1} per bond. In a previous study[18] we have shown that moving to a larger basis set or to other DFT functionals does affect the DFT energetics of the catalyst systems, but calculated energy differences are similar and the observed trends of the energy differences are essentially the same. Due to the limited comparability of our idealized model systems to experimental catalysts, we anyway limit our conclusions to qualitative observations and omit comparisons to specific experimental values. Our choice of the meta-GGA TPSS functional and the def2-SVP basis set has been shown to be reasonable in several previous studies, as it shows a very good cost/performance ratio for the systems under consideration[27, 28, 18, 19, 13]. A comparison of some exemplary TPSS/def2-SVP energy differences with those from PBE/def2-SVP and TPSS/def2-TZVP on the basis of TPSS/def2-SVP geometries, which document the good agreement of energetics calculated with different functionals and basis sets for our systems, can be found in the supporting information (cmp. Tables S1-S3).

Reaction pathways were predicted using the chain-of-state method implemented in the woelfling module of TURBOMOLE [29] and the found initial transition state structures were then further optimized with the eigenvalue following trust-region image minimization (TRIM)[30] algorithm. All transition states were finally validated by intrinsic reaction coordinate (IRC)[31] calculations. To allow for a qualitative comparison of the calculated results to experimental studies, Gibbs free reaction enthalpies and free activation enthalpies

were determined within the harmonic oscillator and rigid rotor approximation under reaction conditions of 473.15 K and 0.1 MPa with a scaling factor of 1.0190 for the TPSS functional[32]. Favorable adsorption energies and dissociation energies are provided with a negative sign, energy barriers like activation barriers with a positive sign. To arrive at a deeper understanding of the relevant metal-support, hydrogen-support and metal-hydrogen interactions, we studied intrinsic bond orbitals (IBOs)[33], intrinsic atomic orbital (IAO) charge analyses[33] as well as electron density differences. As the π-system of the different support materials can be described well by Hückel theory (cmp. Figure S1 for a validation of Hückel vs. DFT), we had a closer look at Hückel orbital energies and population analysis. To model the molecular system after spillover of hydrogen to the support materials within Hückel theory, the carbon atom attached to the spillover hydrogen was deleted from the π-system.

3. Results and discussion

3.1. Electronic properties of spillover hydrogen

As a first step, we investigated the electronic properties of spillover hydrogen. When a hydrogen atom spills over to the carbon support material it binds to one carbon atom. In this configuration the corresponding carbon atom comes out of the support plane and changes its hybridization partially from sp^2 to sp^3 (cmp. Figure 5a). Consequently, the intrinsic bond orbital (IBO) analysis shows an sp^3 hybrid C-H bonding orbital (cmp. Figure 5b).

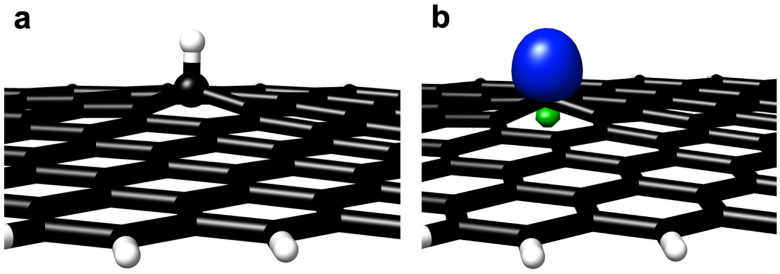

Figure 5: Spillover hydrogen on the graphene support material: (a) geometry; (b) sp^3 hybrid C-H IBO.

Besides the local change of the carbon support geometry also the electronic structure of the support material is affected as the carbon atom attached to the spillover hydrogen does not contribute to the π-system any more. Accordingly, the spillover hydrogen disturbs the π-system of the support material, which leads to a very unfavorable free H_2 dissociation enthalpy (H_2 + 2 CMC $\rightarrow$ 2 H-CMC) of $\Delta G_{\mathrm{diss}} = +\ 362.0$ kJ mol^{-1}. The perturbing effect of spillover hydrogen on the π-system can further be validated with the Hückel orbital energies, which show that the spillover hydrogen shifts the highest occupied molecular orbital (HOMO), containing an unpaired electron, up to the Fermi-level (cmp. Figure S2 a).

To get further insight into the properties of spillover hydrogen itself, we calculated the electron density difference for spillover hydrogen on the graphene support material (cmp. Figure 6). Like the IBO analysis, the electron density difference plot also proposes that a chemical bond between the spillover hydrogen and one carbon atom is formed as an electron density shift from the π-bonds of the bound carbon atom to an sp^3 hybrid C-H bonding orbital can be observed. Moreover, the plot shows that electron density is shifted from the H s orbital to the π orbitals of the surrounding C atoms. This suggests that spillover hydrogen is positively charged. Based on IAO atomic charge analyses, we found that the partial charge of spillover hydrogen ($q = +\ 0.16$) is more positive than the partial charge of hydrogen atoms located at the edge of the support material or of the hydrogen atoms in the methane molecule (both $q = +\ 0.13$).

In contrast to the suggestion of Yang et al.[8], we do not find the spillover hydrogen in the state of a 'real' proton, as the electron of the spillover hydrogen atom is localized in an sp^3 hybrid C-H bonding orbital with the H nucleus located at a position where the electron density is higher than for an isolated H atom (cmp. Figure 6c). However, spillover hydrogen atoms possess a relatively high positive partial charge due to electron density shifted from the H s orbital to the π-system.

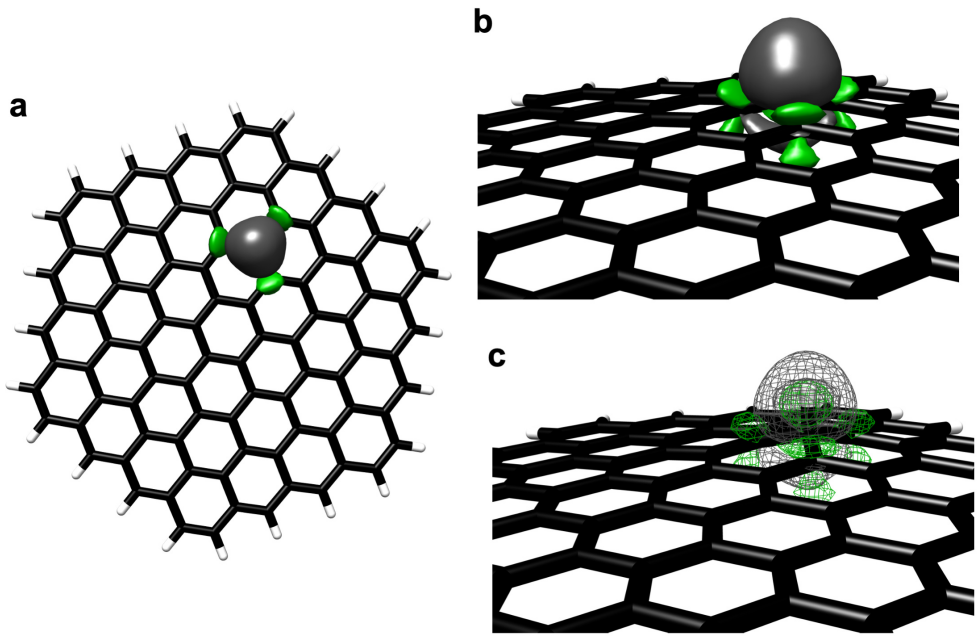

Figure 6: Electron density difference plot for spillover hydrogen on the graphene support material: (a) top view; (b) side view; (c) side view represented with a mesh to reveal inside changes. Density gain is colored in green; density loss is colored in grey.

Furthermore, we studied the effect of nitrogen doping on the properties of spillover hydrogen. Doping with pyridine-like nitrogen atoms slightly increases the positive Gibbs free enthalpy for the H_2 dissociation (for a spillover hydrogen next to the pyridinic N) to $\Delta G_{\text{diss}} = +\ 364.8$ kJ mol^{-1}. As the electronegative character of the pyridinic N leads to a positive charge at the neighboring carbon atoms, one would expect that doping with pyridine-like nitrogen atoms would more significantly hinder the binding of a hydrogen radical. However, the higher structural flexibility at the defect allows for geometrical deformations of the support and, therefore, allows for a H-C bond with a stronger sp^3 character, which compensates for the unfavorable electronic effect of the pyridinic N.

In contrast to doping with pyridinic nitrogen, doping with a graphitic nitrogen atom significantly decreases the free enthalpy for the dissociation of H_2 to $\Delta G_{\text{diss}} = +\ 150.4$ kJ mol^{-1}. This observation can again be explained using

Hückel theory: The graphitic nitrogen atom possesses an additional (in comparison to C) electron in the π-system, which is unpaired and facilitates the binding of a hydrogen radical. This can be validated with the Hückel orbital energies, which show a highest occupied molecular orbital (HOMO) doubly occupied and significantly below the Fermi-level (cmp. Figure S2 b). Furthermore, in the electron density difference it can be observed that the graphitic nitrogen atom leads to a delocalization of shifted electron density from the H s orbital to the π-system of the support material (cmp. Figure 7; and Figure S3 for electron density difference plots for systems with two and six graphitic N atoms).

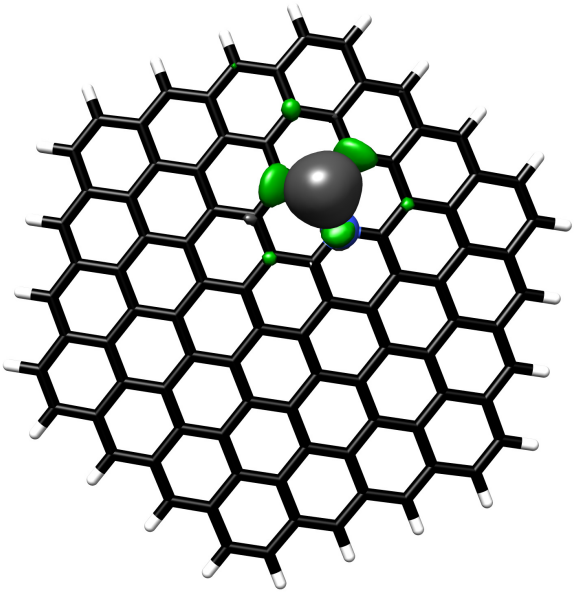

Figure 7: Electron density difference plot for spillover hydrogen on the graphitic N support material. Density gain is colored in green; density loss is colored in grey.

It is important to note that the extent of the effect of the graphitic nitrogen atom on the π-system depends on its position with respect to the spillover hydrogen (cmp. Figure 8 for a sketch of the different positions). The Hückel stabilization energies of all different positions with respect to the most stable *ortho*-position is shown in Table 1. Positive relative values indicate a lower stabilization energy and, therefore, a smaller effect of the graphitic N.

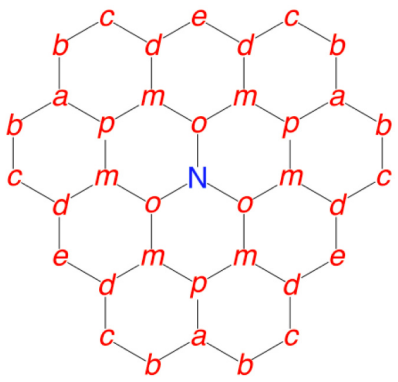

Figure 8: Sketch of spillover hydrogen atom positions on graphitic N-doped graphene support.

spillover hydrogen position	Hückel stabilization energy w.r.t. o-position/β
o	0.00
m	0.51
p	0.25
a	0.51
b	0.42
c	0.49
d	0.48
e	0.50

Table 1: Hückel stabilization energy for the different spillover hydrogen positions sketched in Figure 8 with respect to the most stable *ortho*-position in units of the resonance parameter β.

The extent of the effect is very similar to arene substitution patterns and can be summarized as follows:

- 1_{st} shell $> 2^{\text{nd}}$ shell
- 1_{st} shell: $o > p > m$
- 2^{nd} shell: $b > d > c > e > a$

The decoration of the support material with palladium clusters in general increases the stability of spillover hydrogen atoms as the cluster takes over most of the spin density of the hydrogen radical (cmp. Figure 9). The positive free enthalpy of the H_2 dissociation for a spillover hydrogen atom directly next to a Pd_{21} cluster is reduced to +230.0 kJ mol^{-1} compared to +362.0 kJ mol^{-1} for the pure graphene support system.

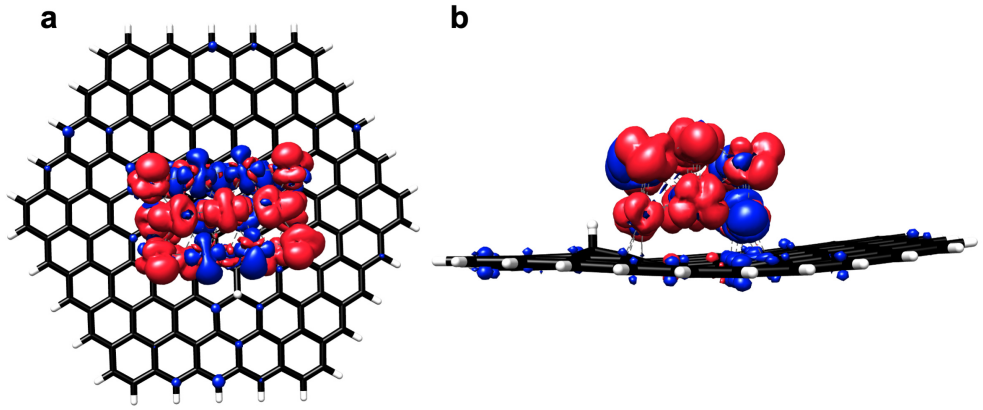

Figure 9: Plot of the spin density for a spillover hydrogen atom located directly next to a Pd_{21} cluster: (a) top view; (b) side view.

3.2. Hydrogen spillover pathways

As a second step, we investigated the hydrogen spillover process on carbon-supported Pd nanoparticles. In our previous study[18] it was shown that carbon-supported Pd clusters can adsorb and dissociate several hydrogen molecules. In experiments, the Pd cluster is most probably covered with hydrogen before the hydrogen spillover process takes place.

To elucidate the configuration of several chemisorbed hydrogen molecules on the Pd nanoparticles, a geometry of the carbon-supported Pd_{21} cluster loaded with 26 hydrogen atoms was optimized (cmp. Figure 10). The most stable positions of hydrogen atoms on the Pd cluster are triangular positions at the top of the cluster, bridging three palladium atoms. When, subsequently, several hydrogen molecules are chemisorbed on the cluster, hydrogen atoms are attached

to the side of the cluster and to even less stable bridge positions on top of Pd-Pd bonds. Several studies on Pd crystals suggest that hydrogen could also be absorbed inside the cluster.[34]

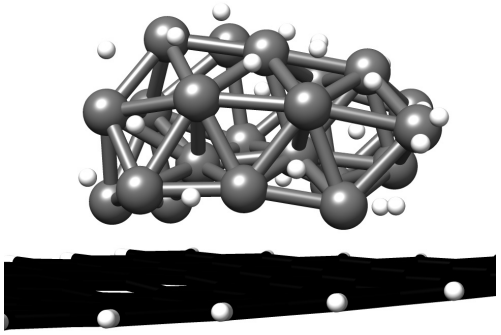

Figure 10: Geometry of carbon-supported Pd_{21} loaded with 26 hydrogen atoms.

We determined the reaction pathways for the hydrogen spillover process from the Pd_{21} cluster to the three different support materials using a model system with (only) one hydrogen atom, which is located in a triangular position at the side of the cluster. For the system with the lowest activation energy (Pd_{21} / graphitic N support), also the pathway from a less stable position, in which the H atom bridges a Pd-Pd bond at the bottom of the cluster, was considered. (The corresponding pathways for the pure graphene support and the pyridinic N support have not been studied; however, the effect of changing the starting point from the triangle to the bridge position on the energetics should be very similar).

A sketch of the hydrogen spillover reaction pathway from Pd_{21} to the support doped with graphitic N is shown in Figure 11 (cmp. Figures S4 and S5 for the corresponding pathways on graphene and support doped with pyridinic N). Table 2 shows the activation energies (ΔE_{act}) and the free activation enthalpies (ΔG_{act}) for the hydrogen spillover from Pd_{21} on the three different support materials. For the graphitic N support, also the activation energy and free activation enthalpy from the less stable reactant are listed. Table 3 shows the corresponding reaction energies ($\Delta E_{\mathrm{react}}$) and free reaction enthalpies ($\Delta G_{\mathrm{react}}$).

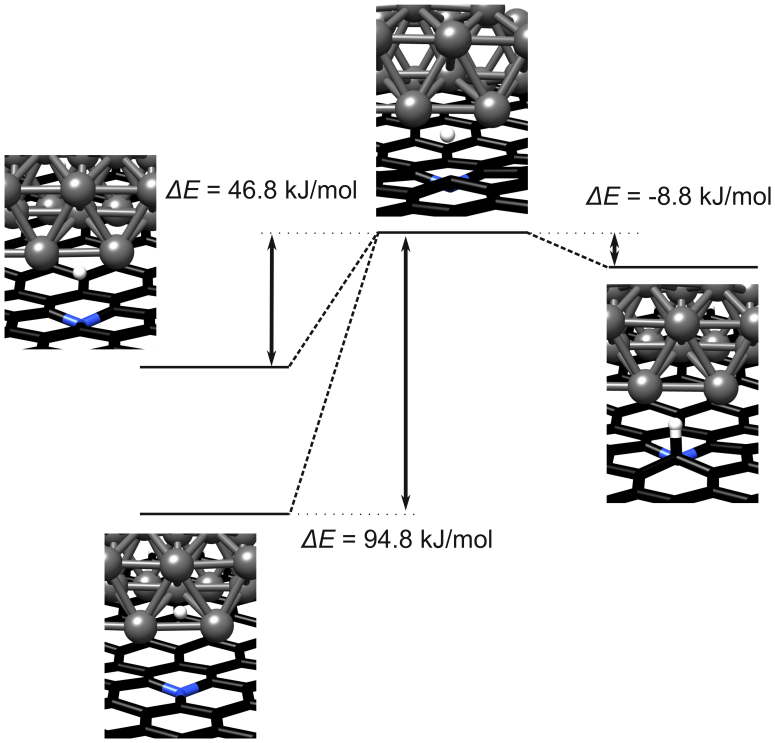

Figure 11: Hydrogen spillover pathway from Pd_{21} to the graphitic N support material from two different initial sites.

model system	ΔE_{act}/kJ mol^{-1}	ΔG_{act}/kJ mol^{-1}
Pd_{21} on graphene support; triangle site	130.8	140.8
Pd_{21} on graphitic N support; triangle site	94.8	97.9
Pd_{21} on graphitic N support; bridge site	46.8	50.4
Pd_{21} on pyridinic N support; triangle site	193.8	200.3

Table 2: Activation energies and free activation enthalpies for the hydrogen spillover from Pd_{21} onto different support materials.

model system	$\Delta E_{\mathrm{react}}$/kJ mol^{-1}	$\Delta G_{\mathrm{react}}$/kJ mol^{-1}
Pd_{21} on graphene support; triangle site	129.2	143.4
Pd_{21} on graphitic N support; triangle site	86.0	94.4
Pd_{21} on graphitic N support; bridge site	38.0	47.0
Pd_{21} on pyridinic N support; triangle site	187.9	187.4

Table 3: Reaction energies and free reaction enthalpies for the hydrogen spillover from Pd_{21} onto different support materials.

On the pure graphene support material the hydrogen spillover reaction starting from the triangle site shows quite a high activation energy and free activation enthalpy. Even if one assumes that starting from the less stable bridge position will decrease the Gibbs free reaction enthalpy by around 45 kJ mol^{-1} (approximated from the result for the graphitic N system), it still mounts up to around 100 kJ mol^{-1}. This indicates that the hydrogen spillover to pure carbon support materials is kinetically difficult, which is also in agreement with previous ab initio molecular dynamics (AIMD) simulations, that have not found a single case of hydrogen spillover from Pd_6 or Pd_{13} clusters to pure graphene[35].

Doping with graphitic N atoms significantly decreases the activation energy and free activation enthalpy of the spillover reaction (for the triangle site to around 95 kJ mol^{-1}; for the bridge site to around 50 kJ mol^{-1}). This effect can be explained on the basis of Hammond's postulate: In general, the hydrogen spillover reaction is an endothermic reaction (cmp. Table 3). The transition state is very similar to the product state, which is called 'late' transition state. As the doping with graphitic N atoms decreases the positive reaction energy and, therefore, stabilizes the product state (due to its additional electron; cmp. previous section), the doping also stabilizes the transition state.

Analogous to the explanation for the decrease of the activation energy for the graphitic N system, also the increase of the activation energy for the pyridinic N system can be explained using Hammond's postulate. As described in the previous section, the positively charged carbon atoms next to the pyridinic N

significantly hinder the binding of the spillover hydrogen. In comparison with the free support material, the binding of the Pd cluster on the surface defect prevents a change of the support geometry. Accordingly, doping with pyridinic nitrogen destabilizes the product of the hydrogen spillover (cmp. Table 3) and, therefore, also increases the activation energy.

In general, our calculations reveal that the hydrogen spillover is significantly facilitated by graphitic N atoms. The free activation enthalpy for the spillover from the less stable bridge site is only around 50 kJ mol^{-1}. According to the Arrhenius law

$$\nu = \nu_0 \exp\left[\frac{-\Delta E_{\mathrm{act}}}{k_{\mathrm{B}}T}\right] \tag{1}$$

with the activation energy $\Delta E_{\mathrm{act}} = 46.8$ kJ mol^{-1} and a common estimate of the pre-exponential value of $\nu_0 = \frac{k_{\mathrm{B}}T}{h} = 1 \cdot 10^{13}$ s^{-1} [17, 36, 37] one can expect a hydrogen migration rate of $\nu \sim 7 \cdot 10^{7}$ s^{-1} at 473.15 K. This sufficiently high rate gives some evidence that doping with graphitic nitrogen atoms could actually enable the hydrogen spillover process on Pd/NMC, which is also in agreement with the experimental observation of hydrogen spillover on Pt/NMC by Yang et al.[8].

3.3. Hydrogen bonds formed by spillover hydrogen and water molecules

To get an insight into the interaction of spillover hydrogen with residual moisture, we optimized the geometry of a water molecule close to spillover hydrogen. The equilibrium geometry indicates that the spillover hydrogen atom somehow interacts with the oxygen atom of the water molecule (cmp. Figure 12). However, the intrinsic bond orbital (IBO) analysis does not find any C-H - O bonding orbital. Accordingly, the spillover hydrogen atom is not strongly acidic, i.e. it does not protonate H_2O to form H_3O^+, which is in agreement with our previous findings, showing that spillover hydrogen is positively charged but is not in the state of acidic protons.

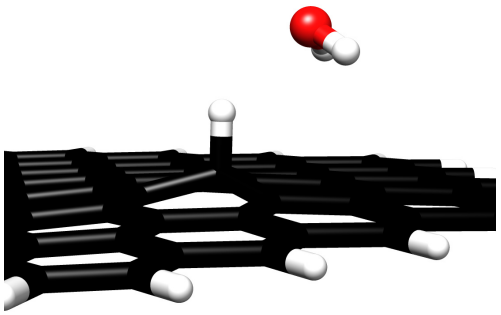

Figure 12: Equilibrium geometry of water on a spillover hydrogen.

To elucidate the details of the C-H - O interaction, we calculated the electron density difference of the spillover hydrogen - water system (cmp. Figure 13a) and compared it to the electron density difference of the water dimer (cmp. Figure 13b). The electron density differences of these two systems are nearly equivalent. This indicates that the previously found positive partial charge of spillover hydrogen is high enough so that it can form hydrogen bonds with water molecules. The energy of such a hydrogen bond is $E_{\mathrm{hbond}} = -37.0$ kJ mol^{-1} at a hydrogen bond length of $r_{\mathrm{b}} = 2.24$ Å; compared to $E_{\mathrm{hbond}} = -28.7$ kJ mol^{-1} and $r_{\mathrm{b}} = 1.90$ Å for the water dimer. This is in agreement with the experimental studies of Yang et al.[8], Li et al.[9] and Wang et al.[10], which propose that spillover hydrogen is stabilized by water molecules.

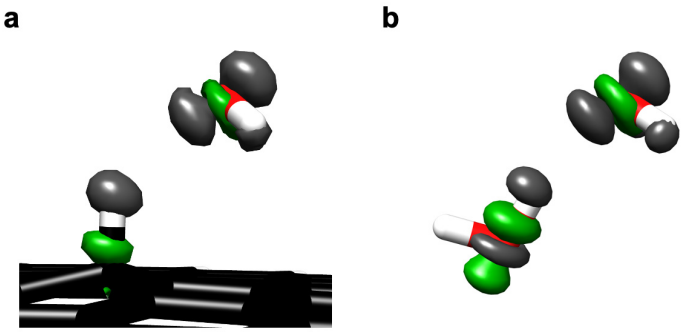

Figure 13: Electron density difference plots: (a) interaction of water with a spillover hydrogen; (b) interaction of the water dimer. Density gain is colored in green; density loss is colored in grey.

3.4. Diffusion of spillover hydrogen

To investigate if spillover hydrogen can play a role in hydrogenation reactions and if it lends itself for the purpose of hydrogen storage, it is important to also study the diffusion of spillover hydrogen on the support material. Table 4 lists the activation energies (ΔE_{act}) and the free activation enthalpies (ΔG_{act}) for the diffusion pathways on the three different support materials, which are sketched in Figure 14. In all these pathways the spillover hydrogen diffuses in a chemisorbed state from one to the neighboring carbon atom, surpassing a transition state in which the H atom bridges a carbon-carbon bond.

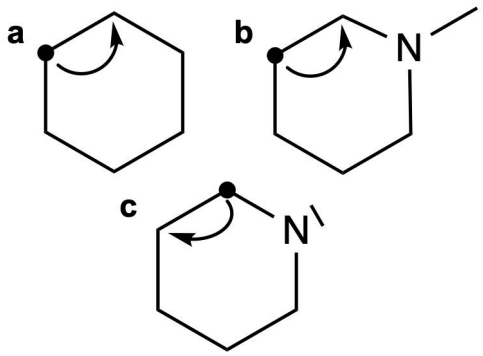

Figure 14: Sketch of spillover hydrogen diffusion pathways: (a) diffusion on pure graphene support material; (b) diffusion on graphitic N support material; (c) diffusion on pyridinic N support material.

diffusion pathway	ΔE_{act}/kJ mol^{-1}	ΔG_{act}/kJ mol^{-1}
a: on pure graphene support material	105.0	107.6
b: on graphitic N support material	121.5	123.9
c: on pyridinic N support material	45.1	46.9

Table 4: Activation energies and free activation enthalpies for spillover hydrogen diffusion on different support materials.

diffusion pathway	$\Delta E_{\mathrm{react}}$/kJ mol^{-1}	$\Delta G_{\mathrm{react}}$/kJ mol^{-1}
a: on pure graphene support material	∼0.0	∼0.0
b: on graphitic N support material	-62.6	-62.3
c: on pyridinic N support material	-53.4	-32.5

Table 5: Reaction energies and free reaction enthalpies for spillover hydrogen diffusion on different support materials.

On the pure graphene support material the chemisorbed diffusion pathway (pathway a) shows a quite high activation energy and Gibbs free activation enthalpy. An IBO analysis and an IAO charge calculation reveal that the spillover hydrogen in the transition state is bound to two carbon atoms and is significantly stronger positively charged compared to spillover hydrogen in the equilibrium geometry ($q = +\ 0.25$ compared to $q = +\ 0.16$). Due to the bridging position of the spillover hydrogen the valence electrons of two carbon atoms are partly taken out of the π-system, which explains the unfavorable energy of the transition state. However, the activation energy and free activation enthalpy of the chemisorbed diffusion pathway can be significantly reduced by a hydrogen bonded water molecule via a Grotthus-like mechanism ($\Delta G_{\mathrm{act1}} = 77.7$ kJ mol^{-1}; cmp. Figure S6 and Table S4 for the reaction pathway).

The smallest activation energy and free activation enthalpy can be observed for pathway c, in which the spillover hydrogen atom is located close to a pyridinic nitrogen atom. The found Gibbs free activation enthalpy is only 46.9 kJ mol^{-1}, which corresponds to an expected hydrogen migration rate of $\nu \sim 1 \cdot 10^{8}$ s^{-1} at 473.15 K (cmp. eqn (1)). According to the IBO analysis, the spillover hydrogen in the transition state is solely bound to the carbon atom of the product state. In contrast to the pure graphene support material, it is not symmetrically bound to the two carbon atoms of reactant and product. This effect can be explained by the different charges of the carbon atoms (reactant: positively charged; product: negatively charged), induced by the pyridinic nitrogen dopant. As a consequence, the perturbation of the π-system, and therefore also

the activation energy and free activation enthalpy, is significantly lowered.

Close to graphitic N dopants the calculated activation energy and Gibbs free activation enthalpy for the spillover hydrogen diffusion are very high, which is a consequence of its significant spillover hydrogen stabilization. This result indicates that spillover hydrogen will accumulate close to graphitic N atoms in the support material.

When we studied the diffusion of hydrogen spillover to the next but one neighboring carbon atom on the pure graphene support material, we observed that the chemisorbed spillover hydrogen first desorbs via a first transition state to a physisorption minimum, diffuses in this well, and then adsorbs at the next but one neighboring carbon atom, surpassing a second transition state (cmp. Figure 15). According to IBO analyses and IAO charge calculations, in both transition states the spillover hydrogen is physisorbed as a hydrogen atom and not bound in a chemisorbed state. In the physisorption minimum the hydrogen atom is in a doublet spin state (the corresponding spin density is shown in Figure S7).

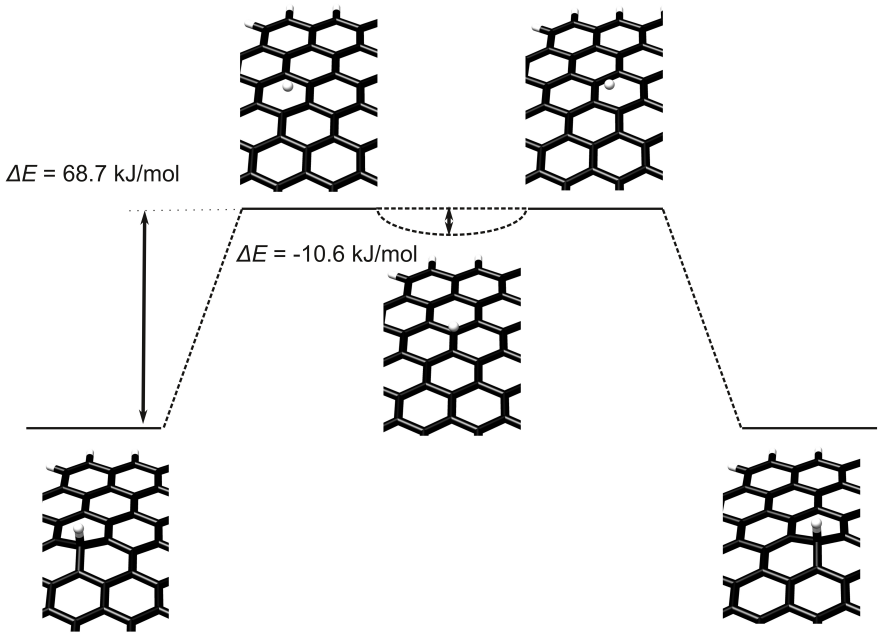

Figure 15: Spillover hydrogen diffusion pathway via a physisorption minimum.

It is important to note that the activation energy and free activation enthalpy for the change of spillover hydrogen from the chemisorbed state to the physisorption minimum is significantly lower compared to the activation energy and free activation enthalpy of the chemisorbed diffusion (ΔE_{act} = 68.5 kJ mol^{-1} and ΔG_{act} = 70.2 kJ mol^{-1} compared to ΔE_{act} = 105.0 kJ mol^{-1} and ΔG_{act} = 107.6 kJ mol^{-1}). This observation is in agreement with previous studies, reporting on barrierless diffusion of physisorbed spillover hydrogen atoms.[38, 36] Compared to the chemisorbed diffusion, the hydrogen atom in the transition state of the change to the physisorbed state is not chemisorbed at two, but only physisorbed at one carbon atom, leading to a smaller perturbation of the π-system and, therefore, to a significantly reduced activation energy and free activation enthalpy. Accordingly, on the pure graphene support material, hydrogen diffusion should occur via a physisorption pathway. The free activation enthalpy for the change of the hydrogen atom from the chemisorbed to the physisorbed state is 70.2 kJ mol^{-1}, which corresponds to an expected rate of $\nu \sim 3.5 \cdot 10^5$ s^{-1} at 473.15 K (cmp. eqn (1)).

Based on these observations we also studied the change from the chemisorbed to the physisorbed state for the initial configurations of the nitrogen-doped systems in pathways b and c. The corresponding activation energies and free activation enthalpies for all systems are summarized in Table 6.

model system	ΔE_{act}/kJ mol^{-1}	ΔG_{act}/kJ mol^{-1}
pure graphene support	68.5	70.2
pyridinic N support	80.0	76.3
graphitic N support	107.6	107.4

Table 6: Activation energies and free activation enthalpies for the change from the chemisorbed to the physisorbed state.

Close to a pyridinic N atom the activation energy and free activation enthalpy is slightly higher compared to the pure graphene system, which can be explained with the slightly more stable reactant in the pyridinic system. As the transition state of the chemisorbed diffusion pathway is significantly favored

(H atom solely bound to the C atom of the product state), spillover hydrogen diffusion, close to pyridinic N atoms, should occur via a chemisorbed diffusion once H was bound at such a position.

Close to a graphitic N atom the activation energy and free activation enthalpy is significantly higher compared to the pure graphene system. This can also be explained with the high stability of the reactant. Even though the physisorbed diffusion pathway is noticeable facilitated compared to the chemisorbed diffusion pathway (H atom physisorbed at one C atom compared to chemisorption at two C atoms in the transition state), the free activation enthalpy for the change from the physisorbed to the chemisorbed state still mounts up to 107.4 kJ mol^{-1}.

The expected rates of $\nu \sim 1 \cdot 10^8$ s^{-1} for the hydrogen atom migration in the vicinity of pyridinic nitrogen atoms and of $\nu \sim 3.5 \cdot 10^5$ s^{-1} for the change from the chemisorbed to the physisorbed state on the pure graphene support material indicate that spillover hydrogen atoms should be mobile on the carbon surface. This was also experimentally proposed by Yang et al.[8]. Moreover, spillover hydrogen will accumulate close to graphitic N atoms.

3.5. Desorption of spillover hydrogen

To further clarify the possible usage of spillover hydrogen in the context of hydrogen storage, also the desorption of two neighboring spillover hydrogens to H_2 has to be considered. The Tables 7 and 8 show the activation energies (ΔE_{act}) and free activation enthalpies (ΔG_{act}) as well as the reaction energies ($\Delta E_{\mathrm{react}}$) and free reaction enthalpies ($\Delta G_{\mathrm{react}}$) of the desorption pathways on the different support materials (cmp. Figures S8, S9 and S10 for the reaction pathways).

It is observed that the spillover hydrogen desorption is highly kinetically hindered on all support materials. Based on the previous observation that the change from the chemisorbed to the physisorbed state for spillover hydrogen on the graphene support material shows an activation energy of only 68.5 kJ mol^{-1}, also the hydrogen desorption via an intermediate in which one

support material	ΔE_{act}/kJ mol^{-1}	ΔG_{act}/kJ mol^{-1}
graphene support	232.0	231.2
graphitic N support	128.4	128.3
pyridinic N support	176.8	169.2

Table 7: Activation energies and free activation enthalpies for spillover hydrogen desorption on different support materials.

support material	ΔE_{react}/kJ mol^{-1}	ΔG_{react}/kJ mol^{-1}
graphene support	-199.9	-370.2
graphitic N support	-138.4	-194.3
pyridinic N support	-183.8	-243.8

Table 8: Reaction energies and free reaction enthalpies for spillover hydrogen desorption on different support materials.

hydrogen atom is physisorbed should be considered. It is important to note that the change from the chemisorbed to the physisorbed state is significantly hindered by a neighboring hydrogen atom and the activation energy is increased up to 163.2 kJ mol^{-1} for the graphene support system. This can be explained by the fact that the reactant of a chemisorbed spillover hydrogen is stabilized by a neighboring chemisorbed spillover hydrogen atom, as the second hydrogen atom cancels out the radical state of the system. Accordingly, also the hydrogen desorption via a physisorbed intermediate is unfavorable and the formation of spillover hydrogen atom domains is very likely.

Of course, two physisorbed spillover hydrogen atoms coming close together could easily desorb as H_2. However, as the free activation enthalpy for the diffusion from the support material back to the Pd cluster is very small (e.g. 3.5 kJ mol^{-1} for the spillover on the graphitic N support material), spillover hydrogen will rather diffuse back to the Pd cluster than desorb. These results suggest that, if hydrogen spillover on Pd/NMC occurs, the spillover hydrogen would be reversible stored on the carbon support material. This is in agreement with the study of Yang et al.[8], which gives experimental evidence of reversibly

stored spillover hydrogen species on Pt/NMC.

4. Conclusions

Using quantum chemistry we were able to provide an in-depth inside into the hydrogen spillover process on carbon-supported palladium nanoparticles and into the effect of doping with graphitic and pyridinic nitrogen on such processes. We found that the hydrogen spillover reaction is significantly facilitated by graphitic nitrogen atoms, leading to a relatively low Gibbs free activation enthalpy of around 50 kJ mol^{-1} and a feasible migration rate of around $7 \cdot 10^7$ s^{-1} for the spillover of a hydrogen atom from a Pd-Pd bridge position at reaction conditions of 473.15 K and 0.1 MPa. This observation can be explained on the basis of Hammond's postulate as the graphitic nitrogen stabilizes the product state. Diffusion of spillover hydrogen atoms takes place with feasible migration rates at pure graphene support via a physisorbed pathway and in the vicinity of pyridinic nitrogen atoms via a chemisorbed pathway. Close to graphitic nitrogen atoms no diffusion should be observed, as the graphitic nitrogen stabilizes the spillover hydrogen binding due to its additional electron distributed to the π-system. Spillover hydrogen desorption is kinetically hindered on all support materials.

Based on these results and the results of our previous study[13] the following can be concluded: Hydrogen spillover from Pd to pure carbon support materials (as in Pd/CMC) is kinetically difficult. In Pd/NMC the palladium nanoparticles are preferentially anchored on pyridinic nitrogen atoms. Graphitic nitrogen atoms, which make up around 6 % of the N functional groups of the NMC surface used in Ref. 13, significantly reduces the barriers of the hydrogen spillover process. This gives some evidence that graphitic nitrogen atoms could actually enable the hydrogen spillover process on Pd/NMC. The calculated positive Gibbs free reaction enthalpies for all spillover reaction pathways are due to the fact that our calculations just include one hydrogen atom on the cluster. In the chemical equilibrium of a high hydrogen coverage on the supported Pd nanopar-

ticle, as it is present when the hydrogen spillover occurs, ΔG of the hydrogen chemisorption on the Pd cluster should be zero. The calculated free chemisorption enthalpy of H_2 on our model system is in the order of -60 kJ mol^{-1}, which will compensate for the remaining positive free reaction enthalpy of the spillover process. Moreover, in the chemical equilibrium the supported Pd cluster is most probably (after hydrogen spillover) continuously reloaded with hydrogen from the gas phase, which changes the overall reaction equation.

Besides their effect on the spillover process, graphitic nitrogen atoms can serve as anchoring sites for the spillover hydrogen species. When the hydrogen spillover process actually occurs on Pd/NMC, the spillover hydrogen will be reversibly stored on the carbon support material as the barriers for migrating back from the carbon support to the Pd nanoparticle are quite small and spillover hydrogen desorption is unlikely.

In general, we do not find that spillover hydrogen is in the state of 'real' protons. However, the spillover hydrogen is positively charged and can be stabilized by water molecules of residual moisture via hydrogen bonds.

Declaration of competing interests

The authors declare no competing financial interest.

Acknowledgements

This work has been supported by the Deutsche Forschungsgemeinschaft within the framework of the Sino-German initiative "Novel Functional Materials for Sustainable Chemistry" through grant Ha 2588/9-1.

Appendix A. Supplementary material

References

[1] W. C. Conner, J. L. Falconer, Spillover in heterogeneous catalysis, Chem. Rev. 95 (1995) 759 – 788.

[2] R. Prins, Hydrogen spillover. facts and fiction, Chem. Rev. 112 (2012) 2714 – 2738.

[3] A. Lueking, R. T. Yang, Hydrogen spillover from a metal oxide catalyst onto carbon nanotubes—implications for hydrogen storage, J. Catal. 206 (2002) 165 – 168.

[4] A. J. Lachawiec, G. Qi, R. T. Yang, Hydrogen storage in nanostructured carbons by spillover: Bridge-building enhancement, Langmuir 21 (2005) 11418 – 11424.

[5] C. I. Contescu, C. M. Brown, Y. Liu, V. V. Bhat, N. C. Gallego, Detection of hydrogen spillover in palladium-modified activated carbon fibers during hydrogen adsorption, J. Phys. Chem. C 113 (2009) 5886 – 5890.

[6] J. L. Blackburn, C. Engtrakul, J. B. Bult, K. Hurst, Y. Zhao, Q. Xu, P. A. Parilla, L. J. Simpson, J.-D. R. Rocha, M. R. Hudson, C. M. Brown, T. Gennett, Spectroscopic identification of hydrogen spillover species in ruthenium-modified high surface area carbons by diffuse reflectance infrared fourier transform spectroscopy, J. Phys. Chem. C 116 (2012) 26744 – 26755.

[7] X. M. Liu, Y. Tang, E. S. Xu, T. C. Fitzgibbons, G. S. Larsen, H. R. Gutierrez, H.-H. Tseng, M.-S. Yu, C.-S. Tsao, J. V. Badding, V. H. Crespi, A. D. Lueking, Evidence for ambient-temperature reversible catalytic hydrogenation in pt-doped carbons, Nano Lett. 13 (2013) 137 – 141.

[8] F. Yang, B. Hu, W. Xia, B. Peng, J. Shen, M. Muhler, On the nature of spillover hydrogen species on platinum/nitrogen-doped mesoporous carbon composites: A temperature-programmed nitrobenzene desorption study, J. Catal. 365 (2018) 55 – 62.

[9] Q. Li, A. D. Lueking, Effect of surface oxygen groups and water on hydrogen spillover in pt-doped activated carbon, J. Phys. Chem. C 115 (2011) 4273 – 4282.

[10] L. Wang, F. H. Yang, R. T. Yang, M. A. Miller, Effect of surface oxygen groups in carbons on hydrogen storage by spillover, Ind. Eng. Chem. Res. 48 (2009) 2920 – 2926.

[11] H. Cheng, L. Chen, A. C. Cooper, X. Sha, G. P. Pez, Hydrogen spillover in the context of hydrogen storage using solid-state materials, Energy Environ. Sci. 1 (2008) 338 – 354.

[12] L. Wang, R. T. Yang, Hydrogen storage on carbon-based adsorbents and storage at ambient temperature by hydrogen spillover, Catal. Rev. 52 (2010) 411 – 461.

[13] L. Warczinski, B. Hu, T. Eckhard, B. Peng, M. Muhler, C. Hättig, Anchoring of palladium nanoparticles on n-doped mesoporous carbon, Phys. Chem. Chem. Phys. 22 (2020) 21317 – 21325.

[14] A. Granja-DelRío, J. A. Alonso, M. J. López, Steric and chemical effects on the hydrogen adsorption and dissociation on free and graphene–supported palladium clusters, Comput. Theor. Chem. 1107 (2017) 23 – 29.

[15] I. López-Corral, E. Germán, A. Juan, M. A. Volpe, G. P. Brizuela, Dft study of hydrogen adsorption on palladium decorated graphene, J. Phys. Chem. C 115 (2011) 4315 – 4323.

[16] C. M. Ramos-Castillo, J. U. Reveles, R. R. Zope, R. de Coss, Palladium clusters supported on graphene monovacancies for hydrogen storage, J. Phys. Chem. C 119 (2015) 8402 – 8409.

[17] E. Rangel, E. Sansores, E. Vallejo, A. Hernández-Hernández, P. A. López-Pérez, Study of the interplay between n-graphene defects and small pd clusters for enhanced hydrogen storage via a spill-over mechanism, Phys. Chem. Chem. Phys. 18 (2016) 33158 – 33170.

[18] L. Warczinski, C. Hättig, A quantum chemical study of hydrogen adsorption on carbon-supported palladium clusters, Phys. Chem. Chem. Phys. 21 (2019) 21577 – 21587.

[19] B. Hu, L. Warczinski, Q. Fu, M. Lu, M. Li, C. Hättig, M. Muhler, B. Peng, Selective hydrogenolysis of 5-hydroxymethylfurfural to 2,5-dimethylfuran by formic acid over pd supported on n-doped mesoporous carbon, under review (2020).

[20] TURBOMOLE V7.1 2016, V7.2.1 2017 and V7.3 2018, a development of University of Karlsruhe and Forschungszentrum Karlsruhe GmbH, 1989-2007, TURBOMOLE GmbH, since 2007; available from `http://www.turbomole.com`., 2016-2018.

[21] J. Tao, J. P. Perdew, V. N. Staroverov, G. E. Scuseria, Climbing the density functional ladder: Nonempirical meta–generalized gradient approximation designed for molecules and solids, Phys. Rev. Lett. 91 (2003) 146401.

[22] F. Weigend, R. Ahlrichs, Balanced basis sets of split valence, triple zeta valence and quadruple zeta valence quality for h to rn: Design and assessment of accuracy, Phys. Chem. Chem. Phys. 7 (2005) 3297 – 3305.

[23] D. Andrae, U. Häußermann, M. Dolg, H. Stoll, H. Preuß, Energy-adjustedab initio pseudopotentials for the second and third row transition elements, Theor. Chim. Acta 77 (1990) 123 – 141.

[24] M. Sierka, A. Hogekamp, R. Ahlrichs, Fast evaluation of the coulomb potential for electron densities using multipole accelerated resolution of identity approximation, J. Chem. Phys. 118 (2003) 9136 – 9148.

[25] F. Weigend, Accurate coulomb-fitting basis sets for h to rn, Phys. Chem. Chem. Phys. 8 (2006) 1057 – 1065.

[26] S. Grimme, J. Antony, S. Ehrlich, H. Krieg, A consistent and accurate ab initio parametrization of density functional dispersion correction (dft-d) for the 94 elements h-pu, J. Chem. Phys. 132 (2010) 154104.

[27] J. Koßmann, C. Hättig, Investigation of interstitial hydrogen and related defects in zno, Phys. Chem. Chem. Phys. 14 (2012) 16392 – 16399.

[28] D. Stodt, H. Noei, C. Hättig, Y. Wang, A combined experimental and computational study on the adsorption and reactions of no on rutile tio2, Phys. Chem. Chem. Phys. 15 (2013) 466 – 472.

[29] P. Plessow, Reaction path optimization without neb springs or interpolation algorithms, J. Chem. Theory Comput. 9 (2013) 1305 – 1310.

[30] T. Helgaker, Transition-state optimizations by trust-region image minimization, Chem. Phys. Lett. 182 (1991) 503 – 510.

[31] K. Fukui, The path of chemical reactions - the irc approach, Acc. Chem. Res. 14 (1981) 363 – 368.

[32] M. K. Kesharwani, B. Brauer, J. M. L. Martin, Frequency and zero-point vibrational energy scale factors for double-hybrid density functionals (and other selected methods): Can anharmonic force fields be avoided?, J. Phys. Chem. A 119 (2015) 1701 – 1714.

[33] G. Knizia, Intrinsic atomic orbitals: An unbiased bridge between quantum theory and chemical concepts, J. Chem. Theory Comput. 9 (2013) 4834 – 4843.

[34] L. L. Jewell, B. H. Davis, Review of absorption and adsorption in the hydrogen–palladium system, Appl. Catal., A 310 (2006) 1 – 15.

[35] M. Blanco-Rey, J. I. Juaristi, M. Alducin, M. J. López, J. A. Alonso, Is spillover relevant for hydrogen adsorption and storage in porous carbons doped with palladium nanoparticles?, J. Phys. Chem. C 120 (2016) 17357 – 17364.

[36] H. González-Herrero, E. C. del Río, P. Mallet, J.-Y. Veuillen, J. J. Palacios, J. M. Gómez-Rodríguez, I. Brihuega, F. Ynduráin, Hydrogen physisorption channel on graphene: a highway for atomic h diffusion, 2D Mater. 6 (2019) 021004.

[37] A. A. Gokhale, S. Kandoi, J. P. Greeley, M. Mavrikakis, J. A. Dumesic, Molecular-level descriptions of surface chemistry in kinetic models using density functional theory, Chem. Eng. Sci. 59 (2004) 4679 – 4691.

[38] G. M. Psofogiannakis, G. E. Froudakis, Dft study of the hydrogen spillover mechanism on pt-doped graphite, J. Phys. Chem. C 113 (2009) 14908 – 14915.

Part III

Preliminary Results and Concluding Remarks

8 Preliminary Study: Ethylene Hydrogenation on Carbon-Supported Pd Nanoparticles and Reactivity of Spillover Hydrogen

8.1 Introduction

Around the year 1897, Paul Sabatier observed that solid nickel can significantly facilitate the hydrogenation of alkenes with H_2 at low temperatures[106]. This was the first report on heterogeneous catalyzed alkene hydrogenation and was later acknowledged with the Nobel Prize in Chemistry[107]. In 1934, Horiuti and Polanyi[108] studied the hydrogenation of ethylene and benzene on platinum black and on an active nickel catalyst. Based on their experimental observations they proposed the fundamental mechanism of heterogeneous catalyzed alkene hydrogenation. The so-called 'Horiuti-Polanyi mechanism' follows four steps: I.) chemisorption of hydrogen, resulting in adsorbed hydrogen atoms on the catalyst; II.) alkene adsorption on the catalyst; III.) hydrogen atom transfer to one carbon atom; IV.) hydrogen atom transfer to a second carbon atom.[108]

Since that time, plenty of studies on heterogeneous catalyzed alkene hydrogenation have been published. Today, common heterogeneous catalysts for alkene hydrogenation are supported metal nanoparticles.[107]

In the studies presented in the previous chapters, we have investigated mesoporous carbon supported Pd nanoparticles (Pd/CMC and Pd/NMC) as catalysts for hydrogenation reactions. We observed that these catalyst systems can adsorb and dissociate several hydrogen molecules (cmp. Chapter 4) and can provide excellent catalytic activity and selectivity (cmp. Chapter 6). Additionally, in our previous

study (cmp. Chapter 7) and in the study of Yang et al.[37], theoretical as well as experimental evidence for spillover hydrogen as a reversibly stored hydrogen source on the Pd nanoparticle decorated carbon support was found. However, Yang et al. proposed that these spillover hydrogen atoms are chemically inactive and are not accessible for hydrogenation reactions while located on the carbon support material.

This chapter shows a preliminary study on the hydrogenation of ethylene on mesoporous carbon supported Pd nanoparticles. In this study, we compare the reactivity of hydrogen located on the Pd nanoparticles to the reactivity of spillover hydrogen atoms. As a first step, we investigate the hydrogenation of ethylene with two adsorbed hydrogen atoms on carbon-supported Pd_{21} and reveal if the alkene hydrogenation on this system also follows the Horiuti-Polanyi mechanism. Secondly, we study the equivalent reaction with spillover hydrogen atoms. We aim to verify if spillover hydrogen can actually hydrogenate alkenes while located on the carbon support material. As our computational study on the hydrogen spillover process in Chapter 7 showed that graphitic nitrogen species serve as anchoring sites for spillover hydrogen atoms, we also consider spillover hydrogen located next to a graphitic nitrogen atom.

8.2 Computational Details

Like all of our previous studies (cmp. Chapters 4 to 7) the present study on ethylene hydrogenation is also performed using density functional theory (DFT), the TPSS[66] functional, the def2-SVP[65] basis set with Stuttgart-Cologne 28-electron effective core potentials (def2-ecp)[87] for the Pd atoms, and the TURBOMOLE[67] program package. Again, the multipole accelerated resolution of identity (MARI-J) approximation[98] with optimized auxiliary basis sets[109] and Grimme's D3[95] correction for London dispersion interactions are included.

To model the hydrogenation of ethylene on carbon-supported palladium nanoparticles, we chose a Pd_{21} cluster supported on a hydrogen terminated graphene layer of 150 carbon atoms with two hydrogen atoms adsorbed at the fcc positions of the cluster (cmp. Figure 8.1), which was previously shown to be the most stable configuration of two hydrogen atoms on carbon-supported Pd_{21} (cmp. Chapter 4). The corresponding pathway with spillover hydrogen is modeled on the basis of two neighboring spillover hydrogen atoms attached to a hydrogen terminated graphene layer of 96 carbon atoms (cmp. Figure 8.2a). The chosen configuration of two neighboring spillover hydrogen atoms is relatively stable as one hydrogen atoms cancels out the radical state induced by the other one (cmp. Chapter 7) and, therefore, should also be present in experimental catalyst systems. For the graphitic nitrogen doped system a carbon atom next to the spillover hydrogen species is replaced by a nitrogen atom (cmp. Figure 8.2a).

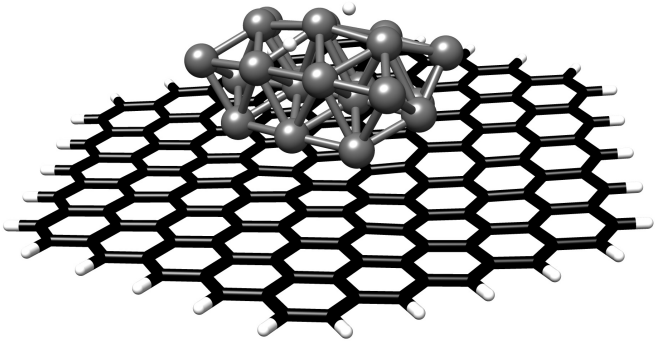

Figure 8.1: Model system for ethylene hydrogenation on carbon-supported Pd_{21} with two H atoms located at the fcc positions.

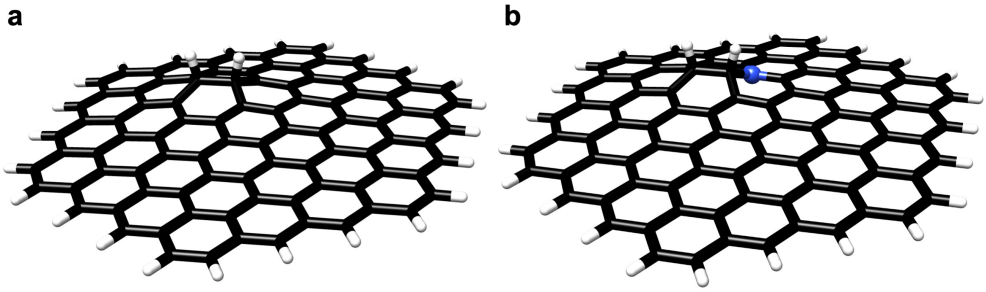

Figure 8.2: Model systems for ethylene hydrogenation with two neighboring spillover H atoms: (a) pure graphene support material; (b) graphitic nitrogen doped graphene surface.

The adsorption minima of ethylene and ethane on these three model systems were determined by ground-state geometry optimizations. All given relative energies include zero-point vibrational energies (ZPVEs) from vibrational analysis.
The reactions pathways of the ethylene hydrogenation were determined using the chain-of-states method implemented in the woelfling module of TURBOMOLE[110]. The found transition state structures were then further optimized with the eigenvalue following trust-region image minimization (TRIM)[111] algorithm and finally validated by intrinsic reaction coordinate (IRC)[112] calculations. Gibbs free reaction enthalpies and free activation enthalpies were determined within the harmonic oscillator and rigid rotor approximation under reaction conditions of 433.15 K and 0.5 MPa using a scaling factor of 1.0190 appropriate for the TPSS functional[113]. In general, favorable energy differences like adsorption energies are given with a negative sign, while energy barriers like activation barriers have a positive sign.
To obtain an in-depth insight into the reaction mechanisms, we investigated the details of electronic structure using intrinsic bond orbitals (IBOs)[114], natural population analyses (NPAs)[115] as well as electron density differences.

8.3 Results and Discussion

8.3.1 Ethylene Hydrogenation on Carbon-Supported Pd_{21}

To evaluate the reactivity of spillover hydrogen atoms in the hydrogenation of ethylene, we first studied the ethylene hydrogenation on the supported Pd_{21} cluster as a reference. As the first step of the reaction, i.e. the H_2 dissociation on the Pd nanoparticle, was already the subject of our study presented in Chapter 4, we have investigated the reaction mechanism after dissociative hydrogen adsorption (skipping step I) and for the hydrogen dissociation we only show the corresponding reaction energy and Gibbs free reaction enthalpy. Consequently, we have chosen,

as a starting point for the reaction pathway optimization, a carbon-supported Pd_{21} cluster with two hydrogen atoms adsorbed at the fcc sites and ethylene in the gas phase (cmp. Figure 8.3a). As end point a geometry of carbon-supported Pd_{21} with the ethane molecule in the gas phase was given (cmp. Figure 8.3b). Between these two points the reaction pathway was optimized without predetermining any intermediate.

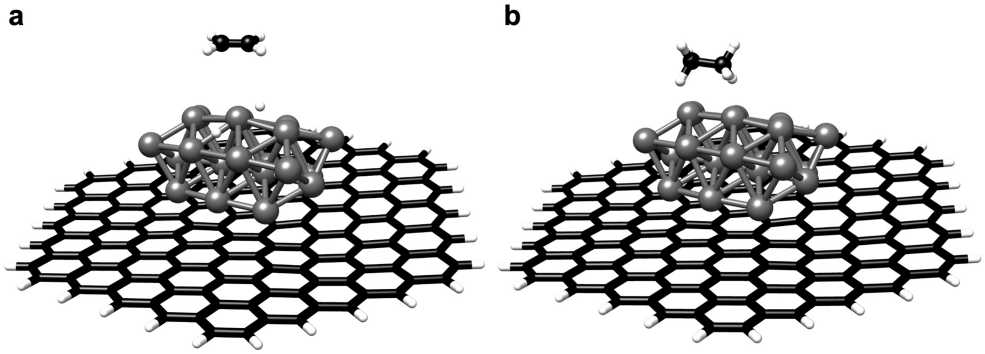

Figure 8.3: Geometries of the starting and end point of our reaction pathway optimization: (a) carbon-supported Pd_{21} with two H adsorbed at fcc sites + ethylene in the gas phase; (b) carbon-supported Pd_{21} + ethane in the gas phase.

Figure 8.4 shows the obtained reaction pathway of ethylene hydrogenation on carbon-supported Pd_{21} in detail. Table 8.1 summarizes the corresponding energy and Gibbs free enthalpy differences. For the steps I and II the reaction energies and Gibbs free reaction enthalpies are calculated on the basis of separated reactants (carbon-supported Pd_{21} + H_2 in the gas phase; carbon-supported Pd_{21} + ethylene in the gas phase). The calculated reaction energy and Gibbs free reaction enthalpy for step IV is based on separated products (carbon-supported Pd_{21} + ethane in the gas phase).

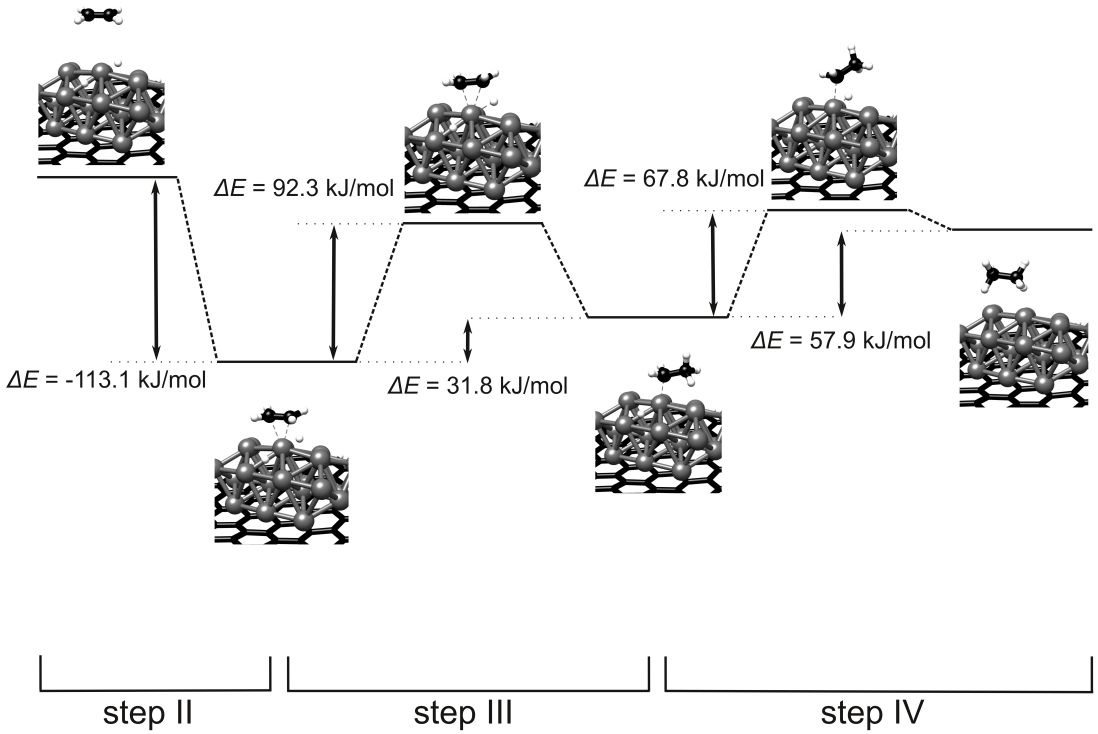

Figure 8.4: Sketch of a possible reaction pathway for ethylene hydrogenation on carbon-supported Pd_{21}. The dissociative hydrogen adsorption (step I) is not shown.

step	ΔE_{react}/kJ mol^{-1}	ΔG_{react}/kJ mol^{-1}	ΔE_{act}/kJ mol^{-1}	ΔG_{act}/kJ mol^{-1}
I	-111.1	-80.1	/	/
II	-113.1	-59.2	/	/
III	31.8	44.0	92.3	166.7
IV	57.9	2.6	67.8	58.7
II-IV	-23.4	-12.5	/	/

Table 8.1: Energy and Gibbs free enthalpy differences for ethylene hydrogenation on carbon-supported Pd_{21}.

After the dissociative hydrogen adsorption (step I) the found reaction mechanism consists of the following steps:

II. Ethylene adsorption

The ethylene molecule adsorbs at the central top Pd atom of the Pd_{21} cluster, which releases an energy of 113.1 kJ mol $^{-1}$. To obtain an in-depth insight into the interaction of ethylene with Pd_{21}, we calculated the electron density

difference, which is plotted in Figure 8.5. As a comparison, Figure 8.6 shows the binding IBOs and the electron density difference for the interaction of ethylene with one palladium atom.

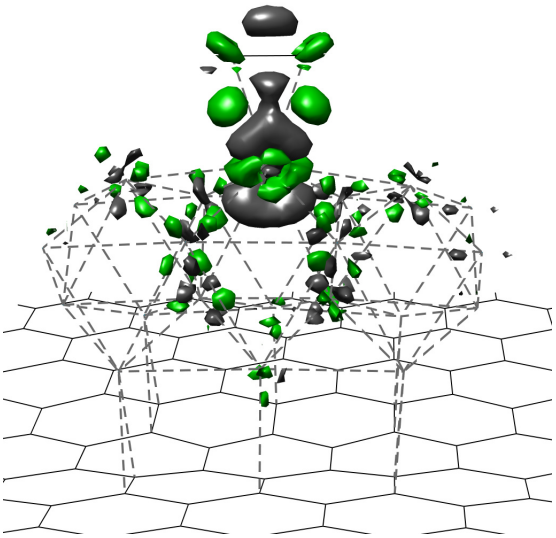

Figure 8.5: Electron density difference plot for the ethylene adsorption on carbon-supported Pd_{21}. Density gain is colored in green; density loss is colored in grey.

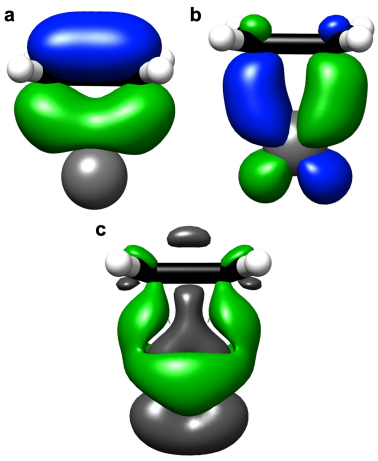

Figure 8.6: Visualization of the bonding IBOs and the electron density difference for the ethylene-Pd system: (a) π-5s IBO; (b) π^*-4d_{xz} IBO; (c) electron density difference (density gain is colored in green; density loss is in grey).

The IBOs in Figure 8.6a and b reveal that the interaction of ethylene with a Pd atom consists of the interaction of the empty Pd 5s with the occupied

ethylene π orbital and the interaction of the occupied Pd $4d_{xz}$ orbital with the empty ethylene π^* orbital (assuming a coordinate system with the x-axis parallel to the ethylene double bond and the z-axis parallel to the line from the Pd atom to the ethylene double bond center). In accordance with this, the electron density difference in Figure 8.6c shows a density loss for the Pd $4d_{xz}$ and the ethylene π orbital as well as a density gain for the Pd 5s and the ethylene π^* orbital. Furthermore, repulsive interactions of occupied orbitals can be expected, especially between the occupied Pd $4d_{z^2}$ and the occupied ethylene π orbital.

The electron density difference for the ethylene-Pd_{21} system is very similar to the electron density difference plot for the ethylene adsorption on a single Pd atom. Also here, an electron density loss for the Pd $4d_{xz}$ and the ethylene π orbital as well as a density gain for the Pd 5s and the ethylene π^* orbital can be observed. However, in this system the Pd $4d_{z^2}$ - ethylene π repulsion is reduced by a depopulation of the Pd $4d_{z^2}$ orbital and electron density is shifted to some neighboring Pd atoms.

In general, the adsorption of ethylene on carbon-supported Pd_{21} is alike the one of H_2 shown in Chapter 4 and is in agreement with the Dewar-Chatt-Duncanson model for π-complexes between alkenes and metals[116,117], which describes the alkene-metal interaction as a combination of σ-bonding and π-backbonding. As proposed in the Dewar-Chatt-Duncanson model, also in the ethylene-Pd_{21} system the hybridization of the ethylene carbon atoms is slightly changed from sp^2 to sp^3, accompanied by a light bending of the hydrogen atoms away from the Pd, and the C=C bond is elongated (1.40 Å compared to 1.34 Å for gas-phase ethylene).

III. Hydrogen atom transfer 1

One hydrogen atom migrates from the fcc position to the ethylene molecule, surpasses an activation energy barrier of 92.3 kJ mol^{-1} and binds to one of the

ethylene carbon atoms. The other ethylene carbon atom builds a σ-bond to the central top Pd atom of Pd_{21}.

IV. Hydrogen atom transfer 2

The second adsorbed hydrogen atom migrates to the ethylene molecule, surpasses an activation energy barrier of 67.8 kJ mol $^{-1}$ and binds to the second ethylene carbon atom. The product ethane desorbs.

In general, the observed mechanism is in accordance with the Horiuti-Polanyi mechanism. It is important to note that the activation energy and the Gibbs free activation enthalpy of the hydrogen atom transfer 1 are relatively high. However, in experiments the Pd cluster is usually saturated with hydrogen atoms. Thus, hydrogen atoms are not only located in the most stable fcc positions but also in less favorable triangle sites or are even less strongly bound to only two Pd atoms (bridge site) (cmp. Chapter 7). This will significantly reduce the activation energy and the Gibbs free activation enthalpy of the hydrogen atom transfer.
Furthermore, a high hydrogen coverage will turn the endergonic reaction of step III + step IV (positive Gibbs free reaction enthalpy of 46.7 kJ mol^{-1}) to an exergonic process, as in the chemical equilibrium of a high hydrogen coverage, ΔG of the hydrogen dissociation (negative Gibbs free reaction enthalpy of -80.1 kJ mol^{-1}) should be zero.

8.3.2 Ethylene Hydrogenation with Spillover Hydrogen

As a comparison to the ethylene hydrogenation on the Pd nanoparticles, Figure 8.7 shows the detailed mechanism of a possible reaction pathway for ethylene hydrogenation with two neighboring spillover hydrogen atoms on the pure graphene support material. The corresponding energy and Gibbs free enthalpy differences are listed in Table 8.2. Step 0 corresponds to the formation of two neighboring spillover hydrogen atoms on the support material, which would consist of multiple

steps in the experimental catalyst systems (dissociative hydrogen adsorption on the Pd nanoparticle, hydrogen spillover, hydrogen atom diffusion). For the steps 0 and I the reaction energies and Gibbs free reaction enthalpies are calculated based on separated reactants (graphene support material + H_2 in the gas phase; two neighboring spillover hydrogen atoms on the graphene support material + ethylene in the gas phase). For step II the reaction energy and Gibbs free reaction enthalpy is calculated on the basis of separated products (graphene support material + ethane in the gas phase).

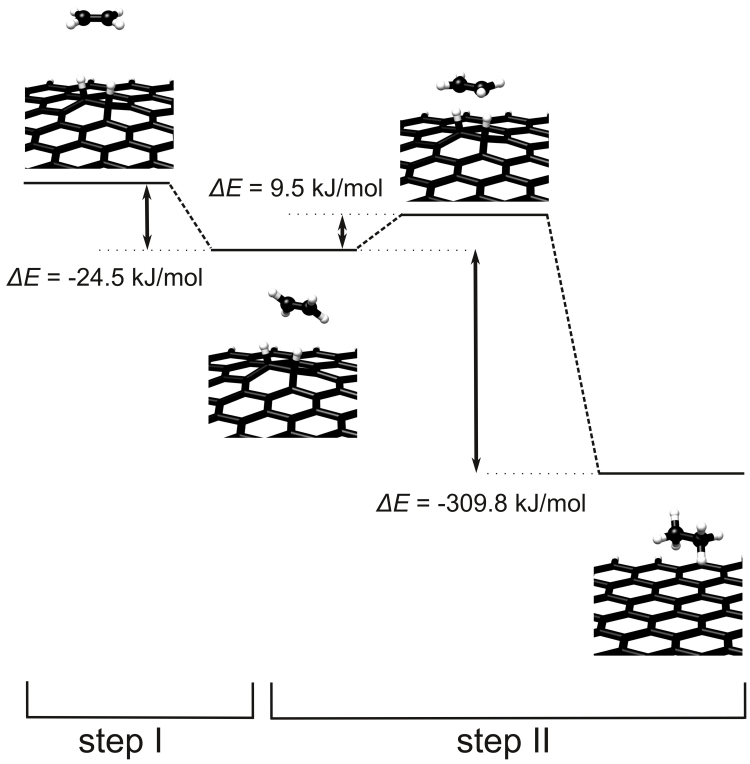

Figure 8.7: Sketch of a possible reaction pathway for ethylene hydrogenation with spillover hydrogen on the pure graphene support material.

step	$\Delta E_{\mathrm{react}}$/kJ mol^{-1}	$\Delta G_{\mathrm{react}}$/kJ mol^{-1}	ΔE_{act}/kJ mol^{-1}	ΔG_{act}/kJ mol^{-1}
0	199.8	243.8	/	/
I	-24.5	21.1	/	/
II	-309.8	-357.5	9.5	31.0
I+II	-334.3	-336.4	/	/

Table 8.2: Energy and Gibbs free enthalpy differences for ethylene hydrogenation with spillover hydrogen on the pure graphene support material.

The obtained reaction mechanism with spillover hydrogen consists of two steps:

I. Ethylene adsorption

The ethylene molecule adsorbs at the two spillover hydrogen atoms in a parallel fashion, which releases an energy of 24.5 kJ mol^{-1}. The interaction of ethylene with spillover hydrogen is much weaker than the interaction of ethylene with Pd. The corresponding electron density difference plot in Figure 8.8 and the results of the NPA and IBO analyses reveal that this weak interaction is purely based on van der Waals forces: for the spillover hydrogen atoms the H s orbitals are depopulated and the C-H bonds are polarized, leading to a slightly higher positive partial charge at the spillover hydrogen atoms; in the ethylene molecule the π orbital is depopulated and the two lower C-H bonds are polarized, which causes a slightly higher positive partial charge at two ethylene H atoms and a slightly higher negative partial charge at the ethylene carbon atoms. No bonding orbitals between ethylene and spillover hydrogen can be found.

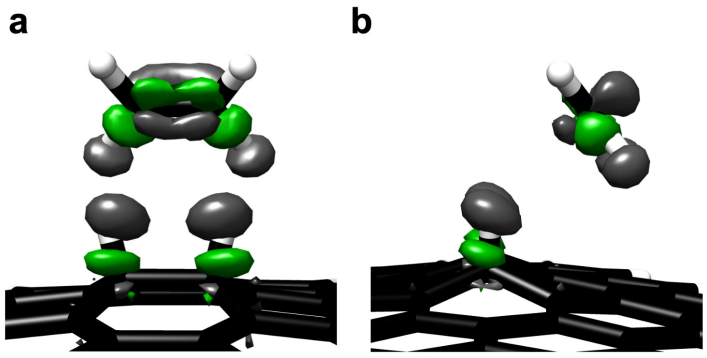

Figure 8.8: Electron density difference plot for the ethylene adsorption on spillover hydrogen from two different perspectives: (a) front view; (b) side view. Density gain is colored in green; density loss is colored in grey.

II. Concerted transfer of two hydrogen atoms

The two spillover hydrogen atoms are transfered simultaneously to the ethylene molecule in a concerted fashion. This step needs an activation energy of only 9.5 kJ mol^{-1}. Subsequently, the formed ethane molecule is desorbed.

Table 8.3 shows the energy and Gibbs free enthalpy differences for the equivalent reaction pathway with two spillover hydrogen atoms located next to a graphitic nitrogen atom.

step	$\Delta E_{\mathrm{react}}$/kJ mol^{-1}	$\Delta G_{\mathrm{react}}$/kJ mol^{-1}	ΔE_{act}/kJ mol^{-1}	ΔG_{act}/kJ mol^{-1}
0	145.7	189.8	/	/
I	-25.1	23.8	/	/
II	-255.2	-306.1	32.2	49.6
I+II	-280.3	-282.4	/	/

Table 8.3: Energy and Gibbs free enthalpy differences for ethylene hydrogenation with spillover hydrogen next to a graphitic N atom.

At the chosen reaction conditions of 433.15 K and 0.5 MPa both the nitrogen-free and the graphitic nitrogen doped system show a positive Gibbs free reaction enthalpy for the ethylene adsorption on spillover hydrogen (step I; 21.1 kJ mol^{-1} and 23.3 kJ mol^{-1}). Due to the weak electronic interaction of ethylene with the spillover hydrogen atoms, the favorable adsorption energy is quite small and does not compensate for the positive entropic contribution, originating in the decrease of the number of sub-systems from two (graphene support with two spillover hydrogen atoms + ethylene in the gas phase) to one (ethylene adsorbed at the spillover hydrogen atoms). This result suggests that the experimental ethylene hydrogenation with spillover hydrogen should proceed in a single step, in which the two spillover hydrogen atoms are transfered to the ethylene molecule in a concerted fashion (step II). For this one-step process the Gibbs free activation enthalpy is 52.1 kJ mol^{-1} for the nitrogen-free system and 73.3 kJ mol^{-1} for the graphitic nitrogen doped system. Moreover, for the reaction starting from the adsorbed spillover hydrogen atoms, the total Gibbs free reaction enthalpy is highly exergonic for both systems (steps I+II; -336.4 kJ mol^{-1} for the N-free and -282.4 kJ mol^{-1} for the graphitic N doped system). Based on these values, one would expect that experimental ethylene hydrogenation with spillover hydrogen should be possible, which is contradictory to the conclusions of Yang et al.[37], proposing that spillover

hydrogen atoms are not accessible for hydrogenation reactions while located on the carbon support material.

8.4 Conclusions

The aim of this study was to compare the reactivity of hydrogen atoms adsorbed on Pd nanoparticles to the reactivity of spillover hydrogen atoms. For this purpose, we performed a case study on ethylene hydrogenation on carbon-supported Pd catalysts.

The ethylene hydrogenation on the supported Pd nanoparticles follows the Horiuti-Polanyi mechanism: I) dissociative hydrogen adsorption; II) ethylene adsorption; III) hydrogen atom transfer 1; IV) hydrogen atom transfer 2. The ethylene adsorption on the Pd nanoparticles is based on a relatively strong interaction of ethylene with one Pd atom, which consists of an ethylene π - Pd 5s and an ethylene π^* - Pd $4d_{xz}$ charge transfer. Even though we find a relatively high first Gibbs free activation enthalpy and a positive Gibbs free reaction enthalpy for the reaction step III + step IV, experimental ethylene hydrogenation on carbon-supported Pd_{21} should occur as the expected high hydrogen coverage on the cluster will significantly decrease the Gibbs free activation enthalpy and will turn the reaction steps III and IV into an exergonic process.

The found reaction mechanism for ethylene hydrogenation with spillover hydrogen atoms is significantly different. At the chosen reaction conditions the adsorption of ethylene on two neighboring spillover hydrogen atoms is an endergonic process. As a consequence, the experimental ethylene hydrogenation with spillover hydrogen should proceed in only one step: the concerted transfer of the two spillover hydrogen atoms to the ethylene molecule. Our results for both the nitrogen-free and the graphitic nitrogen doped hydrogen spillover system suggest that the ethylene hydrogenation with spillover hydrogen atoms should actually be possible

in experiments. This finding disagrees with the study of Yang et al., in which it is proposed that spillover hydrogen atoms are stored on the support material in a chemically inactive state and, as a consequence, are not directly accessible for hydrogenations.

However, the outcome of this case study should be regarded as a preliminary result that has to be further validated in future studies. On the one hand, the chosen model systems with only two adsorbed hydrogen atoms are relatively far from experimental catalysts, for which a high hydrogen coverage on the Pd cluster as well as on the support material can be expected. Thus, the reaction pathway studies should be repeated utilizing model systems with a higher hydrogen loading. This will, particularly for the Pd_{21} model system, require an extensive and relatively costly subsequent computational study. On the other hand, the conclusions of Yang et al. were based on an experimental study of nitrobenzene hydrogenation and did not include any results for alkene hydrogenation. Accordingly, an experimental study of the ethylene hydrogenation on Pd/CMC and Pd/NMC should also be performed to allow our results to be qualitatively compared to experimental systems.

Moreover, we have previously shown that the nitrogen doping of the carbon support material can significantly affect the catalyzed hydrogenation reactions (cmp. Chapter 6). Consequently, the influence of nitrogen doping on the Horiuti-Polanyi mechanism of the ethylene hydrogenation on the Pd nanoparticles should also be investigated in future computational studies.

9 Summary and Outlook

In the project presented in the previous chapters, my collaborators and I have studied several aspects of heterogeneous catalyzed hydrogenation reactions on carbon-supported palladium nanoparticles.

As a first step, I have investigated the metal-support interactions in Pd/CMC and studied the dissociative hydrogen adsorption on these catalyst systems. I found that palladium clusters show quite strong attractive interactions with the support material that are directed and partially covalent. The hydrogen dissociation on Pd nanoparticles consists of two steps: 1) barrierless H_2 physisorption; 2) dissociative chemisorption with a very small activation barrier. At room temperature, the H_2 dissociation should occur spontaneously both on free and on carbon-supported palladium clusters. Moreover, both systems can adsorb and dissociate several hydrogen molecules. The carbon support material does not change the mechanism of the H_2 dissociation but has some effect on the activation and reaction energies. Compared to free Pd clusters, it facilitates the dissociation of several hydrogen molecules as the support material stabilizes geometrical deformations of the Pd clusters.

Furthermore, the study demonstrated that special properties of carbon-supported Pd nanoparticles can only be studied when larger cluster sizes like Pd_{21} are also taken into account. Larger clusters possess several different possible H_2 adsorption sites and allow for various hydrogen atom configurations. The carbon support material equalizes the adsorption and dissociation energies at different sites on the clusters and, therefore, enables the hydrogen adsorption and dissociation at various positions. The migration of hydrogen atoms between different positions on the clusters was found to possess only very small activation barriers both on free and on carbon-supported palladium clusters. Based on these results, it can

be expected that in experiments a high hydrogen coverage as well as a relatively free migration of hydrogen atoms on the carbon-supported nanoparticles should be present.
In general, this study was the starting point for all our subsequent investigations as the unmodified carbon support was the reference for studying the effects of nitrogen doping. Besides the basic insights into metal-support interactions in Pd/CMC, an important achievement of this study was the computational setup I have built. The chosen model systems, especially the larger Pd_{21} system, have been shown to be reasonable. On top of that, I found out which setting of the DFT calculations has to be chosen in order to achieve accurate and reliable results.

In the paper 'Anchoring of palladium nanoparticles on N-doped mesoporous carbon', I have studied, together with my collaborators, the Pd/NMC system and determined the composition of different nitrogen species in the NMC support material. With the help of N 1s binding energies taken from DOS calculations the peaks of experimental N 1s XP spectra of NMC could be assigned to pyridinic, pyrrolic, graphitic and N-O-like nitrogen species.
Furthermore, the performed DFT calculations provided an in-depth insight into the effect of nitrogen doping on the relevant metal-support interactions. All considered nitrogen functional groups (pyridinic, pyrrolic and graphitic N) increase the adsorption energy of the Pd clusters on the support material. For pyrrolic and graphitic nitrogen species this is, in the first place, an effect of covalent and electrostatic character. Pyridinic nitrogen doped carbon materials show particularly strong interactions with Pd as, in such materials, a charge transfer between two pyridinic nitrogens and one Pd atom of the supported nanoparticle can be observed. Based on these findings and based on a comparison of the experimental N 1s XP spectrum of pure NMC to the one of Pd decorated NMC, it could be concluded that pyridinic nitrogen atoms are the preferential adsorption sites for

Pd nanoparticles on NMC.

Moreover, the interaction of a Pd nanoparticle with two pyridinic nitrogen atoms results in a change of the Pd oxidation state. As a consequence, the supported Pd nanoparticles become bifunctional, containing both Pd^0 and Pd^{2+} active centers, which is also manifested in an additional XP Pd 3d peak for Pd/NMC compared to Pd/CMC.

In a subsequent study, it was found that this bifunctionality of the Pd nanoparticles in Pd/NMC can significantly affect catalyzed hydrogenation reactions. My experimental collaborators studied the conversion of 5-hydroxymethylfurfural (HMF) to 2,5-dimethylfuran (DMF) on Pd/CMC and Pd/NMC. For the Pd/NMC system, a remarkable HMF conversion of more than 99.9 % and a DMF yield of more than 97 % could be obtained after two hours by adding, on top of H_2, formic acid to the reaction. The experimental results showed that the conversion of HMF to DMF can proceed via two different pathways, which differ in the order of the hydrogenolysis of the hydroxymethyl group and the hydrogenation of the aldehyde group (cmp. Figure 9.1).

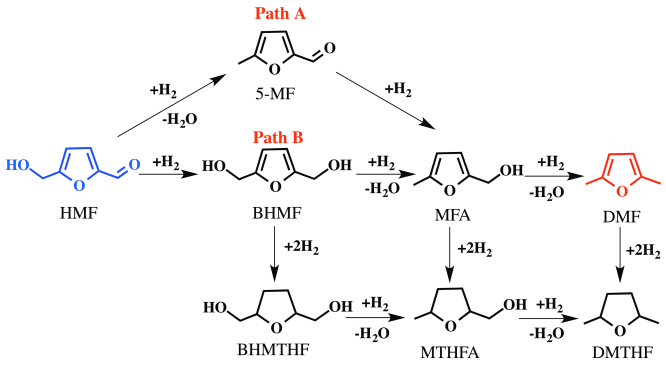

Figure 9.1: Sketch of the reaction network for the hydrogenolysis of HMF to DMF; reproduced from the manuscript in Chapter 6.

Formic acid shifts the reaction pathway to path A as it forms a protonated intermediate and thus lowers the activation barrier of the C-OH bond cleavage.

In general, the conversion of HMF to DMF on Pd/NMC using formic acid and H_2

is a complex multi-step process. Both the Pd^0 and Pd^{2+} centers of the bifunctional Pd/NMC are needed at different steps of the reaction to allow for a highly effective and selective conversion and to avoid the formation of undesired byproducts as ring-hydrogenated species (cmp. Figure 9.2). My DFT calculations revealed that the Pd^{2+} centers of the supported Pd nanoparticles (stabilized by pyridinic nitrogen atoms) enhance the formic acid dissociation to the formate anion and H^+ as well as stabilize H^- species formed by heterolytic H_2 dissociation. This jointly improves the hydrogenolysis of the C-OH bond.

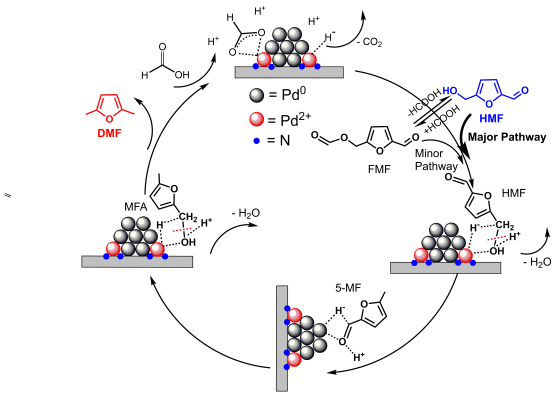

Figure 9.2: Proposed reaction mechanism for the conversion of HMF to DMF over Pd/NMC utilizing H_2 and formic acid; reproduced from the manuscript in Chapter 6.

As I observed in a comprehensive study on the hydrogen spillover process, nitrogen doping does not only influence the catalyzed reactions but also affects the hydrogen spillover from the catalyst to the carbon support material. The reason for the significantly facilitated hydrogen spillover on Pd/NMC compared to Pd/CMC are graphitic nitrogen atoms which stabilize the hydrogen spillover product due to their additional electron donated to the π-system. The calculated reaction barriers propose that hydrogen spillover on experimental Pd/NMC catalysts should actually be possible.

The formed chemisorbed spillover hydrogen atoms are positively charged and can interact with water molecules via hydrogen bonds. Due to the strong stabilizing effect of graphitic nitrogen atoms, spillover hydrogen will accumulate close to

graphitic nitrogen species. On the pure graphene support and close to pyridinic nitrogen atoms spillover hydrogen is mobile. It is important to note that, at a pure graphene support, the calculations propose a diffusion of spillover hydrogen via a physisorbed pathway, in which the spillover hydrogen atoms change from the chemisorbed to the physisorbed state.
As spillover hydrogen desorption should not be observed and spillover hydrogen atoms can easily migrate back to the Pd cluster, spillover hydrogen species should be reversibly stored on the NMC support material.

Finally, I compared the reactivity of spillover hydrogen atoms located on the carbon support material with the reactivity of hydrogen atoms adsorbed on the Pd nanoparticles. For this purpose, I performed a preliminary case study on the hydrogenation of ethylene on carbon-supported Pd nanoparticles.
As a first step, the ethylene hydrogenation on carbon-supported Pd_{21} was investigated. I found that ethylene shows a relatively strong interaction with palladium, based on an ethylene π - Pd 5s and an ethylene π^* - Pd $4d_{xz}$ charge transfer. The process of ethylene hydrogenation on Pd/CMC follows the Horiuti-Polanyi mechanism: I) dissociative hydrogen adsorption; II) ethylene adsorption; II) hydrogen atom transfer 1; IV) hydrogen atom transfer 2. Even though I found quite high activation barriers for the ethylene hydrogenation on the utilized model systems, it can be expected that experimental ethylene hydrogenation on Pd/CMC should still occur due to a high hydrogen coverage on the nanoparticles.
Secondly, I studied the ethylene hydrogenation with spillover hydrogen atoms located on the carbon support material, also considering spillover hydrogen located next to graphitic nitrogen atoms. The found reaction mechanisms significantly differ from the one for ethylene hydrogenation on carbon-supported Pd_{21}. The calculated activation and reaction enthalpies propose that ethylene hydrogenation with spillover hydrogen proceeds in only one step, in which the two spillover

hydrogen atoms are transfered to the ethylene molecule in a concerted fashion. In contrast to the findings of Yang et al.[37], which suggest that spillover hydrogen atoms are stored on the carbon support material in a chemically inactive state, the calculated free activation enthalpies indicate that ethylene hydrogenation with spillover hydrogen atoms should be possible on both CMC and NMC support materials. However, these preliminary conclusions have to be further validated as the utilized model systems with only two adsorbed hydrogen atoms are relatively far from experimental catalysts. As a result, the presented studies on ethylene hydrogenation should be repeated with model systems possessing a higher hydrogen loading on the Pd cluster as well as on the support material. The impact of nitrogen doping on the Horiuti-Polanyi mechanism should also be considered. Moreover, the quantum chemical calculations should be supported with experimental investigations on ethylene hydrogenation on Pd/NMC.

In general, the presented studies provide an in-depth insight into metal-support interactions of carbon-supported Pd nanoparticles and significantly improve the understanding of the catalyzed reactions. Our collaborative findings concerning the bifunctionality of the Pd nanoparticles in Pd/NMC should especially be of substantial interest. The investigation of the HMF conversion has impressively shown that the novel Pd/NMC is a highly active and selective catalyst, that can provide almost perfect yields and selectivity. The obtained insights into the metal-support interactions and the evidence for the catalyst's bifunctionality open up the possibility of designing promising alternative setups for many other heterogeneous catalyzed reactions.

Furthermore, our studies on the hydrogen spillover process and on the properties of spillover hydrogen will attract attention. The evidence for reversibly stored hydrogen on Pd/NMC should trigger further investigations on the application of Pd/NMC as a hydrogen storage system.

Besides the remaining questions concerning the reactivity of spillover hydrogen atoms and the influence of nitrogen doping on the Horiuti-Polanyi mechanism, there are important issues left that should be addressed in future studies.

So far, the effect of oxygen doping on the carbon-supported palladium nanoparticles and, therefore, on the catalyzed hydrogenation reactions has not been investigated as the interaction between Pd and surface oxygen was found to be weak[118] and oxygen-doped systems showed much lower catalytic activities than nitrogen-doped systems[30]. However, oxygen functional groups could still have an effect on the Pd/CMC and Pd/NMC catalyst systems and especially combinations of nitrogen- and oxygen-containing defects should be considered. Based on the insights obtained in the present project, a computational study on oxygen functional groups in the support materials should be manageable with a relatively low effort.

Furthermore, all the presented studies have been performed in the gas phase. As most of the industrial heterogeneous catalyzed reactions are performed in solution, the influence of solvents on the metal-support interactions should also be studied. However, this will require the establishment of new computational setups.

Bibliography

References

[1] Ostwald, W. *Phys. Z.* **1902**, *3*, 313.

[2] Ertl, G. *Angew. Chem., Int. Ed.* **2008**, *47*, 3524 – 3535.

[3] MarketsandMarkets, Industrial Catalyst Market by Type (Heterogeneos & Homogeneous), by Material (Metal, Chemical, Zeolites and Organometallic Materials), by Application and by Region - Global Trends and Forecasts to 2020. Available at: `https://www.marketsandmarkets.com/Market-Reports/industrial-catalyst-market-66222915.html`, 2016; Accessed: 24 September 2020.

[4] Julkapli, N. M.; Bagheri, S. *Int. J. Hydrogen Energy* **2015**, *40*, 948 – 979.

[5] Bell, A. T. *Science* **2003**, *299*, 1688 – 1691.

[6] ReportsAndData, Industrial Catalyst Market Size, Share & Analysis, By Type (Homogeneous Catalyst, Heterogeneous Catalyst, Biocatalysts), By Raw Material (Chemicals, Metals, Organometallic Material, Zeolites), By Application (Chemical Synthesis, Petroleum Refinery, Petrochemicals, Others), By End-User (Oil and Gas Industry, Chemical Industry, Automotive and Transportation Industry, Energy Industry, Manufacturing Industry, Pharmaceutical and Medical Industry, Others), And Segment Forecasts, 2017-2027. Available at: `https://www.reportsanddata.com/report-detail/industrial-catalyst-market`, 2020; Accessed: 24 September 2020.

[7] Bradley, J. S. In *Clusters and Colloids*; Schmid, G., Ed.; Wiley-VCH Verlag GmbH, 2007; pp 459 – 544.

[8] Rampino, L. D.; Nord, F. F. *J. Am. Chem. Soc.* **1941**, *63*, 2745 – 2749.

[9] Parravano, G. *J. Catal.* **1970**, *18*, 320 – 328.

[10] Haruta, M.; Kobayashi, T.; Sano, H.; Yamada, N. *Chem. Lett.* **1987**, *16*, 405 – 408.

[11] Astruc, D.; Lu, F.; Aranzaes, J. R. *Angew. Chem., Int. Ed.* **2005**, *44*, 7852 – 7872.

[12] El-Sayed, M. A. *Acc. Chem. Res.* **2001**, *34*, 257 – 264.

[13] De Jong, K. P.; Geus, J. W. *Catal. Rev.* **2000**, *42*, 481 – 510.

[14] Li, C.; Zhao, A.; Xia, W.; Liang, C.; Muhler, M. *J. Phys. Chem. C* **2012**, *116*, 20930 – 20936.

[15] Huang, Y.; Yang, F.; Xu, Z.; Shen, J. *J. Colloid Interface Sci.* **2011**, *363*, 193 – 198.

[16] Xia, W. *Catal. Sci. Technol.* **2016**, *6*, 630 – 644.

[17] Kratky, V.; Kralik, M.; Mecarova, M.; Stolcova, M.; Zalibera, L.; Hronec, M. *Appl. Catal., A* **2002**, *235*, 225 – 231.

[18] Appl, M. In *Ammonia*; Appl, M., Ed.; Wiley-VCH Verlag GmbH, 2007; pp 5 – 8.

[19] Ludwig, W.; Savara, A.; Dostert, K.-H.; Schauermann, S. *J. Catal.* **2011**, *284*, 148 – 156.

[20] Conner, W. C.; Falconer, J. L. *Chem. Rev.* **1995**, *95*, 759 – 788.

[21] Prins, R. *Chem. Rev.* **2012**, *112*, 2714 – 2738.

[22] Li, H.; Li, L.; Li, Y. *Nanotechnol. Rev.* **2013**, *2(5)*, 515 – 528.

[23] Greeley, J.; K Nørskov, J.; Mavrikakis, M. *Annu. Rev. Phys. Chem.* **2002**, *53*, 319 – 348.

[24] Lenz Baldez, R. N.; Piquini, P.; Schmidt, A. A.; Kuroda, M. A. *Phys. Chem. Chem. Phys.* **2017**, *19*, 22153 – 22160.

[25] Rangel, E.; Sansores, E.; Vallejo, E.; Hernández-Hernández, A.; López-Pérez, P. A. *Phys. Chem. Chem. Phys.* **2016**, *18*, 33158 – 33170.

[26] Ramos-Castillo, C. M.; Reveles, J. U.; Zope, R. R.; de Coss, R. *J. Phys. Chem. C* **2015**, *119*, 8402 – 8409.

[27] Wei, Q.; Tong, X.; Zhang, G.; Qiao, J.; Gong, Q.; Sun, S. *Catalysts* **2015**, *5*, 1574 – 1602.

[28] Shi, G.; Zhao, Y.; Huang, Y.; Shen, J. *Chin. J. Catal.* **2010**, *31*, 961 – 964.

[29] Chen, H.; Dai, L.; Xie, J.; Bai, Z.; Jia, M.; Shen, J. *Chin. J. Catal.* **2011**, *32*, 1771 – 1781.

[30] Chen, P.; Chew, L. M.; Kostka, A.; Muhler, M.; Xia, W. *Catal. Sci. Technol.* **2013**, *3*, 1964 – 1971.

[31] Schneider, W. B.; Benedikt, U.; Auer, A. A. *ChemPhysChem* **2013**, *14*, 2984 – 2989.

[32] Lischka, M.; Groß, A. *Phys. Rev. B* **2002**, *65*, 075420.

[33] Shamsiev, R. S.; Danilov, F. O. *Russ. Chem. Bull.* **2017**, *66*, 395 – 400.

[34] Granja-DelRío, A.; Alonso, J. A.; López, M. J. *Comput. Theor. Chem.* **2017**, *1107*, 23 – 29.

[35] Rangel, E.; Sansores, E. *Int. J. Hydrogen Energy* **2014**, *39*, 6558 – 6566.

[36] Bulushev, D. A.; Zacharska, M.; Shlyakhova, E. V.; Chuvilin, A. L.; Guo, Y.; Beloshapkin, S.; Okotrub, A. V.; Bulusheva, L. G. *ACS Catal.* **2016**, *6*, 681 – 691.

[37] Yang, F.; Hu, B.; Xia, W.; Peng, B.; Shen, J.; Muhler, M. *J. Catal.* **2018**, *365*, 55 – 62.

[38] Adams, B. D.; Chen, A. *Mater. Today* **2011**, *14*, 282 – 289.

[39] Psofogiannakis, G. M.; Froudakis, G. E. *J. Phys. Chem. C* **2009**, *113*, 14908 – 14915.

[40] Juarez-Mosqueda, R.; Mavrandonakis, A.; Kuc, A. B.; Pettersson, L. G. M.; Heine, T. *Front. Chem.* **2015**, *3*, 2.

[41] Blanco-Rey, M.; Juaristi, J. I.; Alducin, M.; López, M. J.; Alonso, J. A. *J. Phys. Chem. C* **2016**, *120*, 17357 – 17364.

[42] Deák, P. *Phys. Status Solidi B* **2000**, *217*, 9 – 21.

[43] Makov, G.; Payne, M. C. *Phys. Rev. B* **1995**, *51*, 4014 – 4022.

[44] Petrantoni, M.; Hemeryck, A.; Ducéré, J.-M.; Estève, A.; Rossi, C.; Djafari Rouhani, M.; Estève, D.; Landa, G. *J. Phys. Chem. Solids* **2010**, *71*, 130 – 133.

[45] Posada-Pérez, S.; Viñes, F.; Ramirez, P. J.; Vidal, A. B.; Rodriguez, J. A.; Illas, F. *Phys. Chem. Chem. Phys.* **2014**, *16*, 14912 – 14921.

[46] Quesne, M. G.; Silveri, F.; de Leeuw, N. H.; Catlow, C. R. A. *Front. Chem.* **2019**, *7*, 182.

[47] Yu, L.; Ruzsinszky, A.; Yan, Q. *J. Phys. Chem. Lett.* **2019**, *10*, 7311 – 7317.

[48] Tonner, R.; Rosenow, P.; Jakob, P. *Phys. Chem. Chem. Phys.* **2016**, *18*, 6316 – 6328.

[49] Sholl, D. S.; Steckel, J. A. *Density Functional Theory*; John Wiley & Sons, Ltd, 2009; Chapter 4, pp 83 – 112.

[50] Kratzer, P.; Neugebauer, J. *Front. Chem.* **2019**, *7*, 106.

[51] Sun, W.; Ceder, G. *Surf. Sci.* **2013**, *617*, 53 – 59.

[52] Hinuma, Y.; Kumagai, Y.; Oba, F.; Tanaka, I. *Comput. Mater. Sci.* **2016**, *113*, 221 – 230.

[53] Deák, P.; Giber, J. *Phys. Lett. A* **1982**, *88*, 237 – 240.

[54] Bredow, T.; Evarestov, R. A.; Jug, K. *Phys. Status Solidi B* **2000**, *222*, 495 – 516.

[55] Bredow, T.; Geudtner, G.; Jug, K. *J. Comput. Chem.* **2001**, *22*, 89 – 101.

[56] Peintinger, M. F.; Bredow, T. *J. Comput. Chem.* **2014**, *35*, 839 – 846.

[57] Bennett, A. J.; McCaroll, B.; Messmer, R. P. *Phys. Rev. B* **1971**, *3*, 1397.

[58] Zunger, A. *J. Phys. C: Solid State Phys.* **1974**, *7*, 96 – 106.

[59] Staemmler, V. In *Theoretical Aspects of Transition Metal Catalysis*; Frenking, G., Ed.; Topics in Organometallic Chemistry; Springer, 2005; pp 219 – 256.

[60] Sauer, J.; Ugliengo, P.; Garrone, E.; Saunders, V. R. *Chem. Rev.* **1994**, *94*, 2095 – 2160.

[61] Whitten, J. L.; Yang, H. *Surf. Sci. Rep.* **1996**, *24*, 55 – 124.

[62] Burow, A. M.; Sierka, M.; Döbler, J.; Sauer, J. *J. Chem. Phys.* **2009**, *130*, 174710.

[63] Nava, P.; Sierka, M.; Ahlrichs, R. *Phys. Chem. Chem. Phys.* **2003**, *5*, 3372 – 3381.

[64] Sinanoğlu, O.; Tuan, D. F. *J. Chem. Phys.* **1963**, *38*, 1740 – 1748.

[65] Weigend, F.; Ahlrichs, R. *Phys. Chem. Chem. Phys.* **2005**, *7*, 3297 – 3305.

[66] Tao, J.; Perdew, J. P.; Staroverov, V. N.; Scuseria, G. E. *Phys. Rev. Lett.* **2003**, *91*, 146401.

[67] TURBOMOLE V7.1 2016, V7.2.1 2017 and V7.3 2018, a development of University of Karlsruhe and Forschungszentrum Karlsruhe GmbH, 1989-2007, TURBOMOLE GmbH, since 2007; available from `http://www.turbomole.com`.

[68] Raghavachari, K.; Trucks, G. W.; Pople, J. A.; Head-Gordon, M. *Chem. Phys. Lett.* **1989**, *157*, 479 – 483.

[69] Helgaker, T.; Coriani, S.; Jørgensen, P.; Kristensen, K.; Olsen, J.; Ruud, K. *Chem. Rev.* **2012**, *112*, 543 – 631.

[70] Szalay, P. G.; Müller, T.; Gidofalvi, G.; Lischka, H.; Shepard, R. *Chem. Rev.* **2012**, *112*, 108 – 181.

[71] Chan, G. K.-L.; Head-Gordon, M. *J. Chem. Phys.* **2002**, *116*, 4462 – 4476.

[72] Bredow, T.; Jug, K. *Theor. Chem. Acc.* **2005**, *113*, 1 – 14.

[73] Ahlswede, B.; Jug, K. *J. Comput. Chem.* **1999**, *20*, 563 – 571.

[74] Porezag, D.; Frauenheim, T.; Köhler, T.; Seifert, G.; Kaschner, R. *Phys. Rev. B* **1995**, *51*, 12947 – 12957.

[75] Grimme, S.; Bannwarth, C.; Shushkov, P. *J. Chem. Theory Comput.* **2017**, *13*, 1989 – 2009.

[76] Bannwarth, C.; Ehlert, S.; Grimme, S. *J. Chem. Theory Comput.* **2019**, *15*, 1652 – 1671.

[77] Cramer, C. J.; Truhlar, D. G. *Phys. Chem. Chem. Phys.* **2009**, *11*, 10757 – 10816.

[78] Yu, H. S.; Li, S. L.; Truhlar, D. G. *J. Chem. Phys.* **2016**, *145*, 130901.

[79] Becke, A. D. *J. Chem. Phys.* **2013**, *138*, 074109.

[80] Stephens, P. J.; Devlin, F. J.; Chabalowski, C. F.; Frisch, M. J. *J. Phys. Chem.* **1994**, *98*, 11623 – 11627.

[81] Becke, A. D. *J. Chem. Phys.* **2014**, *140*, 18A301.

[82] Furche, F.; Perdew, J. P. *J. Chem. Phys.* **2006**, *124*, 044103.

[83] Zhao, Y.; Truhlar, D. G. *J. Chem. Phys.* **2006**, *124*, 224105.

[84] Staroverov, V. N.; Scuseria, G. E.; Tao, J.; Perdew, J. P. *J. Chem. Phys.* **2003**, *119*, 12129 – 12137.

[85] Wang, N. X.; Wilson, A. K. *J. Chem. Phys.* **2004**, *121*, 7632 – 7646.

[86] Wang, N. X.; Wilson, A. K. *Mol. Phys.* **2005**, *103*, 345 – 358.

[87] Andrae, D.; Häußermann, U.; Dolg, M.; Stoll, H.; Preuß, H. *Theor. Chim. Acta* **1990**, *77*, 123 – 141.

[88] Russo, T. V.; Martin, R. L.; Hay, P. J. *J. Phys. Chem.* **1995**, *99*, 17085 – 17087.

[89] Jensen, F. *Wiley Interdiscip. Rev.: Comput. Mol. Sci.* **2013**, *3*, 273 – 295.

[90] Jurečka, P.; Černý, J.; Hobza, P.; Salahub, D. R. *J. Comput. Chem.* **2007**, *28*, 555 – 569.

[91] Goerigk, L.; Grimme, S. *Phys. Chem. Chem. Phys.* **2011**, *13*, 6670 – 6688.

[92] Bühl, M.; Reimann, C.; Pantazis, D. A.; Bredow, T.; Neese, F. *J. Chem. Theory Comput.* **2008**, *4*, 1449 – 1459.

[93] Klimeš, J.; Michaelides, A. *J. Chem. Phys.* **2012**, *137*, 120901.

[94] Berland, K.; Cooper, V. R.; Lee, K.; Schröder, E.; Thonhauser, T.; Hyldgaard, P.; Lundqvist, B. I. *Rep. Prog. Phys.* **2015**, *78*, 066501.

[95] Grimme, S.; Antony, J.; Ehrlich, S.; Krieg, H. *J. Chem. Phys.* **2010**, *132*, 154104.

[96] Grimme, S. *Chem. - Eur. J.* **2012**, *18*, 9955 – 9964.

[97] Rabuck, A. D.; Scuseria, G. E. *J. Chem. Phys.* **1999**, *110*, 695 – 700.

[98] Eichkorn, K.; Weigend, F.; Treutler, O.; Ahlrichs, R. *Theor. Chem. Acc.* **1997**, *97*, 119 – 124.

[99] Sierka, M.; Hogekamp, A.; Ahlrichs, R. *J. Chem. Phys.* **2003**, *118*, 9136 – 9148.

[100] Császár, P.; Pulay, P. *J. Mol. Struct.* **1984**, *114*, 31 – 34.

[101] Treutler, O.; Ahlrichs, R. *J. Chem. Phys.* **1995**, *102*, 346 – 354.

[102] Banerjee, J.; Behnle, S.; Galbraith, M. C. E.; Settels, V.; Engels, B.; Tonner, R.; Fink, R. F. *J. Comput. Chem.* **2018**, *39*, 844 – 852.

[103] Warczinski, L.; Hättig, C. *Phys. Chem. Chem. Phys.* **2019**, *21*, 21577 – 21587.

[104] Warczinski, L.; Hättig, C. *Phys. Chem. Chem. Phys.* **2020**, *22*, 8233 – 8234.

[105] Warczinski, L.; Hu, B.; Eckhard, T.; Peng, B.; Muhler, M.; Hättig, C. *Phys. Chem. Chem. Phys.* **2020**, *22*, 21317 – 21325.

[106] Sabatier, P. *La catalyse en chimie organique*; Encyclopédie de science chimique appliquée; Librairie polytechnique: Paris et Liége, 1913.

[107] Mattson, B.; Foster, W.; Greimann, J.; Hoette, T.; Le, N.; Mirich, A.; Wankum, S.; Cabri, A.; Reichenbacher, C.; Schwanke, E. *J. Chem. Educ.* **2013**, *90*, 613 – 619.

[108] Horiuti, I.; Polanyi, M. *Trans. Faraday Soc.* **1934**, *30*, 1164 – 1172.

[109] Weigend, F. *Phys. Chem. Chem. Phys.* **2006**, *8*, 1057 – 1065.

[110] Plessow, P. *J. Chem. Theory Comput.* **2013**, *9*, 1305 – 1310.

[111] Helgaker, T. *Chem. Phys. Lett.* **1991**, *182*, 503 – 510.

[112] Fukui, K. *Acc. Chem. Res.* **1981**, *14*, 363 – 368.

[113] Kesharwani, M. K.; Brauer, B.; Martin, J. M. L. *J. Phys. Chem. A* **2015**, *119*, 1701 – 1714.

[114] Knizia, G. *J. Chem. Theory Comput.* **2013**, *9*, 4834 – 4843.

[115] Reed, A. E.; Weinstock, R. B.; Weinhold, F. *J. Chem. Phys.* **1985**, *83*, 735 – 746.

[116] Dewar, M. J. S. *Bull. Soc. Chim. Fr.* **1951**, C79.

[117] Chatt, J.; Duncanson, L. A. *J. Chem. Soc.* **1953**, 2939 – 2947.

[118] Adjizian, J. J.; De Marco, P.; Suárez-Martínez, I.; El Mel, A. A.; Snyders, R.; Gengler, R. Y. N.; Rudolf, P.; Ke, X.; Van Tendeloo, G.; Bittencourt, C.; Ewels, C. *Chem. Phys. Lett.* **2013**, *571*, 44 – 48.

Appendix

Supporting information for: Quantum chemical study of hydrogen adsorption on carbon-supported palladium clusters

Lisa Warczinski*, Christof Hättig*

July 31, 2019

*Lehrstuhl für Theoretische Chemie, Ruhr-Universität Bochum, 44780 Bochum, Germany

Comparison of three different functionals for the hydrogen adsorption energy on free Pd_6

functional	ΔE_{ads} in kJ/mol
TPSS	-49.2
PBE	-63.4
BP86	-61.0

Comparison of two different basis sets for the hydrogen adsorption energy on free Pd_6

basis set	ΔE_{ads} in kJ/mol
def2-SVP	-49.2
def2-TZVP	-38.2

Comparison of three different functionals for the incremental adsorption energies for an increasing number of H_2 molecules on free Pd_6 in kJ/mol

number of H_2	TPSS	PBE	BP86
1	-49.2	-70.5	-60.4
2	-43.8	-65.5	-54.8
3	-43.7	-68.2	-56.5
4	-37.8	-59.2	-48.2
5	-33.7	-54.8	-43.4
6	-24.2	-41.6	-29.8
7	-64.8	-112.7	-103.3

Comparison of two different basis sets for the incremental adsorption energies for an increasing number of H_2 molecules on free Pd_6 in kJ/mol

number of H_2	def2-SVP	def2-TZVP
1	-49.2	-59.6
2	-43.8	-41.4
3	-43.7	-49.8
4	-37.8	-54.6
5	-33.7	-39.8
6	-24.2	-31.8
7	-64.8	-64.0

Comparison of two different functionals for the dispersion contribution to the metal-support interactions in the Pd_6 system

functional	total binding energy in kJ/mol	dispersion contribution in kJ/mol
TPSS	195.7	95.0
PBE	172.9	70.3

Comparison of two different functionals for the dispersion contribution to the metal-support interactions in the Pd_{21} system

functional	total binding energy in kJ/mol	dispersion contribution in kJ/mol
TPSS	549.7	301.5
PBE	451.0	220.0

Supporting Information

Anchoring of palladium nanoparticles on N-doped mesoporous carbon

Lisa Warczinski[a]*, Bin Hu[b,c], Till Eckhard[b], Baoxiang Peng[b,c], Martin Muhler[b,c] and Christof Hättig[a]

[a] Chair of Theoretical Chemistry, Ruhr-University Bochum, 44780 Bochum, Germany

[b] Laboratory of Industrial Chemistry, Ruhr-University Bochum, 44780 Bochum, Germany

[c] Max Planck Institute for Chemical Energy Conversion, 45470 Mülheim a.d. Ruhr, Germany

Corresponding author. Email: lisa.warczinski@ruhr-uni-bochum.de (L. W)

Experimental

Table S1. Physicochemical properties of the carbon materials and supported catalysts.

Sample	Pd[a] [wt%]	S_{BET}[b] [m^2g^{-1}]	V_{pore} [cm^3g^{-1}]	D_{pore}[c] [nm]	$D_{particle}$[d] [nm]
NMC	–	657	0.7	4.9	–
CMC	–	997	1.2	5.0	–
Pd/NMC	0.95	625	0.7	4.7	3.4
Pd/CMC	0.98	971	1.2	4.9	4.2

[a] Pd loading determined by AAS;

[b] Specific surface area (BET method);

[c] Average pore diameter (BJH method);

[d] Mean particle size from TEM.

Table S2. Chemical compositions of NMC, CMC, Pd/NMC, and Pd/CMC.

Sample	N (wt/at %)		O (at %)
	bulk[a]	surf.[b]	surf.[b]
NMC	13.4	10.6	6.3
CMC	–	–	11.0
Pd/NMC	13.3	10.1	8.1
Pd/CMC	–	–	11.5

[a] Bulk composition determined by elemental analysis;

[b] Surface composition determined by XPS.

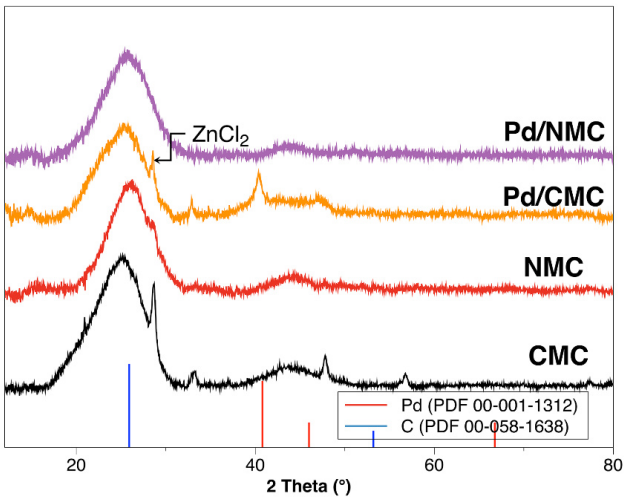

Figure S1. XRD patterns of Pd/NMC, Pd/CMC and the mesoporous carbon supports.

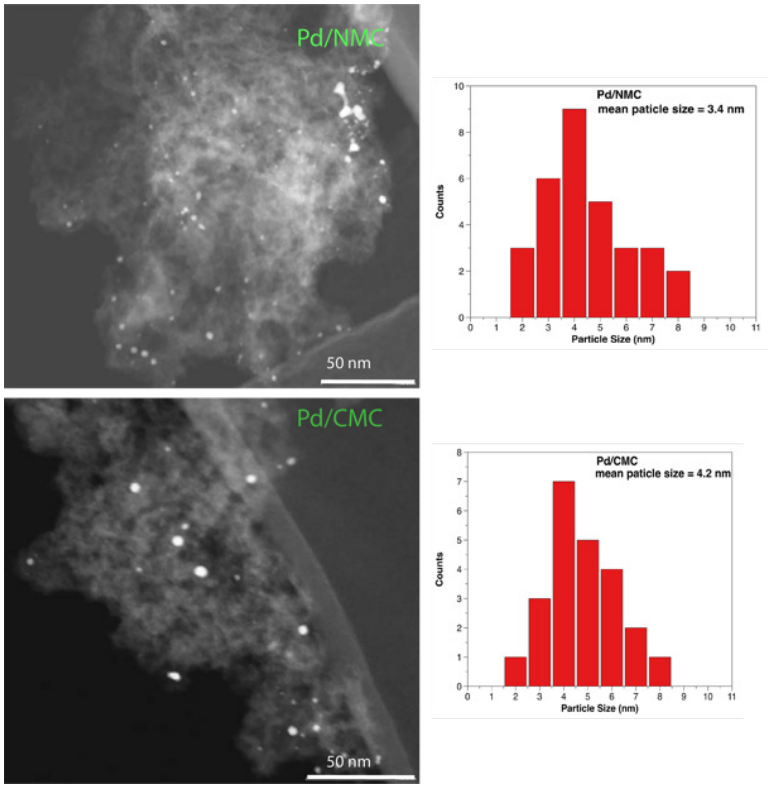

Figure S2. HAADF-STEM images and Pd particle size distributions for Pd/NMC and Pd/CMC.

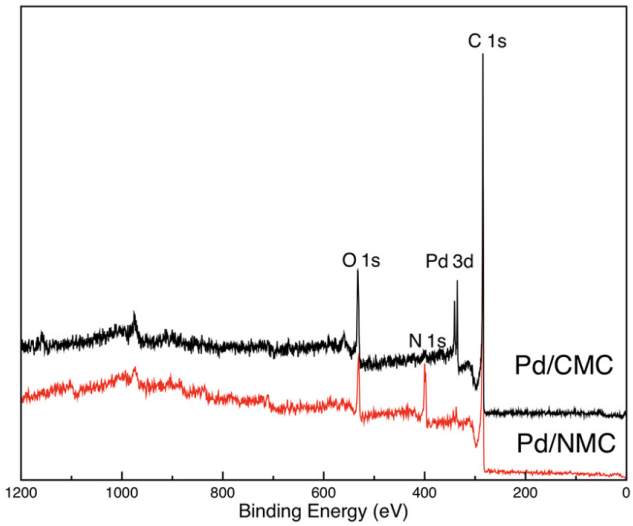

Figure S3. XP survey spectra of Pd/NMC and Pd/CMC.

Computational

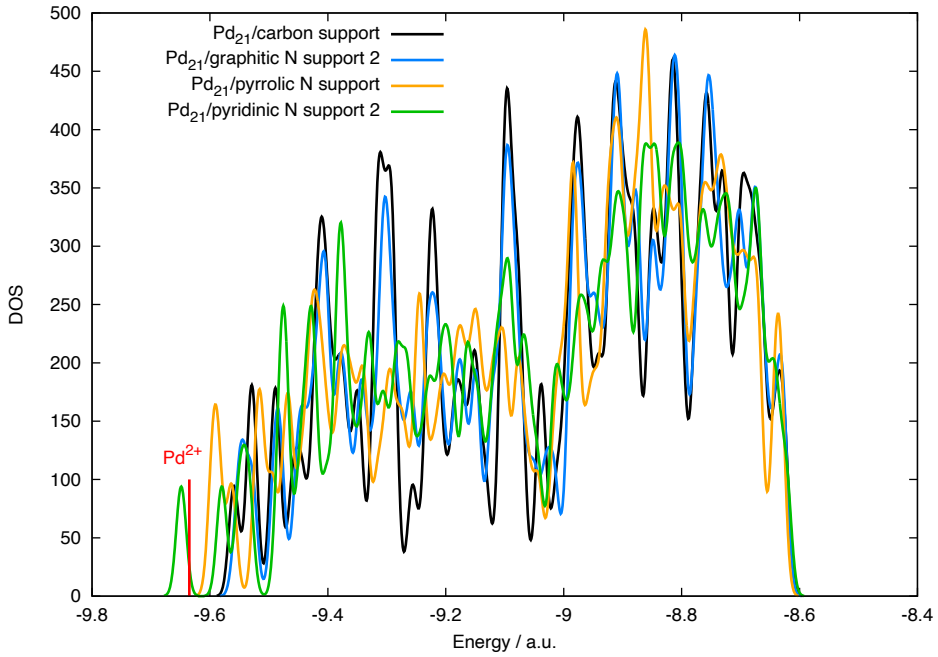

Figure S4. Pd 3d density of states plot for the different Pd_{21} systems.

Coordinates of the studied structures

180
Graphitic N support material
C 11.1286669 0.6897803 0.0769510
C 11.1310353 -0.6788594 0.0747329
C 9.9012069 -1.4390640 0.0727021
C 9.8849673 -2.8352104 0.0704892
C 8.6690148 -3.5796552 0.0684565
C 8.6455055 -4.9925504 0.0662302
C 7.4373606 -5.7216759 0.0642087
C 7.4035693 -7.1482871 0.0620368
C 6.2050660 -7.8627055 0.0600422

C	6.1643253	-9.3080801	0.0578234
C	4.9797686	-9.9930362	0.0559343
C	3.7078441	-9.3056469	0.0559964
C	2.4896215	-9.9857925	0.0540851
C	1.2392073	-9.3014376	0.0541562
C	0.0037781	-9.9866408	0.0522224
C	-1.2285859	-9.3043134	0.0523428
C	-2.4824760	-9.9903636	0.0503888
C	-3.6990802	-9.3132479	0.0505853
C	-4.9695746	-10.0037452	0.0485697
C	-6.1534577	-9.3201533	0.0488651
C	-6.1943737	-7.8746826	0.0510879
C	-7.3923292	-7.1668439	0.0514023
C	-7.4303984	-5.7404130	0.0536230
C	-8.6364548	-5.0195416	0.0539315
C	-8.6639583	-3.6050501	0.0561616
C	-9.8811937	-2.8707714	0.0565210
C	-9.9056171	-1.4731789	0.0587362
C	-11.1375156	-0.7198628	0.0590165
C	-11.1391337	0.6495800	0.0612729
C	-9.9107337	1.4098469	0.0632473
C	-9.8969611	2.8096458	0.0654343
C	-8.6836372	3.5549100	0.0674090
C	-8.6598919	4.9682951	0.0696575
C	-7.4504424	5.6986467	0.0716441
C	-7.4180246	7.1239129	0.0739518
C	-4.9975222	9.9736171	0.0801481
C	-6.2192771	7.8413614	0.0758978
C	-6.1813944	9.2863125	0.0782471
C	-2.5067571	9.9729765	0.0819343
C	-3.7247527	9.2889874	0.0799526
C	-0.0187869	9.9772460	0.0837157
C	-1.2555188	9.2920152	0.0817172
C	2.4683117	9.9811547	0.0855514
C	1.2155383	9.2961727	0.0835426
C	4.9574519	9.9910117	0.0873478
C	6.1429969	9.3084263	0.0871548
C	3.6857364	9.3019388	0.0853616
C	6.1858309	7.8624899	0.0848636
C	7.3845870	7.1506638	0.0845788
C	7.4216157	5.7226869	0.0823030
C	8.6301943	4.9970771	0.0819887

C	8.6576202	3.5825403	0.0797437
C	9.8753132	2.8421452	0.0794421
C	9.8963626	1.4456818	0.0772423
C	8.6497597	0.7128868	0.0751960
C	8.6522033	-0.7099274	0.0729670
C	7.4178827	-1.4303521	0.0709594
C	7.4177992	-2.8579080	0.0686666
C	6.1838126	-3.5755026	0.0665848
C	6.1840003	-5.0023400	0.0643476
C	4.9500335	-5.7186887	0.0622934
C	4.9470444	-7.1483905	0.0601413
C	3.7166519	-7.8591470	0.0581245
C	2.4759269	-7.1479937	0.0582257
C	1.2385754	-7.8582410	0.0562814
C	0.0000002	-7.1461182	0.0564751
C	-1.2319724	-7.8614928	0.0545200
C	-2.4702130	-7.1508741	0.0547709
C	-3.7122282	-7.8652197	0.0528147
C	-4.9353549	-7.1559606	0.0530801
C	-4.9432387	-5.7222146	0.0553399
C	-6.1767163	-5.0174705	0.0556057
C	-6.1753112	-3.5943723	0.0578719
C	-7.4135583	-2.8797964	0.0581572
C	-7.4240082	-1.4548595	0.0604314
C	-8.6600910	-0.7402656	0.0607631
C	-8.6647419	0.6842768	0.0629582
C	-7.4287426	1.4068355	0.0648787
C	-7.4310412	2.8335021	0.0671046
C	-6.1968073	3.5509203	0.0690518
C	-6.1973327	4.9806448	0.0713155
C	-3.7314944	7.8424697	0.0775921
C	-4.9650443	5.6981761	0.0732587
C	-4.9620015	7.1292704	0.0755778
C	-1.2550543	7.8475028	0.0793815
C	-2.4902715	7.1339768	0.0773222
C	1.2198299	7.8508340	0.0812532
C	-0.0164181	7.1381651	0.0791842
C	3.6978665	7.8535896	0.0830849
C	4.9275502	7.1459383	0.0828241
C	2.4564663	7.1409601	0.0810750
C	4.9346898	5.7141188	0.0805296
C	6.1696431	5.0005542	0.0802467

C	6.1737428	3.5730094	0.0779567
C	7.4096865	2.8579248	0.0776837
C	7.4131443	1.4299712	0.0754361
C	6.1740959	0.7108180	0.0734492
C	6.1765167	-0.7148989	0.0711816
C	4.9394560	-1.4329349	0.0690907
C	4.9399243	-2.8603228	0.0667502
C	3.7049337	-3.5745593	0.0646845
C	3.7079064	-5.0045643	0.0624224
C	2.4748148	-5.7174382	0.0603838
C	1.2336599	-5.0039782	0.0606136
C	-0.0020763	-5.7098508	0.0586639
C	-1.2430890	-4.9978382	0.0589291
C	-2.4732115	-5.7263356	0.0570015
C	-3.6991526	-5.0039128	0.0573317
C	-3.7016219	-3.5780789	0.0595745
C	-4.9317937	-2.8717285	0.0598722
C	-4.9524528	-1.4436133	0.0620927
C	-6.1831429	-0.7352350	0.0623807
C	-6.1878502	0.6938858	0.0645849
C	-4.9516275	1.4065262	0.0664846
C	-4.9553811	2.8360404	0.0687301
C	-2.4892406	5.7002492	0.0750089
C	-3.7211707	3.5543798	0.0706943
C	-3.7229445	4.9849239	0.0729585
C	-0.0145570	5.7039363	0.0768907
C	-1.2507465	4.9887747	0.0748236
C	2.4589755	5.7085412	0.0787946
C	3.6953203	4.9975398	0.0785413
C	1.2208828	4.9927595	0.0767060
C	3.6981822	3.5667401	0.0762296
C	4.9332238	2.8549137	0.0759697
C	4.9345889	1.4251868	0.0737028
C	3.6999820	0.7099216	0.0716248
C	3.7013026	-0.7205808	0.0693363
C	2.4662835	-1.4363545	0.0673406
C	2.4637508	-2.8620352	0.0649445
C	1.2247756	-3.5789365	0.0628749
C	-0.0156610	-2.8628173	0.0631709
C	-1.2493091	-3.5735205	0.0611464
N	-2.4726603	-2.8696368	0.0614566
C	-2.4768775	-1.4511831	0.0637029

C	-3.7093087	-0.7414335	0.0639426
C	-3.7102412	0.6919405	0.0662144
C	-1.2495641	3.5588098	0.0725546
C	-2.4811936	1.4118753	0.0682601
C	-2.4840344	2.8434298	0.0704958
C	1.2225538	3.5614254	0.0743811
C	2.4600281	2.8506503	0.0741522
C	2.4610786	1.4225647	0.0719095
C	-0.0128694	2.8450954	0.0723833
C	-0.0117519	1.4139923	0.0701209
C	1.2252109	0.7078778	0.0699154
C	1.2260344	-0.7233309	0.0676201
C	-0.0026743	-1.4347134	0.0655492
C	-1.2468086	-0.7367413	0.0657741
C	-1.2504148	0.6966223	0.0680613
H	-4.9956083	11.0692861	0.0818167
H	-0.0204991	11.0732724	0.0854282
H	12.0788459	-1.2287745	0.0744121
H	2.4667260	11.0772964	0.0873099
H	-10.8280672	-3.4226530	0.0550448
H	2.4877456	-11.0818023	0.0524857
H	-10.8486566	3.3532619	0.0656342
H	-9.5851364	-5.5679474	0.0523758
H	-8.3684332	7.6699578	0.0741892
H	-7.1336322	9.8282739	0.0784472
H	4.9515174	11.0866634	0.0890141
H	-12.0831905	-1.2733314	0.0572560
H	-12.0872100	1.1991510	0.0617623
H	8.3533491	-7.6953396	0.0619737
H	7.1156235	-9.8516204	0.0576311
H	10.8242570	3.3908419	0.0810171
H	12.0746258	1.2429026	0.0786810
H	-4.9629807	-11.0992310	0.0467253
H	8.3335464	7.6992362	0.0861790
H	9.5956828	-5.5385927	0.0660468
H	-9.6101189	5.5141450	0.0698133
H	-7.1052532	-9.8625502	0.0474847
H	4.9754734	-11.0886348	0.0543040
H	9.5794025	5.5449380	0.0835264
H	10.8353887	-3.3812051	0.0702964
H	7.0935178	9.8533298	0.0888317
H	-2.4793835	-11.0863174	0.0486659

H -8.3407288 -7.7160998 0.0499487
H 0.0045150 -11.0824921 0.0505784
H -2.5088733 11.0690931 0.0837404

179
Pyridinic N b support material
C 11.2389295 0.7339786 -0.0186717
C 11.2541223 -0.6333272 -0.0387681
C 10.0289831 -1.4010085 -0.0379923
C 10.0226273 -2.7958189 -0.0638953
C 8.8095079 -3.5475354 -0.0657203
C 8.7867812 -4.9598727 -0.0933919
C 7.5789981 -5.6929892 -0.0950930
C 7.5424712 -7.1195369 -0.1182246
C 6.3415409 -7.8297899 -0.1127000
C 6.2967630 -9.2747606 -0.1289505
C 5.1084982 -9.9516739 -0.1154205
C 3.8386811 -9.2590678 -0.0851505
C 2.6233919 -9.9408978 -0.0625528
C 1.3742637 -9.2547051 -0.0297182
C 0.1423590 -9.9457206 0.0030828
C -1.0917495 -9.2668215 0.0404401
C -2.3393262 -9.9606988 0.0793742
C -3.5615493 -9.2906858 0.1161616
C -4.8292266 -9.9864481 0.1562746
C -6.0184681 -9.3103302 0.1892446
C -6.0683681 -7.8648099 0.1855578
C -7.2698943 -7.1559493 0.2138590
C -7.3112578 -5.7285817 0.2063341
C -8.5216009 -5.0028011 0.2286139
C -8.5512634 -3.5894476 0.2161788
C -9.7692207 -2.8480206 0.2314173
C -9.7883861 -1.4520387 0.2141775
C -11.0201058 -0.6951105 0.2259223
C -11.0198417 0.6730700 0.2060565
C -9.7885237 1.4307256 0.1736793
C -9.7721664 2.8262048 0.1526355
C -8.5552891 3.5683800 0.1223187
C -8.5347212 4.9802631 0.1019165
C -7.3265329 5.7112657 0.0756919
C -7.3005542 7.1364582 0.0568035
C -4.8913319 9.9924593 0.0016236

C	-6.1043666	7.8556255	0.0353373
C	-6.0721227	9.3012043	0.0183477
C	-2.4012114	9.9996861	-0.0117801
C	-3.6160907	9.3113574	0.0005088
C	0.0890969	10.0102022	-0.0166399
C	-1.1463331	9.3224752	-0.0095694
C	2.5800058	10.0155746	-0.0130437
C	1.3264825	9.3312693	-0.0092926
C	5.0717039	10.0211911	-0.0063342
C	6.2555741	9.3349033	0.0026977
C	3.7982182	9.3352399	-0.0035251
C	6.2944496	7.8888990	0.0157325
C	7.4894080	7.1703892	0.0218848
C	7.5194141	5.7426230	0.0314875
C	8.7281767	5.0188018	0.0296861
C	8.7527612	3.6062591	0.0304553
C	9.9755854	2.8738371	0.0158187
C	9.9999718	1.4806080	0.0036714
C	8.7544773	0.7432927	0.0098663
C	8.7739783	-0.6773153	-0.0107010
C	7.5461185	-1.4017065	-0.0082592
C	7.5571097	-2.8293108	-0.0374592
C	6.3316606	-3.5518923	-0.0404896
C	6.3267985	-4.9743558	-0.0701153
C	5.0890468	-5.6863998	-0.0709825
C	5.0833325	-7.1117667	-0.0876650
C	3.8468870	-7.8120101	-0.0749660
C	2.6061358	-7.0942533	-0.0490310
C	1.3725531	-7.8129042	-0.0271057
C	0.1361982	-7.0999639	0.0030608
C	-1.0979111	-7.8222105	0.0398397
C	-2.3405319	-7.1249936	0.0766121
C	-3.5790580	-7.8443184	0.1140589
C	-4.8131118	-7.1435812	0.1486489
C	-4.8254401	-5.7141676	0.1445659
C	-6.0615260	-5.0032594	0.1722962
C	-6.0694810	-3.5766999	0.1641554
C	-7.3036241	-2.8626218	0.1841485
C	-7.3053481	-1.4361018	0.1684058
C	-8.5406483	-0.7192134	0.1821035
C	-8.5390500	0.7022641	0.1630481
C	-7.3020047	1.4228807	0.1325784

C	-7.3039000	2.8482653	0.1131170
C	-6.0693552	3.5661469	0.0861218
C	-6.0733508	4.9943672	0.0690406
C	-3.6187573	7.8642884	0.0145912
C	-4.8422219	5.7128347	0.0466886
C	-4.8449064	7.1446537	0.0313148
C	-1.1440133	7.8785444	0.0027394
C	-2.3764913	7.1597776	0.0139315
C	1.3310778	7.8861619	0.0036814
C	0.0953227	7.1732345	0.0078143
C	3.8090531	7.8873685	0.0102845
C	5.0365939	7.1744854	0.0207351
C	2.5685275	7.1770728	0.0134710
C	5.0404233	5.7417877	0.0345368
C	6.2688611	5.0190453	0.0400377
C	6.2676360	3.5884673	0.0507248
C	7.5069321	2.8801195	0.0413087
C	7.5086123	1.4523476	0.0337944
C	6.2705113	0.7302882	0.0464114
C	6.3012801	-0.6913468	0.0232745
C	5.0767867	-1.4181755	0.0244483
C	5.0878831	-2.8382958	-0.0128014
C	3.8571775	-3.5471866	-0.0250761
C	3.8476395	-4.9704908	-0.0507613
C	2.6046783	-5.6614129	-0.0425945
C	1.3653336	-4.9200609	-0.0305511
C	0.1324547	-5.6647756	-0.0012343
C	-1.1113767	-4.9748767	0.0373495
C	-2.3479245	-5.6966280	0.0765901
C	-3.5883469	-4.9944082	0.1082457
C	-3.5993131	-3.5684881	0.0994045
C	-4.8305475	-2.8564766	0.1309823
C	-4.8298654	-1.4287279	0.1234370
C	-6.0655421	-0.7161481	0.1379726
C	-6.0596259	0.7089625	0.1206816
C	-4.8178927	1.4248171	0.0904922
C	-4.8270195	2.8532455	0.0774367
C	-2.3721862	5.7260432	0.0262141
C	-3.5896050	3.5669506	0.0577063
C	-3.5989486	5.0005380	0.0425885
C	0.0989303	5.7401246	0.0208892
C	-1.1336384	5.0190793	0.0252237

C	2.5714985	5.7456814	0.0288802
C	3.8034662	5.0278368	0.0391811
C	1.3348692	5.0360704	0.0352033
C	3.8042192	3.5957106	0.0580727
C	5.0265593	2.8672606	0.0663977
C	5.0049121	1.4260164	0.0778652
C	3.7674649	0.7058469	0.1119990
C	3.8036136	-0.7532612	0.0711277
N	2.6608352	-1.4496751	0.0646196
C	2.6401123	-2.7848898	-0.0029301
C	1.3625840	-3.4888413	-0.0422587
C	0.0877040	-2.7826499	-0.0535915
C	-1.1258708	-3.5499720	0.0257145
C	-2.3638435	-2.8501033	0.0565350
C	-2.3639703	-1.4288701	0.0573256
C	-3.5927700	-0.7120572	0.0919143
C	-3.5777155	0.7128667	0.0750812
C	-1.1278354	3.5896747	0.0374431
C	-2.3201911	1.4149885	0.0564682
C	-2.3493046	2.8554475	0.0538496
C	1.3383467	3.6066569	0.0572635
C	2.5668534	2.8897917	0.0719744
C	2.5156805	1.4542027	0.1309685
C	0.1107994	2.8909586	0.0538487
C	0.1672950	1.4560647	0.0987222
N	1.3363849	0.8128421	0.2002439
N	0.0456036	-1.4411778	-0.1428852
C	-1.0972123	-0.7525635	-0.0154498
C	-1.0789251	0.7029954	0.0432364
H	-4.8932365	11.0879962	-0.0103398
H	0.0849856	11.1061536	-0.0263014
H	12.2060030	-1.1757372	-0.0572762
H	2.5794136	11.1116268	-0.0230893
H	-10.7185660	-3.3953912	0.2556682
H	2.6216473	-11.0369027	-0.0674838
H	-10.7219363	3.3732880	0.1602857
H	-9.4698264	-5.5518614	0.2539705
H	-8.2527439	7.6793363	0.0607755
H	-7.0265800	9.8390888	0.0200147
H	5.0693699	11.1167710	-0.0163373
H	-11.9665950	-1.2466207	0.2507133
H	-11.9662044	1.2252966	0.2147373

H	8.4901352	-7.6699835	-0.1378380
H	7.2452451	-9.8226279	-0.1505619
H	10.9212421	3.4278888	0.0093894
H	12.1792416	1.2965393	-0.0210774
H	-4.8174115	-11.0820117	0.1592654
H	8.4417674	7.7130185	0.0171301
H	9.7377840	-5.5045176	-0.1131848
H	-9.4856429	5.5251549	0.1079511
H	-6.9653742	-9.8606029	0.2185953
H	5.0972242	-11.0471929	-0.1259312
H	9.6778144	5.5658236	0.0224701
H	10.9767838	-3.3349355	-0.0847956
H	7.2075129	9.8772694	-0.0003597
H	-2.3283720	-11.0567461	0.0802634
H	-8.2165613	-7.7077812	0.2408208
H	0.1482434	-11.0416408	0.0020444
H	-2.4077033	11.0957102	-0.0215277

179

Pyridinic N c support material

C	11.1433939	0.6981583	0.0599017
C	11.1449063	-0.6703094	0.0587926
C	9.9144011	-1.4311059	0.0576931
C	9.8969914	-2.8266987	0.0567240
C	8.6794718	-3.5724462	0.0555342
C	8.6536220	-4.9850925	0.0545687
C	7.4440017	-5.7153482	0.0533388
C	7.4080564	-7.1427944	0.0523570
C	6.2088227	-7.8573036	0.0512089
C	6.1658786	-9.3034612	0.0501370
C	4.9805592	-9.9876437	0.0490640
C	3.7069553	-9.3011830	0.0489040
C	2.4883424	-9.9825635	0.0478239
C	1.2338697	-9.2998869	0.0475955
C	-0.0046876	-9.9819208	0.0465688
C	-1.2422267	-9.2980060	0.0463471
C	-2.5007877	-9.9762663	0.0452546
C	-3.7185192	-9.2906210	0.0450475
C	-5.0017318	-9.9620295	0.0439021
C	-6.1840859	-9.2688437	0.0437849
C	-6.2220769	-7.8210043	0.0448755

C	-7.4192925	-7.0935076	0.0448370
C	-7.4407282	-5.6612973	0.0458630
N	-8.6241354	-4.9958284	0.0458437
C	-8.6129050	-3.6383088	0.0469900
C	-9.8446861	-2.9071147	0.0471825
C	-9.8798562	-1.5067064	0.0483967
C	-11.1169204	-0.7532597	0.0485381
C	-11.1300536	0.6172808	0.0497577
C	-9.9092765	1.3964768	0.0509494
C	-9.8982525	2.7939207	0.0522687
C	-8.6837756	3.5483774	0.0533768
C	-8.6613835	4.9621124	0.0547013
C	-7.4535744	5.6973667	0.0557308
C	-7.4216473	7.1251622	0.0570518
C	-5.0027263	9.9773077	0.0604282
C	-6.2243092	7.8434091	0.0581191
C	-6.1860371	9.2896525	0.0593685
C	-2.5105415	9.9798661	0.0614898
C	-3.7268551	9.2949685	0.0603770
C	-0.0192301	9.9869569	0.0625840
C	-1.2543546	9.3008651	0.0613729
C	2.4716070	9.9918228	0.0636296
C	1.2191011	9.3065916	0.0624525
C	4.9629595	10.0017763	0.0645956
C	6.1493373	9.3197739	0.0646212
C	3.6909465	9.3126785	0.0635092
C	6.1938428	7.8738648	0.0633714
C	7.3941174	7.1615815	0.0633396
C	7.4318390	5.7345122	0.0621030
C	8.6428311	5.0068872	0.0621406
C	8.6714137	3.5945132	0.0609259
C	9.8906302	2.8516889	0.0609689
C	9.9112066	1.4562129	0.0598611
C	8.6636072	0.7220866	0.0586772
C	8.6653072	-0.6994899	0.0576262
C	7.4303680	-1.4212286	0.0565036
C	7.4294331	-2.8490168	0.0554351
C	6.1957896	-3.5672400	0.0542296
C	6.1922811	-4.9950329	0.0532145
C	4.9573246	-5.7116903	0.0521046
C	4.9503059	-7.1423603	0.0510974
C	3.7188143	-7.8535438	0.0499535

C	2.4776175	-7.1433683	0.0497861
C	1.2391962	-7.8555405	0.0485988
C	0.0021050	-7.1446757	0.0484399
C	-1.2381438	-7.8540987	0.0473610
C	-2.4737544	-7.1402809	0.0472479
C	-3.7202271	-7.8448162	0.0460845
C	-4.9491748	-7.1289456	0.0459971
C	-4.9394768	-5.7039349	0.0470416
C	-6.1664259	-4.9822108	0.0469458
C	-6.1542367	-3.5650071	0.0480464
C	-7.3898544	-2.8705648	0.0481178
C	-7.4053023	-1.4472620	0.0494093
C	-8.6463269	-0.7466264	0.0495453
C	-8.6558372	0.6755175	0.0508068
C	-7.4246563	1.4065032	0.0519711
C	-7.4290759	2.8333791	0.0532299
C	-6.1967564	3.5565254	0.0542982
C	-6.1978720	4.9832114	0.0555883
C	-3.7329582	7.8477883	0.0591477
C	-4.9640657	5.7033708	0.0567593
C	-4.9625214	7.1332581	0.0580338
C	-1.2523758	7.8569155	0.0601131
C	-2.4883532	7.1419972	0.0590193
C	1.2246465	7.8625507	0.0611975
C	-0.0120193	7.1495323	0.0599984
C	3.7040829	7.8653566	0.0622610
C	4.9364585	7.1565919	0.0621737
C	2.4637257	7.1529555	0.0611294
C	4.9450000	5.7261836	0.0609610
C	6.1812895	5.0120785	0.0608790
C	6.1874189	3.5845552	0.0596651
C	7.4227125	2.8688890	0.0597073
C	7.4269912	1.4412732	0.0586304
C	6.1887131	0.7221955	0.0575235
C	6.1906253	-0.7043013	0.0563986
C	4.9539052	-1.4225881	0.0551626
C	4.9542208	-2.8503246	0.0540924
C	3.7195098	-3.5660976	0.0529774
C	3.7169380	-4.9969158	0.0519536
C	2.4820433	-5.7110937	0.0507948
C	1.2439277	-4.9969567	0.0506504
C	0.0075137	-5.7106060	0.0494431

C	-1.2260823	-4.9963067	0.0493450
C	-2.4661028	-5.7090663	0.0482592
C	-3.6968515	-4.9942251	0.0482271
C	-3.6905014	-3.5658805	0.0493117
C	-4.9192146	-2.8494543	0.0492695
C	-4.9292728	-1.4273225	0.0505023
C	-6.1715512	-0.7221576	0.0505986
C	-6.1792542	0.7009804	0.0518074
C	-4.9441592	1.4222876	0.0528888
C	-4.9499792	2.8476225	0.0541348
C	-2.4855202	5.7105758	0.0577521
C	-3.7158999	3.5653284	0.0553238
C	-3.7193268	4.9944946	0.0566138
C	-0.0079113	5.7160090	0.0587276
C	-1.2429866	5.0008439	0.0576308
C	2.4687501	5.7209960	0.0598733
C	3.7052892	5.0095360	0.0598486
C	1.2305054	5.0053118	0.0586390
C	3.7101405	3.5791030	0.0586140
C	4.9468147	2.8657628	0.0585598
C	4.9502431	1.4382176	0.0574555
C	3.7144155	0.7216060	0.0562632
C	3.7167064	-0.7076864	0.0550980
C	2.4819338	-1.4234808	0.0539714
C	2.4827086	-2.8517059	0.0528859
C	1.2466607	-3.5676420	0.0517184
C	0.0119652	-2.8531494	0.0516366
C	-1.2223700	-3.5677398	0.0504399
C	-2.4562428	-2.8521636	0.0504544
C	-2.4604176	-1.4252238	0.0516094
C	-3.6962121	-0.7115298	0.0516475
C	-3.7030022	0.7146704	0.0528149
C	-1.2386983	3.5727047	0.0563866
C	-2.4691456	1.4300977	0.0540001
C	-2.4745821	2.8564713	0.0552335
C	1.2350278	3.5765619	0.0574127
C	2.4738021	2.8633580	0.0574192
C	2.4775411	1.4354170	0.0562372
C	-0.0000873	2.8613444	0.0562962
C	0.0043220	1.4323996	0.0551122
C	1.2413523	0.7191840	0.0551060
C	1.2445091	-0.7085927	0.0539442

C	0.0102657	-1.4237402	0.0527784
C	-1.2253082	-0.7096248	0.0527914
C	-1.2299707	0.7173330	0.0539551
H	-5.0027127	11.0729491	0.0613678
H	-0.0216587	11.0829562	0.0638636
H	12.0927122	-1.2201854	0.0585781
H	2.4701638	11.0879276	0.0647772
H	-10.7749046	-3.4840690	0.0463905
H	2.4894676	-11.0786856	0.0472298
H	-10.8512800	3.3356685	0.0525668
H	-8.3721529	7.6711231	0.0573204
H	-7.1380703	9.8318640	0.0594717
H	4.9572514	11.0973931	0.0652440
H	-12.0605638	-1.3099510	0.0475809
H	-12.0848584	1.1550984	0.0498017
H	8.3572446	-7.6910031	0.0526203
H	7.1163046	-9.8484800	0.0502040
H	10.8396740	3.4001679	0.0619668
H	12.0899556	1.2501677	0.0609323
H	-5.0102058	-11.0577314	0.0430920
H	8.3424708	7.7112132	0.0643480
H	9.6034126	-5.5320639	0.0549712
H	-9.6124334	5.5070326	0.0551021
H	-7.1364656	-9.8102337	0.0427707
H	4.9772555	-11.0832736	0.0483282
H	9.5914599	5.5558701	0.0632989
H	10.8473563	-3.3728964	0.0569972
H	7.0990724	9.8659736	0.0656655
H	-2.5046743	-11.0724491	0.0446726
H	-8.3829429	-7.6128770	0.0440604
H	-0.0047299	-11.0779832	0.0461123
H	-2.5143299	11.0759698	0.0625948

180

Pyrrolic N d support material

C	11.1506130	0.7125900	-0.0194519
C	11.1746853	-0.6514082	-0.0176423
C	9.9545023	-1.4233761	-0.0213964
C	9.9924220	-2.8153726	-0.0222664
C	8.8030558	-3.5930105	-0.0321496
C	8.8254233	-5.0091871	-0.0324998

C	7.6410162	-5.7810781	-0.0451164
C	7.6272144	-7.2181129	-0.0337680
C	6.4428557	-7.9694585	-0.0345567
C	6.3921260	-9.4190158	-0.0100514
C	5.2039093	-10.1092802	0.0027305
C	3.9191666	-9.4355006	-0.0072353
C	2.6802378	-10.0922000	0.0198114
C	1.4249562	-9.3923768	0.0226630
C	0.1682756	-10.0387290	0.0616532
C	-1.0507369	-9.3177324	0.0754442
C	-2.3149077	-9.9655723	0.1115114
C	-3.5052574	-9.2431897	0.1253577
C	-4.7798404	-9.9208527	0.1556693
C	-5.9528391	-9.2245062	0.1671231
C	-5.9663434	-7.7809809	0.1523785
C	-7.1625107	-7.0734739	0.1627514
C	-7.1881686	-5.6536813	0.1517664
C	-8.4075197	-4.9475258	0.1606830
C	-8.4504703	-3.5422911	0.1536187
C	-9.6861462	-2.8273889	0.1615551
C	-9.7400783	-1.4351724	0.1575293
C	-10.9869003	-0.7009642	0.1648651
C	-11.0165454	0.6673320	0.1616013
C	-9.8007073	1.4511255	0.1515234
C	-9.8068040	2.8477909	0.1483082
C	-8.6018600	3.6165988	0.1391949
C	-8.5904511	5.0308964	0.1342127
C	-7.3882014	5.7809131	0.1243011
C	-7.3582136	7.2105078	0.1164918
C	-4.9326649	10.0717753	0.0807085
C	-6.1614743	7.9362020	0.1044585
C	-6.1177494	9.3833290	0.0944514
C	-2.4307272	10.0733281	0.0588162
C	-3.6537415	9.3929887	0.0751137
C	0.0730458	10.0643356	0.0329263
C	-1.1738298	9.3913292	0.0516581
C	2.5719607	10.0396445	0.0041674
C	1.3073813	9.3736974	0.0237235
C	5.0652578	10.0105419	-0.0245297
C	6.2391748	9.3070453	-0.0335312
C	3.7822472	9.3425290	-0.0059130
C	6.2592954	7.8603617	-0.0257165

C	7.4419789	7.1237736	-0.0332592
C	7.4508613	5.6963456	-0.0261949
C	8.6504513	4.9630385	-0.0306074
C	8.6599192	3.5541349	-0.0249491
C	9.8808390	2.8287238	-0.0256266
C	9.9030188	1.4392376	-0.0221580
C	8.6573344	0.6987116	-0.0218515
C	8.6831861	-0.7195467	-0.0246662
C	7.4596617	-1.4597188	-0.0329557
C	7.5394986	-2.8895717	-0.0418823
C	6.3428749	-3.6414691	-0.0626561
C	6.3810186	-5.0809702	-0.0662883
C	5.1806227	-5.8489760	-0.0792063
C	5.1770827	-7.2767894	-0.0558105
C	3.9439284	-7.9933075	-0.0423121
C	2.7014537	-7.2891977	-0.0517494
C	1.4403201	-7.9514660	-0.0116892
C	0.2087981	-7.2050504	0.0055831
C	-1.0363277	-7.8719394	0.0528030
C	-2.2387307	-7.0941255	0.0743644
C	-3.4872010	-7.7904235	0.1091997
C	-4.7064234	-7.0654306	0.1257110
C	-4.6951043	-5.6315830	0.1162709
C	-5.9383181	-4.9288366	0.1317966
C	-5.9514282	-3.5039536	0.1275250
C	-7.2072957	-2.8069902	0.1392057
C	-7.2533976	-1.3836699	0.1373477
C	-8.5059783	-0.6829568	0.1463907
C	-8.5403290	0.7369409	0.1445668
C	-7.3204660	1.4778672	0.1364474
C	-7.3427146	2.9065928	0.1344608
C	-6.1224221	3.6439928	0.1269021
C	-6.1312289	5.0729623	0.1210760
C	-3.6664046	7.9470890	0.0863238
C	-4.9026794	5.8020509	0.1103198
C	-4.8989166	7.2309536	0.1007354
C	-1.1813527	7.9489165	0.0633976
C	-2.4230747	7.2425881	0.0814184
C	1.3005445	7.9283440	0.0340975
C	0.0557482	7.2333758	0.0551481
C	3.7783449	7.8939976	0.0023614
C	4.9947988	7.1607274	-0.0084986

C	2.5307090	7.2011851	0.0225699
C	4.9830037	5.7255625	-0.0023891
C	6.1965610	4.9803458	-0.0127594
C	6.1798672	3.5441942	-0.0093576
C	7.4112706	2.8270588	-0.0175896
C	7.4059417	1.3990472	-0.0185565
C	6.1620336	0.6698724	-0.0166361
C	6.1835145	-0.7603217	-0.0302412
C	4.9480190	-1.5010697	-0.0443394
C	5.0959856	-2.9398135	-0.0740089
C	3.9479761	-3.7444039	-0.1051848
C	3.9450382	-5.1627578	-0.1020989
C	2.7168207	-5.8763810	-0.0882908
C	1.4831345	-5.1762146	-0.0772992
C	0.2165013	-5.7745662	-0.0189710
C	-0.9595062	-4.9328364	0.0221713
C	-2.2142744	-5.6392163	0.0635696
C	-3.4458689	-4.9119758	0.0909748
C	-3.4320463	-3.4674677	0.0932471
C	-4.7093835	-2.7788812	0.1132216
C	-4.7766923	-1.3545161	0.1172176
C	-6.0297731	-0.6525403	0.1280454
C	-6.0722233	0.7746647	0.1300454
C	-4.8590157	1.5139838	0.1258594
C	-4.8776763	2.9387844	0.1241410
C	-2.4271049	5.8137305	0.0932326
C	-3.6545726	3.6708660	0.1162790
C	-3.6592261	5.0977978	0.1075487
C	0.0518928	5.8028884	0.0670941
C	-1.1896648	5.1028296	0.0877501
C	2.5232856	5.7686003	0.0310767
C	3.7420366	5.0246135	0.0162033
C	1.2804181	5.0807639	0.0551273
C	3.7310737	3.5883973	0.0202400
C	4.9349517	2.8241197	0.0040106
C	4.9002686	1.3733744	-0.0007824
C	3.6428405	0.6499377	0.0110568
C	3.6338191	-0.8121053	-0.0223376
C	2.4793234	-1.7181902	-0.0418418
C	2.7284232	-3.0981131	-0.1008180
C	1.5256310	-3.7967662	-0.0870794
C	0.4513459	-2.8960854	-0.0187197

C	-0.9069116	-3.4497626	0.0290380
C	-2.1809526	-2.7332192	0.0769392
C	-2.2850671	-1.2710061	0.1030116
C	-3.5660224	-0.6144071	0.1138738
C	-3.6155927	0.8106328	0.1215381
C	-1.1921229	3.6839611	0.0999595
C	-2.4095561	1.5503107	0.1196211
C	-2.4205901	2.9701776	0.1141422
C	1.2755157	3.6523186	0.0654063
C	2.4888029	2.9031964	0.0447977
C	2.4247304	1.4652702	0.0495173
C	0.0359216	2.9709403	0.0915603
C	0.0718664	1.5506714	0.1047135
N	1.2191773	0.8706077	0.0890227
N	1.0874571	-1.6554895	0.0012683
H	0.5784337	-0.7742474	0.0667987
N	-1.1709752	-0.5181288	0.1158869
C	-1.1934238	0.8155009	0.1191033
H	-4.9365327	11.1675213	0.0730842
H	0.0818878	11.1604166	0.0245363
H	12.1275351	-1.1922014	-0.0147272
H	2.5883772	11.1356437	-0.0030035
H	-10.6200769	-3.4010234	0.1713013
H	2.6606994	-11.1881024	0.0461848
H	-10.7671140	3.3763009	0.1529170
H	-9.3469266	-5.5116391	0.1739048
H	-8.3101677	7.7541615	0.1191883
H	-7.0677862	9.9292522	0.0976037
H	5.0792604	11.1060805	-0.0307975
H	-11.9220158	-1.2720821	0.1731876
H	-11.9752445	1.1979064	0.1670556
H	8.5893828	-7.7437651	-0.0177209
H	7.3390506	-9.9706560	0.0016254
H	10.8259532	3.3833430	-0.0283832
H	12.0830991	1.2876430	-0.0183986
H	-4.7816818	-11.0162382	0.1678285
H	8.4033375	7.6501317	-0.0448791
H	9.7967764	-5.5169609	-0.0203960
H	-9.5471702	5.5658669	0.1373725
H	-6.9140967	-9.7493701	0.1884230
H	5.2145227	-11.2049471	0.0244968
H	9.6063430	5.4988505	-0.0382426

H 10.9630400 -3.3245321 -0.0170246
H 7.1984595 9.8362190 -0.0472399
H -2.3533076 -11.0607523 0.1268535
H -8.1128215 -7.6189131 0.1804668
H 0.1283455 -11.1337752 0.0840501
H -2.4319638 11.1695780 0.0502493

182
Pyrrolic N e support material
C 11.1410816 0.7165895 -0.3902491
C 11.1650832 -0.6451233 -0.3021910
C 9.9465326 -1.4129319 -0.1931470
C 9.9796527 -2.8027385 -0.1137118
C 8.7873540 -3.5722059 -0.0340927
C 8.8038549 -4.9858250 0.0282197
C 7.6163232 -5.7479112 0.0767747
C 7.6005653 -7.1814614 0.1308488
C 6.4144481 -7.9250156 0.1590275
C 6.3672231 -9.3729798 0.2061688
C 5.1803433 -10.0625728 0.2200975
C 3.8982131 -9.3869458 0.1886077
C 2.6647433 -10.0494400 0.1889198
C 1.4105981 -9.3536901 0.1498520
C 0.1598934 -10.0083112 0.1300331
C -1.0610556 -9.2944425 0.0820492
C -2.3211404 -9.9496970 0.0312259
C -3.5134249 -9.2333866 -0.0346272
C -4.7855515 -9.9126045 -0.1146409
C -5.9580569 -9.2182994 -0.1900337
C -5.9748518 -7.7745507 -0.1811912
C -7.1670685 -7.0627771 -0.2538417
C -7.1917230 -5.6424861 -0.2193306
C -8.4057656 -4.9298215 -0.2854988
C -8.4424712 -3.5259910 -0.2293155
C -9.6710456 -2.8043232 -0.2978662
C -9.7172697 -1.4147611 -0.2304784
C -10.9582695 -0.6756586 -0.3030672
C -10.9825793 0.6901715 -0.2388505
C -9.7677457 1.4610430 -0.0932438
C -9.7716050 2.8541023 -0.0388463
C -8.5684191 3.6108178 0.0925412
C -8.5588820 5.0211144 0.1117135

C	-7.3582724	5.7629196	0.2028709
C	-7.3330195	7.1890762	0.1769258
C	-4.9167593	10.0443197	0.1429752
C	-6.1383849	7.9118227	0.2131422
C	-6.1003199	9.3565914	0.1537830
C	-2.4231822	10.0421435	0.1304609
C	-3.6418660	9.3624067	0.1897550
C	0.0661238	10.0327374	0.0261339
C	-1.1713006	9.3579865	0.1421912
C	2.5465840	10.0112966	-0.1658333
C	1.2955685	9.3422630	-0.0084704
C	5.0225017	9.9893663	-0.4079645
C	6.1955993	9.2910479	-0.4874909
C	3.7536910	9.3173768	-0.2358931
C	6.2239977	7.8475420	-0.4049394
C	7.4068187	7.1181688	-0.4872153
C	7.4262080	5.6941106	-0.4076451
C	8.6264389	4.9661830	-0.4788503
C	8.6452846	3.5592558	-0.4011892
C	9.8662429	2.8339260	-0.4507652
C	9.8953816	1.4464927	-0.3661185
C	8.6542898	0.7091653	-0.2489766
C	8.6777552	-0.7067269	-0.1724127
C	7.4538089	-1.4407434	-0.0824918
C	7.5254684	-2.8673506	-0.0308509
C	6.3233725	-3.6102287	0.0105219
C	6.3567903	-5.0441857	0.0596372
C	5.1506716	-5.8010936	0.0864600
C	5.1496777	-7.2286079	0.1340511
C	3.9189614	-7.9438077	0.1485356
C	2.6774758	-7.2380960	0.1155029
C	1.4225132	-7.9113560	0.1176621
C	0.1924506	-7.1724874	0.0826669
C	-1.0485795	-7.8492756	0.0701610
C	-2.2533058	-7.0808362	0.0318381
C	-3.4983272	-7.7813896	-0.0292559
C	-4.7180001	-7.0604651	-0.0925809
C	-4.7081035	-5.6290637	-0.0615767
C	-5.9458630	-4.9215525	-0.1055883
C	-5.9548660	-3.4982287	-0.0287753
C	-7.2024931	-2.7972783	-0.0896889
C	-7.2376737	-1.3768230	-0.0107813

C	-8.4845802	-0.6726412	-0.0811749
C	-8.5120302	0.7430392	-0.0091485
C	-7.2932843	1.4730878	0.1464957
C	-7.3149576	2.8978957	0.1951992
C	-6.0965025	3.6253150	0.3231102
C	-6.1064040	5.0526027	0.3076667
C	-3.6495202	7.9192632	0.2835975
C	-4.8790902	5.7773623	0.3648862
C	-4.8794548	7.2044577	0.2955178
C	-1.1725708	7.9196079	0.2577696
C	-2.4088916	7.2126819	0.3400317
C	1.2956928	7.9011155	0.1047335
C	0.0625655	7.2040494	0.2586459
C	3.7567364	7.8715876	-0.1412786
C	4.9714878	7.1457235	-0.2285402
C	2.5216648	7.1759669	0.0408571
C	4.9667086	5.7142851	-0.1466334
C	6.1816380	4.9792015	-0.2404214
C	6.1735832	3.5486818	-0.1672818
C	7.4041248	2.8351123	-0.2594142
C	7.4064793	1.4099174	-0.2026756
C	6.1690584	0.6847402	-0.0888460
C	6.1820257	-0.7406722	-0.0540304
C	4.9405658	-1.4724545	-0.0211913
C	5.0748427	-2.9062322	-0.0113183
C	3.9146615	-3.6914219	-0.0075004
C	3.9151674	-5.1090166	0.0512138
C	2.6872945	-5.8225740	0.0656129
C	1.4549664	-5.1205744	0.0211903
C	0.1986230	-5.7395695	0.0459560
C	-0.9805894	-4.9127240	0.0483468
C	-2.2312392	-5.6291614	0.0448176
C	-3.4636461	-4.9121409	0.0237835
C	-3.4525877	-3.4763168	0.1324220
C	-4.7192334	-2.7791503	0.1189279
C	-4.7691048	-1.3584318	0.2248297
C	-6.0160551	-0.6544368	0.1508474
C	-6.0491826	0.7679989	0.2443242
C	-4.8361822	1.4936952	0.4314926
C	-4.8564289	2.9173530	0.4501526
C	-2.4078539	5.7859010	0.4551244
C	-3.6319912	3.6437661	0.5475047

C	-3.6383887	5.0707466	0.4679582
C	0.0654994	5.7772238	0.3971384
C	-1.1701807	5.0741667	0.5210417
C	2.5195836	5.7467446	0.1501421
C	3.7370489	5.0124541	0.0420096
C	1.2917178	5.0541633	0.3639782
C	3.7321913	3.5810793	0.1283179
C	4.9396886	2.8328820	0.0082240
C	4.9181275	1.3872727	0.0352497
C	3.6764684	0.6716658	0.2001798
C	3.6338220	-0.7756366	0.0103426
C	2.4591882	-1.6519016	-0.1354755
C	2.6925276	-3.0310782	-0.0863792
C	1.4849111	-3.7328099	-0.0723400
C	0.4014342	-2.8476284	-0.1115413
C	-0.9385147	-3.4322272	0.0636772
C	-2.2134849	-2.7504112	0.2685926
C	-2.3172680	-1.3376011	0.6106357
C	-3.5627272	-0.6371135	0.4621159
C	-3.5980907	0.7860482	0.5818510
C	-1.1670404	3.6586853	0.6792632
C	-2.3919893	1.5178367	0.7816853
C	-2.4014099	2.9413494	0.6930090
C	1.2958111	3.6293792	0.5266616
C	2.5123668	2.8925502	0.3929142
C	2.5066828	1.4648957	0.5547411
C	0.0662363	2.9461176	0.7537021
C	0.0879474	1.5433208	1.0455849
C	1.3277944	0.8865240	1.0682345
H	1.3771823	-0.1379458	1.4279402
N	1.0351109	-1.5720490	-0.2395703
H	0.5283097	-0.7026633	-0.3850322
C	-1.2224602	-0.5953350	1.0982353
H	-0.3512378	-1.1426945	1.4485969
C	-1.1794509	0.8068839	1.0605440
H	-4.9161607	11.1385642	0.0874124
H	0.0685363	11.1253333	-0.0598400
H	12.1168422	-1.1876421	-0.3176005
H	2.5519354	11.1045818	-0.2435611
H	-10.6040026	-3.3690942	-0.4065976
H	2.6488295	-11.1453208	0.2153404
H	-10.7250365	3.3902910	-0.1091750

H -9.3448918 -5.4865749 -0.3792954
H -8.2839430 7.7298313 0.1072868
H -7.0520640 9.8973282 0.1068448
H 5.0240528 11.0828867 -0.4755717
H -11.8903521 -1.2406996 -0.4146282
H -11.9341057 1.2301172 -0.2993411
H 8.5610025 -7.7100000 0.1456945
H 7.3155813 -9.9215908 0.2286323
H 10.8065616 3.3880164 -0.5493133
H 12.0726228 1.2864846 -0.4779250
H -4.7858616 -11.0081098 -0.1180693
H 8.3580781 7.6468836 -0.6167393
H 9.7717664 -5.5001278 0.0301459
H -9.5105386 5.5591653 0.0333261
H -6.9158736 -9.7458004 -0.2555795
H 5.1879894 -11.1578899 0.2535448
H 9.5740365 5.5043303 -0.5937288
H 10.9469629 -3.3180144 -0.1243038
H 7.1462684 9.8194841 -0.6187956
H -2.3528430 -11.0452195 0.0327569
H -8.1161015 -7.6052530 -0.3312044
H 0.1274096 -11.1037393 0.1439681
H -2.4236167 11.1354801 0.0527499

178
Pyrrolic N f support material
C 11.1484066 0.7037482 -0.1095013
C 11.1505226 -0.6648561 -0.1097149
C 9.9221142 -1.4264880 -0.0463485
C 9.9038604 -2.8220852 -0.0672519
C 8.6875387 -3.5681990 -0.0186653
C 8.6593142 -4.9801910 -0.0660323
C 7.4498975 -5.7099670 -0.0381150
C 7.4106435 -7.1355591 -0.1120792
C 6.2106760 -7.8484512 -0.1088171
C 6.1639077 -9.2914140 -0.2044073
C 4.9770974 -9.9726275 -0.2236210
C 3.7055611 -9.2865861 -0.1456513
C 2.4853153 -9.9630506 -0.1891827
C 1.2323305 -9.2802597 -0.1218449
C -0.0075256 -9.9541047 -0.2014480
C -1.2435969 -9.2683616 -0.1506318

C	-2.5026165	-9.9336052	-0.2724913
C	-3.7178242	-9.2431315	-0.2454837
C	-4.9992149	-9.8981786	-0.4054901
C	-6.1778931	-9.1983918	-0.4047880
C	-6.2138880	-7.7619962	-0.2291026
C	-7.4071543	-7.0251741	-0.2531359
C	-7.4391418	-5.6065402	-0.0714982
C	-8.6401307	-4.8327432	-0.1487892
C	-8.6625099	-3.4258182	0.0343893
C	-9.8551489	-2.5797052	-0.1487532
C	-9.7495003	-1.1921703	0.0235873
N	-10.5370423	-0.0145099	-0.1746482
H	-11.4957832	-0.0158521	-0.5098131
C	-9.7532905	1.1654669	0.0246628
C	-9.8633560	2.5528238	-0.1464807
C	-8.6733833	3.4025648	0.0372453
C	-8.6554318	4.8097138	-0.1449690
C	-7.4568433	5.5872501	-0.0673478
C	-7.4293141	7.0060905	-0.2482562
C	-5.0303002	9.8865446	-0.4004211
C	-6.2383051	7.7465952	-0.2242448
C	-6.2068199	9.1831506	-0.3994497
C	-2.5338434	9.9296279	-0.2683931
C	-3.7468497	9.2353970	-0.2410908
C	-0.0389284	9.9578900	-0.1981621
C	-1.2727672	9.2682747	-0.1471341
C	2.4537614	9.9747278	-0.1864086
C	1.2030033	9.2879532	-0.1189890
C	4.9454579	9.9922760	-0.2210382
C	6.1344529	9.3148743	-0.2019803
C	3.6761226	9.3021610	-0.1431150
C	6.1858154	7.8720484	-0.1066368
C	7.3880807	7.1629446	-0.1100379
C	7.4318804	5.7374228	-0.0363938
C	8.6436429	5.0114242	-0.0645024
C	8.6763304	3.5994476	-0.0175243
C	9.8950096	2.8571176	-0.0663453
C	9.9176307	1.4615306	-0.0458721
C	8.6731776	0.7265056	0.0334027
C	8.6754038	-0.6953940	0.0331750
C	7.4427952	-1.4180281	0.1013097
C	7.4106435	-7.1355591	-0.1120792

C	6.2106760	-7.8484512	-0.1088171
C	6.1639077	-9.2914140	-0.2044073
C	4.9770974	-9.9726275	-0.2236210
C	3.7055611	-9.2865861	-0.1456513
C	2.4853153	-9.9630506	-0.1891827
C	1.2323305	-9.2802597	-0.1218449
C	-0.0075256	-9.9541047	-0.2014480
C	-1.2435969	-9.2683616	-0.1506318
C	-2.5026165	-9.9336052	-0.2724913
C	-3.7178242	-9.2431315	-0.2454837
C	-4.9992149	-9.8981786	-0.4054901
C	-6.1778931	-9.1983918	-0.4047880
C	-6.2138880	-7.7619962	-0.2291026
C	-7.4071543	-7.0251741	-0.2531359
C	-7.4391418	-5.6065402	-0.0714982
C	-8.6401307	-4.8327432	-0.1487892
C	-8.6625099	-3.4258182	0.0343893
C	-9.8551489	-2.5797052	-0.1487532
C	-9.7495003	-1.1921703	0.0235873
N	-10.5370423	-0.0145099	-0.1746482
H	-11.4957832	-0.0158521	-0.5098131
C	-9.7532905	1.1654669	0.0246628
C	-9.8633560	2.5528238	-0.1464807
C	-8.6733833	3.4025648	0.0372453
C	-8.6554318	4.8097138	-0.1449690
C	-7.4568433	5.5872501	-0.0673478
C	-7.4293141	7.0060905	-0.2482562
C	-5.0303002	9.8865446	-0.4004211
C	-6.2383051	7.7465952	-0.2242448
C	-6.2068199	9.1831506	-0.3994497
C	-2.5338434	9.9296279	-0.2683931
C	-3.7468497	9.2353970	-0.2410908
C	-0.0389284	9.9578900	-0.1981621
C	-1.2727672	9.2682747	-0.1471341
C	2.4537614	9.9747278	-0.1864086
C	1.2030033	9.2879532	-0.1189890
C	4.9454579	9.9922760	-0.2210382
C	6.1344529	9.3148743	-0.2019803
C	3.6761226	9.3021610	-0.1431150
C	6.1858154	7.8720484	-0.1066368
C	7.3880807	7.1629446	-0.1100379
C	7.4318804	5.7374228	-0.0363938

C	8.6436429	5.0114242	-0.0645024
C	8.6763304	3.5994476	-0.0175243
C	9.8950096	2.8571176	-0.0663453
C	9.9176307	1.4615306	-0.0458721
C	8.6731776	0.7265056	0.0334027
C	8.6754038	-0.6953940	0.0331750
C	7.4427952	-1.4180281	0.1013097
C	7.4403729	-2.8457734	0.0725247
C	6.2075656	-3.5645482	0.1204706
C	6.2009906	-4.9911564	0.0586541
C	4.9654739	-5.7071564	0.0778888
C	4.9545587	-7.1349957	-0.0153910
C	3.7218053	-7.8434716	-0.0289837
C	2.4826971	-7.1349716	0.0623319
C	1.2420514	-7.8424904	0.0197422
C	0.0066569	-7.1327648	0.1020350
C	-1.2361514	-7.8337887	0.0166732
C	-2.4708453	-7.1192479	0.0775615
C	-3.7179596	-7.8091605	-0.0614065
C	-4.9458848	-7.0886159	-0.0379076
C	-4.9401336	-5.6775335	0.1634896
C	-6.1714294	-4.9537534	0.1708381
C	-6.1569230	-3.5540713	0.3919081
C	-7.3798494	-2.8286411	0.3609190
C	-7.3126058	-1.4391174	0.5694975
C	-8.4822399	-0.7008136	0.4310495
C	-8.4844416	0.6778106	0.4316796
C	-7.3171450	1.4197267	0.5707125
C	-7.3887853	2.8092094	0.3632326
C	-6.1681293	3.5384977	0.3945984
C	-6.1870296	4.9382788	0.1743950
C	-3.7424969	7.8014173	-0.0573797
C	-4.9579906	5.6659274	0.1671367
C	-4.9681632	7.0770621	-0.0336954
C	-1.2608179	7.8337464	0.0198626
C	-2.4932289	7.1153420	0.0809657
C	1.2172674	7.8502414	0.0223242
C	-0.0158422	7.1366036	0.1047193
C	3.6969499	7.8591059	-0.0267149
C	4.9319514	7.1545474	-0.0133344
C	2.4601134	7.1466412	0.0645686
C	4.9474099	5.7267085	0.0796103

C	6.1852033	5.0145951	0.0601693
C	6.1963055	3.5879573	0.1215830
C	7.4313848	2.8730461	0.0734219
C	7.4383131	1.4452713	0.1017664
C	6.2035530	0.7251379	0.1873331
C	6.2058027	-0.7018003	0.1871038
C	4.9716334	-1.4214204	0.2576623
C	4.9691566	-2.8490854	0.2190345
C	3.7348613	-3.5655705	0.2605821
C	3.7279795	-4.9944463	0.1792328
C	2.4914241	-5.7072576	0.1801622
C	1.2556060	-4.9958037	0.2829385
C	0.0162117	-5.7060109	0.2510581
C	-1.2164492	-4.9947997	0.3452198
C	-2.4611302	-5.6992464	0.2594184
C	-3.6927900	-4.9860506	0.3254879
C	-3.6788960	-3.5695900	0.5142841
C	-4.9089526	-2.8569357	0.5752391
C	-4.8773115	-1.4391696	0.7271254
C	-6.0970387	-0.7195291	0.7355504
C	-6.0992897	0.7038752	0.7361262
C	-4.8818283	1.4273932	0.7281911
C	-4.9179371	2.8451715	0.5772900
C	-2.4790502	5.6953338	0.2623715
C	-3.6901144	3.5617431	0.5165729
C	-3.7084598	4.9782557	0.3284929
C	-0.0017810	5.7098616	0.2533574
C	-1.2321712	4.9947498	0.3475917
C	2.4733730	5.7189410	0.1820480
C	3.7121687	5.0100336	0.1808185
C	1.2398258	5.0035488	0.2847857
C	3.7235832	3.5811464	0.2617487
C	4.9601382	2.8685506	0.2199464
C	4.9671283	1.4408686	0.2581305
C	3.7357577	0.7228464	0.3500021
C	3.7380192	-0.7073081	0.3497608
C	2.5058174	-1.4251833	0.4182162
C	2.5014691	-2.8532744	0.3658441
C	1.2643653	-3.5699063	0.3909162
C	0.0330450	-2.8581922	0.4977812
C	-1.2051177	-3.5725792	0.4891386
C	-2.4369382	-2.8602340	0.5862681

C	-2.4212217	-1.4348576	0.6903757
C	-3.6477548	-0.7194979	0.7591321
C	-3.6500060	0.7115882	0.7596198
C	-1.2163618	3.5725187	0.4909572
C	-2.4257271	1.4308657	0.6912667
C	-2.4459272	2.8562486	0.5879603
C	1.2530937	3.5776507	0.3923035
C	2.4924400	2.8649189	0.3668502
C	2.5013058	1.4368233	0.4187292
C	0.0240315	2.8620176	0.4990785
C	0.0366646	1.4328916	0.5713191
C	1.2705991	0.7185265	0.5131220
C	1.2728565	-0.7108012	0.5128339
C	0.0411684	-1.4290677	0.5706422
C	-1.1885231	-0.7148974	0.6600971
C	-1.1907743	0.7148056	0.6604797
H	-5.0435383	10.9739547	-0.5346472
H	-0.0455474	11.0475765	-0.3155080
H	12.0971234	-1.2141916	-0.1635520
H	2.4481080	11.0665102	-0.2836313
H	-10.7834874	-3.0665058	-0.4652846
H	2.4831753	-11.0549015	-0.2866011
H	-10.7932693	3.0369698	-0.4625563
H	-8.3750115	7.5346118	-0.4173855
H	-7.1585373	9.7090985	-0.5350123
H	4.9354174	11.0849934	-0.3007004
H	8.3576439	-7.6828187	-0.1837042
H	7.1125641	-9.8357790	-0.2682760
H	10.8418169	3.4058354	-0.1306082
H	12.0933277	1.2560452	-0.1631905
H	-5.0090443	-10.9856140	-0.5400262
H	8.3334118	7.7132560	-0.1815477
H	9.6067687	-5.5264920	-0.1373420
H	-9.5909782	5.3330339	-0.3764036
H	-7.1279170	-9.7272209	-0.5408690
H	4.9705844	-11.0653886	-0.3034423
H	9.5894677	5.5607621	-0.1356994
H	10.8522969	-3.3678010	-0.1316530
H	7.0813945	9.8622812	-0.2657690
H	-2.5091836	-11.0216230	-0.4060155
H	-8.3511281	-7.5565183	-0.4227569
H	-0.0106652	-11.0438674	-0.3190788

H -2.5438565 11.0175873 -0.4016008
H -9.5739663 -5.3587887 -0.3806492

180
N-O-like support material
C 11.1429698 0.7001442 0.0596548
C 11.1451594 -0.6682726 0.0586039
C 9.9149480 -1.4293310 0.0575642
C 9.8982686 -2.8248448 0.0565484
C 8.6811614 -3.5707239 0.0554569
C 8.6563770 -4.9832481 0.0544334
C 7.4474095 -5.7138810 0.0533746
C 7.4130945 -7.1411616 0.0523506
C 6.2147152 -7.8565322 0.0512523
C 6.1736332 -9.3025940 0.0502003
C 4.9890450 -9.9877511 0.0491097
C 3.7151003 -9.3020935 0.0489821
C 2.4976276 -9.9846294 0.0478842
C 1.2426794 -9.3030407 0.0476933
C 0.0062440 -9.9866898 0.0465041
C -1.2321800 -9.3038795 0.0463097
C -2.4873883 -9.9844407 0.0450844
C -3.7066983 -9.3000940 0.0449138
C -4.9853799 -9.9765155 0.0436320
C -6.1703941 -9.2868531 0.0435555
C -6.2069038 -7.8422842 0.0446483
C -7.4099906 -7.1189597 0.0446188
C -7.4013322 -5.7062695 0.0457426
N -8.6235804 -5.0022751 0.0457081
O -9.7250618 -5.6416036 0.0444949
C -8.6274268 -3.5919041 0.0469505
C -9.8577356 -2.8973428 0.0470285
C -9.8873237 -1.4939453 0.0482470
C -11.1228098 -0.7442212 0.0483537
C -11.1325642 0.6268680 0.0495913
C -9.9102890 1.4006190 0.0508655
C -9.8983398 2.7987926 0.0521570
C -8.6840353 3.5500867 0.0533603
C -8.6612198 4.9640567 0.0546425
C -7.4535394 5.6975333 0.0558109
C -7.4214197 7.1252261 0.0570759
C -5.0026432 9.9762734 0.0604689

C	-6.2241165	7.8427497	0.0581650
C	-6.1859738	9.2889204	0.0593633
C	-2.5111440	9.9777989	0.0614722
C	-3.7273258	9.2932259	0.0603954
C	-0.0207807	9.9845057	0.0624235
C	-1.2554593	9.2983220	0.0613930
C	2.4693372	9.9897846	0.0634290
C	1.2173704	9.3041321	0.0623529
C	4.9603412	10.0004535	0.0643954
C	6.1467957	9.3186910	0.0643258
C	3.6887030	9.3108873	0.0633533
C	6.1913811	7.8728626	0.0631889
C	7.3918071	7.1610095	0.0631348
C	7.4297945	5.7340987	0.0619910
C	8.6410263	5.0071529	0.0619239
C	8.6698598	3.5949174	0.0608263
C	9.8893055	2.8527753	0.0607824
C	9.9103787	1.4573883	0.0596980
C	8.6630998	0.7228941	0.0586387
C	8.6654035	-0.6985377	0.0575836
C	7.4307012	-1.4206288	0.0564984
C	7.4306026	-2.8481906	0.0554365
C	6.1973054	-3.5669137	0.0543749
C	6.1950429	-4.9945356	0.0533297
C	4.9608188	-5.7118438	0.0522206
C	4.9555137	-7.1425114	0.0511706
C	3.7251743	-7.8545324	0.0500552
C	2.4830820	-7.1452751	0.0499593
C	1.2459500	-7.8584485	0.0487835
C	0.0080514	-7.1483992	0.0486435
C	-1.2308324	-7.8595816	0.0474086
C	-2.4673195	-7.1471385	0.0472564
C	-3.7107836	-7.8550225	0.0460291
C	-4.9422478	-7.1414872	0.0458902
C	-4.9369003	-5.7146860	0.0470119
C	-6.1655034	-4.9899373	0.0469553
C	-6.1543418	-3.5705529	0.0481318
C	-7.3918023	-2.8749796	0.0481612
C	-7.4099960	-1.4487870	0.0494322
C	-8.6509175	-0.7443430	0.0494992
C	-8.6581569	0.6788147	0.0507938
C	-7.4260647	1.4064100	0.0520158

C	-7.4298613	2.8333774	0.0532997
C	-6.1971864	3.5553285	0.0545149
C	-6.1981695	4.9823228	0.0557611
C	-3.7335743	7.8459116	0.0591982
C	-4.9646247	5.7017305	0.0569137
C	-4.9628180	7.1319387	0.0581115
C	-1.2536630	7.8542948	0.0602155
C	-2.4893511	7.1394823	0.0591248
C	1.2228596	7.8600807	0.0611783
C	-0.0135824	7.1467690	0.0601206
C	3.7018915	7.8635829	0.0621979
C	4.9343123	7.1552039	0.0621257
C	2.4618160	7.1507263	0.0611053
C	4.9429918	5.7248159	0.0609861
C	6.1794233	5.0112595	0.0609358
C	6.1857422	3.5837827	0.0598194
C	7.4213865	2.8688107	0.0597742
C	7.4260852	1.4413464	0.0586649
C	6.1879435	0.7218390	0.0575581
C	6.1904073	-0.7045461	0.0564933
C	4.9539550	-1.4232612	0.0554359
C	4.9551078	-2.8509071	0.0543546
C	3.7207974	-3.5673015	0.0532163
C	3.7196880	-4.9979682	0.0521534
C	2.4853412	-5.7129940	0.0510131
C	1.2462677	-4.9998049	0.0509040
C	0.0106582	-5.7144815	0.0497246
C	-1.2245219	-5.0011746	0.0496032
C	-2.4634689	-5.7153625	0.0483524
C	-3.6958485	-5.0007849	0.0482299
C	-3.6912336	-3.5722967	0.0493797
C	-4.9229382	-2.8565353	0.0493406
C	-4.9318951	-1.4321263	0.0505768
C	-6.1739168	-0.7262518	0.0506441
C	-6.1815839	0.6981794	0.0519452
C	-4.9462954	1.4187187	0.0531780
C	-4.9514546	2.8449300	0.0544482
C	-2.4867034	5.7078604	0.0579373
C	-3.7173806	3.5622955	0.0555989
C	-3.7204748	4.9918183	0.0568315
C	-0.0096154	5.7131480	0.0589589
C	-1.2445441	4.9977898	0.0578375

C	2.4668078	5.7187049	0.0599505
C	3.7034619	5.0076602	0.0598737
C	1.2287983	5.0026270	0.0588976
C	3.7084279	3.5772559	0.0587366
C	4.9454067	2.8645830	0.0587017
C	4.9490735	1.4371049	0.0575748
C	3.7134016	0.7199840	0.0565147
C	3.7161782	-0.7092011	0.0554158
C	2.4814630	-1.4255834	0.0542429
C	2.4831041	-2.8538324	0.0531436
C	1.2474026	-3.5703814	0.0519783
C	0.0117337	-2.8566920	0.0518950
C	-1.2226949	-3.5722316	0.0507157
C	-2.4577195	-2.8573611	0.0506364
C	-2.4618024	-1.4297733	0.0518102
C	-3.6986774	-0.7166983	0.0518186
C	-3.7052675	0.7101472	0.0530840
C	-1.2405409	3.5693369	0.0566300
C	-2.4710562	1.4260363	0.0542442
C	-2.4762857	2.8528553	0.0554883
C	1.2332774	3.5737791	0.0577381
C	2.4722074	2.8610531	0.0576791
C	2.4760146	1.4330416	0.0565137
C	-0.0018455	2.8580693	0.0565749
C	0.0025642	1.4289674	0.0553561
C	1.2400917	0.7164087	0.0553350
C	1.2434219	-0.7114787	0.0541845
C	0.0093133	-1.4272631	0.0530108
C	-1.2272778	-0.7139492	0.0529889
C	-1.2317386	0.7134990	0.0541890
H	-5.0020608	11.0719077	0.0615271
H	-0.0233226	11.0805001	0.0632556
H	12.0931098	-1.2178880	0.0585061
H	2.4674831	11.0858812	0.0643627
H	-10.7774386	-3.4872080	0.0462224
H	2.4994462	-11.0807210	0.0471990
H	-10.8509183	3.3410956	0.0522834
H	-8.3719085	7.6711554	0.0572479
H	-7.1380720	9.8310000	0.0593295
H	4.9541956	11.0960620	0.0652563
H	-12.0660321	-1.3011825	0.0474400
H	-12.0857749	1.1673276	0.0496382

H 8.3628454 -7.6883880 0.0524753
H 7.1247042 -9.8464753 0.0503421
H 10.8380968 3.4016725 0.0617066
H 12.0891864 1.2527346 0.0605722
H -4.9899373 -11.0721460 0.0426595
H 8.3400385 7.7108351 0.0640722
H 9.6064925 -5.5296454 0.0544357
H -9.6121041 5.5090981 0.0547372
H -7.1224004 -9.8284396 0.0427421
H 4.9863279 -11.0833744 0.0483001
H 9.5894593 5.5564330 0.0627748
H 10.8487992 -3.3707382 0.0566244
H 7.0964990 9.8649368 0.0651759
H -2.4898421 -11.0805148 0.0442442
H -8.3790624 -7.6237242 0.0438409
H 0.0070768 -11.0826695 0.0456956
H -2.5145648 11.0738996 0.0624480

201
Pd_{21}/carbon support
Pd 1.3343183 -2.2870989 5.5362042
Pd 0.6375829 -1.0851538 3.1762575
Pd 0.0047613 0.0001066 5.7139339
Pd -0.6310673 1.0891022 3.1777930
Pd -1.2159387 -2.2295213 4.7818120
Pd -2.5322751 0.0394780 4.7881736
Pd -0.5556067 -3.3631808 2.3328889
Pd -2.0664408 -1.2065933 2.4286304
Pd 3.2058936 -1.1677826 2.3377730
Pd 2.5414681 -0.0385520 4.7869065
Pd 2.0736866 1.2115474 2.4286534
Pd 1.2246439 2.2304959 4.7828084
Pd 1.9812057 -3.3896349 3.0632050
Pd 0.2182840 -4.4605055 4.6446880
Pd 3.7768519 -2.3858219 4.6519220
Pd -1.3242038 2.2882715 5.5401050
Pd -3.7679997 2.3859608 4.6579214
Pd -0.2089369 4.4619776 4.6477344
Pd -3.2003765 1.1714703 2.3407528
Pd 0.5600145 3.3669536 2.3340909
Pd -1.9752210 3.3929695 3.0684702

C	11.1484039	0.6982853	0.1791168
C	11.1522968	-0.6693789	0.1240868
C	9.9234361	-1.4321144	0.0878384
C	9.9070408	-2.8265824	0.0186441
C	8.6906757	-3.5742703	-0.0238840
C	8.6653632	-4.9851265	-0.1008128
C	7.4558150	-5.7169995	-0.1411884
C	7.4200833	-7.1424632	-0.2036655
C	6.2201813	-7.8578951	-0.2241476
C	6.1789602	-9.3030790	-0.2724625
C	4.9944400	-9.9891021	-0.2706182
C	3.7203619	-9.3056312	-0.2216773
C	2.5028825	-9.9904989	-0.1997970
C	1.2485954	-9.3121551	-0.1372965
C	0.0122580	-9.9973618	-0.0920994
C	-1.2240572	-9.3174291	-0.0124286
C	-2.4773691	-10.0006856	0.0377582
C	-3.6951298	-9.3211653	0.1082005
C	-4.9678073	-10.0078521	0.1505302
C	-6.1522477	-9.3240907	0.2055747
C	-6.1954675	-7.8779834	0.2231170
C	-7.3948119	-7.1637990	0.2589000
C	-7.4323142	-5.7361157	0.2614175
C	-8.6431605	-5.0066839	0.2732857
C	-8.6734814	-3.5936043	0.2571735
C	-9.8933918	-2.8507433	0.2495458
C	-9.9161020	-1.4552128	0.2106772
C	-11.1490710	-0.6982348	0.1887802
C	-11.1529499	0.6693964	0.1330280
C	-9.9240884	1.4319376	0.0929116
C	-9.9077021	2.8262505	0.0207208
C	-8.6913414	3.5737967	-0.0242289
C	-8.6660282	4.9845596	-0.1028538
C	-7.4564806	5.7164029	-0.1439317
C	-7.4207639	7.1418205	-0.2076883
C	-4.9952394	9.9886621	-0.2705163
C	-6.2208840	7.8573112	-0.2276038
C	-6.1796692	9.3024941	-0.2761279
C	-2.5039387	9.9903876	-0.1900551
C	-3.7212424	9.3053715	-0.2170303
C	-0.0137045	9.9974159	-0.0723398
C	-1.2497943	9.3121573	-0.1233365

C	2.4756835	10.0006804	0.0633296
C	1.2225923	9.3174176	0.0075050
C	4.9660306	10.0077432	0.1795063
C	6.1505783	9.3239235	0.2316514
C	3.6935445	9.3210653	0.1314309
C	6.1941390	7.8777417	0.2405019
C	7.3936507	7.1635578	0.2708959
C	7.4313654	5.7358726	0.2668969
C	8.6422816	5.0064758	0.2752473
C	8.6727231	3.5934448	0.2542289
C	9.8926623	2.8506454	0.2443966
C	9.9154155	1.4551534	0.2036434
C	8.6696805	0.7191087	0.1794362
C	8.6741047	-0.7018704	0.1220319
C	7.4411403	-1.4266399	0.0928280
C	7.4399951	-2.8525789	0.0120759
C	6.2065439	-3.5732423	-0.0395653
C	6.2027388	-4.9997199	-0.1128182
C	4.9674733	-5.7166658	-0.1417807
C	4.9611818	-7.1459553	-0.1884524
C	3.7293967	-7.8594779	-0.1876790
C	2.4864248	-7.1536029	-0.1413872
C	1.2499856	-7.8685045	-0.1111669
C	0.0107341	-7.1619510	-0.0357862
C	-1.2278070	-7.8735714	0.0201604
C	-2.4651668	-7.1651010	0.1034992
C	-3.7070045	-7.8742467	0.1385332
C	-4.9374642	-7.1632460	0.1947711
C	-4.9452734	-5.7316643	0.2166218
C	-6.1818827	-5.0150277	0.2431363
C	-6.1902318	-3.5857763	0.2413426
C	-7.4259875	-2.8673864	0.2402537
C	-7.4323816	-1.4383080	0.2110372
C	-8.6703472	-0.7192732	0.1846267
C	-8.6747561	0.7016658	0.1266347
C	-7.4417741	1.4262939	0.0947820
C	-7.4406603	2.8521329	0.0124724
C	-6.2071933	3.5728370	-0.0382548
C	-6.2034049	4.9992182	-0.1136235
C	-3.7302090	7.8591790	-0.1845881
C	-4.9681590	5.7162098	-0.1424055
C	-4.9618921	7.1454975	-0.1894035

C	-1.2510427	7.8684253	-0.1010331
C	-2.4872737	7.1534078	-0.1360106
C	1.2265975	7.8734351	0.0333270
C	-0.0117556	7.1618277	-0.0270150
C	3.7057507	7.8740048	0.1531403
C	4.9362500	7.1629686	0.2084026
C	2.4640534	7.1648354	0.1140859
C	4.9443123	5.7313140	0.2228497
C	6.1809955	5.0147334	0.2467384
C	6.1894858	3.5855019	0.2402009
C	7.4252681	2.8671829	0.2364019
C	7.4317135	1.4381316	0.2058664
C	6.1963943	0.7173236	0.1959247
C	6.2016137	-0.7110522	0.1424639
C	4.9726983	-1.4389705	0.1165906
C	4.9660655	-2.8620522	-0.0028725
C	3.7290725	-3.5787819	-0.0555242
C	3.7249330	-5.0042344	-0.1127135
C	2.4868733	-5.7214793	-0.1124381
C	1.2483969	-5.0157307	-0.0543751
C	0.0111069	-5.7322506	0.0000336
C	-1.2264762	-5.0298594	0.1209464
C	-2.4690946	-5.7338761	0.1501847
C	-3.7055223	-5.0183528	0.2041842
C	-3.7157802	-3.5869012	0.2303127
C	-4.9519360	-2.8682896	0.2352147
C	-4.9604422	-1.4386953	0.2287083
C	-6.1970430	-0.7175437	0.2004358
C	-6.2022221	0.7107846	0.1456110
C	-4.9733220	1.4387142	0.1204436
C	-4.9667254	2.8617041	-0.0000356
C	-2.4876196	5.7212098	-0.1098339
C	-3.7297315	3.5784662	-0.0532266
C	-3.7256259	5.0038737	-0.1117480
C	-0.0120080	5.7320201	0.0039682
C	-1.2491499	5.0154697	-0.0524473
C	2.4681818	5.7334839	0.1551579
C	3.7046529	5.0179206	0.2068284
C	1.2255612	5.0294532	0.1246723
C	3.7150391	3.5864722	0.2296476
C	4.9512304	2.8679734	0.2325846
C	4.9598175	1.4384232	0.2251540

C	3.7293224	0.7216790	0.2228754
C	3.7283387	-0.7194178	0.1967735
C	2.4765004	-1.4383616	0.1063640
C	2.4877055	-2.8717356	0.0032091
C	1.2528467	-3.5873435	0.0033812
C	0.0150527	-2.8642937	0.1094407
C	-1.2316099	-3.5924475	0.2003228
C	-2.4822085	-2.8753940	0.2271277
C	-2.4788583	-1.4351764	0.2380750
C	-3.7300003	-0.7219907	0.2262421
C	-3.7289682	0.7191496	0.2008545
C	-1.2535132	3.5869425	0.0039774
C	-2.4771266	1.4381321	0.1091936
C	-2.4883968	2.8714718	0.0045928
C	1.2307332	3.5918175	0.2007325
C	2.4814526	2.8748343	0.2265492
C	2.4780377	1.4346242	0.2352621
C	-0.0158156	2.8638661	0.1088091
C	-0.0069542	1.4264775	0.0306145
C	1.2278681	0.7113359	0.0807675
C	1.2340961	-0.7153845	0.0303585
C	0.0062262	-1.4268158	0.0314876
C	-1.2286625	-0.7116799	0.0832084
C	-1.2348656	0.7151317	0.0317845
H	-4.9935009	11.0838380	-0.3022414
H	-0.0150840	11.0932238	-0.0904762
H	12.1013816	-1.2166673	0.1040332
H	2.4762363	11.0966806	0.0482258
H	-10.8419760	-3.3996742	0.2672646
H	2.5064857	-11.0863618	-0.2222539
H	-10.8589366	3.3703247	-0.0047629
H	-9.5916700	-5.5556362	0.2879371
H	-8.3697633	7.6897522	-0.2328158
H	-7.1304306	9.8457063	-0.3124066
H	4.9629691	11.1033357	0.1703658
H	-12.0950626	-1.2505571	0.2154383
H	-12.1020154	1.2167896	0.1150469
H	8.3690741	-7.6904431	-0.2280818
H	7.1297666	-9.8463859	-0.3060677
H	10.8412371	3.3995851	0.2623393
H	12.0944028	1.2507234	0.2029979
H	-4.9649567	-11.1033693	0.1347288

H	8.3420592	7.7126410	0.2919197
H	9.6154905	-5.5308628	-0.1255246
H	-9.6161566	5.5302780	-0.1278868
H	-7.1019603	-9.8695817	0.2340622
H	4.9926434	-11.0842663	-0.3027407
H	9.5907616	5.5554516	0.2909345
H	10.8582766	-3.3706716	-0.0065215
H	7.1001379	9.8694580	0.2640731
H	-2.4781630	-11.0965828	0.0164343
H	-8.3432902	-7.7128324	0.2780164
H	0.0134796	-11.0930987	-0.1141554
H	-2.5075999	11.0862575	-0.2121149

201

Pd_{21}/graphitic N support 1

Pd	1.3774922	-2.1917790	5.4397412
Pd	0.6853569	-1.0086645	3.0687411
Pd	0.0471045	0.0768907	5.6052649
Pd	-0.5913119	1.1878607	3.0801510
Pd	-1.1830390	-2.1591303	4.6583653
Pd	-2.4800534	0.1243577	4.6829453
Pd	-0.4548565	-3.2849044	2.2069638
Pd	-1.9904314	-1.0735308	2.3130869
Pd	3.2386189	-1.1426467	2.2243548
Pd	2.5869470	0.0460328	4.6721319
Pd	2.1174462	1.2623403	2.3056349
Pd	1.2878405	2.3111095	4.6506865
Pd	2.0596675	-3.3479010	3.0108264
Pd	0.2380226	-4.3762284	4.5544578
Pd	3.8416712	-2.2825762	4.5734045
Pd	-1.2514338	2.3733051	5.4753561
Pd	-3.6966196	2.4747412	4.5733112
Pd	-0.1236204	4.5282340	4.5187142
Pd	-3.1875042	1.2828609	2.2346023
Pd	0.5756767	3.4316383	2.1817589
Pd	-1.9287884	3.4933793	2.9768098
C	11.1296860	0.6816862	0.3611094
C	11.1341854	-0.6860252	0.3072334
C	9.9066045	-1.4474288	0.2260937
C	9.8908106	-2.8421665	0.1627412
C	8.6758514	-3.5882160	0.0769418

C	8.6527362	-4.9998103	0.0091608
C	7.4454038	-5.7306181	-0.0703830
C	7.4112646	-7.1569364	-0.1195493
C	6.2125059	-7.8711153	-0.1694577
C	6.1709977	-9.3167610	-0.2008167
C	4.9862502	-10.0015223	-0.2207866
C	3.7124359	-9.3156710	-0.2098144
C	2.4944725	-9.9975442	-0.1961032
C	1.2410881	-9.3154367	-0.1593257
C	0.0061448	-10.0002956	-0.1087578
C	-1.2274469	-9.3165157	-0.0437305
C	-2.4806389	-9.9977830	0.0223345
C	-3.6971684	-9.3183321	0.0939311
C	-4.9672115	-10.0057868	0.1646878
C	-6.1485941	-9.3199200	0.2359678
C	-6.1891050	-7.8740526	0.2435897
C	-7.3871265	-7.1638838	0.3091588
C	-7.4243511	-5.7376975	0.3086959
C	-8.6311660	-5.0113481	0.3632736
C	-8.6570727	-3.5983217	0.3491940
C	-9.8757264	-2.8581898	0.3856061
C	-9.9004993	-1.4629203	0.3490095
C	-11.1335937	-0.7072789	0.3718760
C	-11.1390296	0.6602111	0.3178537
C	-9.9119516	1.4213461	0.2352800
C	-9.8985523	2.8170301	0.1670532
C	-8.6866729	3.5633759	0.0759346
C	-8.6660315	4.9755656	0.0019072
C	-7.4604679	5.7061744	-0.0828193
C	-7.4283213	7.1330079	-0.1322672
C	-5.0080976	9.9816869	-0.2116823
C	-6.2310323	7.8490328	-0.1805881
C	-6.1918843	9.2950862	-0.2034207
C	-2.5169193	9.9824817	-0.1702067
C	-3.7331222	9.2980118	-0.1995807
C	-0.0272746	9.9863652	-0.0601555
C	-1.2614890	9.3027058	-0.1314533
C	2.4606050	9.9872418	0.0959450
C	1.2098029	9.3042812	0.0093098
C	4.9486450	9.9933966	0.2550841
C	6.1324812	9.3094250	0.3212168
C	3.6781791	9.3069459	0.1690955

C	6.1770415	7.8634040	0.3083588
C	7.3760164	7.1493545	0.3644027
C	7.4148026	5.7220664	0.3432675
C	8.6251383	4.9921568	0.3854549
C	8.6557992	3.5795049	0.3539212
C	9.8746548	2.8352219	0.3840122
C	9.8974657	1.4399000	0.3400634
C	8.6528936	0.7050766	0.2668624
C	8.6577794	-0.7160982	0.2103428
C	7.4259885	-1.4393233	0.1336390
C	7.4256218	-2.8659978	0.0594419
C	6.1941359	-3.5856155	-0.0357135
C	6.1927212	-5.0125003	-0.0947550
C	4.9585880	-5.7281946	-0.1557218
C	4.9534655	-7.1576465	-0.1806676
C	3.7221484	-7.8693130	-0.1994240
C	2.4795499	-7.1605257	-0.1895973
C	1.2419024	-7.8714262	-0.1605047
C	0.0026165	-7.1601325	-0.1066877
C	-1.2305598	-7.8738330	-0.0376402
C	-2.4670024	-7.1632569	0.0384171
C	-3.7082118	-7.8712082	0.1023620
C	-4.9323715	-7.1577180	0.1772804
C	-4.9390735	-5.7246516	0.1835223
C	-6.1736994	-5.0164629	0.2454838
C	-6.1732561	-3.5925582	0.2425266
C	-7.4090858	-2.8738589	0.2882819
C	-7.4198659	-1.4462885	0.2600399
C	-8.6563755	-0.7294082	0.2794727
C	-8.6627736	0.6935282	0.2221997
C	-7.4329074	1.4174214	0.1443747
C	-7.4360992	2.8423768	0.0598688
C	-6.2057829	3.5609954	-0.0448225
C	-6.2066589	4.9884934	-0.1102869
C	-3.7414371	7.8506587	-0.2047255
C	-4.9747820	5.7063285	-0.1761951
C	-4.9708893	7.1374376	-0.1945705
C	-1.2620425	7.8586420	-0.1521997
C	-2.4973029	7.1437311	-0.1985271
C	1.2141996	7.8610459	-0.0029411
C	-0.0228598	7.1507999	-0.0971750
C	3.6908709	7.8601514	0.1609934

C	4.9212980	7.1488483	0.2304966
C	2.4513954	7.1510487	0.0799105
C	4.9298994	5.7179315	0.2196675
C	6.1660074	5.0013812	0.2717112
C	6.1750152	3.5727222	0.2472503
C	7.4094290	2.8540084	0.2840823
C	7.4159513	1.4248879	0.2457130
C	6.1813409	0.7051455	0.1824330
C	6.1871755	-0.7230304	0.1305049
C	4.9584199	-1.4504529	0.0587916
C	4.9528411	-2.8744258	-0.0545051
C	3.7167044	-3.5887427	-0.1437025
C	3.7159419	-5.0148368	-0.1749985
C	2.4794376	-5.7295158	-0.1884902
C	1.2392945	-5.0210916	-0.1580416
C	0.0017999	-5.7282094	-0.0958545
C	-1.2381156	-5.0227060	0.0224232
C	-2.4691558	-5.7364283	0.0621316
C	-3.6968315	-5.0112300	0.1245053
C	-3.7030240	-3.5841009	0.1232597
C	-4.9323113	-2.8729078	0.1891498
C	-4.9511041	-1.4431661	0.1971332
C	-6.1843760	-0.7255538	0.2071651
C	-6.1913938	0.7027938	0.1508286
C	-4.9640091	1.4237624	0.0736817
C	-4.9649361	2.8495071	-0.0619515
C	-2.4963029	5.7116901	-0.2157107
C	-3.7346855	3.5669574	-0.1658753
C	-3.7328836	4.9937221	-0.2024878
C	-0.0234393	5.7207564	-0.1117182
C	-1.2571547	5.0046384	-0.1964075
C	2.4562122	5.7198704	0.0862334
C	3.6914894	5.0045092	0.1532517
C	1.2141262	5.0149978	0.0120254
C	3.7025415	3.5736084	0.1492338
C	4.9377926	2.8556896	0.1847493
C	4.9458922	1.4271574	0.1651211
C	3.7141306	0.7111286	0.1159875
C	3.7123652	-0.7310318	0.0826952
C	2.4657696	-1.4485486	-0.0389326
C	2.4737643	-2.8809397	-0.1237020
C	1.2382185	-3.5971049	-0.1143462

C	-0.0027105	-2.8678080	0.0070970
C	-1.2478927	-3.5884781	0.1267560
N	-2.4892961	-2.8843723	0.0596340
C	-2.4693345	-1.4635348	0.1937520
C	-3.7181447	-0.7432677	0.1742916
C	-3.7154778	0.7034160	0.1283776
C	-1.2599137	3.5739838	-0.1701754
C	-2.4768810	1.4256370	-0.0334987
C	-2.4923319	2.8579443	-0.1507060
C	1.2177577	3.5760754	0.0493315
C	2.4694215	2.8604436	0.0988603
C	2.4637115	1.4223807	0.0837527
C	-0.0254987	2.8487844	-0.0731717
C	-0.0158397	1.4108267	-0.1474174
C	1.2193057	0.7012824	-0.0961706
C	1.2268006	-0.7247091	-0.1321877
C	0.0018466	-1.4332597	-0.1065629
C	-1.2338584	-0.7336041	-0.0406034
C	-1.2446451	0.6969160	-0.1218815
H	-5.0070381	11.0773091	-0.2195023
H	-0.0288257	11.0822643	-0.0472963
H	12.0826920	-1.2344413	0.3235864
H	2.4601136	11.0833146	0.1052792
H	-10.8219678	-3.4087552	0.4365181
H	2.4949540	-11.0935587	-0.1993372
H	-10.8503580	3.3605370	0.1805829
H	-9.5792375	-5.5585451	0.4117519
H	-8.3783112	7.6795166	-0.1168965
H	-7.1436286	9.8378109	-0.2045265
H	4.9446152	11.0889911	0.2654107
H	-12.0776388	-1.2602180	0.4313097
H	-12.0875841	1.2084674	0.3342544
H	8.3602334	-7.7053226	-0.1064250
H	7.1218238	-9.8611074	-0.2017964
H	10.8224800	3.3829855	0.4391616
H	12.0747201	1.2331055	0.4205775
H	-4.9640168	-11.1012905	0.1603136
H	8.3227604	7.6985920	0.4227500
H	9.6026761	-5.5461875	0.0254538
H	-9.6168174	5.5203498	0.0188309
H	-7.0989641	-9.8622314	0.2885973
H	4.9833453	-11.0970067	-0.2376108

H 9.5724346 5.5406099 0.4401533
H 10.8413448 -3.3878577 0.1773896
H 7.0805394 9.8548928 0.3844245
H -2.4815489 -11.0938692 0.0187859
H -8.3339924 -7.7133217 0.3594539
H 0.0062581 -11.0961146 -0.1098517
H -2.5207634 11.0785385 -0.1609769

201
Pd_{21}/graphitic N support 2
Pd 1.2458595 -2.5328421 5.3325420
Pd 0.4205627 -1.5168255 2.9165017
Pd -0.1736112 -0.3576801 5.3986904
Pd -0.9115059 0.6641826 2.9027967
Pd -1.3540387 -2.6743707 4.6090521
Pd -2.7852848 -0.4766266 4.5454728
Pd -0.7435233 -3.9732295 2.2269609
Pd -2.1957168 -1.7137014 2.2000411
Pd 2.9698599 -1.4231768 1.9755718
Pd 2.3679382 -0.2823734 4.4047562
Pd 1.6382254 0.8368965 2.0442216
Pd 0.9465617 1.9173340 4.4655243
Pd 1.8415921 -3.7036776 2.8242557
Pd 0.2390972 -4.8024770 4.5507378
Pd 3.6532868 -2.5790790 4.3069490
Pd -1.6143362 1.7997195 5.3035735
Pd -4.0552878 1.8526215 4.4072866
Pd -0.6392605 4.0487966 4.4346328
Pd -3.5399432 0.6041127 2.1179624
Pd 0.2879254 3.0867350 2.1076262
Pd -2.2885276 2.8827894 2.7880356
C 11.1525484 0.7162914 0.2670158
C 11.1583023 -0.6475198 0.1542959
C 9.9312597 -1.4048183 0.0389131
C 9.9176574 -2.7965577 -0.0663386
C 8.7034243 -3.5404676 -0.1643575
C 8.6814620 -4.9516179 -0.2312428
C 7.4735355 -5.6825434 -0.2812320
C 7.4393368 -7.1089353 -0.2798730
C 6.2398604 -7.8228741 -0.2527191
C 6.1992078 -9.2675863 -0.1992660
C 5.0156096 -9.9485979 -0.1113482

C	3.7443933	-9.2595761	-0.0709149
C	2.5321991	-9.9374520	0.0691789
C	1.2832668	-9.2509467	0.1354989
C	0.0537668	-9.9242057	0.3096989
C	-1.1786395	-9.2364264	0.3859605
C	-2.4253124	-9.9145524	0.5400760
C	-3.6416971	-9.2313147	0.5845419
C	-4.9107408	-9.9137946	0.7095052
C	-6.0948096	-9.2284140	0.7259565
C	-6.1395076	-7.7865655	0.6191664
C	-7.3401821	-7.0756748	0.6102946
C	-7.3796391	-5.6543391	0.4922007
C	-8.5920290	-4.9301733	0.4676207
C	-8.6248795	-3.5236603	0.3457966
C	-9.8463824	-2.7857761	0.3210138
C	-9.8720508	-1.3948132	0.2103086
C	-11.1069127	-0.6412695	0.1952363
C	-11.1152686	0.7243177	0.1058588
C	-9.8884693	1.4864391	0.0249314
C	-9.8751143	2.8809524	-0.0397533
C	-8.6596810	3.6279740	-0.1020574
C	-8.6350291	5.0401904	-0.1367043
C	-7.4266984	5.7726346	-0.1740500
C	-7.3914831	7.1988442	-0.1742054
C	-4.9647196	10.0423181	-0.1207057
C	-6.1909588	7.9121586	-0.1759595
C	-6.1493459	9.3578146	-0.1536294
C	-2.4744498	10.0363750	-0.0325402
C	-3.6917869	9.3556533	-0.1041328
C	0.0118326	10.0313253	0.1207343
C	-1.2227103	9.3525628	0.0081692
C	2.4947019	10.0216346	0.3179245
C	1.2446722	9.3446239	0.1871887
C	4.9771909	10.0173381	0.5263907
C	6.1583679	9.3293869	0.5901951
C	3.7083413	9.3362687	0.3902481
C	6.2006001	7.8851453	0.5195491
C	7.3971836	7.1680562	0.5629938
C	7.4343884	5.7435525	0.4754192
C	8.6440361	5.0138062	0.4905008
C	8.6749652	3.6049071	0.3882528
C	9.8946607	2.8632462	0.3861638

C	9.9191314	1.4720654	0.2752915
C	8.6752651	0.7413356	0.1611583
C	8.6812137	-0.6753152	0.0423774
C	7.4501416	-1.3949862	-0.0729452
C	7.4531040	-2.8182912	-0.1780300
C	6.2216547	-3.5363874	-0.2795562
C	6.2205888	-4.9639983	-0.3093125
C	4.9863188	-5.6799794	-0.3173335
C	4.9816032	-7.1086373	-0.2550881
C	3.7514336	-7.8154058	-0.1646851
C	2.5106731	-7.1031470	-0.1362458
C	1.2826231	-7.8108399	0.0276142
C	0.0501281	-7.0973462	0.1128787
C	-1.1826270	-7.7961972	0.2957859
C	-2.4174515	-7.0808730	0.3707204
C	-3.6549664	-7.7874026	0.4948394
C	-4.8843996	-7.0736893	0.5107867
C	-4.8939097	-5.6456348	0.4089754
C	-6.1314680	-4.9346998	0.3929360
C	-6.1419054	-3.5115739	0.2750286
C	-7.3791753	-2.8000329	0.2470527
C	-7.3879936	-1.3770218	0.1294839
C	-8.6282777	-0.6611001	0.1148986
C	-8.6385007	0.7572355	0.0242025
C	-7.4069227	1.4797651	-0.0554107
C	-7.4087769	2.9065120	-0.1178724
C	-6.1775038	3.6277238	-0.1811462
C	-6.1740005	5.0542963	-0.1993877
C	-3.7014958	7.9099952	-0.1521173
C	-4.9377735	5.7677348	-0.2142605
C	-4.9324156	7.1978274	-0.1877927
C	-1.2244142	7.9099263	-0.0580639
C	-2.4600527	7.2004849	-0.1473050
C	1.2474246	7.9018873	0.1254474
C	0.0121593	7.1971157	-0.0093429
C	3.7186191	7.8900631	0.3296852
C	4.9456802	7.1754862	0.3930582
C	2.4800305	7.1858991	0.2011760
C	4.9521042	5.7457013	0.3259310
C	6.1862180	5.0271382	0.3598350
C	6.1940480	3.6011511	0.2688005
C	7.4294127	2.8832992	0.2765651

C	7.4371154	1.4590566	0.1670288
C	6.2031685	0.7425447	0.0571845
C	6.2087104	-0.6800586	-0.0650526
C	4.9795869	-1.4010858	-0.1788127
C	4.9812141	-2.8246257	-0.3078896
C	3.7466473	-3.5415648	-0.3828798
C	3.7443960	-4.9662591	-0.3470884
C	2.5064946	-5.6745506	-0.2568626
C	1.2697442	-4.9598408	-0.2235384
C	0.0537919	-5.6704696	0.0164976
C	-1.1780534	-4.9508396	0.1819430
C	-2.4259025	-5.6537532	0.3047809
C	-3.6555868	-4.9301502	0.3192790
C	-3.6667286	-3.5017751	0.2371336
C	-4.9035114	-2.7937942	0.1986027
C	-4.9131879	-1.3722690	0.0968615
C	-6.1528529	-0.6601707	0.0450690
C	-6.1678287	0.7659183	-0.0505302
C	-4.9412154	1.4936371	-0.1216621
C	-4.9365352	2.9155988	-0.2061437
C	-2.4606621	5.7698106	-0.2095500
C	-3.6981668	3.6238585	-0.2615379
C	-3.6957920	5.0519462	-0.2403658
C	0.0116041	5.7676757	-0.0727335
C	-1.2242278	5.0604646	-0.1962297
C	2.4814793	5.7540702	0.1535779
C	3.7144283	5.0365542	0.2139339
C	1.2427531	5.0519899	0.0315508
C	3.7219401	3.6062774	0.1463010
C	4.9575557	2.8876774	0.1628780
C	4.9653516	1.4614254	0.0644634
C	3.7373007	0.7497003	-0.0328336
C	3.7346775	-0.6851249	-0.1316875
C	2.4829649	-1.4023524	-0.2753747
C	2.5011393	-2.8327933	-0.3877002
C	1.2603537	-3.5287713	-0.3441790
C	0.0266871	-2.7997570	-0.2711492
C	-1.1716867	-3.5116588	0.0868751
C	-2.4178666	-2.7819593	0.1913619
C	-2.4003998	-1.3407877	0.0912944
C	-3.6749582	-0.6388195	0.0681404
C	-3.6887972	0.7869587	-0.0853044

C	-1.2301124	3.6325444	-0.2413200
C	-2.4429898	1.4755233	-0.2839038
C	-2.4554578	2.9079851	-0.2867337
C	1.2448390	3.6147056	0.0206070
C	2.4915922	2.8991553	0.0485458
C	2.4941023	1.4654186	-0.0222939
C	-0.0029672	2.8965776	-0.1455952
C	0.0042506	1.4604748	-0.2879948
C	1.2442676	0.7477265	-0.1813246
C	1.2378471	-0.6774427	-0.3486729
C	0.0092823	-1.3805676	-0.3601774
N	-1.2090185	-0.6602018	-0.3055039
C	-1.2175952	0.7516230	-0.3349535
H	-4.9618178	11.1376943	-0.0976258
H	0.0119206	11.1262048	0.1690308
H	12.1066829	-1.1963250	0.1520170
H	2.4957799	11.1167188	0.3648258
H	-10.7925305	-3.3338424	0.3967843
H	2.5359582	-11.0308257	0.1450984
H	-10.8263582	3.4254114	-0.0322720
H	-9.5383262	-5.4775465	0.5449565
H	-8.3400684	7.7477782	-0.1590493
H	-7.1002554	9.9019707	-0.1568543
H	4.9733879	11.1117456	0.5778611
H	-12.0502815	-1.1946042	0.2624725
H	-12.0651529	1.2705150	0.1009782
H	8.3886213	-7.6567920	-0.2707895
H	7.1493603	-9.8127340	-0.2171854
H	10.8412139	3.4092302	0.4714978
H	12.0963043	1.2660417	0.3546378
H	-4.9048894	-11.0067082	0.7859496
H	8.3437946	7.7121489	0.6588687
H	9.6317031	-5.4974587	-0.2169213
H	-9.5850245	5.5865032	-0.1199338
H	-7.0435055	-9.7688402	0.8161809
H	5.0119108	-11.0429265	-0.0584611
H	9.5907915	5.5589261	0.5776337
H	10.8685093	-3.3418457	-0.0629489
H	7.1059580	9.8695400	0.6929206
H	-2.4227888	-11.0082216	0.6111655
H	-8.2868826	-7.6220287	0.6907897
H	0.0552927	-11.0174083	0.3873603

H -2.4761847 11.1316673 0.0084732

200

Pd_{21}/pyridnic N support 1

Pd 3.4982626 -2.2057356 5.5377713
Pd 2.7664300 -1.1085506 3.1326668
Pd 2.0820339 -0.0302029 5.6220304
Pd 1.2916100 1.0172247 3.1608658
Pd 0.9555347 -2.3864062 4.6691573
Pd -0.4873341 -0.2347627 4.6741892
Pd 1.5481328 -3.5351962 2.3014523
Pd 0.3024498 -1.2268445 2.2437137
Pd 5.3955132 -0.9682763 2.2830455
Pd 4.6202254 0.1043908 4.6245380
Pd 3.7941792 1.1420341 2.1194160
Pd 3.1428960 2.2778942 4.5279634
Pd 4.1747329 -3.2648600 2.9471313
Pd 2.5916921 -4.4705301 4.6026261
Pd 5.9242749 -2.2143969 4.5838449
Pd 0.5936197 2.1118744 5.5918764
Pd -1.8987492 1.9740617 4.7095882
Pd 1.5271904 4.3420609 4.5261951
Pd -1.3676132 0.8257008 2.2977094
Pd 2.1965501 3.3305807 2.1246111
Pd -0.2541867 3.1105805 3.0835084
C 11.1340780 0.7066607 0.1769130
C 11.1463444 -0.6601577 0.2371314
C 9.9210362 -1.4285591 0.2315608
C 9.9113594 -2.8247719 0.2763668
C 8.6982730 -3.5797837 0.2504918
C 8.6702457 -4.9938424 0.2955616
C 7.4617436 -5.7294551 0.2723718
C 7.4181520 -7.1559532 0.3353108
C 6.2149599 -7.8660532 0.3243948
C 6.1640893 -9.3098653 0.3911400
C 4.9748953 -9.9871499 0.3762270
C 3.7055775 -9.2971757 0.2957362
C 2.4868883 -9.9756510 0.2716641
C 1.2369337 -9.2906624 0.1913095
C 0.0021210 -9.9750802 0.1472512
C -1.2306015 -9.2926756 0.0569518

C	-2.4821151	-9.9785427	0.0056857
C	-3.7004357	-9.3018630	-0.0681502
C	-4.9723199	-9.9901480	-0.1106208
C	-6.1575342	-9.3077770	-0.1659328
C	-6.2012883	-7.8617488	-0.1813854
C	-7.4007861	-7.1468651	-0.2077886
C	-7.4377954	-5.7194928	-0.1977243
C	-8.6476401	-4.9880988	-0.1919593
C	-8.6743993	-3.5760297	-0.1507368
C	-9.8917323	-2.8302186	-0.1175010
C	-9.9081485	-1.4365431	-0.0474218
C	-11.1383570	-0.6768464	-0.0015444
C	-11.1352129	0.6890811	0.0782003
C	-9.9023545	1.4449464	0.1197352
C	-9.8822466	2.8371396	0.2028096
C	-8.6630506	3.5789028	0.2408684
C	-8.6376482	4.9878815	0.3134013
C	-7.4272466	5.7177537	0.3307465
C	-7.3956725	7.1426601	0.3819081
C	-4.9787708	9.9952501	0.3732092
C	-6.1977001	7.8599813	0.3716569
C	-6.1602752	9.3055620	0.4076932
C	-2.4907311	10.0022931	0.2416017
C	-3.7051214	9.3141282	0.2983563
C	-0.0012540	10.0132236	0.0870673
C	-1.2372953	9.3259852	0.1563099
C	2.4900476	10.0173871	-0.0619473
C	1.2345200	9.3354079	0.0000658
C	4.9834434	10.0190562	-0.1662094
C	6.1669819	9.3314045	-0.1969551
C	3.7078350	9.3365090	-0.1270187
C	6.2074572	7.8847568	-0.1910009
C	7.4022590	7.1633114	-0.1822707
C	7.4329844	5.7343065	-0.1459229
C	8.6397593	5.0045866	-0.0960336
C	8.6620183	3.5918074	-0.0333469
C	9.8795823	2.8511659	0.0360975
C	9.8984249	1.4572501	0.1074939
C	8.6530434	0.7217551	0.1112862
C	8.6697621	-0.7009561	0.1725861
C	7.4456063	-1.4318219	0.1673827
C	7.4502814	-2.8611897	0.1802795

C	6.2241625	-3.5896330	0.1417047
C	6.2123125	-5.0114593	0.1890339
C	4.9701427	-5.7243859	0.1765967
C	4.9583257	-7.1506498	0.2457669
C	3.7210725	-7.8511551	0.2357667
C	2.4800310	-7.1365839	0.1685752
C	1.2410825	-7.8479874	0.1490992
C	0.0065698	-7.1346131	0.0716511
C	-1.2312398	-7.8486409	0.0178003
C	-2.4706812	-7.1446124	-0.0644613
C	-3.7114629	-7.8554027	-0.0997407
C	-4.9435906	-7.1470842	-0.1553697
C	-4.9513989	-5.7171090	-0.1679838
C	-6.1863482	-4.9991458	-0.1802129
C	-6.1922682	-3.5710945	-0.1551793
C	-7.4251086	-2.8524221	-0.1278973
C	-7.4243479	-1.4261265	-0.0595929
C	-8.6586506	-0.7054637	-0.0123076
C	-8.6542154	0.7129022	0.0709364
C	-7.4162534	1.4315482	0.1121909
C	-7.4131398	2.8557025	0.1974648
C	-6.1775448	3.5714993	0.2297100
C	-6.1756880	4.9991890	0.2849865
C	-3.7114220	7.8670325	0.2759052
C	-4.9420724	5.7178308	0.2803344
C	-4.9399264	7.1486401	0.3129288
C	-1.2378081	7.8830380	0.1398823
C	-2.4708989	7.1630358	0.2057135
C	1.2365322	7.8909412	-0.0210930
C	0.0002690	7.1796412	0.0518777
C	3.7188994	7.8895110	-0.1457834
C	4.9467306	7.1748524	-0.1784898
C	2.4745474	7.1825545	-0.1056456
C	4.9517952	5.7422109	-0.1748460
C	6.1805484	5.0148817	-0.1468102
C	6.1801630	3.5839310	-0.0989780
C	7.4143805	2.8686485	-0.0321525
C	7.4127190	1.4408755	0.0427530
C	6.1750207	0.7253449	0.0523010
C	6.1989768	-0.7082166	0.1423196
C	4.9581211	-1.4449087	0.0969763
C	4.9807729	-2.8805421	0.0880994

C	3.7466370	-3.5859365	0.0594179
C	3.7325166	-5.0134755	0.1082456
C	2.4862061	-5.7068543	0.1248379
C	1.2441769	-4.9749160	0.1104222
C	0.0065237	-5.6993341	0.0460867
C	-1.2357409	-5.0025064	-0.0600981
C	-2.4735173	-5.7146355	-0.1017784
C	-3.7119369	-5.0033259	-0.1479827
C	-3.7216751	-3.5747500	-0.1423857
C	-4.9526255	-2.8541157	-0.1368426
C	-4.9503500	-1.4258861	-0.0802693
C	-6.1852337	-0.7090258	-0.0274201
C	-6.1767931	0.7145809	0.0664715
C	-4.9352948	1.4289351	0.1203004
C	-4.9364821	2.8554246	0.1921808
C	-2.4706363	5.7293686	0.1914942
C	-3.6993608	3.5724116	0.1995890
C	-3.7002821	5.0056970	0.2293817
C	0.0007569	5.7474086	0.0436222
C	-1.2335995	5.0227932	0.1182787
C	2.4765388	5.7561646	-0.1215241
C	3.7128845	5.0353713	-0.1628890
C	1.2362188	5.0534565	-0.0350607
C	3.7187842	3.6055040	-0.1301251
C	4.9377185	2.8698774	-0.1012904
C	4.9120406	1.4260202	-0.0223172
C	3.6494649	0.6845152	-0.0716423
C	3.6824529	-0.7858369	-0.0956776
N	2.5509898	-1.4850003	-0.1848193
C	2.5341013	-2.8138624	-0.0220467
C	1.2477325	-3.5195568	0.1206484
C	-0.0459729	-2.8337908	0.0752075
C	-1.2534217	-3.5779025	-0.0658392
C	-2.4880308	-2.8635742	-0.1020121
C	-2.4907041	-1.4403966	-0.0627773
C	-3.7152045	-0.7125032	-0.0413450
C	-3.6987224	0.7106606	0.0853828
C	-1.2346356	3.5956250	0.1082807
C	-2.4471848	1.4209036	0.1563637
C	-2.4622882	2.8630835	0.1613993
C	1.2350904	3.6172812	0.0012219
C	2.4717839	2.8891371	-0.0593421

C	2.3962099	1.4417353	-0.1583052
C	0.0001816	2.8910108	0.0210115
C	0.0658041	1.4625294	-0.0619064
N	1.2201746	0.8102346	-0.2184562
N	-0.0861256	-1.4783463	0.2229480
C	-1.2387804	-0.7659694	0.0771979
C	-1.1827296	0.6978502	0.1219313
H	-4.9790734	11.0906117	0.3974463
H	-0.0049042	11.1091357	0.1024246
H	12.0975665	-1.2016287	0.2871754
H	2.4917199	11.1133877	-0.0471120
H	-10.8425577	-3.3751292	-0.1393115
H	2.4830195	-11.0709538	0.3116374
H	-10.8310614	3.3848424	0.2375438
H	-9.5973509	-5.5349947	-0.2067076
H	-8.3458408	7.6875701	0.4217313
H	-7.1121575	9.8455162	0.4595123
H	4.9841758	11.1147043	-0.1630760
H	-12.0865255	-1.2252835	-0.0302436
H	-12.0809590	1.2413276	0.1133018
H	8.3629849	-7.7079395	0.3978559
H	7.1100883	-9.8588883	0.4536283
H	10.8287830	3.3991374	0.0346876
H	12.0763826	1.2658175	0.1785137
H	-4.9679746	-11.0856285	-0.0932801
H	8.3546777	7.7058140	-0.1874366
H	9.6193958	-5.5385719	0.3557586
H	-9.5870269	5.5344028	0.3475161
H	-7.1068238	-9.8540819	-0.1927949
H	4.9642752	-11.0815878	0.4259513
H	9.5909193	5.5489585	-0.0949731
H	10.8647938	-3.3628993	0.3276899
H	7.1181890	9.8747092	-0.2181877
H	-2.4798328	-11.0743331	0.0313923
H	-8.3495407	-7.6955414	-0.2241705
H	0.0014056	-11.0704997	0.1804728
H	-2.4971074	11.0982659	0.2577740

200

Pd_{21}/pyridinic N support 2

Pd	-0.8490785	-2.2223707	5.0436034

Pd	-2.0143265	-1.1266058	2.7978686
Pd	-2.3938713	-0.1179542	5.3390366
Pd	-3.5229698	0.9384368	2.9870279
Pd	-3.5029076	-2.4965238	4.4935732
Pd	-5.0329651	-0.3901539	4.7076363
Pd	-2.9943639	-3.5066016	1.9614044
Pd	-4.6659794	-1.4178553	2.2163397
Pd	0.8742558	-0.6360772	1.6380224
Pd	0.0080119	0.1855314	4.1578696
Pd	-1.0647522	1.1221753	1.8664752
Pd	-1.5363843	2.2518774	4.2576903
Pd	-0.3780968	-3.0820410	2.3725395
Pd	-1.7834148	-4.4682498	4.1254808
Pd	1.4521369	-1.9665771	3.8232894
Pd	-3.9522266	1.9934996	5.4899243
Pd	-6.4969593	1.7791504	4.8799190
Pd	-3.1547088	4.2748544	4.4118021
Pd	-6.1917575	0.8148294	2.4045569
Pd	-2.6963657	3.2740106	1.9312679
Pd	-5.0514729	3.0635511	3.1340409
C	11.0479723	0.7026117	0.6502787
C	11.0545193	-0.6644945	0.6244010
C	9.8267432	-1.4235484	0.5408279
C	9.8159658	-2.8167200	0.4862414
C	8.6020089	-3.5603092	0.3954672
C	8.5798579	-4.9697949	0.3233690
C	7.3748306	-5.7000657	0.2244861
C	7.3464272	-7.1234133	0.1448625
C	6.1500179	-7.8351619	0.0530093
C	6.1147217	-9.2786784	-0.0196023
C	4.9322891	-9.9608942	-0.1007997
C	3.6597065	-9.2743226	-0.1193063
C	2.4480330	-9.9612263	-0.1829189
C	1.1946195	-9.2823103	-0.1977609
C	-0.0361116	-9.9754866	-0.2301098
C	-1.2741194	-9.2989817	-0.2230369
C	-2.5260456	-9.9884648	-0.1951496
C	-3.7481142	-9.3157106	-0.1419095
C	-5.0190254	-10.0047765	-0.0730854
C	-6.2047099	-9.3246891	0.0112345
C	-6.2524326	-7.8786616	0.0312522
C	-7.4471334	-7.1623520	0.1428773

C	-7.4847761	-5.7330670	0.1701512
C	-8.6848179	-4.9995055	0.3198847
C	-8.7082808	-3.5841864	0.3634918
C	-9.9074596	-2.8330478	0.5608531
C	-9.9112612	-1.4364647	0.6275168
C	-11.1175183	-0.6711242	0.8603494
C	-11.1019302	0.6964503	0.9232407
C	-9.8800977	1.4541664	0.7536495
C	-9.8555009	2.8507783	0.7546064
C	-8.6567916	3.5974799	0.5321800
C	-8.6335741	5.0096878	0.4827954
C	-7.4415156	5.7333551	0.2521697
C	-7.4119043	7.1608290	0.1998090
C	-5.0151164	10.0065603	-0.1658264
C	-6.2287789	7.8747604	0.0070851
C	-6.1919214	9.3205812	-0.0335056
C	-2.5280536	10.0046781	-0.3280264
C	-3.7438523	9.3219839	-0.2606359
C	-0.0353953	10.0042383	-0.3480305
C	-1.2731807	9.3224680	-0.3562512
C	2.4545072	10.0003529	-0.2442339
C	1.2001546	9.3200554	-0.2986477
C	4.9401197	10.0013081	-0.0680108
C	6.1171297	9.3144873	0.0567867
C	3.6675158	9.3176038	-0.1421471
C	6.1500967	7.8694978	0.1214667
C	7.3383376	7.1515598	0.2568518
C	7.3627943	5.7258352	0.3239166
C	8.5663093	4.9997539	0.4496506
C	8.5832221	3.5901683	0.5002544
C	9.7985492	2.8495823	0.5874048
C	9.8151167	1.4562979	0.5933367
C	8.5670050	0.7243442	0.5292407
C	8.5754545	-0.6946697	0.5043361
C	7.3427874	-1.4144718	0.4304615
C	7.3509705	-2.8396397	0.3762896
C	6.1240724	-3.5597409	0.2950996
C	6.1226575	-4.9822784	0.2062392
C	4.8903578	-5.6933024	0.1011405
C	4.8912898	-7.1204004	0.0287582
C	3.6617605	-7.8274840	-0.0594484
C	2.4197600	-7.1171321	-0.0839502

C	1.1915792	-7.8393534	-0.1653833
C	-0.0441762	-7.1316471	-0.2073031
C	-1.2785568	-7.8547536	-0.2257952
C	-2.5230318	-7.1576084	-0.2080952
C	-3.7644956	-7.8696080	-0.1421679
C	-4.9966125	-7.1646357	-0.0590959
C	-5.0081251	-5.7354766	-0.0513730
C	-6.2377437	-5.0144368	0.0569093
C	-6.2445543	-3.5869478	0.0793410
C	-7.4667518	-2.8625391	0.2259176
C	-7.4579745	-1.4358668	0.2745422
C	-8.6723010	-0.7075690	0.4749549
C	-8.6548573	0.7140343	0.5492134
C	-7.4232538	1.4429410	0.3903483
C	-7.4242816	2.8776833	0.3342811
C	-6.2098637	3.5856946	0.0841217
C	-6.2049518	5.0126316	0.0623967
C	-3.7535138	7.8747876	-0.2590880
C	-4.9815227	5.7305872	-0.1247660
C	-4.9772755	7.1606935	-0.1376436
C	-1.2747634	7.8794110	-0.3608730
C	-2.5135320	7.1664768	-0.3421276
C	1.2004382	7.8763897	-0.2777966
C	-0.0372644	7.1690410	-0.3338033
C	3.6724453	7.8706719	-0.0941593
C	4.8941053	7.1568666	0.0413715
C	2.4339242	7.1632410	-0.1742217
C	4.8914363	5.7270740	0.1079944
C	6.1129883	5.0047787	0.2543151
C	6.1046127	3.5764222	0.3312408
C	7.3350194	2.8666742	0.4466516
C	7.3281672	1.4411350	0.4778750
C	6.0866259	0.7236246	0.4414398
C	6.1010596	-0.6988951	0.4115912
C	4.8707625	-1.4245771	0.3696677
C	4.8823807	-2.8471870	0.3004988
C	3.6512632	-3.5559178	0.1948496
C	3.6476111	-4.9804041	0.0806566
C	2.4132064	-5.6831236	-0.0138225
C	1.1797161	-4.9527961	-0.0667585
C	-0.0464310	-5.6954591	-0.2012079
C	-1.2882954	-5.0126097	-0.2565091

C	-2.5264345	-5.7331905	-0.2244124
C	-3.7674599	-5.0308364	-0.1416209
C	-3.7737404	-3.5931199	-0.1347662
C	-5.0100705	-2.8711263	-0.0279763
C	-4.9823291	-1.4315389	-0.0288031
C	-6.2204300	-0.7178454	0.1456336
C	-6.1907012	0.7229864	0.1543822
C	-4.9713569	1.4389033	-0.1529995
C	-4.9845410	2.8605734	-0.1194238
C	-2.5151743	5.7383579	-0.3525857
C	-3.7474695	3.5823703	-0.2154954
C	-3.7454335	5.0228902	-0.2531794
C	-0.0369488	5.7355138	-0.3226906
C	-1.2709916	5.0261633	-0.3666503
C	2.4320392	5.7322248	-0.1252468
C	3.6551226	5.0145084	0.0260840
C	1.1959005	5.0241568	-0.2128053
C	3.6498315	3.5838639	0.1109702
C	4.8631052	2.8571869	0.2828986
C	4.8340788	1.4254502	0.3880824
C	3.5876049	0.7076968	0.4055889
C	3.6123270	-0.7456098	0.4662178
N	2.4755102	-1.4928651	0.5925784
C	2.4263410	-2.8213058	0.2674083
C	1.1704242	-3.5136008	0.0303101
C	-0.0867803	-2.8136186	-0.2354543
C	-1.2987265	-3.5828091	-0.2751289
C	-2.5383745	-2.8653255	-0.2909142
C	-2.5355467	-1.4369766	-0.3989123
C	-3.7558431	-0.7127105	-0.3029236
C	-3.7490502	0.7145270	-0.3422127
C	-1.2650436	3.5986182	-0.3294708
C	-2.4954017	1.4077737	-0.3816137
C	-2.5024944	2.8550954	-0.2915653
C	1.1960427	3.5988382	-0.1530255
C	2.4177591	2.8791664	0.0257490
C	2.3694661	1.4581803	0.1933182
C	-0.0305427	2.8925505	-0.2418796
C	-0.0066625	1.4568569	-0.1314094
N	1.1760584	0.8164936	0.1293577
N	-0.1038353	-1.4699137	-0.4329414
C	-1.2654265	-0.7804466	-0.4647429

C	-1.2398864	0.6801704	-0.3518674
H	-5.0152998	11.1020183	-0.1846529
H	-0.0340028	11.1002395	-0.3521305
H	12.0015247	-1.2142259	0.6618711
H	2.4586088	11.0961741	-0.2698096
H	-10.8530227	-3.3747068	0.6779319
H	2.4540167	-11.0566888	-0.2171258
H	-10.7915872	3.3993128	0.9088816
H	-9.6294437	-5.5459901	0.4205415
H	-8.3526108	7.7090172	0.3259876
H	-7.1392149	9.8638767	0.0553521
H	4.9423462	11.0961365	-0.1100020
H	-12.0591608	-1.2166735	0.9872615
H	-12.0320106	1.2491889	1.0957449
H	8.2961160	-7.6702454	0.1600024
H	7.0665022	-9.8209472	-0.0053705
H	10.7466362	3.3975458	0.6344097
H	11.9902779	1.2586595	0.7087681
H	-5.0134530	-11.1003762	-0.0816563
H	8.2888600	7.6942685	0.3144374
H	9.5300585	-5.5156852	0.3415778
H	-9.5693026	5.5612260	0.6273652
H	-7.1505312	-9.8744726	0.0705201
H	4.9287491	-11.0552846	-0.1515791
H	9.5155623	5.5452026	0.4973168
H	10.7667326	-3.3614290	0.5088301
H	7.0678129	9.8560105	0.1143108
H	-2.5185542	-11.0844987	-0.1952021
H	-8.3922453	-7.7119383	0.2214521
H	-0.0271699	-11.0712645	-0.2421820
H	-2.5296415	11.1007302	-0.3276263

201

Pd_{21}/pyrrolic N support

Pd	5.9300436	-2.9988783	5.3358121
Pd	4.9270567	-3.6929063	2.7941872
Pd	3.5883757	-4.1454598	5.2584407
Pd	2.5978082	-4.6669729	2.6311495
Pd	5.7598390	-5.5974337	4.5159545
Pd	3.3864225	-6.6384952	4.3198638
Pd	7.3660290	-5.2264822	2.3436028
Pd	4.8219665	-6.2949409	2.0362053

Pd	5.3413031	-1.2067993	1.9192050
Pd	3.9084865	-1.6666220	4.2553718
Pd	2.7878353	-2.0071298	1.8349427
Pd	1.5346265	-2.7371102	4.1506396
Pd	7.3155847	-2.6203673	2.9570028
Pd	8.0546853	-4.3570497	4.7454259
Pd	6.3432287	-0.6247759	4.3196915
Pd	1.2266925	-5.2239303	5.0195890
Pd	0.9613929	-7.6792848	4.1815812
Pd	-0.8164791	-3.9286884	4.0417499
Pd	2.3079935	-7.2480803	1.8918488
Pd	0.3612599	-3.2811615	1.7509123
Pd	0.2081023	-5.8001026	2.5590355
C	11.1407930	0.8010995	0.4320409
C	11.1602458	-0.5624415	0.5248175
C	9.9521185	-1.3340772	0.3901367
C	9.9626477	-2.7275597	0.5132792
C	8.7894002	-3.4895604	0.3372633
C	8.7689383	-4.9105676	0.5862891
C	7.6238479	-5.7036457	0.2330581
C	7.6172056	-7.1333084	0.4115642
C	6.4506400	-7.9042081	0.2566254
C	6.4025279	-9.3365394	0.3965657
C	5.2270263	-10.0433249	0.2840730
C	3.9587812	-9.3915176	0.0653195
C	2.7254616	-10.0594264	0.0597829
C	1.4754687	-9.3655769	-0.0167350
C	0.2258658	-10.0052880	0.0888284
C	-0.9899389	-9.2848338	0.0868189
C	-2.2400383	-9.9360168	0.2385940
C	-3.4356855	-9.2235085	0.2630553
C	-4.6989965	-9.9052196	0.4021842
C	-5.8750143	-9.2141701	0.4275457
C	-5.8959626	-7.7748842	0.3328805
C	-7.0938340	-7.0722602	0.3611044
C	-7.1240596	-5.6552599	0.2962415
C	-8.3456992	-4.9561094	0.3253276
C	-8.3949453	-3.5523340	0.2881733
C	-9.6330768	-2.8445009	0.3171763
C	-9.6924687	-1.4529766	0.3059387
C	-10.9421300	-0.7249756	0.3345716
C	-10.9771110	0.6429686	0.3340662

C	-9.7642821	1.4302492	0.3070887
C	-9.7760445	2.8264806	0.3131790
C	-8.5742802	3.5983475	0.2887770
C	-8.5697031	5.0121099	0.2874485
C	-7.3710757	5.7658541	0.2614395
C	-7.3491233	7.1948723	0.2515029
C	-4.9404635	10.0665924	0.1650184
C	-6.1564608	7.9254909	0.2180080
C	-6.1213377	9.3724742	0.2027819
C	-2.4414974	10.0798318	0.0863287
C	-3.6595051	9.3931675	0.1351697
C	0.0581788	10.0837447	-0.0085434
C	-1.1830285	9.4035935	0.0482882
C	2.5535324	10.0726784	-0.1100906
C	1.2943113	9.3993524	-0.0544387
C	5.0450502	10.0576623	-0.1912594
C	6.2225999	9.3610130	-0.2101019
C	3.7664633	9.3821750	-0.1490914
C	6.2506848	7.9145968	-0.1881245
C	7.4373694	7.1861383	-0.1698672
C	7.4539839	5.7589101	-0.1287977
C	8.6552821	5.0349505	-0.0547311
C	8.6693550	3.6258885	0.0105484
C	9.8843590	2.9094908	0.1545557
C	9.9060751	1.5186606	0.2318112
C	8.6704107	0.7749483	0.1183398
C	8.7032878	-0.6440172	0.1577584
C	7.5003503	-1.3954728	-0.0203464
C	7.5707104	-2.8201721	-0.0319839
C	6.3895657	-3.5822192	-0.3001783
C	6.4134528	-5.0158953	-0.1907507
C	5.2138437	-5.7902771	-0.3176664
C	5.2063533	-7.2131474	-0.0274068
C	3.9753993	-7.9538855	-0.1035318
C	2.7448943	-7.2435649	-0.3373226
C	1.4809219	-7.9193924	-0.1832690
C	0.2406563	-7.1757761	-0.2770774
C	-0.9871269	-7.8465462	-0.0689632
C	-2.1892236	-7.0794731	-0.0166063
C	-3.4267444	-7.7767716	0.1519753
C	-4.6436365	-7.0562534	0.2073258
C	-4.6340268	-5.6235914	0.1482885

C	-5.8786358	-4.9272106	0.2067644
C	-5.8973118	-3.5042761	0.1817026
C	-7.1552807	-2.8134040	0.2304950
C	-7.2060417	-1.3916114	0.2272389
C	-8.4613999	-0.6971110	0.2688171
C	-8.5011976	0.7218828	0.2738046
C	-7.2836635	1.4659730	0.2502051
C	-7.3122421	2.8937213	0.2611034
C	-6.0948057	3.6347065	0.2430589
C	-6.1112330	5.0631674	0.2399127
C	-3.6637489	7.9473125	0.1536028
C	-4.8868007	5.7966284	0.2101600
C	-4.8913276	7.2255118	0.1958899
C	-1.1824875	7.9611972	0.0687126
C	-2.4180665	7.2480035	0.1256745
C	1.2949189	7.9540438	-0.0415119
C	0.0564383	7.2514323	0.0262586
C	3.7697505	7.9339045	-0.1404354
C	4.9895987	7.2076006	-0.1641425
C	2.5270813	7.2336713	-0.0887191
C	4.9844589	5.7734225	-0.1500560
C	6.2022569	5.0360593	-0.1383975
C	6.1914629	3.6019255	-0.1165316
C	7.4247632	2.8934620	-0.0476040
C	7.4235140	1.4673369	-0.0151876
C	6.1835421	0.7373817	-0.0968411
C	6.2169897	-0.7012318	-0.1033857
C	4.9848756	-1.4696339	-0.2775964
C	5.1516561	-2.9095191	-0.5031459
C	4.0105850	-3.7101095	-0.7367265
C	3.9985811	-5.1316675	-0.6719120
C	2.7604106	-5.8506538	-0.6812913
C	1.5198682	-5.1654520	-0.7498138
C	0.2543085	-5.7610311	-0.4949990
C	-0.9162005	-4.9333703	-0.2941333
C	-2.1631101	-5.6301653	-0.0906964
C	-3.3901783	-4.9024773	0.0296152
C	-3.3807666	-3.4588312	0.0362308
C	-4.6584133	-2.7764252	0.1227792
C	-4.7285269	-1.3536119	0.1474423
C	-5.9842271	-0.6574987	0.1958857
C	-6.0322653	0.7682788	0.2171055

C	-4.8208368	1.5099193	0.2139873
C	-4.8470125	2.9342951	0.2264343
C	-2.4133979	5.8187216	0.1506657
C	-3.6270136	3.6697393	0.2095695
C	-3.6404887	5.0969535	0.1927084
C	0.0605323	5.8208218	0.0516000
C	-1.1737228	5.1124587	0.1229443
C	2.5261945	5.8010416	-0.0764540
C	3.7473274	5.0646663	-0.1202163
C	1.2903679	5.1044544	-0.0001749
C	3.7411510	3.6295036	-0.1196849
C	4.9494406	2.8745856	-0.1380269
C	4.9189596	1.4290532	-0.1575967
C	3.6627856	0.6975104	-0.1799228
C	3.6573767	-0.7653938	-0.2910421
C	2.5162272	-1.6959921	-0.4597334
C	2.7754504	-3.0672067	-0.7605972
C	1.5671401	-3.7745425	-0.7693250
C	0.5018002	-2.8822529	-0.4552883
C	-0.8619537	-3.4390041	-0.2141588
C	-2.1363994	-2.7191608	-0.0288068
C	-2.2344072	-1.2641196	0.0938027
C	-3.5179316	-0.6122726	0.1449047
C	-3.5738741	0.8111248	0.1944912
C	-1.1669491	3.6925896	0.1566126
C	-2.3687899	1.5517658	0.2056629
C	-2.3897351	2.9729072	0.2008981
C	1.2929817	3.6754389	0.0259179
C	2.5056950	2.9338492	-0.0533444
C	2.4485048	1.4942642	-0.0494363
C	0.0629809	2.9826130	0.1216428
C	0.1096507	1.5610279	0.1636396
N	1.2584359	0.8812218	0.0995291
N	1.1150583	-1.6127483	-0.4574949
H	0.6209060	-0.7712342	-0.1324937
N	-1.1156565	-0.5165603	0.1654143
C	-1.1486458	0.8195759	0.2032146
H	-4.9491302	11.1622101	0.1537494
H	0.0606800	11.1797559	-0.0184504
H	12.1003707	-1.0967576	0.6993647
H	2.5633132	11.1687129	-0.1171227
H	-10.5636485	-3.4223942	0.3525178

H	2.7073441	-11.1476797	0.1820010
H	-10.7378101	3.3518014	0.3376031
H	-9.2809641	-5.5239355	0.3844232
H	-8.3036856	7.7336204	0.2674611
H	-7.0742371	9.9129913	0.2215929
H	5.0522970	11.1532094	-0.2021937
H	-11.8742709	-1.3004182	0.3577924
H	-11.9372130	1.1705716	0.3565432
H	8.5618715	-7.6298937	0.6570177
H	7.3391731	-9.8654893	0.6023130
H	10.8245796	3.4680007	0.2228707
H	12.0660979	1.3800021	0.5243289
H	-4.6905047	-10.9975802	0.4829071
H	8.3957554	7.7179248	-0.1722681
H	9.7221347	-5.4112777	0.7898731
H	-9.5284895	5.5430571	0.3040315
H	-6.8311972	-9.7390702	0.5267330
H	5.2350142	-11.1326796	0.3966183
H	9.6078202	5.5759210	-0.0274282
H	10.8984206	-3.2379669	0.7650309
H	7.1788752	9.8951017	-0.2357408
H	-2.2631928	-11.0269824	0.3386238
H	-8.0402296	-7.6184823	0.4424194
H	0.1918123	-11.0935731	0.2093833
H	-2.4483124	11.1759104	0.0729848

Supporting Information

Formic Acid-Assisted Selective Hydrogenolysis of 5-Hydroxymethylfurfural to 2,5-Dimethylfuran over Bifunctional Pd Nanoparticles Supported on N-doped Mesoporous Carbon

Bin Hu[a],[b], Lisa Warczinski[c], Xiaoyu Li[a], Mohong Lu[d], Johannes Bitzer[a], Markus Heidelmann[e], Till Eckhard[a], Qi Fu[a], Jonas Schulwitz[a], Mariia Merko[a], Mingshi Li[d], Wolfgang Kleist[a], Christof Hättig[c], Martin Muhler[a],[b], and Baoxiang Peng[a],[b]*

[a] Laboratory of Industrial Chemistry, Ruhr-University Bochum, 44780 Bochum, Germany

[b] Max Planck Institute for Chemical Energy Conversion, 45470 Mülheim a.d. Ruhr, Germany

[c] Chair of Theoretical Chemistry, Ruhr-University Bochum, 44780 Bochum, Germany

[d] Jiangsu Key Laboratory of Advanced Catalytic Materials and Technology, School of Petrochemical Engineering, Changzhou University, Changzhou, PR China

[e] Interdisciplinary Center for Analytics on the Nanoscale, University of Duisburg-Essen, 47057 Duisburg, Germany

Corresponding author. Email: baoxiang.peng@techem.rub.de (B. P)

List of abbreviations

HMF	5-(Hydroxymethyl)furfural
LA	Levulinic acid
FDCA	2,5-Furan-dicarboxylic
EL	Ethyl levulinate
DMF	2,5-Dimethylfuran
DFF	2,5-Diformylfuran
FA	Formic acid
BHMF	2,5-Bis(hydroxymethyl)furan
5-MF	5-Methylfurfrual
MFA	2-(Hydroxymethyl)-5-methylfuran
DMTHF	2,5-Dimethyltetrahydrofuran
FMF	5-[(Formyloxy)methyl]furfural
BHMTHF	2,5-Bis(hydroxymethyl)tetrahydrofuran
MTHFA	5-Methyltetrahydrofurfuryl alcohol

Experimental

Materials

All commercially available reagents were used as received without further purification unless otherwise specified. Palladium chloride (99%), formic acid (97%), acetic acid (glacial), pyridine (98.0%), acetic anhydride (98.0%), 5-(hydroxymethyl)furfural (HMF, 98%), 2,5-bis(hydroxymethyl)furan (BHMF, 95%), 5-methylfurfural (5-MF, 98%), 2,5-dimethylfuran (DMF, 99%), 2-(hydroxymethyl)-5-methylfuran (MFA, 95%), 2,5-dimethyltetrahydrofuran (DMTHF, 96%), were obtained from Sigma-Aldrich. Tetrahydrofuran (THF, 99%) and acetonitrile (99.99%) were supplied by Thermo Fisher.

Mesoporous carbon (CMC) was prepared from fructose (99% ADM) using $ZnCl_2$ as template and catalyst.[1] N-containing mesoporous carbon (NMC) was synthesized by carbonization of melamine (99%, Sigma-Aldrich) and formaldehyde (37 wt% in water, Sigma-Aldrich) using $CaCl_2$ (>95%, Fluka) as template.[2] As-prepared NMC and CMC were purified by 1.5 M HNO_3 aqueous solution at room temperature for 72 h followed by washing and filtration in deionized water several times until the pH of the filtrate became neutral. The purified NMC and CMC supports were dried at 80 °C overnight and were ground for further use. After purification, the amounts of the porogen residuals in the catalysts determined by ICP-MS are 0.04 wt% $CaCl_2$ for Pd/NMC and 0.06 wt% $ZnCl_2$ for Pd/CMC. Activated carbon (AC, Norit SX2) was obtained from Sigma-Aldrich as reference support.

Catalyst preparation

The supported Pd catalysts Pd/NMC, Pd/CMC, and Pd/AC were prepared using a sol-immobilization method. Briefly, an aqueous solution of $PdCl_2$ of the desired concentration was prepared. Subsequently, a polyvinyl alcohol (PVA) solution (1 wt%, MW = 9000 -10000 g/mol) was added (PVA/Pd (wt/wt) = 1.2). Then, a freshly prepared $NaBH_4$ aqueous solution (0.1 M) was added, which formed a dark-brown colloidal solution containing the Pd nanoparticles (NPs). After 30 min of sol generation, the powder support was added to the dark-brown colloidal solution at proper pH under vigorous stirring. The required amount of support was calculated to achieve a Pd loading of 1 wt%. After 2 h, the catalyst was obtained after filtration,

washing with distilled water, and drying at 80 °C overnight.

Characterization

XRD patterns were recorded using a Philips X'Pert MPD diffractometer with Cu Kα radiation and post-monochromator in a 2θ range from 5° to 80°. Elemental analysis of Pd was performed by AAS with a PerkinElmer AAS Model Analyst200 after acid digestion. ICP-MS measurements were performed with a iCAP RQ ASX-560 instrument to detect the leached Pd amount in the reaction solution. Scanning transmission electron microscopy (STEM) and transmission electron microscopy (TEM) measurements were carried out on a probe-side aberration-corrected JEOL JEM-2200FS with an acceleration voltage of 200kV. The effective area of the detector was 200 mm^2. The specimens for STEM and TEM were prepared by ultrasonically dispersing the powder samples in high-purity ethanol and then allowing a drop of the suspension to evaporate on a Au grid coated with carbon.

X-ray photoelectron spectroscopy (XPS) measurements were performed in an ultrahigh vacuum setup equipped with a high-resolution Gammadata Scienta SES 2002 analyzer. A monochromatic Al Kα X-ray source (1486.6 eV, anode operating at 14.5 kV and 30.5 mA) was used as incident radiation. The pressure inside the measuring chamber was kept in the range of 3.5 to 7×10^{-10} mbar during each measurement. The analyzer slit width was set at 0.3 mm and the pass energy was fixed at 200 eV for all measurements. The overall energy was better than 0.5 eV. Charging effects due to the insufficient conductivity of the carbon materials were mediated by using a flood gun (SPECS). All spectra were calibrated based on the C 1s binding energy of 284.5 eV. The CASA XPS program was used to analyze the XP spectra, and a mixed Gaussian-Lorentzian function and a Shirley background subtraction were applied in the fitting of the XPS data.

The TPR experiments were performed with a gas mixture of 2 % hydrogen in helium. The oven was cooled to 95 K with liquid nitrogen, before the feed was switched from pure helium to the reduction gas mixture. The oven was then heated with a constant heating ramp of 1 K/min to 673 K. Hydrogen consumption was recorded during heating to observe the reduction behavior of the catalyst.

X-ray absorption spectroscopy (XAS) experiments were performed at PETRA III Extension beamline P65 (energy range: 4 - 44 keV) at DESY (Deutsches Elektronensynchrotron) in Hamburg (Germany).[3] For the measurements at the Pd K-edge, a Si(311) C-type double crystal monochromator was used. The beam current was 100 mA with a ring energy of 6.08 GeV. The samples were measured in glass capillaries without dilution. All spectra were recorded as continuous scans in fluorescence mode at ambient temperature and pressure in the range of -150 eV to 1000 eV around the edge within 180 sec. For calibration, a palladium foil was measured as a reference simultaneously with the samples.

The data treatment was performed using the Demeter software package.[4] In order to compensate for the oversampling of the continuous scan mode, the data points of the obtained spectra were reduced with the help of the 'rebin'-function of the Athena software (edge region: -50 to +50 eV; pre-edge grid: 5 eV; XANES grid: 0.5 eV; EXAFS grid: 0.05 Å-1). For data evaluation, a Victoreen-type polynomial was subtracted from the spectrum to remove the background using the Athena software. The first inflection point was taken as edge energy E0. No phase shift corrections have been applied. The EXAFS analysis was performed using the Artemis software. Prior to the fitting procedure, the amplitude reduction factor S02 and the Debye-Waller factor σ^2 (Pd-Pd) were determined for a Pd reference foil and used as a fixed parameter for all materials.

Catalytic tests

Hydrogenolysis of HMF with H_2. The catalytic performance of the catalysts for the hydrogenolysis of HMF was tested in a stainless-steel autoclave (Parr Autoclave 4560, 160 mL). Typically, 1.5 mmol HMF and 50 mg catalyst were added into the vessel precharged with 30 mL tetrahydrofuran. After purging with H_2, the reaction was performed at 160 °C, 5 bar initial pressure with a stirring speed of 600 rpm for 5 h. Liquid samples of 0.5 mL were taken via a sampling line after 1, 2, 3, 4, and 5 h. The liquid samples were filtered using membrane filters and then analyzed by gas chromatography (GC). GC analysis was performed using an Agilent 7820A GC system equipped with a DB-XLB column (30 nm × 0.18 nm × 0.18 μm) and a FID detector. All analyses were performed three times each. Biphenyl was used as the internal

standard and the carbon balance based on furan was in the range of 95 to 103 %. For easy comparison, quantification was achieved by using a normalization method. The errors of the measurements were calculated to be 3-4%.

Hydrogenolysis of HMF with formic acid. A similar procedure was applied to the conversion of HMF to DMF with formic acid as the hydrogen donor. Briefly, 1.5 mmol HMF, 50 mg catalyst, and 45 mmol formic acid (30 equiv.) were dissolved in 30 mL THF. After purging and pressurizing with 5 bar N_2, the reaction was conducted at 160 ℃ and 600 rpm. Liquid samples were taken periodically.

Hydrogenolysis of HMF with formic acid in the presence of H_2. A similar procedure was applied to the conversion of HMF to DMF with formic acid in the presence of external H_2. Briefly, 1.5 mmol HMF, 50 mg catalyst, and 45 mmol formic acid (30 equiv.) were dissolved in 30 mL THF. After purging and pressurizing with 5 bar H_2, the reaction was conducted at 160 ℃ and 600 rpm. Liquid samples were taken periodically.

Synthesis of 5-[(formyloxy)methyl]furfural (FMF) from HMF. In a 100-mL Schlenk flask, 16 mmol acetic anhydride and 16 mmol formic acid were stirred at 0 °C under Ar atmosphere for 1 h. A solution of 4 mmol HMF in 20 mL acetonitrile was added to the resulting solution via a syringe. After 20 min stirring, 0.8 mmol pyridine was added. The mixture was stirred for 1 h at 0 °C and additionally for 2 h at room temperature. Solvent and excess reagents were removed under vacuum to yield FMF as orange oil. ^{1}H NMR spectrum of FMF was recorded on Bruker AVIII-300 using $CDCl_3$ as the solvent. The spectrum shown in Figure S15 confirms the successful synthesis of FMF.

Hydrogenolysis of FMF to DMF with formic acid. In a typical experiment, 1.5 mmol FMF, 50 mg Pd/NMC, and 45 mmol formic acid (30 equiv.) were dissolved in 30 mL THF. After purging and pressurizing with 5 bar N_2, the reaction was conducted at 160 ℃ and 600 rpm. Liquid samples were taken periodically.

Reusability study

For catalytic reusability tests, the hydrogenolysis of HMF to DMF was performed with formic acid in the presence of H_2 over Pd/NMC. After 3 h reaction, the catalyst was recycled from the

reaction mixture by centrifugation, washing with THF and acetonitrile, and drying overnight at 80 °C. The recovered Pd/NMC catalyst was subsequently reused for the hydrogenolysis of HMF.

***In situ* ATR-IR spectroscopy**

In situ ATR-IR spectroscopy was employed to monitor the reaction progress and to investigate the reaction pathways. The hydrogenolysis of HMF to DMF over Pd/NMC was carried out in a 300 mL stainless-steel autoclave (Berghof BR-300), and the *in situ* ATR-IR spectra were recorded every 2 min using a Mettler Toledo ReactIR^{TM} 15 spectrometer equipped with a 6.35 mm diameter Dicomp probe. Each spectrum was collected with a resolution of 4 cm^{-1} and 256 scans in the range of 650 to 4000 cm^{-1}.

In a typical run, 45 mmol HMF, 500 mg Pd/NMC catalyst, and the required amount of FA were dissolved in 120 mL THF. After purging with H_2, the reactor was pressurized with 10 bar H_2. The reaction was conducted at 160 °C and was monitored by *in situ* ATR-IR for 6 h. The reference spectra of the standard compounds (i.e., HMF, BHMF, 5-MF, and DMF) were recorded prior to the reaction separately.

Results

Characterization

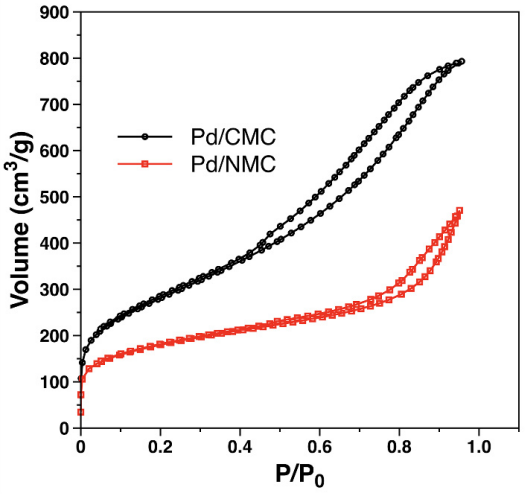

Figure S1. N_2 physisorption isotherms of Pd/NMC and Pd/CMC.

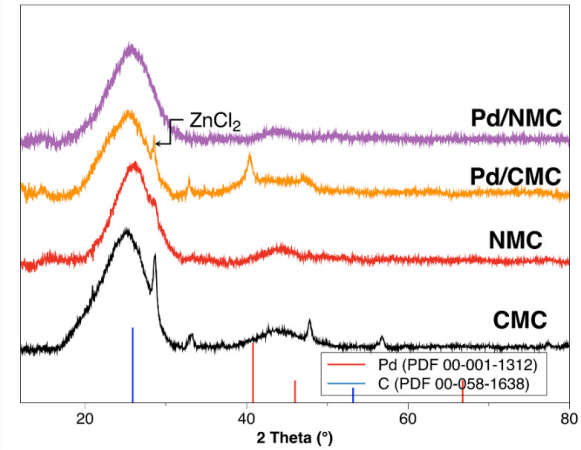

Figure S2. XRD patterns of Pd/NMC, Pd/CMC and the mesoporous carbon supports

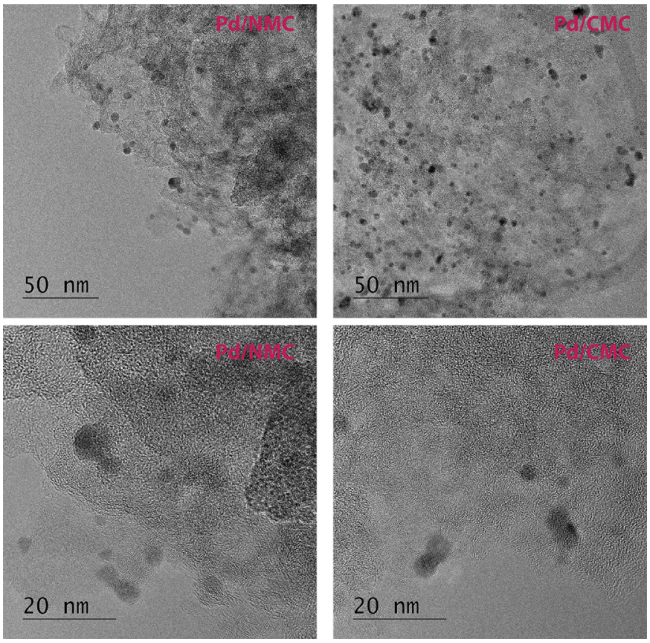

Figure S3. TEM images for Pd/CMC and Pd/NMC as prepared.

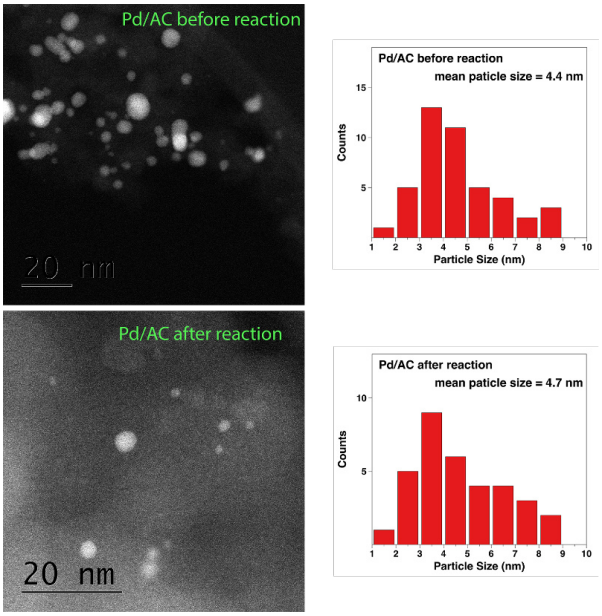

Figure S4. HAADF-STEM images and Pd particle size distributions for Pd/AC before and after reaction.

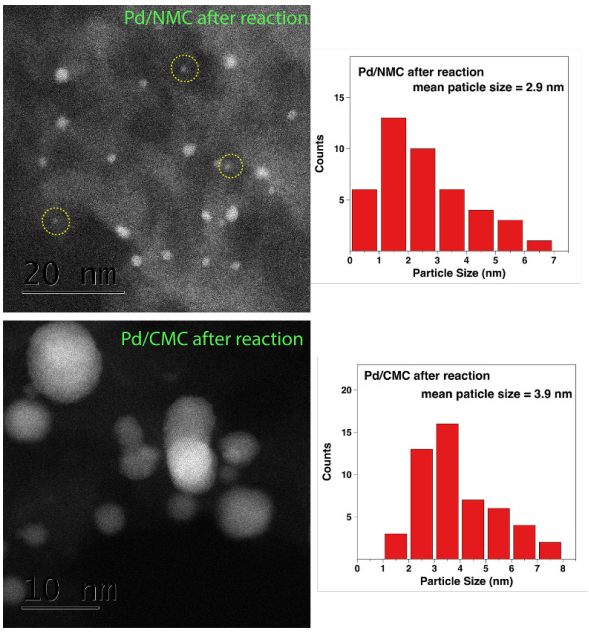

Figure S5. HAADF-STEM images and Pd particle size distributions for Pd/NMC and Pd/CMC after reaction in the presence of FA and H_2. The yellow circles refer to sub-1 nm Pd NPs or clusters.

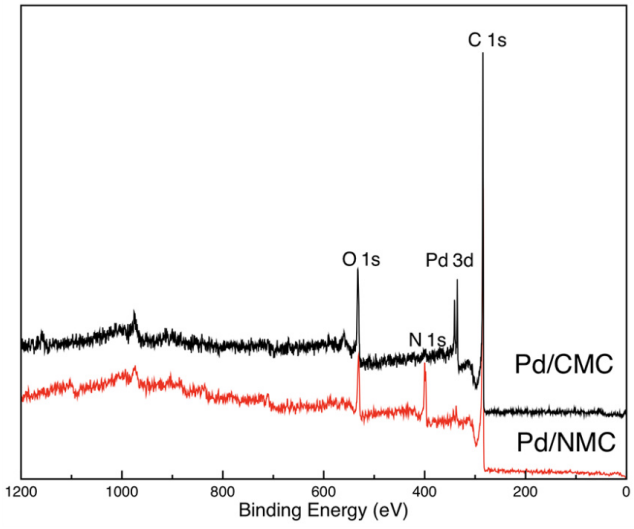

Figure S6. XP survey spectra of Pd/NMC and Pd/CMC as prepared.

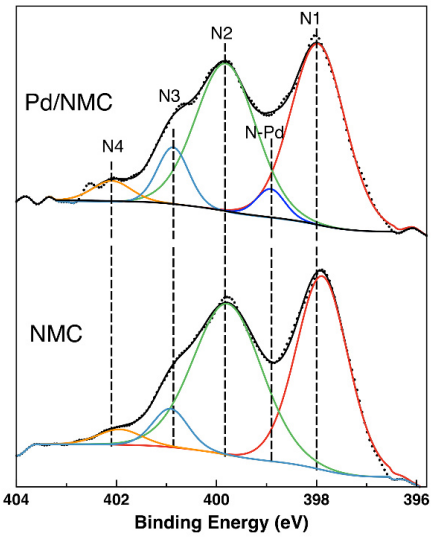

Figure S7. N 1s regions of the deconvoluted XPS results for NMC and Pd/NMC as prepared.[5]

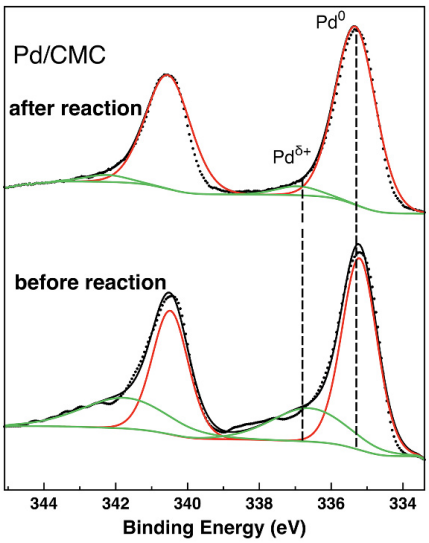

Figure S8. Pd 3d regions of the deconvoluted XPS results for Pd/CMC before and after reaction in the presence of FA and H_2. The XPS spectrum of Pd/CMC before reaction was reported in our previous report.[5]

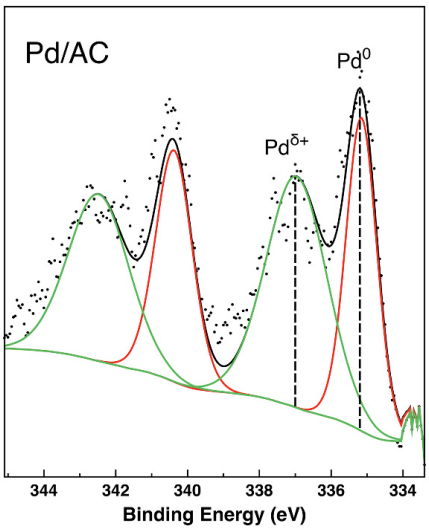

Figure S9. Pd 3d regions of the deconvoluted XPS results for Pd/AC as prepared.

Table S1. Relative abundance (%) of the components in the Pd $3d_{5/2}$ spectra

Sample	component/binding energy (eV)		
	Pd^0 335.0-335.5	$Pd^{\delta+}$ 336.5	Pd^{2+} 337.9
Pd/NMC before reaction	36	14	50
Pd/NMC after reaction	59	11	30
Pd/CMC before reaction*	68	32	–
Pd/CMC after reaction	91	9	–
Pd/AC before reaction	43	57	–

* The results of Pd/CMC before reaction was reported in our previous report[5]

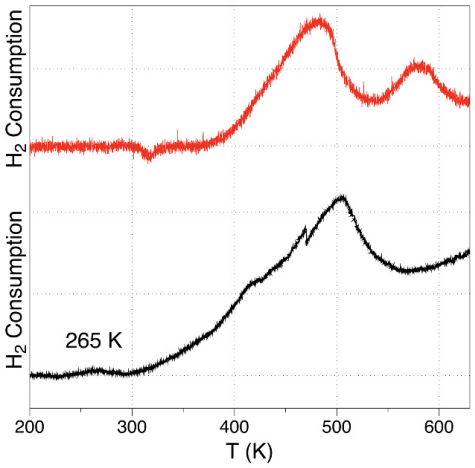

Figure S10. H_2 TPR profiles of Pd/NMC (black line) and Pd/CMC (red line).

The H_2 TPR profiles of the Pd/NMC and Pd/CMC are shown in Figure S10. For Pd/NMC, a reduction peak at 265 K is observed, owing to the reduction of $Pd^{\delta+}$ and Pd^{2+} to Pd^0. By comparison, this reduction peak is not observed for Pd/CMC, probably because the Pd NPs in Pd/CMC are mostly in the reduced metallic state (see Table S1) and the Pd loading is low. The large and broad peaks with onset temperature of 300 K for Pd/NMC and 375 K for Pd/CMC are the reduction of the surface functional groups of NMC and CMC, respectively. There is one negative peak at 315 K, which originates from the decomposition of palladium hydride. This palladium hydride peak is not observed for Pd/NMC, probably due to the overlapping with the broad reduction peak of the surface functional groups.

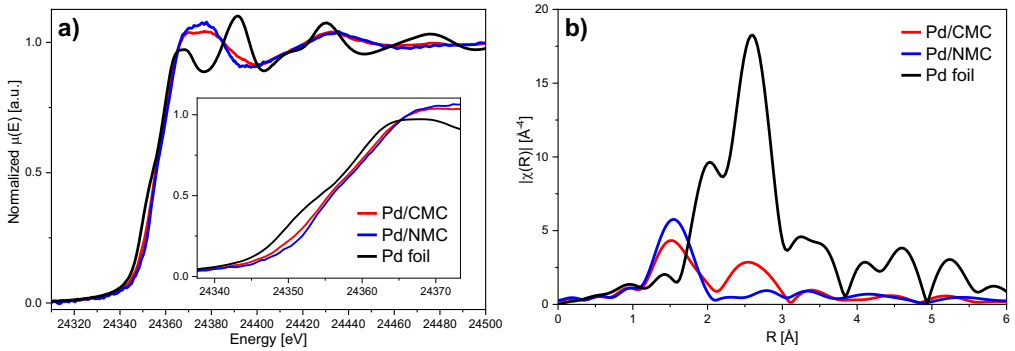

Figure S11. XANES (a) and Fourier-transformed EXAFS (b) spectra of Pd/CMC and Pd/NMC in comparison to a Pd foil. Note that no phase shift corrections have been applied and the real distances are expected to be ≈ 0.4 Å larger.

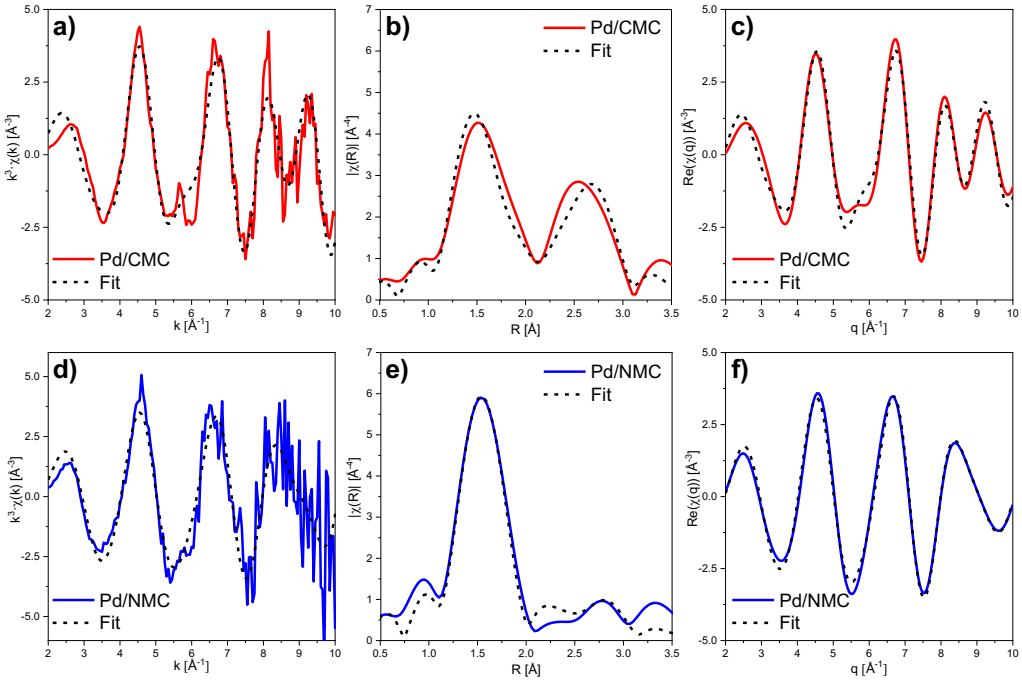

Figure S12. Comparison of experimentally obtained spectra and the corresponding best fit calculations of Pd/CMC (**a** - **c**) and Pd/NMC (**d** - **f**) materials. EXAFS spectra (**a**, **d**), Fourier-transformed EXAFS spectra (**b**, **e**) and the backtransformation thereof (**c**, **f**).

Table S2. Best fit values of Pd/CMC and Pd/NMC materials obtained by EXAFS structure fitting.

Sample	Abs-Bs[a]	N(Bs)[b]	R(Abs-Bs)[c] [Å]	σ^2 [d] [Å²]
Pd/CMC	Pd – O	3.45 ± 0.85	2.02 ± 0.02	0.0062 ± 0.0034
	Pd – Pd	1.96 ± 0.31	2.76 ± 0.03	0.0048*
	S_0^2 [e]= 0.820; ΔE_0 [f] = 6.56 ± 2.56 eV; χ^2_{red}[g] = 17; R[h] = 0.034; N(path)[i] = 2; N(par)[j] = 6; k-range: 2 - 10; R-range: 1 - 3.			
Pd/NMC	Pd – N	4.38 ± 0.52	2.06 ± 0.02	0.0031 ± 0.0012
	Pd – Pd	0.80 ± 0.20	2.76 ± 0.03	0.0048*
	S_0^2 [e]= 0.820; ΔE_0 [f] = 7.97 ± 1.34 eV; χ^2_{red}[g] = 1; R[h] = 0.011; N(path)[i] = 2; N(par)[j] = 6; k-range: 2 - 10; R-range: 1 - 3.			

[a] Abs = X-ray absorbing atom, Bs = backscattering atom. [b] Number of backscattering atoms. [c] Distance between absorbing and backscattering atom. [d] Debye-Waller factor. [e] Amplitude reduction factor. [f] Accounts for the shift of E_0 between theory and experiment. [g] Reduced χ^2 error (considers the number of independent points and number of varied parameters besides the error to the experiment). [h] Fit index. [i] Total number of fitted paths including single and multiple scattering paths. [j] Number of free parameters used for the fit. * Used as fixed parameter

The XANES spectra of both samples were significantly different from metallic palladium and showed a significant whiteline indicating that a major amount of palladium atoms was present in an oxidic state (Figure S11**a**). Furthermore, the edge position shifted to higher energies by approximately 2.5 eV (inset Figure S11**a**), which also suggested the presence of oxidic Pd centers. However, a larger shift of the edge (≈ 5 eV) would be expected for a completely oxidized material containing only Pd^{2+}.[6] Therefore, both materials contain a mixture of Pd^{2+}/$Pd^{\delta+}$ and Pd^0. In accordance with the XPS results, the slightly higher intensity of the whiteline and the slightly larger shift of the edge indicate that a larger fraction of Pd is oxidized in Pd/NMC compared with Pd/CMC.

For Pd/CMC, the Fourier-transformed EXAFS spectra (Figure S11**b**) showed the presence of two shells of backscatterers at 1.54 Å and close to 2.6 Å (note that no phase shift corrections have been applied and the real distances are expected to be ≈ 0.4 Å larger). The comparison to the Pd foil suggested that the shell at 2.6 Å corresponds to a shell of Pd backscatterers in the metallic state. In contrast, the shell at 1.54 Å is expected to be formed by light backscatterers like carbon or oxygen, which would be expected for Pd species that are anchored to the support. For Pd/NMC, also a shell at 1.54 Å from presumably light backscatterers was clearly present. However, the presence of a shell resulting from metallic Pd backscatterers cannot clearly be

confirmed solely by comparison of the spectra. A comparison to a Fourier-transformed EXAFS spectrum of PdO[7] confirmed that no PdO clusters were present in either sample.

In addition to the qualitative evaluation of the Fourier-transformed EXAFS spectra, we performed an EXAFS structure fitting to derive quantitative information about the local chemical environment around the Pd centers. For both materials, the best fits were obtained assuming two different shells of backscatterers (Table 3). The first shell consisted of light backscatterers (N, O or C) and was found at 2.02 and 2.06 Å for Pd/CMC and Pd/NMC, respectively. Although we have assumed oxygen and nitrogen neighbors for the respective materials during the fitting procedure, this technique cannot distinguish these elements due to their similar backscattering properties. The numbers of backscatterers close to 4 is in accordance with a square-planar coordination geometry, which is typically found for many palladium complexes. The second shell was found at 2.76 Å for both materials, which is consistent with Pd backscatterers in a Pd^0 crystal lattice. The number of Pd backscatterers (1.96 for Pd/CMC, 0.80 for Pd/NMC) is small compared to a bulk Pd crystal (expected: 12.0). Note that the small number of Pd backscatterers for Pd/NMC is significant to obtain a good fit. Due to the higher surface/bulk ratio in nanoparticles, the number of backscatterers strongly depends on the cluster diameter.[8] Therefore, the small number of Pd backscatterers suggested that very small Pd particles or clusters are present, which were already shown by the (S)TEM images. The smaller number of Pd backscatterers for Pd/NMC in comparison to Pd/CMC might indicate either a smaller average size of metallic Pd particles or a lower number of Pd^0 atoms, but these cases cannot be distinguished by the EXAFS analysis. Furthermore, a size approximation based on the EXAFS structure fitting was not reasonable, since it cannot fully be excluded that some isolated Pd^{2+} single atom species are present in the material, which would adversely affect the size determination. Nonetheless, the small number of backscatterers and the low intensity of the shell at 2.6 Å in the Fourier-transformed EXAFS spectra support the assumption of small Pd clusters in the lower nanometer regime.

Catalytic results

Table S3. Catalytic activity of different catalysts on HMF hydrogenolysis to DMF

Entry	Catalysts	Reactant	Hydrogen Source	Time (h)	T (°C)	Solvent	Conversion (mol %)	S_{DMF} (mol %)	TOF (h^{-1})	Ref.
1	Pd/NMC	HMF	FA+H_2	2	160	THF	> 99.9	> 97.0	150	T[a]
2	Pd/NMC	HMF	FA	3	160	THF	60.8	64.3	41	T[a]
3	Pd/CMC	HMF	FA+H_2	3	160	THF	90.1	80.0	75	T[a]
4	Pd/CMC	HMF	FA	3	160	THF	19.4	62.9	13	T[a]
5	Pd/C	FMF	FA	15	120	dioxane	> 95.0	> 95.0	1.2×10^{-3}	9
6	Pd/C	FMF	FA+H_2	15	120	dioxane	> 95.0	87.6	0.27×10^{-3}	9
7	Pd/C/Zn	HMF	H_2	8	150	THF	> 99.9	85.0	27.2	10
8	Ni-Co/C	HMF	FA	24	210	THF	> 99.0	90.0	0.1	11
9	Ru/MoO_x/C	HMF	H_2	1	180	n-butyl alcohol	> 99.0	79.8	21.3	12

[a] This work, reaction conditions: 1.5 mmol HMF, 50 mg catalysts, 30 mL THF, 160 °C, 2 or 3 h;

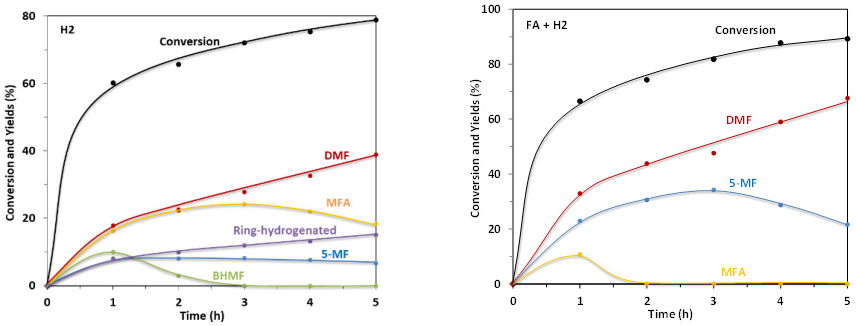

Figure S13. Time course of the hydrogenolysis of HMF to DMF over Pd/CMC with H_2 and with FA + H_2.

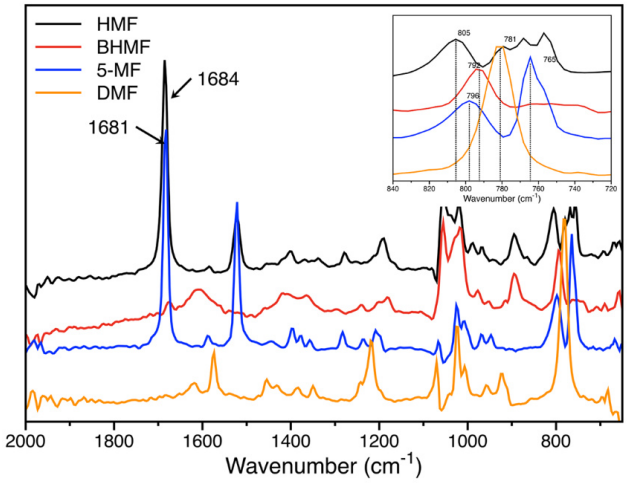

Figure S14. ATR-IR spectra of standard samples at 0.1 M in THF

Table S4. ATR-IR absorption bands of the standard samples in THF

	ν(C=O) (cm^{-1})	ν(C=C) (cm^{-1})	ν(C−H) (cm^{-1})
HMF	**1684**	**1520**	**805,779,767,756**
BHMF	**-**	**1608**	**792**
5-MF	**1681**	**1520**	**796,765**
DMF	**-**	**1573**	**781**

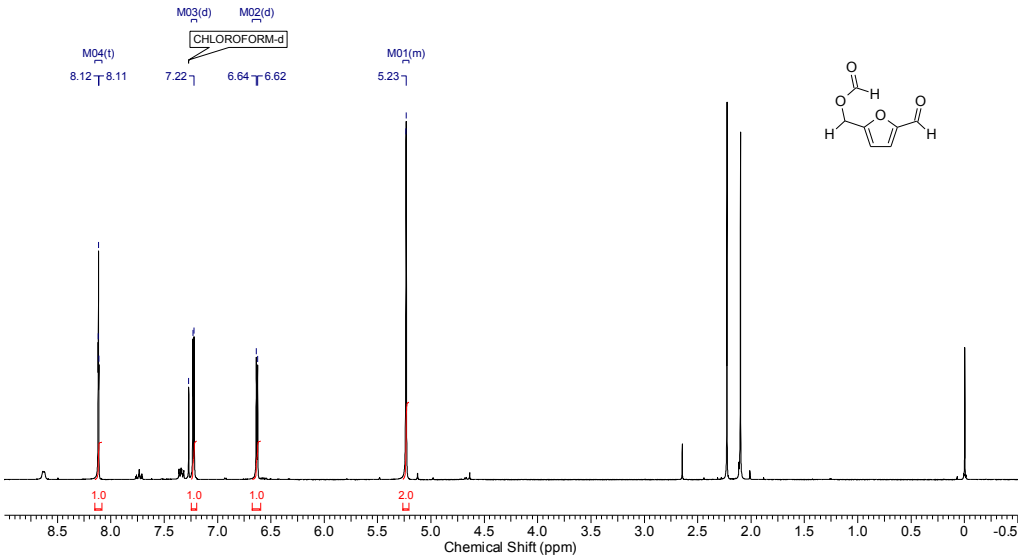

Figure S15. ^{1}H NMR spectrum of FMF, ^{1}H NMR (300 MHz, *CHLOROFORM-d*) δ ppm 8.65 (s, 1 H), 8.12 (t, *J*=0.9 Hz, 1 H), 7.22 (d, *J*=3.6 Hz, 1 H), 6.63 (d, *J*=3.5 Hz, 1 H), 5.21 - 5.26 (m, 2 H).

Computational

Methodology

The quantum chemical study was performed using density functional theory (DFT) with the TPSS[13] functional and def2-SVP[14] basis set, which includes Stuttgart-Cologne effective core potentials (def2-ecp)[15] for the Pd atoms. All calculations were carried out using the TURBOMOLE[16] program package with the multipole accelerated resolution of identity (MARI-J)[17] approximation with optimized auxiliary basis sets[18] and Grimme's D3[19] correction for London dispersion interactions.

The model of Pd/CMC, a Pd_{21} cluster on a hydrogen terminated graphene layer of 150 carbon atoms, has been shown to be a reasonable choice in a previous study.[20] For the bifunctional Pd/NMC system, three carbon atoms of the Pd/CMC system were replaced by nitrogen atoms. The most stable structures of these models as well as the minima of formic acid and hydrogen on these systems were determined by ground-state geometry optimizations. For relative energies, the zero-point vibrational energy (ZPVE) corrections from vibrational analysis were included. As the potential energy surfaces of the Pd/CMC and Pd/NMC systems are often very flat, the vibrational analysis of some systems still shows one (very small) negative frequency. We expect the errors introduced by this to be negligible. For determining reaction pathways and locating initial transition state structures the chain-of-state method implemented in the woelfling module of TURBOMOLE[21] was used. The initial transition state structures were then further optimized with the eigenvalue following trust-region image minimization (TRIM)[22] algorithm and validated by intrinsic reaction coordinate (IRC)[23] calculations. Adsorption energies and dissociation energies are provided with a negative sign, while energy barriers like activation barriers have a positive sign. Atomic charges were determined using natural population analyses (NPAs).[24]

Table S5. Adsorption energies of FA on Pd_{21}

Model system	FA configuration	ΔE_{ads} / kJ mol^{-1}
Pd_{21}/CMC	C=O binding	-129.6
Pd_{21}/CMC	C atom binding	-75.5
Pd_{21}/NMC	C=O binding	-132.5
Pd_{21}/NMC	C atom binding	not stable[a]

[a] For the C atom binding on Pd_{21}/NMC only configurations with imaginary frequencies were found.

Table S6. Dissociation energies of H_2 on Pd_{21} in kJ mol^{-1}

Model system	H atom configuration	TPSS/ def2-SVP	TPSS/ def2-TZVP	PBE/ def2-SVP
Pd_{21}/CMC	2 H in fcc positions	-111.1	-94.9	-122.0
Pd_{21}/CMC	1 H in fcc, 1 H at the edge	-96.0	-86.0	-116.8
Pd_{21}/NMC	2 H in fcc positions	-118.9	-112.4	-131.2
Pd_{21}/NMC	1 H in fcc, 1 H at the edge (close to Pd^{2+})	-116.9	-111.2	-129.1
Pd_{21}/NMC	1 H in fcc, 1 H at the edge (far from Pd^{2+})	-112.6	-108.2	-126.1

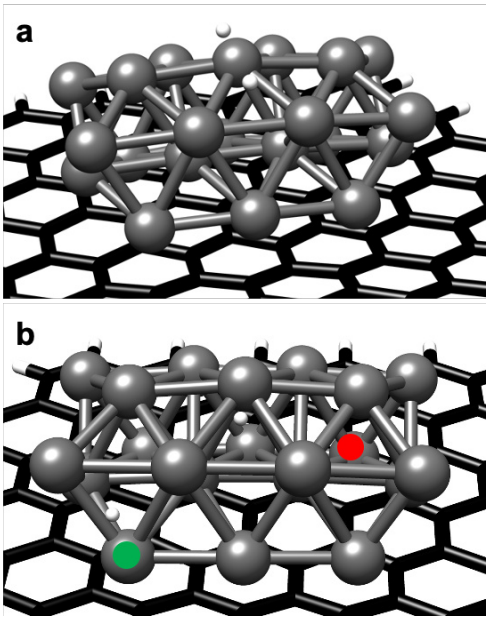

Figure S16. H atom configurations on Pd_{21}/CMC: (a) 2 H in fcc positions; (b) 1 H in fcc, 1 H at the edge. For Pd_{21}/NMC: lower left Pd atom (green; close) or back right Pd atom (red; far) is connected to 2 pyridinic N atoms.

References

1. Y. A. Huang, S. Hu, S. Zuo, Z. Xu, C. Han, J. Shen, *J. Mater. Chem.* **2009**, *19*, 7759-7764.
2. Y. A. Huang, F. Yang, Z. Xu, J. Shen, *J. Colloid Interf. Sci* **2011**, *363*, 193-198.
3. E. Welter, R. Chernikov, M. Herrmann, R. Nemausat, *AIP Conf. Proc.* **2019**, *2054*, 04002.
4. B. Ravel, M. Newville, *J. Synchrotron Rad.* **2005**, *12*, 537-541
5. L. Warczinski, B. Hu, T. Eckhard, B. Peng, M. Muhler, C. Hättig, *Phys. Chem. Chem. Phys.* **2020**, *https://doi.org/10.1039/D0CP03234D*.
6. K. A. Karinshak, P. Lott, M. P. Harold, O. Deutschmann, *ChemCatChem* **2020**, *12*, 3712-3720.
7. K. Okumura, J. Amano, N. Yasunobu, M. Niwa, *J. Phys. Chem. B* **2000**, *104*, 1050–1057.
8. A. Jentys, *Phys. Chem. Chem. Phys.* **1999**, *1*, 4059-4063
9. J. Mitra, X. Zhou, T. Rauchfuss, *Green Chem.* **2015,** *17*, 307-313.
10. B. Saha, C. M. Bohn, M. M. Abu-Omar, *ChemSusChem* **2014,** *7*, 3095-3101.
11. P. Yang, Q. Xia, X. Liu, Y. Wang, *Fuel* **2017,** *187*, 159-166.
12. Y. Yang, Q. Liu, D. Li, J. Tan, Q. Zhang, C. Wang, L. Ma, *RSC Advances* **2017,** *7*, 16311-16318.
13. J. Tao, J. P. Perdew, V. N. Staroverov, G. E. Scuseria, *Phys. Rev. Lett.* **2003,** *91* (14), 146401.
14. F. Weigend, R. Ahlrichs, *Phys. Chem. Chem. Phys.* **2005,** *7* (18), 3297-3305.
15. D. Andrae, U. Häußermann, M. Dolg, H. Stoll, H. Preuß, *Theor. Chim. Acta* **1990,** *77* (2), 123-141.
16. Turbomole V7.3 2018, a development of University of Karlsruhe and Forschungszentrum Karlsruhe GmbH, 1989-2007, TURBOMOLE GmbH, since 2007, available from http://www.turbomole.com.
17. M. Sierka, A. Hogekamp, R. Ahlrichs, R., *J. Chem. Phys.* **2003,** *118* (20), 9136-9148.
18. F. Weigend, *Phys. Chem. Chem. Phys.* **2006,** *8* (9), 1057-1065.
19. S. Grimme, J. Antony, S. Ehrlich, H. Krieg, *J. Chem. Phys.* **2010,** *132* (15), 154104.
20. L. Warczinski, C. Hättig, *Phys. Chem. Chem. Phys.* **2019,** *21* (38), 21577-21587.
21. P. Plessow, *J. Chem. Theory Comput.* **2013,** *9* (3), 1305-1310.
22. T. Helgaker, *Chem. Phys. Lett.* **1991,** *182* (5), 503-510.
23. K. Fukui, *Acc. Chem. Res.* **1981,** *14* (12), 363-368.
24. A. E. Reed, R. B. Weinstock, F. Weinhold, *J. Chem. Phys.* **1985,** *83* (2), 735-746.

Supporting Information
How N Doping Affects Hydrogen Spillover on Carbon-Supported Pd Nanoparticles: New Insights from DFT

Lisa Warczinski[a,*], Christof Hättig[a]

[a]*Chair of Theoretical Chemistry, Ruhr-University Bochum, Universitätsstraße 150, 44780 Bochum, Germany*

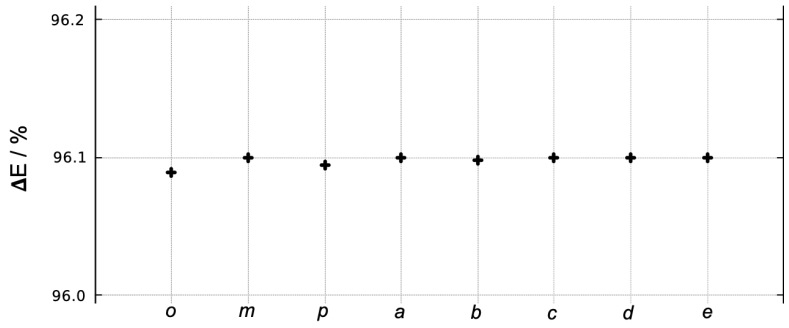

Figure S1: Correlation of Hückel binding energies and DFT energies for the different positions of spillover hydrogen with respect to graphitic N.

model system	TPSS/ def2-SVP	PBE/ def2-SVP	TPSS/ def2-TZVP
Pd_{21} on graphene support; triangle site	130.8	130.7	127.5
Pd_{21} on graphitic N support; bridge site	46.8	45.5	46.3

Table S1: Comparison of activation energies for the hydrogen spillover from Pd_{21} onto different support materials on the basis of TPSS/def2-SVP geometries.

*Corresponding author at: Chair of Theoretical Chemistry, Ruhr-University Bochum, Universitätsstraße 150, 44780 Bochum, Germany

Email address: lisa.warczinski@rub.de (Lisa Warczinski)

pathway	TPSS/ def2-SVP	PBE/ def2-SVP	TPSS/ def2-TZVP
a	105.0	94.3	106.6
b	121.5	114.5	120.1

Table S2: Comparison of activation energies for spillover hydrogen diffusion on different support materials on the basis of TPSS/def2-SVP geometries.

model system	TPSS/ def2-SVP	PBE/ def2-SVP	TPSS/ def2-TZVP
pure graphene support	68.5	76.6	66.5
graphitic N support	107.6	114.0	106.5

Table S3: Comparison of activation energies for the change from the chemisorbed to the physisorbed state on the basis of TPSS/def2-SVP geometries.

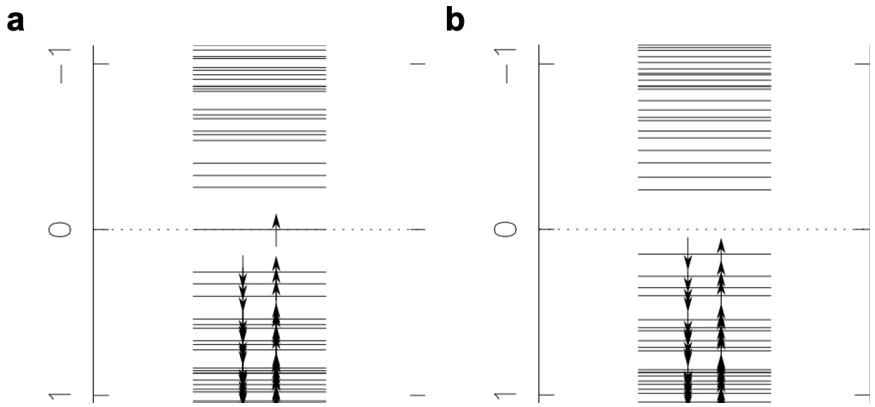

Figure S2: Sketch of Hückel orbitals: (a) one spillover hydrogen connected to one carbon atom of the graphene sheet; (b) one spillover hydrogen connected to one carbon atom directly next to a graphitic N atom.

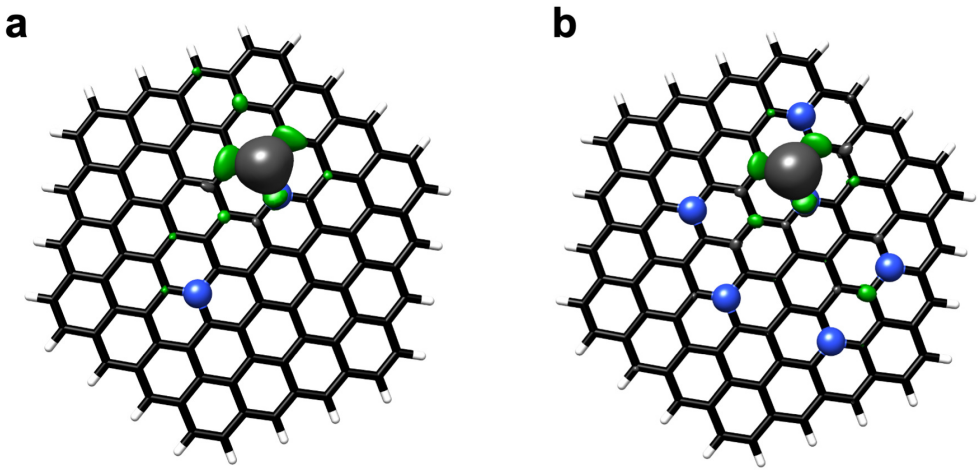

Figure S3: Electron density difference plots for spillover hydrogen on the graphitic N support material: (a) two graphitic N atoms; (b) six graphitic N atoms. Density gain is colored in green; density loss is colored in grey.

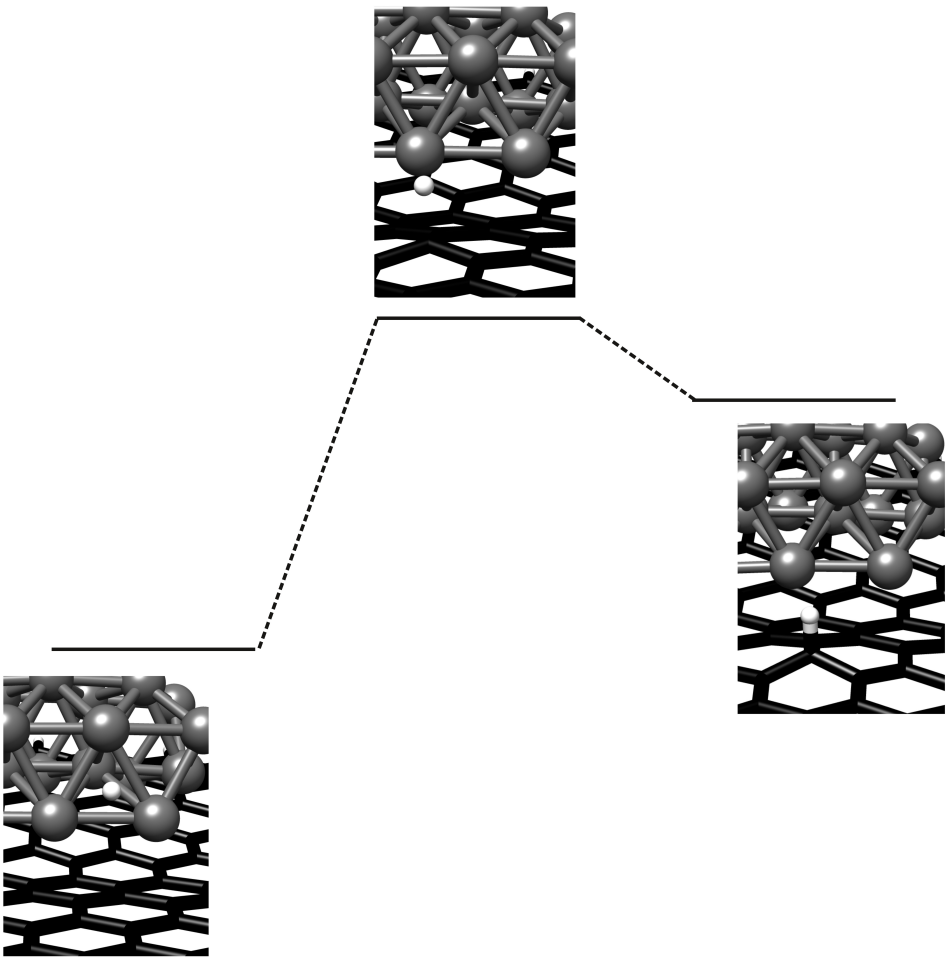

Figure S4: Hydrogen spillover pathway from Pd_{21} to the pure graphene support material.

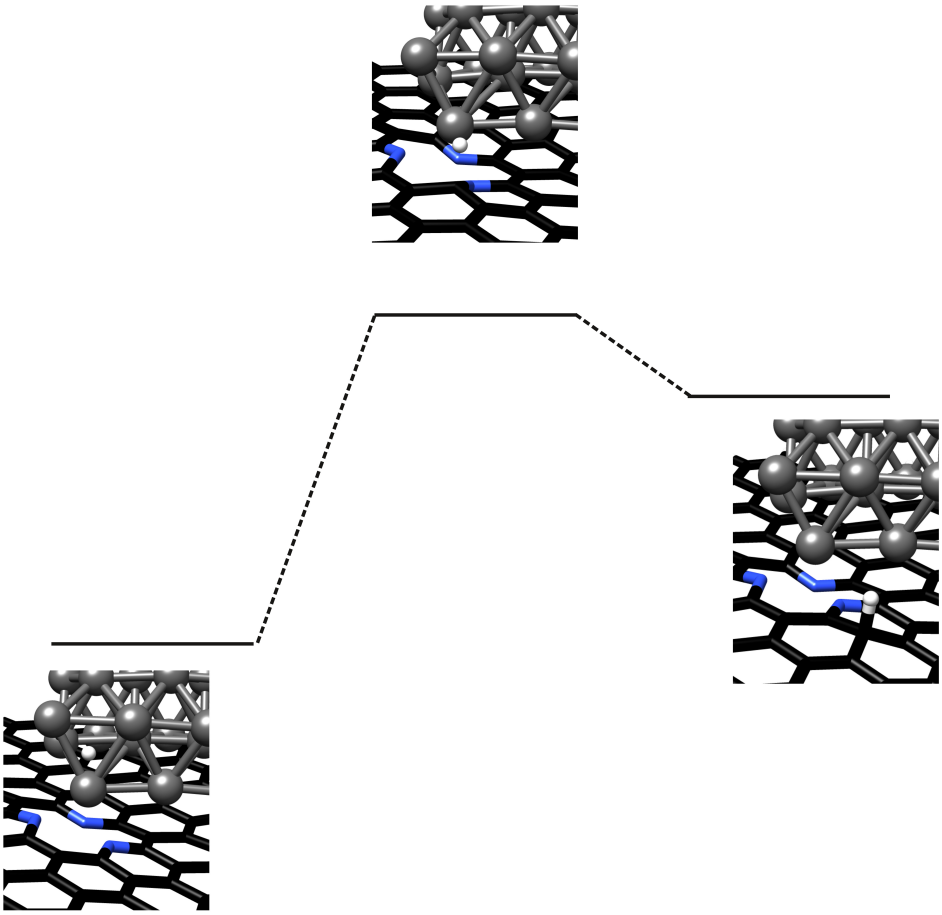

Figure S5: Hydrogen spillover pathway from Pd_{21} to the pyridinic N support material.

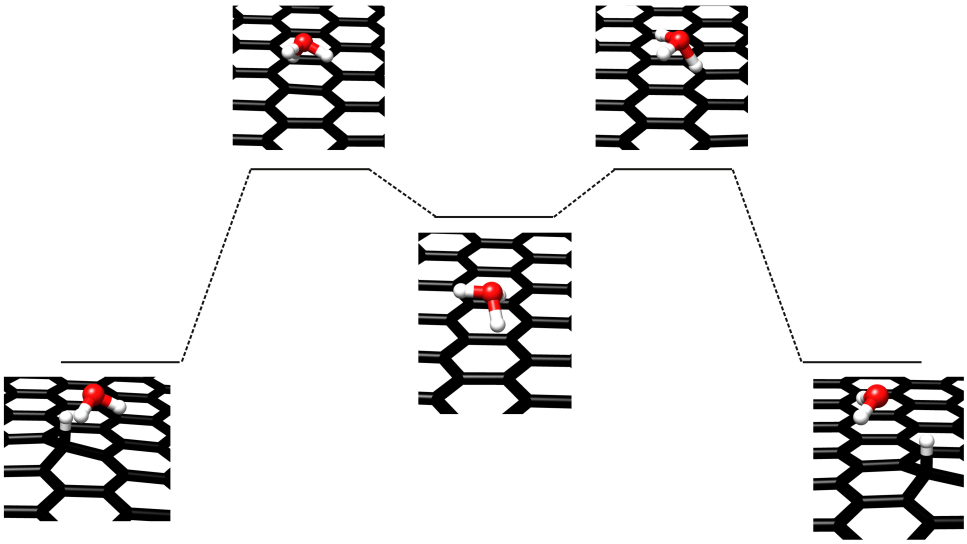

Figure S6: Reaction pathway for spillover hydrogen diffusion via the Grotthus mechanism.

	ΔE/kJ mol^{-1}	ΔG/kJ mol^{-1}
React. - TS 1	+66.2	+77.7
TS 1 - Min.	-6.1	-1.4
Min. - TS 2	+5.9	+0.4
TS 2 - Prod.	-59.9	-73.4

Table S4: Energies and free activation enthalpy differences for spillover hydrogen diffusion via the Grotthus mechanism.

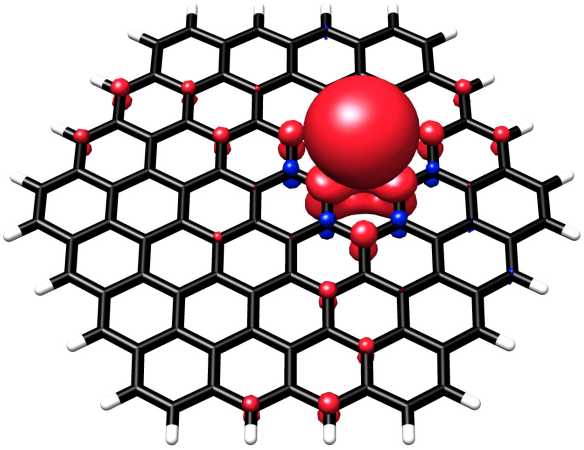

Figure S7: Plot of the spin density for spillover hydrogen in the physisorption minimum.

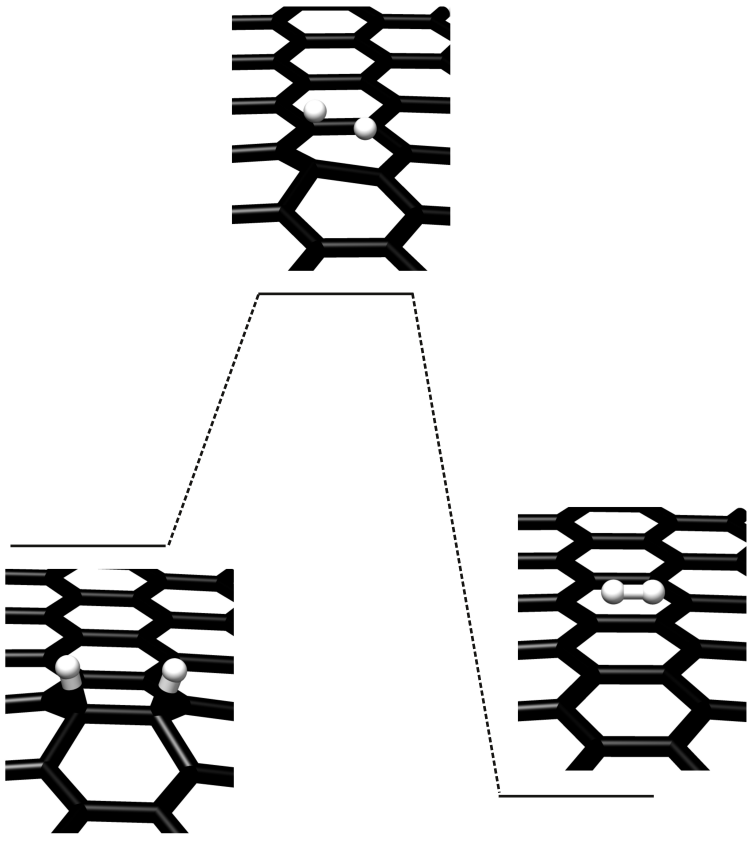

Figure S8: Hydrogen desorption pathway on the pure graphene support.

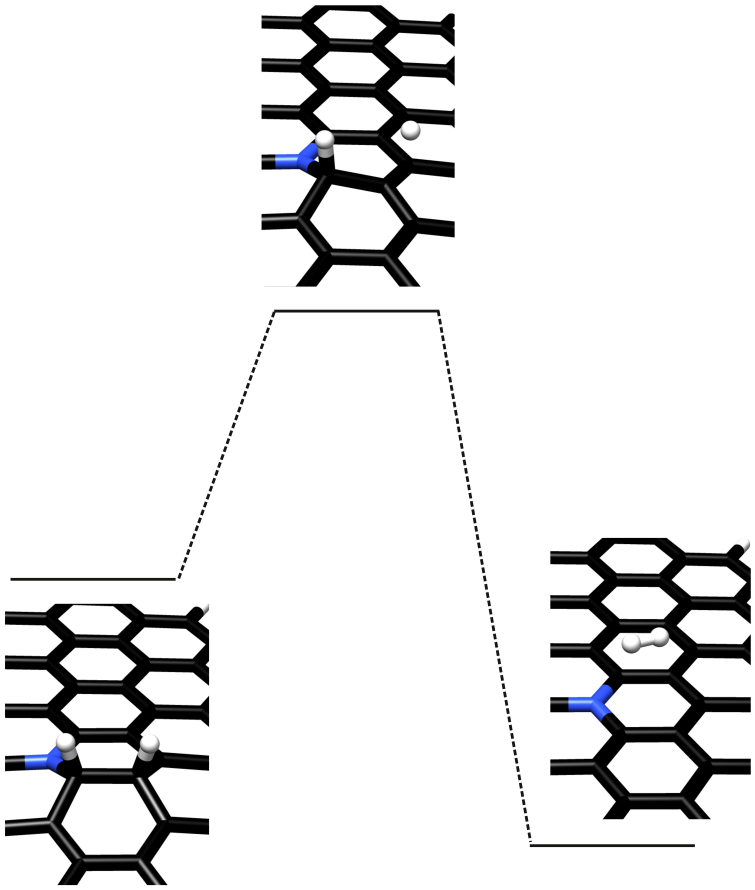

Figure S9: Hydrogen desorption pathway next to a graphitic N atom.

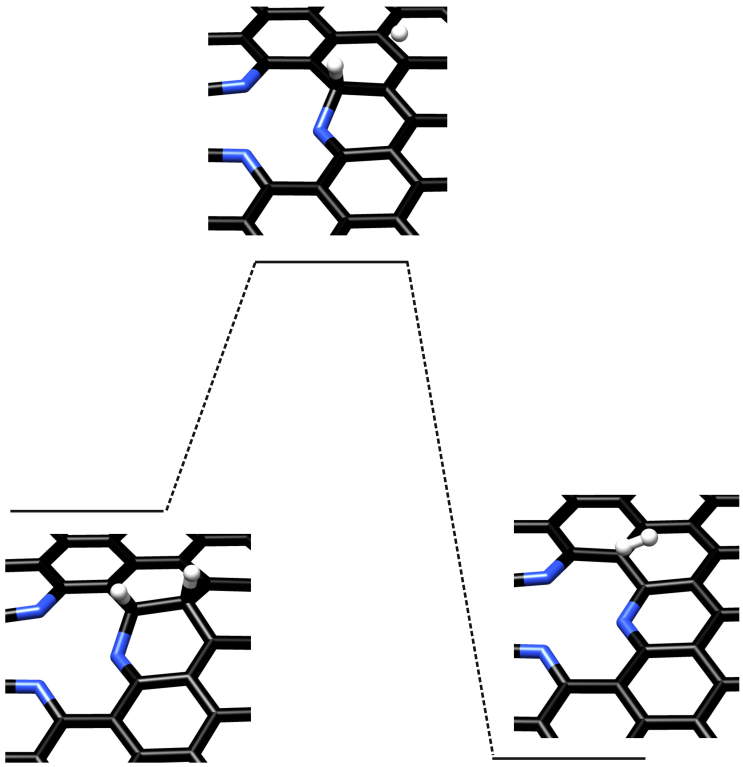

Figure S10: Hydrogen desorption pathway next to a pyridinic N atom.